# Development of a Microchip-Based Flow Cytometer with Integrated Optics – Device Design, Fabrication, and Testing

# Development of a Microchip-Based Flow Cytometer with Integrated Optics – Device Design, Fabrication, and Testing

**By:**

**Benjamin Robert Watts, B. Eng & Mgmt.**

**A Thesis**
**Submitted to the School of Graduate Studies**
**In Partial Fulfillment of the Requirements**
**for the Degree**
**Doctor of Philosophy**

**McMaster University**

| | |
|---|---|
| **DOCTOR OF PHILOSOPHY (2012)** | **McMaster University** |
| **(Engineering Physics)** | **Hamilton, Ontario** |

| | |
|---|---|
| **TITLE:** | **Development of a Microchip-Based Flow Cytometer with Integrated Optics – Device Design, Fabrication, and Testing** |
| **AUTHOR:** | **Benjamin Robert Watts, B. Eng & Mgmt (McMaster University)** |
| **SUPERVISORS:** | **Professor Chang-Qing Xu, Professor Zhiyi Zhang** |
| **NUMBER OF PAGES:** | **xix, 254.** |

## ABSTRACT

Lab-on-a-chip technologies have created a burgeoning number of new and novel devices designed to automate biological processes on-chip in an efficient and inexpensive format. Applications of the new devices have far reaching point-of-care (POC) medicine and diagnostic treatments and for remote and on-line monitoring functions. We have designed a device that has incorporated an advanced optical function via integrated on-chip with the microfluidics that relieves the reliance on traditional bulky and expensive free-space optics and a high-quality light source. The beam is reshaped to an optimized geometry in the microchannel via a 2D system of lenses fabricated between the waveguide and channel - improving the quality and reliability of detection through uniform detection of particles. Numerous beam geometries were created and the quality and spot properties confirmed by testing eac with a couple sizes of fluorescent and non-fluorescent microspheres to test the effect of beam geometry and particle size combination on device performance. The measured coefficient of variation (CV) for fluorescent beads was found to have a particular beam geometry that yielded best device performance based on the bead size. Fluorescent beads 2.5μm in diameter had a CV of 8.5% for a 3.6 μm beam waist while 6 μm beads yielded a 14.6% CV with a 10 μm beam waist. When measuring scatter and fluorescence signal from a 10 μm the 2.5- and 6.0 μm beads gave 11.4% and 15.8% and 15.9% and 20.4% fluorescent and scatter CVs for each set of beads, respectively. Separately testing each beam geometry with 1-, 2-, and 5 μm beads did not yield any predictable ideal beam-bead ideal pairing for best performance. Lastly, further integration of optical function was shown through the on-chip collection of signals; CVs of 29% and 30% were measured for side scatter and forward scatter, respectively, for 5 µm beads.

## ACKNOWLEDGEMENTS

I would like to thank my co-supervisors, Dr. Zhiyi Zhang and Dr. C-Q. Xu, for the support, guidance, and many lessons I have learned during the course of this work. My knowledge of, and tact at applying my craft has been developed and honed by both of you sharing your patience, wisdom, and vision with me.

I would also like to thank Dr. Shiping Zhu, Dr. Dong-qing Li, Jian Sun, Ping Zhao, and Canjun Mu who all engaged me in constructive discussions and provided help where necessary during the course of this work.

Thanks to Jeanette Beaudreau for providing data from the conventional flow cytometer at McMaster, and for helpful discussions of potential device applications.

I extend my deepest thanks to Thomas Kowpak, for being an amazing friend, colleague, teacher of fabrication techniques, and showing me how to keep my sanity through fantasy hockey.

Mike D – thank you for taking in a penniless drifter and providing a bed during the awkward periods when I didn't know whether I lived in Ottawa or Hamilton.

To Julie (and the entire Byrnes/Maurice/Bleser clan); you are a great friend and thank you for all the support and encouragement and for being a rock through all the ups and downs.

Sarah, thank you for coming along at just the right time to provide me with inspiration, love, and sanity. Thank you for never questioning me, accepting a lifelong student, and for being who you are.

Finally, to my family - who never once questioned why I chose this path (even though you could have) and for unrelenting support, and the unwavering expectation that I could do this - thank you.

# CONTENTS

## LIST OF FIGURES

## LIST OF TABLES

# 1 INTRODUCTION

This research is concerned with adapting a conventional flow cytometer to a microfluidics-based device with integrated optics. A microchip-based flow cytometer utilizes microfabrication techniques and the benefits that come with device miniaturization to design device for novel, new, and far reaching applications while attempting to mimic the functionality of the conventional device. Formed devices lead to an inexpensive and portable solution for applications where cost and device reach are the prominent restrictions.

## *1.1 Conventional Flow cytometry*

Flow cytometry is a very powerful analytical technique that allows the cell-by-cell analysis of a population yielding very accurate population-wide metrics.[1] It is accomplished via a sample flown in a very narrow stream (from hydrodynamic focusing) past an interrogation point whose function is usually through optical processes. The individual specimen's unique interaction with the light produces a very specific signature that is characteristic of the particular cell. This signature varies according to the variation of the parameters being measured. Due to the fact that flow cytometry analyzes individual cells as they flow past an interrogation point, and that there are multiple wavelengths simultaneously detected, flow cytometry is able to fully characterize a large population of cells very accurately from the many different simultaneously measured parameters. The speed of analysis due to the flow of the cells and the multi-parametric analysis capabilities give flow cytometry its analytical power. This enables cytometers to discern the tiniest differences from a perceived homogeneous population, and visa versa. Decision criteria for cell sorting is accomplished via analysis of parameters determined from a flow cytometric function and the fast counting techniques eliminates the painstaking labour involved in manual counting.

Analysis techniques of flow cytometry allows the measurement of many individual cell parameters ranging from the size, shape, cell viability, DNA quantity and sequence, cell surface markers, life cycle distribution, and protein content.[*]

### 1.1.1 Basic systems of a flow cytometer

A flow cytometer is the interconnection of four basic subsystems working in conjunction or in parallel with one-another: the flow cell, the optical excitation system, the optical collection system, and the data acquisitions and analysis software. A typical conventional cytometer – with all the subsystems – is shown in Figure 1-1.[2]

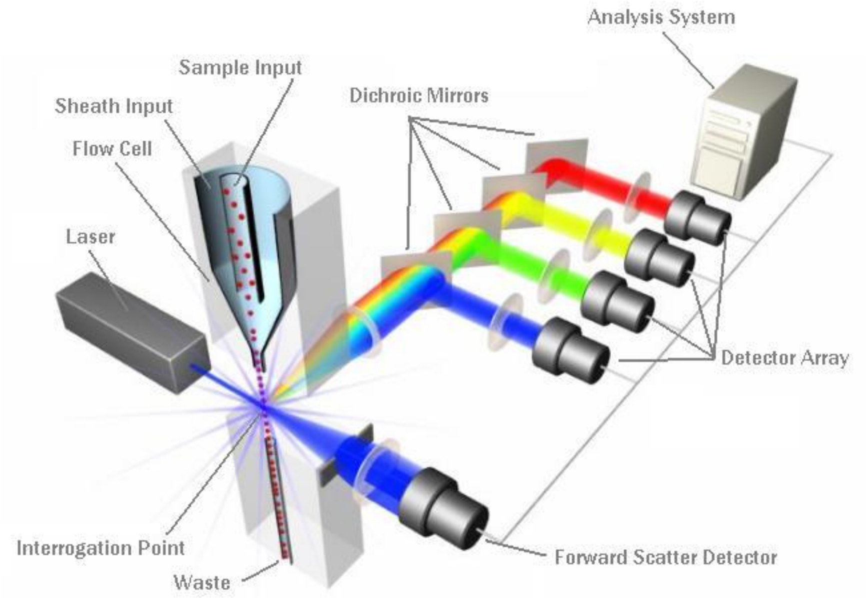

**Figure 1-1: Schematic showing the components and configuration of a typical flow cytometer; showing the flow cell with hydrodynamic focusing, excitation optics, collection optics, and a detection and analysis system. *Source:* Reprinted from reference 2.**

#### 1.1.1.1 Flow Cell

The primary function of the flow cell is to handle the fluids involved with analysis and to deliver the sample from the source to the interrogation point - the point where the excitation beam and sample stream intersect - and past to waste or to

---

[*] This paragraph has been adapted from the authors work in reference 1.

further function via sorting and sequestering. A flow cell may consist of a network of tubes – called microcapillaries – that are often of a size of 10s to 100s of microns, and can serve simple functions to mix, separate, focus, and sort the cells as needed.

A typical flow cell consists of a set of two concentric tubes as shown in Figure 1-1, with a detailed cross-section in Figure 1-2.[3] These figures show the important function of how the fluids come together. The sample fluid, consisting of the prepared cells and analytes, is injected via the inner tube while the concentric outer tube injects an annulus of fluid to focus the sample fluid. This outer fluid, known as a sheath fluid, serves no other purpose than to sever as a buffer for hydrodynamically focusing the sample to a narrow stream in the centre of the tube. Adjusting the flow between the two fluids allow the sample stream width to be controlled so that the stream is approximately one specimen size in diameter – forcing the specimens into a single file flow.

### *1.1.1.1.1 Hydrodynamic focusing*

As mentioned in the previous section, hydrodynamic focusing is the process whereby a sample fluid can be squeezed into narrow stream via fluidic pressure from barrier fluids. This process occurs due to the small capillary tube diameter; the Reynolds number is very low and keeps the fluid flow within the laminar flow regime.[3] A laminar flow regime eliminates mixing of the fluid via turbulent flow. The only mixing mechanism is diffusion which is typically a slow process and can be ignored for most practical channel lengths.

In the flow cell, the sample fluid is squeezed to a tiny narrow stream bounded by the sheath fluid, as shown in Figure 1-2.[3] The purpose of focusing the sample fluid is to limit the physical deviation of the specimens within the channel and to ensure that every specimen in the sample takes a nearly identical path through the optical excitation region. Identical travel though the interrogation region ensures repeatable and uniform excitation of the specimen leading to reliable detection.

For these reasons, hydrodynamic flow is a necessity for reliable flow cytometric function and has been used for decades starting with the earliest devices.[4]

The velocity profile is parabolic in shape and can lead to issues with shear forces at the fluid-fluid interface. These forces can lead to cell death at extremely large fluid pressures and at the resulting high velocities. Thus, very narrow stream widths are difficult to achieve; a delicate balance needs to be struck between confining the cells in a narrow stream and the amount of deviation that can be tolerated by the detection method. The optical interrogation can tuned to correct for relaxed hydrodynamic focus flow.

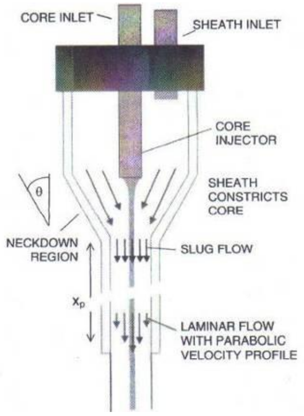

**Figure 1-2: Detailed drawing of an injection nozzle from a conventional flow cell showing how a sample fluid is focused to a narrow stream. Note the velocity profile of the stream is a parabolic shape throughout the tube. *Source:* Reprinted from reference 3.**

### 1.1.1.2 Optical Excitation System

Excitation of the specimens is achieved via optical interrogation methods. One or multiple lasers of different wavelengths are deployed to perform excitation as they each provide a very narrow spectrum of light. This narrow spectrum will limit the wavelengths present in the detection scheme so as they will not interfere with the intended wavelengths of light during detection – as will be discussed in 1.1.1.3.

Furthermore, a laser source provides a high quality beam profile in the shape of a Gaussian distribution. This predictable shape makes it easier to reshape the beam and provide a predictable excitation intensity across the sample stream; a process called beam shaping that will be discussed in 1.1.1.2.1. Figure 1-3[5] shows the excitation beam integrated with a flow cell illustrating the flow of particles past the excitation beam. The sample stream and the excitation beam have an angle of intersection of 90° so that one cell is illuminated at a time. This beam is focused by the beam shaping optics to form a predictable excitation region across the sample stream.

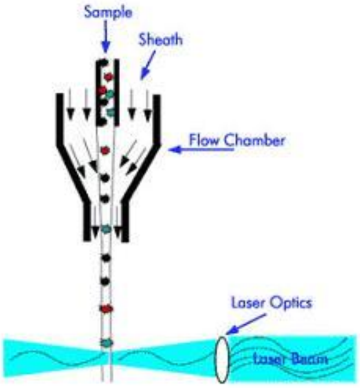

**Figure 1-3: A simplified picture of the flow cell and excitation systems of a flow cytometer – a focused flow of particles past a shaped laser beam – showing a close up of the injection nozzle and the interrogation point where the fluid intersects with a focused excitation laser. *Source:* Reprinted from reference 5.**

### 1.1.1.2.1 Beam shaping

Beam shaping is the ubiquitous practice of reshaping the laser beam to a specific spot geometry in the middle of the channel where the stream of particles intersects and traverses the beam. The ultimate goal of beam shaping is to form a uniform spot of intensity across the stream to ensure each specimen receives the same dose of optical intensity. This ensures that identical particles will emit identical signals for detection. With this reliable detection, any variance in the detected signal is now strongly correlated with parameter variances leading to a more accurate analysis. Through control of the beam waist in the direction of fluid flow the length and time of illumination of specimens can be adjusted. Control of the depth of focus of the beam in a direction perpendicular to fluid flow defines the uniformity of intensity across the sample stream and thus, all the possible trajectories a specimen might traverse through the beam. Through this two dimensional control of the beam one can control the width and intensity of the bursts of light that are emitted from specimens.

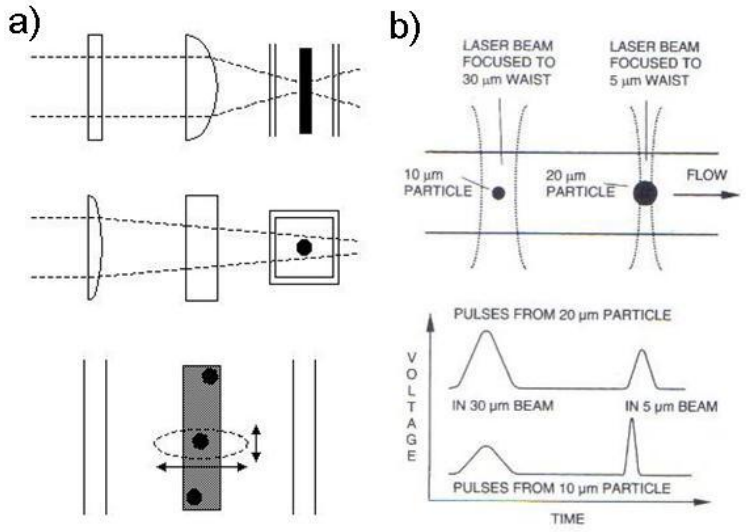

**Figure 1-4: a) Multi-view diagram showing how cross-cylindrical lenses produce a focused spot in the middle of the channel with independent control of the two directions. The result is a spot size of elliptical shape. b) Diagram showing how the spot size affects the measured signals from different sized particles.** ***Source*****: Reprinted from reference 3.**

To shape the beam in the sample stream, conventional cytometers use a system of crossed cylindrical lenses as shown in Figure 1-4a).[3] As each lens controls the refraction of the light in directions that are orthogonal to one another, beam shaping thus allows independent control of the beam's properties in two orthogonal directions. Focusing in the horizontal direction (parallel to fluid flow) controls the waist of the beam and the duration of a specimen in the beam. Vertical focusing controls the beam waist perpendicular to the fluid flow. Combined, complete control is accomplished over the shape of the beam intensity across the sample fluid flow. Notice that a significant portion of the beam is outside of the sample flow stream. This is due to the need to use the central portion of a Gaussian beam profile where it is of nearly uniform intensity. Stretching this portion of the beam across the channel will ensure a uniform intensity profile across the channel and therefore, more reliable detection. This, however, leads to a waste of energy as much of the energy in the beam will never be used for interrogation purposes. Conventional cytometry can use a sufficiently large laser power to compensate for the small amount of beam energy used for excitation to overcome this inefficiency.

The effect of beam size on the detection signal is important. Figure 1-4b) shows how a different beam waist will produce a different signal shape with different sized particles. This effect with large and small particles in large and small beams is demonstrated showing how a large particle may not necessarily produce the largest signal as evident by the comparison of the 10- and 20 μm paricles in a 5 μm beam. If a particle is smaller than the beam waist, pulse duration is uniform and maximum intensity will vary based on the particle size. If a particle is smaller than the beam, the pulse will vary based on particle size while the intensity will be less reliable. This demonstrates the crucial need to tune the excitation beam geometry to the application; it is necessary to calibrate the beam before each test run to ensure alignment and proper beam size for the target specimen.

#### 1.1.1.3 Optical Collection System

As stated earlier, a specimen’s interaction with the beam will produce a variety of wavelengths that are unique to the specimen’s parameters of interest that are present. As such, the flow cytometer’s collection system must be able to collect as much light as possible while being able to simultaneously sort the different wavelengths of light – as discussed in 1.1.2 - and quantify the intensity of each wavelength.

To accomplish this, as each bead produces a brief burst of light when it passes the excitation beam, a large collection angle objective lens is placed in close proximity with the flow cell and focuses on the light from the interrogation region to a complex detection scheme. The objective is placed at an angle of 90° to the flow cell and to beam axis of excitation in order to limit noise on collection. Collected light is carefully aligned to a spatial filter (that will remove extraneous illuminated artifacts near the interrogation region), several dichroic mirrors, and is finally converted by a photon-multiplier tube (PMT) to an electrical current for detections. This complex free-space based detection scheme requires repeated calibration every couple runs to insure that collection is efficient and that the machine is performing optimally.

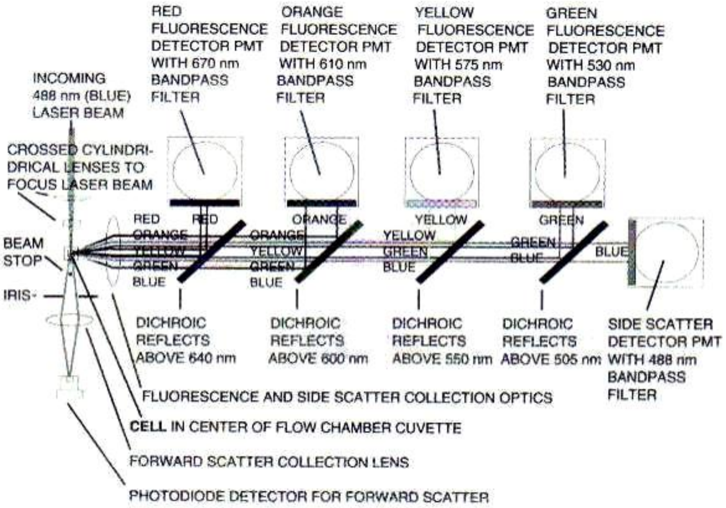

**Figure 1-5: Detailed schematic of a conventional flow cytometer showing all hardware required for excitation, beam shaping, and collection for 6 parameter detection (4 fluorescecne 2 scatter).** ***Source*****: Reprinted from reference 3.**

Simultaneous multi-parameter detection is accomplished through the system's collection of light and separating it via multiple dichroic mirrors allowing detection of both multiple fluorescent and scatter signals. Each dichroic mirror deflects a specific spectrum of light to a PMT to provide ultra-sensitive detection of low light signals. This typical free-space based detection system is depicted by the schematic shown in Figure 1-5 - similar to the one depicted earlier in the picture of a flow cytometer in Figure 1-1.[3] This configuration is able to detect 6 different parameters given by red, orange, yellow, and green fluorescent light, plus two scattered parameter that are the same wavelength as the excitation beam. It is important to select dyes with separated and narrow spectra plus dichroic mirrors with very efficient wavelength selection to ensure that there is no cross-talk between parameters. As scattered light is the same wavelength as the excitation beam, it is typically the last light detected in the train of wavelengths show in Figure 1-5.

Of note in the detection scheme in Figure 1-5, is that forward scattered light is a parameter that needs an entirely separate collection arm than that of the other parameters measured via the different colour fluorescent parameters or the same colour scatter parameter. This will be discussed in detail later in section 1.1.2.2.1, however, it is important to note that this detection arm is in line with the excitation beam axis. Special optical configurations are deployed to reject transmitted light and ensure a strong signal.

#### 1.1.1.4 Data Acquisition and Analysis

Detected burst intensities from specimens must break a certain threshold value of minimum intensity in order to separate bursts from noise or background particulate matter. By setting a certain upper threshold value where larger signals are deemed nonsensical or of a different subpopulation, flow cytometry is able to sub-classify seemingly homogeneous populations. This process, called ‘binning’, is frequently used to define the population(s) of interest.[3] With adequate peak detection algorithms, events can be logged and unique specimen characteristics can be determined via the binned intensity ranges allowing the cytometer to sort specimens. As events can have multiple binned parameters according to the different wavelengths present, the certain combination of wavelengths in each event can determine further differences in specimens.

Analyzing a specific parameter involves constructing a histogram where an event’s intensity is logged according to a range of intensities as shown in the side plots in Figure 1-6.[2] These histograms alone can reveal population characteristics – but only in the most simple of analysis. Some rather simple populations may have independent histograms overlapping, as shown in the bottom collection of histograms from the forward scatter parameter in Figure 1-6. This could incorrectly be assumed a homogeneous population until one looks at the side scatter collection. Creating a plot of two or more of the binned parameters shows distinct specimen populations, as is shown by the 2D scatter plot example in Figure 1-6. This plot shows the two scatter parameters that are associated with each event. Now, the combination of scatter plots allows a seemingly homogeneous population to be discerned as a collection of heterogeneous populations – 3 in this case. By combining different parameters together, flow cytometric analysis capabilities allow separation of data and unique set of data points for each event. This process is only limited by the number of simultaneous parameters that can be collected.

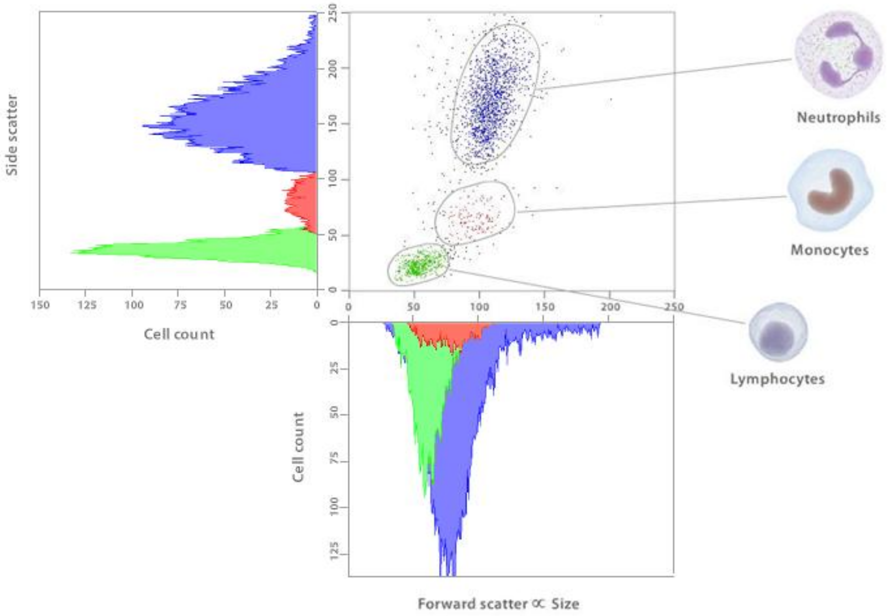

**Figure 1-6: Sample analysis of blood showing obvious distinction of different cell populations based on 2 parameters collected from each cell.** ***Source*****: Reprinted from reference 2.**

### *1.1.1.4.1 Coefficient of Variation*

As discussed above, logged events from a single parameter are binned into small intensity events and a subsequent histogram is formed. A typical histogram is shown in Figure 1-7. The population should form an approximate Gaussian distribution as the process is a statistical one at its core. Through fitting a Gaussian curve to the histogram the calculation of the coefficient of variation (CV) can be done through the parameters of the fitted curve. A Gaussian curve is fit to the histogram in Figure 1-7. Using the fit curve parameters the CV is calculated by dividing the standard deviation by the mean and expressing the answer as a percent. The CV is the standard measure of a cytometer's performance. An ideal CV would yield zero as identical particles should produce identical signals creating a population with zero standard deviation. Errors and imperfections in the cytometer – introduced either through excitation, detection, or flow system processes - will cause variation in the detected signals.

Broadly speaking, the CV is the measure of a cytometer's ability to resolve differences in population characteristics. Typically, an analysis technique will stipulate the acceptable range of CV that can be tolerated. For an application that only requires the detection and decision of a simple absence/presence event will require almost no control of the CV. On the other hand, sizing and DNA content require less than 4% - something that is necessary for cell cycle analysis. Again, the lower the CV, the better the cytometer is at discerning differences in intensities. This will allow more accurate conclusions to be made as variation in detected signal can be attributed to specific cell parameter differences and not to random fluctuations from the cytometer itself.

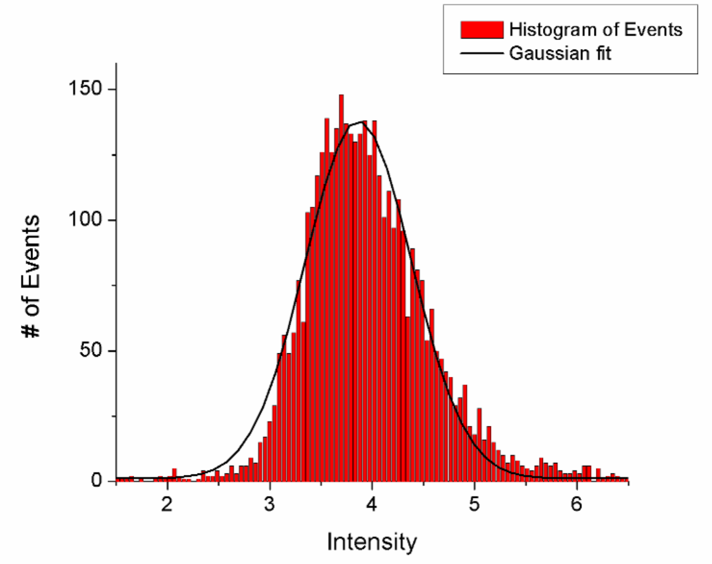

**Figure 1-7: Sample of a Gaussian curve fit to a histogram representing a sample population.**

### *1.1.1.4.2 Double Detections (Doublets)*

Double detections (DD) are events caused by two particles being interpreted as a single particle event. Figure 1-8 shows a picture depicting the multiple ways a double detection can occur and the detriment it has on analysis capabilities. As indicated, if two small particles are simultaneously interrogated it can be interpreted as a larger particle – or a particle with more of a certain feature of interest. Specimens can trigger DD events when specimens are either side-by-side in the sample stream – deemed lateral orientation – or back-to-back in the sample stream – deemed sequential orientation. If only the peak pulse intensity is recorded, ambiguity prevails. However, some DDs can be avoided if the burst area is recorded. This technique has the drawback of requiring extra processing power. Some methods to eliminate DDs can be employed. DDs can be eliminated by diluting the sample concentration. This does not eliminate the occurrences where particles are stuck together, but will sufficiently reduce the chance of two particles being close enough together to be interrogated simultaneously. Diluting sample concentration has the drawback of increasing the sample volume to be analyzed and thus the analysis time.

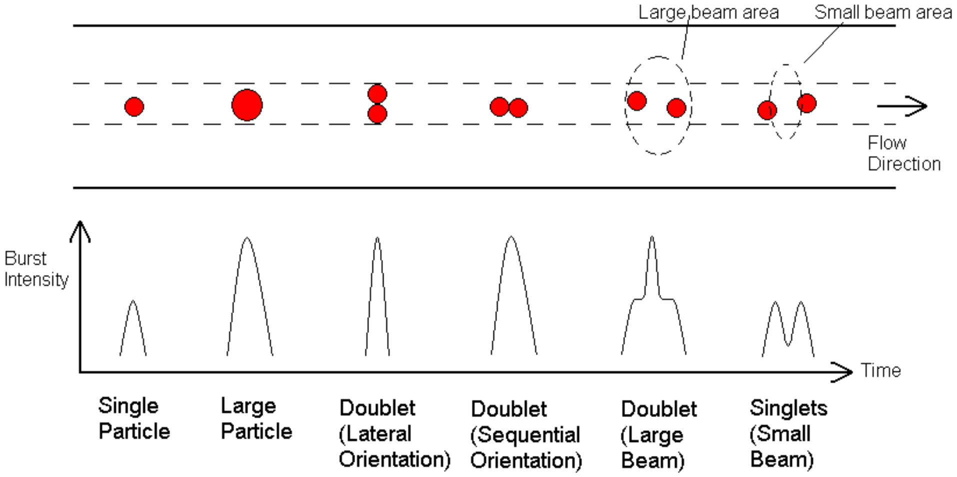

**Figure 1-8: Depiction of several detection possibilities showing single and double events.**

Double detections are better removed by creating a narrow beam waist that is capable of resolving beads that are very close together. A sample interrogation beam is shown in relation to the sample stream width in the flow in Figure 1-8. A change from large beam area to a small beam area can remove the ambiguity of event interpretation. One must be careful about how the small beam affects the pulse of detection, however, as was discussed in Figure 1-4.

##### *1.1.1.4.3 Signal- to-noise ratio (SNR)*

The ability to resolve a peak from the noise is an important feature of any cytometer, and is given by the signal-to-noise ration (SNR). The greater the amplitude of a pulse from a sample compared to the noise, the greater the SNR. The SNR can be expressed in one of two ways: a straight ratio of signal amplitude to noise amplitude or expressed in decibels. A minimum SNR for reliable burst resolution is 3dB or 2 - twice the signal amplitude compared to the noise amplitude. This is not a strict rule, but it will enable a low probability of noise exceeding twice the average signal value.

### 1.1.2 Multiparameter Detection

As already discussed earlier, the power of flow cytometry comes partly from the ability to simultaneously measure multiple parameters, as demonstrated in Figure 1-6. Analysis capabilities are able to distinguish specimens via the unique combination of light signals linked directly to the parameters being measured. The multiple wavelengths are generated by the combination of fluoresced wavelengths (multiple) and scatter directions (two or three).

#### 1.1.2.1 Fluorescence Detection

A fluorescent dye is a molecule that has a very specific fluorophore; a molecule that absorbs a photon to excite an electron, and gives off a photon when the electron relaxes a short time later. A specific absorption band and fluorescence band in the visible range are characteristic of the fluorophore. An example of a fluorescent molecule is the Alexa 488 which absorbs 488nm light and emits 520nm light, as shown in Figure 1-9.[6] Any fluorescent molecule can absorb light but must re-emit the light at a lower energy after the electron relaxes to the ground state. Figure 1-9b) shows a sample of the electronic states an electron progresses through from absorption to emission. It is important that the molecule relaxation emits a photon after a relatively short lifetime – on the order of a few nanoseconds or picoseconds – otherwise the fluorescence emission will occur when the particle has moved well past the point of interrogation. The quantum efficiency of the molecule is given by the number of photons emitted per photons absorbed. For any fluorochome, it is advantageous for the quantum efficiency to be high, as well as increasing the probability of absorbing the photon – through either proper dye selection or a more concentrated beam density.

One detriment to fluorescence is the process of photobleaching; when the dye undergoes a relaxation process that destroys the molecules ability to undergo anymore absorption/relaxation events.[7,8] This typically occurs only after many absorption/relaxation events. As flow cytometry only excites a molecule for only a very brief moment and only once, it is not much of a concern in flow cytometry.

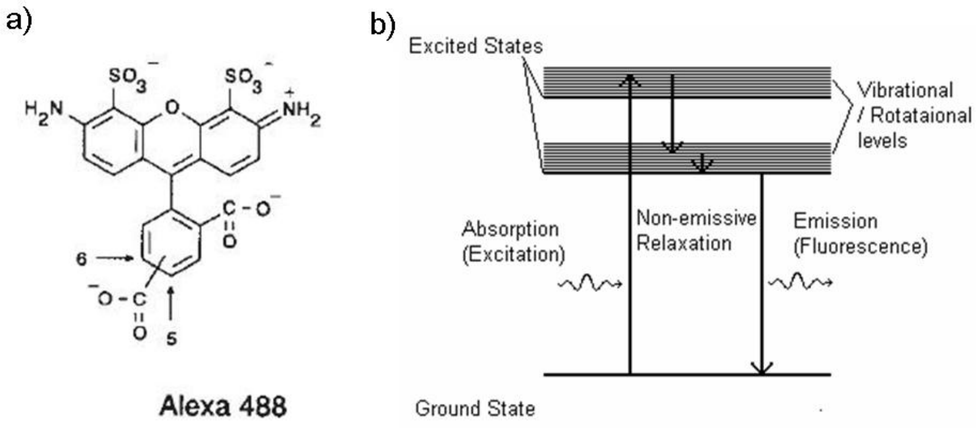

**Figure 1-9: a) Molecule of a fluorescent dye made by Molecular Probes - Alexa 488. This molecule has an absorption maximum of 495nm and has an emission maximum at 519nm. b) A sample of the excitation and fluorescence states of a typical fluorochrome. *Source*: a) reprinted from reference 6.**

Fluorescent dyes are used in flow cytometry to label features of interest. Dyes are added to a sample and stick to the certain features of interest by conjugating the dye; bonding a specific molecule to the dye whose other end binds to a receptor or feature on the cell or specimen.[9,10] Typically, the binding is via the common antibody – antigen binding, such as with Immunoglobulin G (IgG). Other labelling methods include using an oglionucleotide label a specific segment of DNA, or via protein labelling, or via a common steptavidin-biotin ligand labelling method. Many manufacturers provide a vast array of dyes that come prepared for specific assays with the dyes conjugated to a variety of molecules or ligands that allow simple addition of a particular antibody for selective antigen binding. A sample of dyes that are available for typical assay labelling schemes is given in Table 1-1. Strong labelling requires that more dye is present in a cell, allowing greater detection of the parameter of interest. Slight variances in labelling procedures can produce variances in detection and reduce a device's reliability, so it is important to ensure that labelling procedures are thorough and fully label the feature of interest to give an accurate representation of what is present in the sample.

**Table 1-1: List of manufacturers of fluorescent dyes with types of labeling capabilities.**

| Manufacturer | Model | Conjugation Agent | Conjugated Dye | Absorption Max (nm) | Emission Max (nm) |
|---|---|---|---|---|---|
| Invitrogen | A-20170 | Immunoglobulin G (IgG) | AlexaFluor 647 | 647 | 665 |
| Polysciences | 24159-9 | Streptavidin | Yellow-Green fluorescent spheres | 441 | 486 |
| BD Biosciences | 552598 | Bromodeoxyuridine | Allophycocyanine (APC) | 630 | 660 |
| Bangslabs | CM03F | IgG | Various | 400-670 | 460-700 |

When labeling multiple features in a single population, care must be taken when the selecting the multiple fluorescent dyes. The two dyes can be excited by the same source but must have sufficiently separated emission spectra to allow proper resolution of the two parameters. Figure 1-10 shows a spectra chart of Rhodamine B and Nile Red dyes with their absorption and emission spectra.[11] The exicitation spectra from both dyes overlaps and can be subsequently excited using 488 nm laser excitation spectra - shown on the chart with a very narrow linewidth. The emission spectra of the dye are clearly separated, however they do overlap as indicated by the dark region. The bandpass filters shown on the chart in Figure 1-10 are used to prevent overlap of emission from each dye onto the incorrect detector. Both filters have centre wavelengths of 565 nm and 640 nm and both have a linewidth of 10 nm where light will be transmitted. These filters allow a significant amount of emission from the target dye to reach the detector, while only a small amount of undesirable excitation light – given by the dark region – reaches the detector. This cross-talk is unavoidable due to the quantum nature of fluorescent emission, but is adequately minimized through proper dye and filter combinations.

Fluorescent light is inherently a weak signal to detect. As each detector must receive only a filtered portion of the total emission spectrum to eliminate significant cross-talk, each detector only receives a fraction of the fluoresced light due to this filtering. Further reducing the light available for detection is the isotropic nature of fluorescence emission and the small collection angle of a typical detection system, as will be discussed in detail in section 2.1.1.2.2. For these reasons the fluorescent signals are weak and the importance of the extremely narrow spectral linewidth and large power available from a laser is easily seen. A wide linewidth from the light source would further interfere with the emission signals and require event narrower filtering and reduce signals.

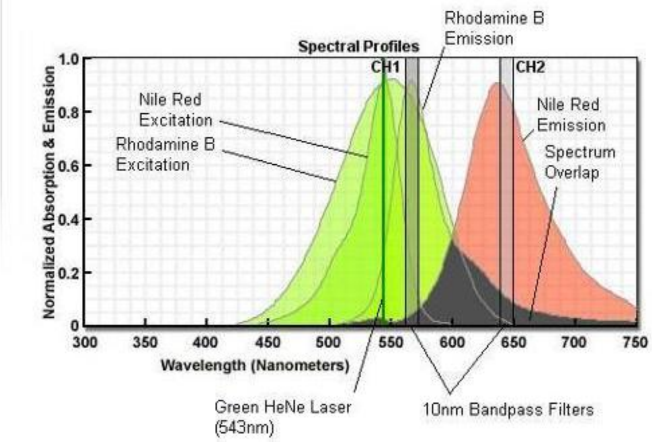

**Figure 1-10: Spectral diagrams for two dyes: Rhodamine B and Nile Red, showing absorption spectra, emission spectra, and band pass filters for detection. *Source*: Reprinted from reference 11.**

With the proper dye, source, and filter it is possible to perform the detection of multiple colours simultaneously[12,13,14] - even up to seventeen colours[15] - leading to very powerful analysis capabilities during a single experimental run.

### 1.1.2.2 Scatter Detection

There are two types of scattering that are defined based on the deviation of the photon from the initial direction of propagation. Both parameters reveal different characteristics from the specimen of interest as the direction of the scattered light is highly dependent on the cell properties such as the cell size, granularity, structure, and surface roughness.

#### *1.1.2.2.1 Forward Scatter*

Forward scattered light is the measure of light that deviates very slightly from the excitation beam axis - typically only 0.5-5°.[3] Figure 1-11a) shows a picture of a cell in an excitation beam and the effect on the light.[2] With proper beam shaping the cell will block the entire excitation beam leading to low noise on the detector and much more reliable detection. The intensity of forward scattered light is typically indicative of the size of the cell[3] due to the quantity of the interference the specimen has with the beam. Forward scatter light can also detect the viability of the cells and distinguish between live and dead cells due to the index of dead cells more closely approximating that of the surrounding medium.

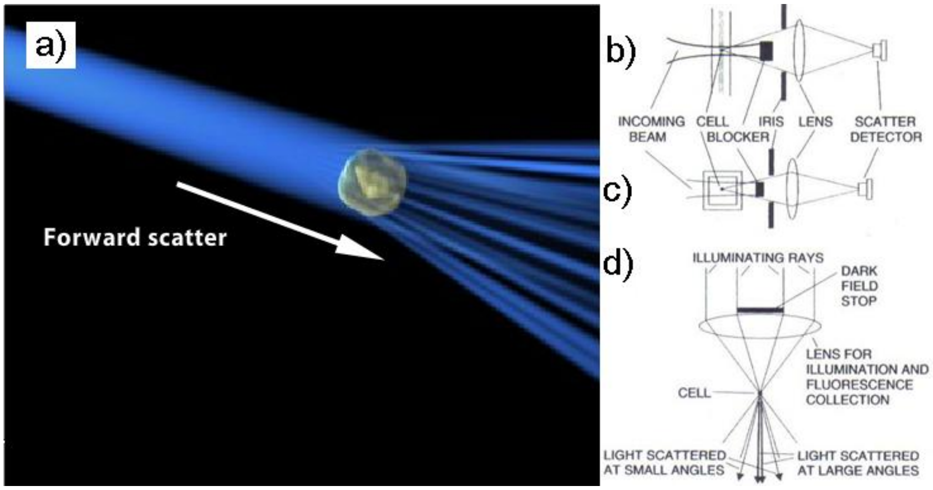

**Figure 1-11: a) cartoon depicting forward scatter by a particle in the excitation beam. Various forward scatter collection schemes; b) a top view and c) side view demonstrate the excitation beam focused on a beam stop after excitation of a particle, and d) a configuration where an obstruction is inserted into oncoming beam to form a dark region on the detector. *Source*: a) reprinted from reference 2, b),c), and d) reprinted from reference 3.**

Due to the near on-axis geometry of forward scatter, the architecture for detection is a bit complex. The very close proximity of forward scatter light and the transmitted excitation beam forces the need to block the excitation beam from the detector to increase the SNR. Figure 1-11 shows a couple configurations that allow blocking of the excitation beam to increase the SNR of the forward scatter signal. Figure 1-11b) and c) show the top and side views of a method where the beam is focused onto a beam stop on the opposite side of the channel.[3] This method requires a fairly collimated beam or a very small focal point; control of beam width is difficult due to the location of beam stop. Figure 1-11d) shows a configuration where an obscuration in the beam generates a dark spot in the image that is coincident with a detector.[3] This method does mean the excitation beam loses a fair amount of excitation intensity due to the blocking high intensity paraxial beam.

#### *1.1.2.2.2 Side Scatter*

Light that deviates significantly from the beam axis is considered side scatter light. There are a wide range of angles for collection possibilities, but it is typically collected at 90° because of the ease of reducing the noise that is simultaneously collected. Specific angles will have a specific intensity signature; however it is cumbersome to detect light as these specific angles – especially as the orientation of the cell is not fixed in the flow stream. Figure 1-12a) shows the side scatter of the light coming from a particle in the beam. Side scatter is much less intense than the forward scattered light due to need for many scattering centres. Side scatter is used as an indicator of the surface roughness of the cell as seen in Figure 1-12b). This parameter also gives insight to the granularity and internal structure of the cell, also shown in Figure 1-12b).

Side scatter detection is accomplished with a simple collection scheme situated perpendicular to the sample flow and the beam direction, and often simultaneously collected with the fluorescent light, as shown in Figure 1-5. This requires much simpler optics than what is required for forward scatter light. A filter is necessary to block any fluorescent light as it will be confused with fluorescent signal as well as a spatial filter as scattering off internal artifacts in the flow cell or illumination of other debris in the sheath stream can be detected as events.

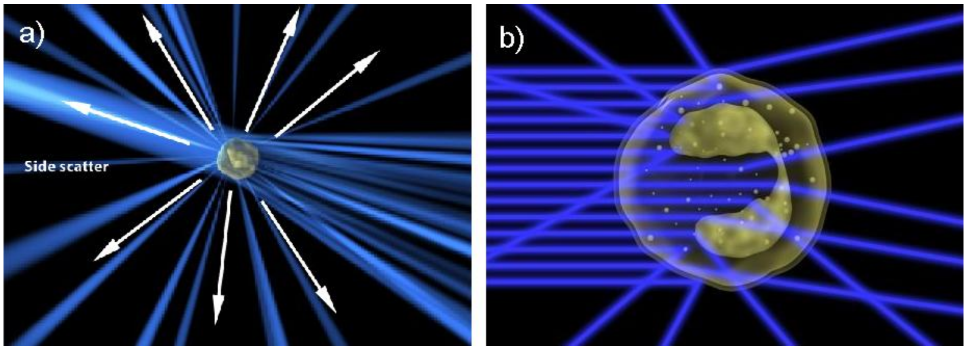

**Figure 1-12: a) Picture depicting the side scattered light from a particle (also showing the forward scattered light). b) the granularity of the cell and internal structure affect the large angle scattering from the particle. *Source*: Reprinted from reference 2.**

### 1.1.3 Applications

Flow cytometry is an established and well developed technology that has found many applications since its first inception. Applications are mainly clinical or diagnostic based applications, while there is a strong contingent of research-based, laboratory, and environmental applications. There are very few in-the-field applications due to the difficulties of making a flow cytometer that is portable and inexpensive.

Clinical applications of flow cytometry range from immunophenotyping,[16,17] and immunology[18,19] to determining cell function[20] and analyzing cell cycle and apoptosis[21]. The diagnosis and monitoring of lymphomas and other lymphoproliferative disorders,[22] such as leukemia[23] and monitoring minimal residual disease during treatments,[24] is a common application of flow cytometry. There are many environmental applications,[25,26] and applications in virology.[27] Flow cytometry rose to prominence due to the use in discovering aids and the monitoring of the progression of the disease through counts of helper T-cells.[16,28]

Flow cytometry has been deemed a necessity to other clinical diagnostics as it can determine the stage of HIV or cancer to help determine the correct treatment.[29]

#### 1.1.3.1 Commercial Devices

Many commercial companies offer flow cytometers available in small bench-top formats. BD Biosciences offers the BD Accuri C6 – a unit that is light-weight and can simultaneously detect and quantify signals from three different fluorescent signals, one forward scatter parameter, and one side scatter parameter.[30] This unit is shown in Figure 1-13 and shows the complex optics necessary to perform detection in a) while the entire compact unit is shown in b).

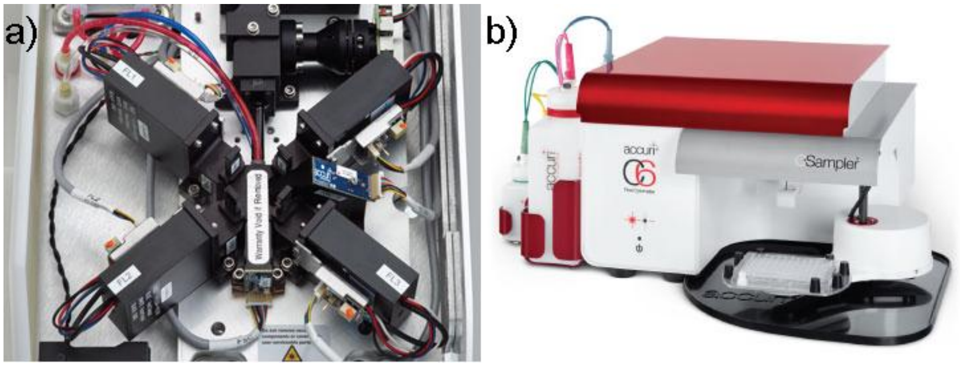

**Figure 1-13: BD Accuri C6 flow cytometer. a) the complex compact optics necessary to perform analysis. b) the unit is small enough to fit on a small bench top and comes with software to completely run the machine. *Source*: Reprinted from reference 30.**

Beckman Coulter offers another small affordable cytometer, the CyAn ADP Analyzer.[31] It is a unit that can simultaneously detect and analyze 9 colours – 7 fluorescent and two scatter – being excited by three different lasers wavelengths. The unit is integrated to a plate loader that allows high throughput and sequential well analysis. This unit is able to achieve a throughput of 70,000 events per second.

Applied Biosystems offers the Attune Acoustic Focusing Cytometer.[32] It is a unit that uses acoustic sound waves to hydrodynmically focus the sample while using two different wavelengths from two lasers, and it is able to simultaneously detect six fluorescent parameters plus two scatter. EMD Millipore offers the guava easyCyte, a cytometer the employs two excitation lasers to detected 8 fluorescent parameter plus 2 scatter parameters while offering a large range of detection; over 5 decades. This unit boasts the advantage of not needing calibration between tests.

#### 1.1.3.2 Advantages and Disadvantages

Conventional flow cytometry is incredibly accurate and provides a clear snap-shot of the exact state of a population through the individual cell-by-cell analysis. It has a very fast rate of analysis and can boast a throughput of over 100,000 cells*s$^{-1}$.[33] Conventional cytometers are very sensitive due to the free-space collection schemes and have extreme analytical capabilities due to the multi-parameter detection capabilities.[15] The cytometers are able to easily couple with a sorting mechanism that allows sequestering and large population enrichments.[33]

Despite the great capabilities of conventional cytometers, there are several drawbacks that limit their applications and deployment. A conventional cytometer's large size and the associated costs limit the deployment of the cytometer to large scale laboratories and medical facilities where a large user base will justify a large cost. This creates roadblocks to access, long queues, and lengthy turn-around times on the results. This large size requires a large sample sizes and consumes large quantities of expensive dyes. Furthermore, the method of detection requires bulky free-space optics that creates machines that are shock-sensitive and expensive.

## *1.2 Microchip-based Flow cytometry*

Microchip-based cytometry aims to remove some of the limitations and restrictions that limit the deployment and applications of conventional flow cytometry by replacing the bulky flow cell with a microchannel fabricated monolithically in a planar fashion. The miniaturized flow cell reduces many of the costs associated with traditional cytometry as it is possible to handle small sample sizes in an automated fashion. Integration capabilities possible through the manufacturing techniques allow further integration of components on-chip.

This further reduces costs and makes devices with a specific designed functionality that are more portable, durable, and capable of remote and on-site applications. This trend towards on-chip devices has been well documented as the Lab-on-a-chip (LOC) or Micro-Total-Analysis System (μTAS) revolution - whereby chemical and biological tasks are completed on-chip without outside handling from an operator whatsoever.[†,34,3536]

Each subsystem of a conventional flow cytometer must be miniaturized and designed to mimic the functionality of the conventional counter-part. This has largely been made possible by the advances in the microelectronics field being adapted to microfabrication techniques.[37]

### 1.2.1 Miniaturized Flow Cell

Early microchip-based flow cytometers only had the flow cell miniaturized.[38,3940] These early attempts still relied on free-space optics to excite and detect optical signals and perform the necessary interrogation. These microchannels are constructed by forming a trench in some sort of layer on a substrate and sealing the trench with another layer. These layers must be transparent to ensure easy optical detection. The reduced channel sizes allow a smaller sample size to be required due to the reduced handling tolerances from the much smaller channel size. Furthermore, integration capabilities allow a network of interconnected channels to be fabricated, creating a fluidic network that can incorporate automated processes like mixing, separation, and sorting all on-chip. More complex processes like sequestering and culturing can also be performed on-chip after a specific analysis has been done.

The channel's small sizes and the result of a small device size make moving fluids via electrokinetic flow a possibility.[41] This is a portable method for driving fluids as syringe pump is bulky and expensive. Fine control of particles is possible via electrokinetic flow.

---

[†] These paragraphs are from the author's published work in reference 1.

### 1.2.1.1 Fabrication

Flow cells have a planar format and therefore typically only have 2D fluidic networks. Though micromachining techniques allow 3D networks they tend to be avoided as the cost and complexity of a device increases – something counter to the purpose of LOC devices. Fabrication techniques used to make these devices are adaptations of very simple photolithography techniques while incorporating aspects from the fields of micromachining.

#### *1.2.1.1.1 Methods*

Basically three methods are employed in the fabrication of microchip-based devices: lithography, soft lithography, and etching/ablating. Conventional lithography techniques involve the creation of a thin layer of photoresist that is patterned with the intended devices through the simple removal of material. Once the device layer is created, a separate layer is bonded on top of the device layer to seal the liquid in the channel. Figure 1-14i) shows a simple picture of the process and how channels are formed. This process forms rigid structures and demands access to a clean room for fabrication and use of conventional lithography fabrication equipment. Bonding a sealing layer on top can be an issue due to the rigid substrates, and several methods have been done with varying results, as shown in Figure 1-14i) – the best typically from top layers that are soft.[42,43]

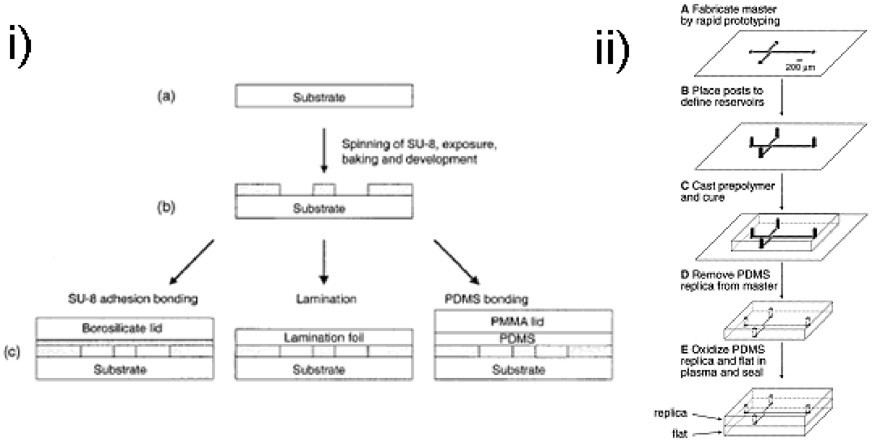

**Figure 1-14: Microfabrication techniques. i) Lithographic based, and ii) soft lithography. *Source*: i) Reprinted from reference 44, ii) reprinted from reference 45.**

Soft lithography, developed by the Whitesides group at Harvard,[37] allows a very rapid and simple fabrication of microfluidic devices.[45] This process involves creating a mold using standard photolithography techniques and then creating a replica of the mold, as demonstrated in Figure 1-14ii). This replica is then typically bonded to a glass slide via an easy oxygen plasma method. Soft lithography utilizes soft elastomers that are easily cast in the mold and very inexpensive. This process enables the fabrication of flexible transparent chips. Once the mold is made, fabrication is done out of a clean room extremely quickly; the elastomer is pulled out of the mold, it is plasma treated, and then bonded to a glass plate to seal the formed channels. Soft lithography enables on the spot fabrication of devices that are ready to test.

The last technique - fabrication from etching or ablation - involves the removal of trench of material to create the channel. Laser ablation can cut a trench of a defined width in the substrate very quickly. Chemical etching via a photolithographically defined mask allows very good precision and control of the depth of the channel.[39] To seal these trenches to form a channel, the process demands that a layer is bonded over the device layer.

#### ***1.2.1.1.2 Materials***

Depending on the choice of fabrication and the designed function of the device, a variety of materials may be suitable for device fabrication. SU-8 is an epoxy-based positive photoresist that is transparent throughout much of the visible spectrum - the spectrum that is of interest for flow cytometric applications and many other biology-based assays.[44] SU-8 tends to be used as a device layer or as a master mold in lithography and soft lithography fabrication methods, respectively. Due to the nature of fabrication – as discussed above – use of SU-8 is restricted to 2D device designs only. Sealing devices via bonding is an issue, but some solutions have been presented, such a SU-8-to-SU-8 sealing,[46] or clamped sealing.[47] These methods are prone to leaking due to a non-complete and conforming contact, and a bulky setup, respectively.

Poly(dimethylsiloxane) (PDMS) is an elasotmer that is deformable and easily conforms to a bonding surface. PDMS has been well documented as a suitable material for microfluidic devices in general.[48] Glass is typically used as a substrate as it allows easy transmission of light for optical excitation and detection via free-space schemes. Silicon is sometimes used as a substrate or structure material due to the extreme compatibility with conventional fabrication techniques.[49] Care must be taken in the device design as a silicon substrate is not transparent and makes optical detection techniques difficult.

### 1.2.1.2 Optical Interrogations

With a miniaturized flow cell optical detection is still performed with a system that is identical to a conventional free-space scheme. A high quality single-mode laser beam is focused to cover the entire microchannel. Figure 1-15 shows a very simple schematic of the optical interrogation of partcles in a miniaturized flow cell. As the microchannel is confined to a plane instead of a cylindrically-shaped capillary tube, the orientations for collection and excitation are limited.

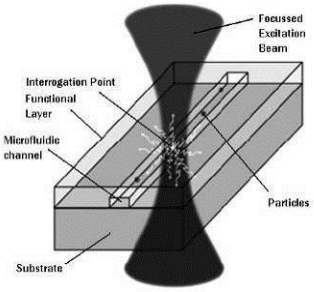

**Figure 1-15: Simple example of microchip-based cytometer. The capillary tube is replaced by a microchannel fabricated in a functional layer on a substrate. *Source*: Reprinted from reference 50.**

Figure 1-16 shows a schematic and a picture of a typical free-space setup for two parameter collection from a microchip-based flow cell. Excitation is oriented at 45° to the chip while collection is oriented at 90°. This is an experimental benchtop setup that employs a quickly fabricated microchip-based flow cell. The easy and quick fabrication of flow cells allows clogs in the microchannel to be dealt with by simply removing the chip and replacing with another fabricated one.

This would still require realignment of the optical system, though machining tolerances would allow accurate alignment in plug-and-play devices.

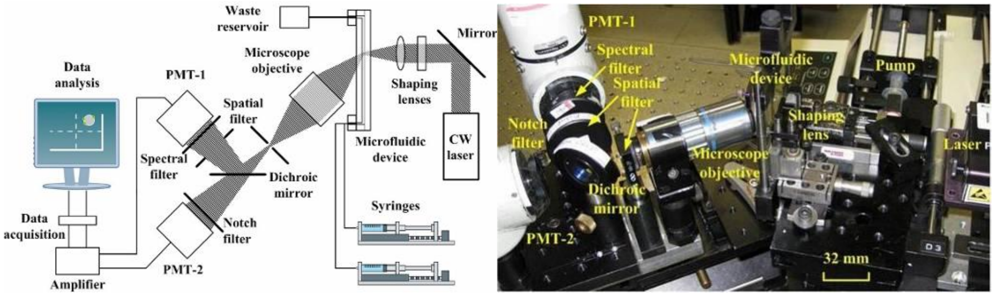

**Figure 1-16: Free-space optical setup showing a schematic (left) and bench-top setup (right) for two parameter collection. *Source*: Reprinted from reference 52.**

### 1.2.1.3 Hydrodynamic Focusing

As discussed in section 1.1.1.1.1, hydrodynamic focusing helps detection reliability by forcing all the specimens to the same physical area within the excitation beam. This leads to predictable and uniform excitation, and thus, reliable and predictable detection of signals. With a planar chip format, the conventional concentric nozzle formation shown in Figure 1-2 is not possible – at least not by any easy and inexpensive means. A planar design limits the device to 2D hydrodynamic focusing – which is actually focusing in only one dimension perpendicular to the flow in the plane of the chip. This is achieved easily via a 3-branched structure,[51] shown in Figure 1-17.[52] The sample stream is focused to a plane perpendicular to the chip, instead of a 1D line in the middle of the channel like in conventional methods – see section 1.1.1.1.1. This means, however, that specimens are free to deviate in any vertical position within the channel.

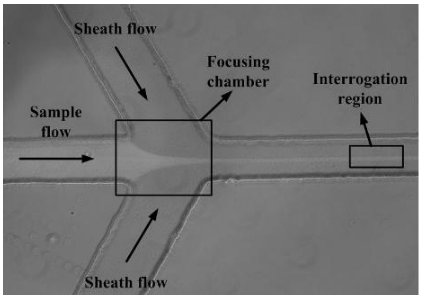

**Figure 1-17: Hydrodynamic focusing of a sample fluid (centre channel) between two sheath fluids creating a narrow stream for interrogation. *Source*: Reprinted from reference 52.**

The theory and phenomena of hydrodynamic focusing on a microchip-based device has been explored experimentally in detail, notably in reference 51. A typical planar structure is shown in Figure 1-18 with all the variables one would have to take into account during design. The work employed numerical models and simulations to develop a relation to describe the resulting focused stream width given flow conditions, channel widths, and fluids used. These findings were summed up in Equation 1-1 below.

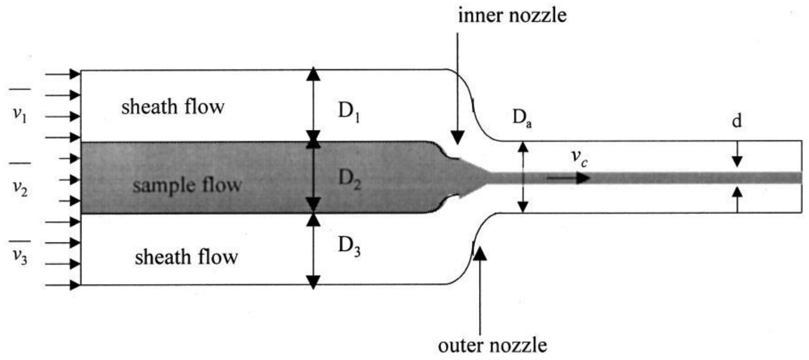

**Figure 1-18: Schematic of a typical input nozzle for 2D hydrodynamic focusing showing all the parameters of interest when designing. *Source*: Reprinted from reference 51.**

$$d = \frac{\overline{v_2}}{v_c} \cdot D_2 = \frac{\rho_a \overline{v_2} \cdot D_2 D_a}{1.5 \cdot (\rho_1 \overline{v_1} D_1 + \rho_2 \overline{v_2} D_2 + \rho_3 \overline{v_3} D_3)}$$

**Equation 1-1: Relation of the focused stream width with the nozzle design parameters for a 2D microchip design. *Source*: Reprinted from reference 52.**

Many designs have been presented that can achieve 3D hydrodynamic focusing in a completely microchip format without very complicated or expensive fabrication techniques. Some solutions employ slightly complicated structures,[53,54,55] - involving multiple layers of fabrication or different planes of injection. Other more simple devices employ very simple structures for 3D hydrodynamic focusing.[56,57] One such design, shown in Figure 1-19a), uses micro-weir structures on the top and bottom surfaces of the channel to force the specimens to a narrow flow in the direction perpendicular to the chip. A typical 3-branched structure focuses the flow in the other, horizontal, direction. Another simple design that employs a completely planar one-shot fabrication design[58] -

shown in Figure 1-19b) – uses the phenomena of microfluidic-drifting to force the flow to be focused vertically. As with the micro-weir design, horizontal focusing is achieved via the typical 3-branched structure. These designs are simple, though they need to be perfected before the can be employed for feasible device use.

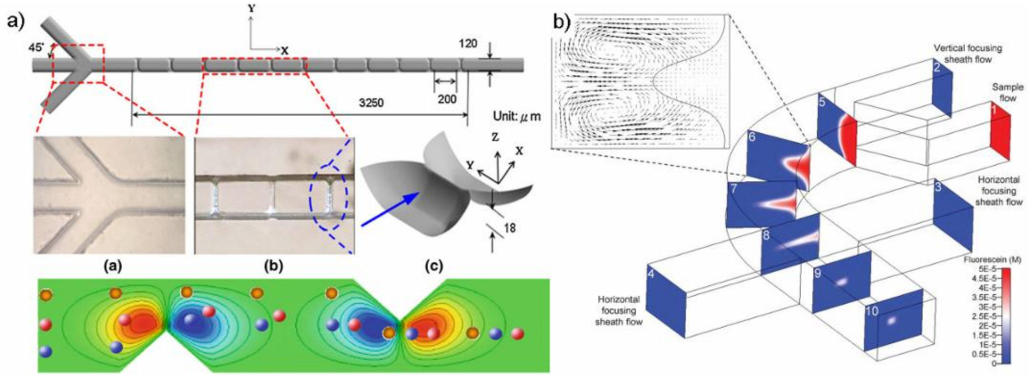

**Figure 1-19: Two examples of 3D hydrodynamic focusing using planar designs. a) 'Micro weirs' on the top and bottom of the channel focuses in the vertical direction, and b) 'microfluidic drifting' uses a curved microchannel to perform the vertical focusing. In both cases, horizontal focusing is accomplished by a 3-branched structure. *Source*: a) Reprinted from reference 58, b) reprinted from reference 56.**

Some designs even eliminate the need for a sheath fluid altogether and can focus the particles based on size with some novel channel designs.[59,60] These designs have been proven to be selective enough for sorting.[61,62] Application to a microchip-based cytometer does show that the performance of the device is drastically improved.[56] This method does, however, complicate device design and function.

### 1.2.1.4 Advantages

Microchip-based devices have numerous advantages over the conventional based systems. First, with a reduced channel size comes the benefit of a reduced requirement on the amount of sample fluid that is required – a drastic benefit when samples volume are rare or in extremely limited quantity, such as in prenatal diagnosis of genetic disorders,[63] or when samples of the cerebrospinal fluid are obtained through a spinal puncture.[63] Furthermore, large cost savings are realized from the reduced demands on expensive labeling dyes due to the reduction in sample fluids required for analysis, while the small size of fluid handling permits smaller power requirements. Second, experimental run times are typically shorter than those of a conventional cytometer due to the reduced sample sizes.[64] Third, due to the lithography based fabrication procedures, these devices are easily produced in a mass-production type scheme that exploits economies of scale that will ease costs and increase quality assurance through repeatable and reliable measurements between devices.[64,65] Fourth, the chips are easily integrated with other on-chip fluidic handling procedures and devices, such as sorters,[66,67,68] mixers, pumps and valves[69] and reactors, which will allow a steady evolution towards a fully LOC device.[70] Furthermore, biohazard threats are minimized as all fluid handling is done on-chip in a completely sealed and easily disposable platform while errors that may be introduced through human handling are eliminated.[‡]

### 1.2.2 Integrated Photonics

While a microchip-based flow cytometer can handle small samples at low cost, a free-space optics-based system is still bulky, expensive, and not portable. To overcome this problem while substantially reducing equipment costs, it is required that some sort of light-delivery mechanism is integrated onto the chip to perform excitation and detection functions. Integrating a light-delivery component onto the device creates automatic alignment to the channel during fabrication, as structures are designed with a CAD program—then converted to a photomask—allowing an optimal optical excitation once fabricated. Through this approach, it is possible to even achieve collection of the light on-chip. This eliminates the need for error prone, cumbersome, and difficult optical alignment that is required by conventional and microchip-based devices that require free-space optics. Another advantage is that the proximity to the sample is enhanced—within a few tens of microns—allowing a great benefit from collection type waveguide, as the efficiency of collection can be as great as 20%.[§]

---

[‡] This paragraph is from the author's published work in reference 1.

[§] This paragraph is from the author's published work in reference 1.

### 1.2.2.1 Guided Optics

Through the creation of a sharp index contrast in the form of a ridge in the device layer, light can be confined and guided within the device layer. The light from the source can be guided in order to direct it towards the point of interrogation. Collection of light signals from the interrogation point can also be done via the on-chip guided optics. This can allow control of the amount and type of light collected from the interrogation point. Furthermore, collection can be increased through the greatly enhanced proximity of the collection optics to the interrogation region. Integration of guided optics on-chip creates designs that are robust and that have automatic alignment that is shock insensitive allowing deployment in applications where handling is an issue.

#### *1.2.2.1.1 Inserted Fibres*

Early attempts with using fibres for excitation and collection first demonstrated the possibility of using guided optics in a chip format.[71] This work was performed by aligning several fibres around a capillary tube to perform excitation and detection. It was noted that the coupling efficiency was a large concern between the source and fibre, as well as between the fibre and capillary tube. It was also noted that a single mode fibre was a necessity as the beam quality of a multimodal fibre is unsuitable for the excitation source in flow cytometry due to the poor illumination profile.

With the advent of microfabrication technologies and the miniaturization of flow cells, attempts to incorporate fibres on-chip was revisited. Early devices utilized simple fabrication methods that formed a trench in the device layer, as discussed above in section 1.2.1.1.1. The depth of the fabricated trench, and thus the device layer, was designed to match the fibre diameter. A fibre could then be inserted into the device right up next to the channel and butt-couple the light into the microchannel. Figure 1-20 shows a device that manufactures trenches to allow the insertion of a fibre to quickly and easily align fibres to the channel.[72] Many other devices have used the same configuration with subtle differences of the method to hold the fibres in place. Some methods involve etching the cladding of the fibre until it matches the trench dimensions and then adding a bit of adhesive to hold the inserted fibre.[49,69,73] Other methods use an elastic bulk material, like PDMS, to press-fit fibres in place once inserted.[72,74,75]

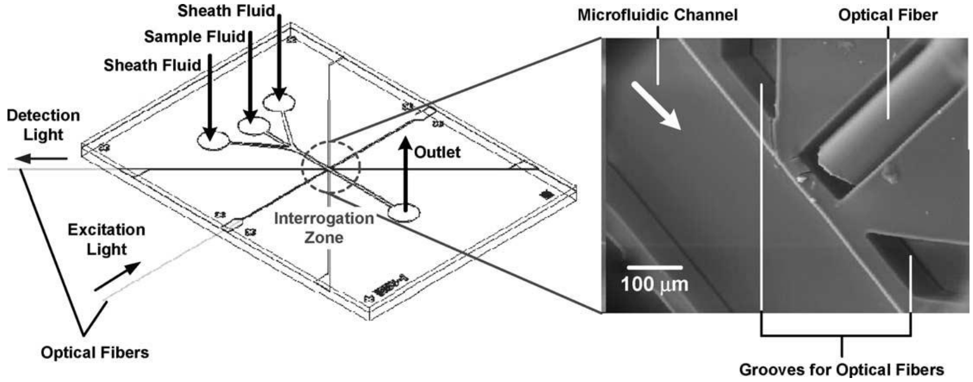

**Figure 1-20: Device showing inserted fibres used to deliver light to the microchannel. *Source*: Reprinted from reference 72.**

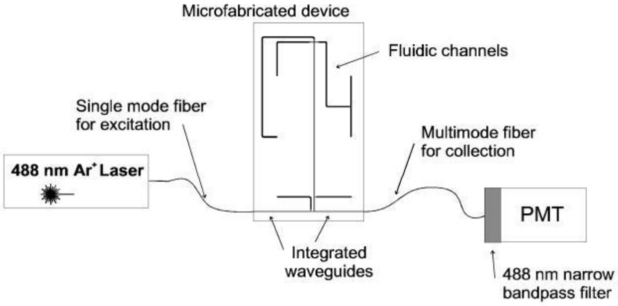

**Figure 1-21: Schematic of a microfluidic device with inserted fibres that allow easy swapping of the microfluidic device. Fluid handling is done on chip and all that is needed external hookup of the source and the detector. *Source*: Reprinted from reference 76.**

Connecting to a device with inserted fibres allows quick connection to the device and creates a cartridge type system where the microchip can be swapped in and out easily, as shown by the schematic in Figure 1-21[76] Expensive and complicated components necessary for device function, such as PMTs and sources, are static and can be reused. These components are quickly and easily connected to microfabricated chips that are cheap, numerous, and disposable. These chips can have a one-time use function and allow for quick changing in the event of a clog.

#### *1.2.2.1.2 Waveguides*

Taking the integrated guiding optics one step further from inserted fibres would be the fabrication of waveguides on-chip. By removing material to form a ridge a waveguide can be formed to create lateral optical confinement. The substrate and sealing layers should simultaneous provide vertical confinement to keep the light within the device. These designs require less complicated fabrication techniques as the device layer thickness can be fairly arbitrary. A device deploying a simple waveguide is shown in Figure 1-22, while the guided beam is well confined and is delivered easily to the microchannel as demonstrated via the fluorescent image of the beam in the channel. Using a waveguide on a chip, further complicated designs can be integrated in this way such as using beamsplitters.[77,78,79]

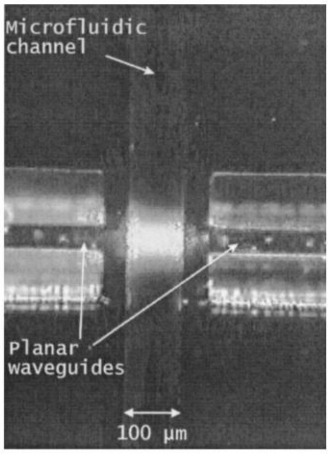

**Figure 1-22: Image of formed ridge waveguides in a single layer of SU-8; two waveguides on opposite sides of the channel with the beam illuminated in the channel. *Source*: Reprinted from reference 44.**

Using integrated waveguides, the proximity of detection is greatly increased thereby increasing the total amount of light that is collected. This is shown in schematically in Figure 1-23[80] as a comparison of the collection angle obtained via free-space and on-chip methods. Figure 1-23a) shows collection with a free-space method while b) shows collection with a waveguide that increases the proximity and thus increases the collection efficiency. A free-space scheme is less than 1% efficient while an intergrated waveguide can have as high as 5 to 10 times improvement. This specific device shown in Figure 1-23c) is fabricated from PDMS and makes waveguide cores via injecting a polymer of higher index into formed voids in the PDMS.

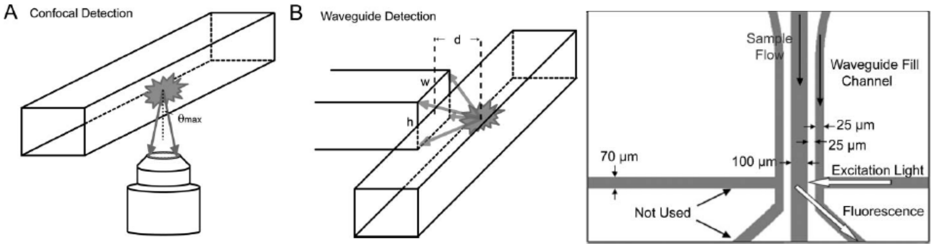

**Figure 1-23: Diagram showing a free space collection from a channel (A), and a waveguide collection from a channel (B) showing the much larger solid angle of collection. A device that uses liquid core waveguides. *Source*: Reprinted from reference 80.**

Using this basic design, some groups have even demonstrated the ability to inject the core with a fluid to allow for optical confinement and tuning of waveguide properties based on the core fluid material.[81,82,83,84]

### 1.2.2.2 Integrated Filters

Interesting adjustments to waveguides has allowed on-chip filtering of unwanted wavelengths through selective absorption, removing another bulky and expensive free-space component. This has been demonstrated via a dye doped polymer[83] and provides a great improvement over other methods where an interference filter is used due to the greater proximity of the waveguide to the interrogation point; an interference filter is thick and moves the detector away from the interrogation point.

One such device used a backplane design to further reduce the background noise on detection by deflecting the injected light up into a top layer that contained the channel.[85] The emitted fluorescent light from the inspection was then coupled down to the backplane and into a waveguide doped with a dye to remove noise that had the same wavelength as the excitation source. The importance of a waveguide was demonstrated through another device with a detector – an avalanche photo diode (APD) - placed behind the device that had a backplane that contained a dye-doped polymer.[83] This backplane serve the function to remove unwanted noise, however it was noted that it needed to be thick to allow large filtering and thick filters (30um) limit collection efficiency to les than 0.2%[83] due to less proximity to the interrogation region. Therefore, incorporating a waveguide allows this distance to be covered without losing the proximity.

Another filtering example is a device that employs Fabry-Perot structures in the cladding region to force a leaky waveguide at the wavelength of light to be removed.[84] Finally, a last device used liquid core waveguides and a diffusion processes in the waveguide to mix dye within the core region that would perform filtering as the light propagated down the waveguide.[86]

#### 1.2.2.3 Refractive Optics

Unfortunately, light brought to microfluidic channels through optical fibers and planar waveguides diverges significantly, with reduced power density through an unshaped beam, as it exits the fibre or planar waveguide and traverses the channel. In an attempt to increase the power density available for excitation, and thus the level of detection in optically integrated devices, microlenses have been integrated with the waveguides to focus light into the centre of the channel with the primary goal of increasing the level of intensity of the excitation light to in turn boost detection signals. These lenses can be fabricated in the same step as the microchannel and waveguides, and as processing is through a photolithographic based means (as discussed earlier) the lenses formed are 2D lenses – cylindrical in shape. Single lens systems have been explored with varying levels of improvement. [**,87],[88],[89],[90]

Figure 1-24[91] shows several possible beam geometries formed in the microchannel from different light insertion methods discussed so far. A scheme that employs free-space optics forms an ideal beam geometry where the intensity is concentrated at the sample flow and is deemed uniform across the sample stream. Input from a waveguide has the affect of the beam diverging as it exits

---

[**] This paragraph is from the author's published work in reference 1.

the waveguide producing an inferior geometry through a very wide beam waist and uneven and non-uniform beam intensity. Some devices that have used on-chip lenses change the beam geometry from divergent to convergent or closely collimate it – however, the beam geometry is still less than ideal.

Photolithographically defined lenses result in lenses that are 2D in nature and only can shape the beam in one dimension – in the plane of the device in the direction of fluid flow. This can allow control of the divergence of the beam, but has a limited ability to shape the beam, let alone perform a complete beam shaping function.

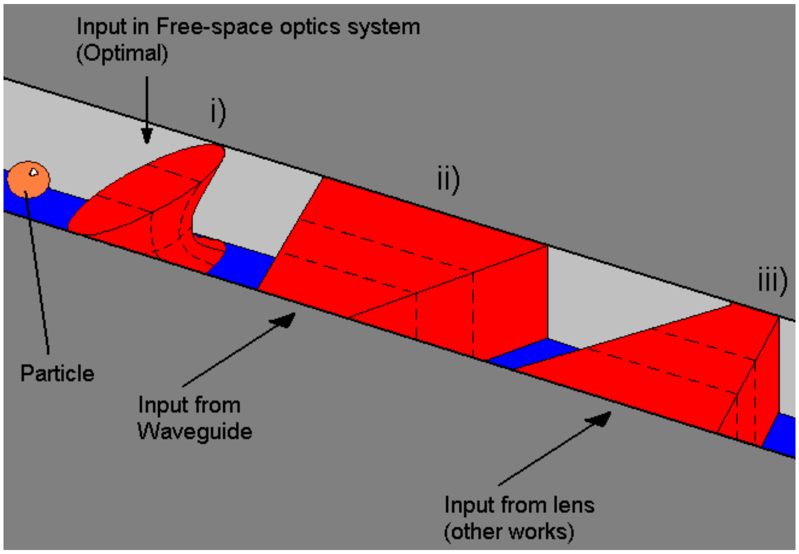

**Figure 1-24: Picture showing the different beam shapes in a microchannel formed by i) free-space system, ii) no lens, and iii) a simple lens. *Source*: Reprinted from reference 91.**[††]

A compound lens system allows for more control of the beam. This system of lenses can shape the beam to a better geometry via more control of the refraction of the beam. Figure 1-25i) shows a device that compared a single lens to a planar system of lenses integrated on chip. The images, shown in Figure 1-25ii), show a marked improvement over the single lens design. This improvement is highlighted and confirmed by the contour maps in Figure 1-25ii) as well. The improvement to the excitation intensity was measured to have increased by 1.67

---

[††] This figure is part of the author's published work from reference 91.

times through the use of a single lens and by 7 times through the use of the compound lens system. This work demonstrated a much improved beam using an integrated lens system; however, it still fell short of what the beam shaping capabilities that are deployed in conventional cytometery. It is crucially important for microchip-based devices to closely mimic the functionality of conventional devices in order to match the analytical capabilities.

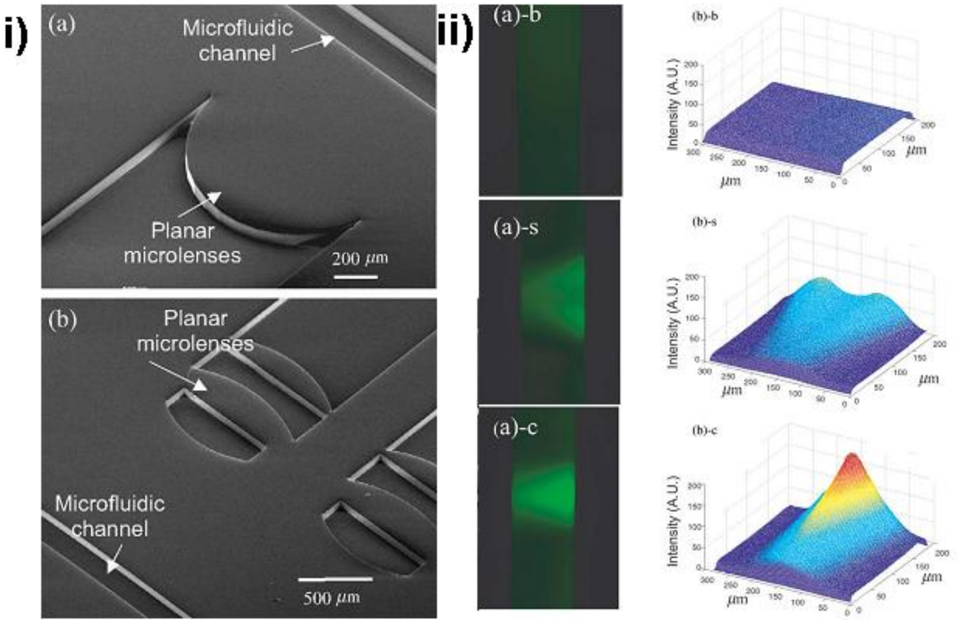

**Figure 1-25: i) SEM images of a device that has a) single lens and b) compound lens system integrated on-chip. ii) imaged beams from a)-b no lens, a)-s single lens, and a)-c compound lens system and the corresponding contour plot.**

There have been many other compound lens systems that have demonstrated varying success and decent detection abilities.[92,93,94,95] However, all still have a lack of beam shaping and wildly varying performance with detection of specimens that is largely blamed on the device's lack of beam shaping. One work even went as far as to integrate a diffractive optical element on top of the chip to demonstrate a very compact design with high beam control capabilities.[96]

More advanced devices with a large level of optical integration have been prototyped, as shown in Figure 1-26.[97] This shows a device with lens system on every optical input and output. These lenses are actually channels that will allow different fluids to fill them so as to allow slight changing of the imaging properties of the lens systems. In the image, FL refers to the fluorescence detection channel, LAS refers to the low angle scatter detection, SS to the side scatter, FS to the forward scatter, and EX the channel provides the excitation for the measurement. This device has not been demonstrated to perform cytometric function; rather it was fabricated as a demonstration of fabrication capabilities and to demonstrate the capabilities of LOC devices in general.

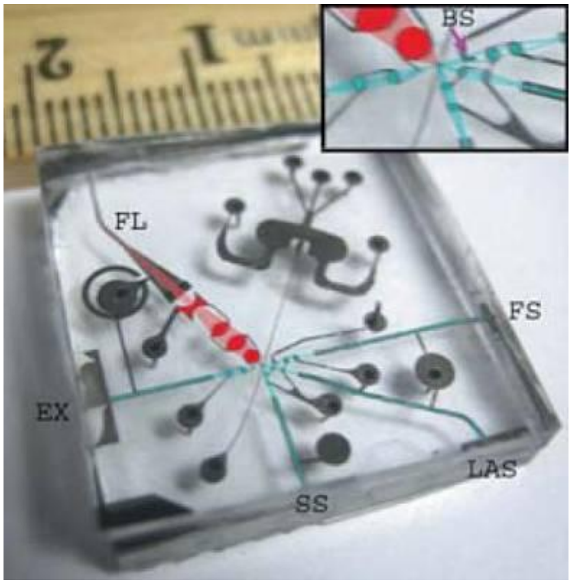

**Figure 1-26: Device showing a very high level of optical integration showing solid core waveguides and liquid filled lenses that perform excitation and side scatter, forward scatter, fluorescence collection. *Source*: Reprinted from reference 97.**

Up until now devices have shown a good level of optical functionality, but not to a level that even closely mimics conventional free-space beam shaping. As conventional cytometry requires beam shaping to improve the reliability of detection, so should any microchip-based flow cytometers.

### 1.2.2.4 Advantages

Advantages of microchip-based devices with integrated optics are astounding and are the key driver behind the potential applications of devices. Firstly, large advantages in the form of cost savings stem from channel miniaturization. Small channel dimensions reduce the sample volume requirements for analysis thereby increasing the sensitivity of analysis – which also translates into reduced costs and less labeling agents required.[‡‡],[98]

Integration of optical components creates further advantages for costs savings and system complexity, with added benefits to the operation, durability, and calibration of the device. The inclusion of optical components on-chip removes the necessity of free-space optics and reduces equipment requirements and costs while increasing the portability and durability of the device. Operation of devices are simplified, as optical systems are designed and manufactured with optimal performance, alignment, and calibration for a specific detection function already completed.[§§,98]

As alluded to in section 1.2.2.1.2, sensitivity of analysis also is increased from the improvements to light delivery and increased intensity due to on-chip integrated optics. Furthermore, the miniaturization and increased proximity of optical components allows increased sensitivity of optical detection.[***,98]

Using microchip-based designs, the resulting device form is simplified and allows easier plug and play capabilities where expensive components can be reused – such as the laser, detector, and software - while the inserted chip – that contains all specificity for the application – integrates seamlessly with components.

Efficient and inexpensive devices can be formed through fabrication of devices with a very specific detection procedure on chip. This enables devices with a one-time use as devices are cheap and disposable. Devices can form a plug-and-play device where specific calibration and test configuration is done in chip design and manufacturing. A reusable "console" that houses a cheap and general "all-purpose" laser and the necessary electronics can be fabricated and would be the only capital expenditure.

---

[‡‡] This sentence is from the author's published work in reference 98.
[§§] This sentence is from the author's published work in reference 98.
[***] This sentence is from the author's published work in reference 98.

## 1.2.3 Applications

### 1.2.3.1 General Device Performance

Early demonstration of a microfabricated device showed a miniaturized flow cell with free-space optics was able to detect *E. coli* bacteria. The fluorescently labelled cells were detected via the simultaneous collection of fluorescence and scatter signals from the cells. Detection events are evident from Figure 1-27, which shows the results from such a test with raw data showing good correlation between events and histograms demonstrating good population characteristics.[40] The device and the detection method had excellent reliability, as the device was able to detect 94% of the bacteria present in the sample.

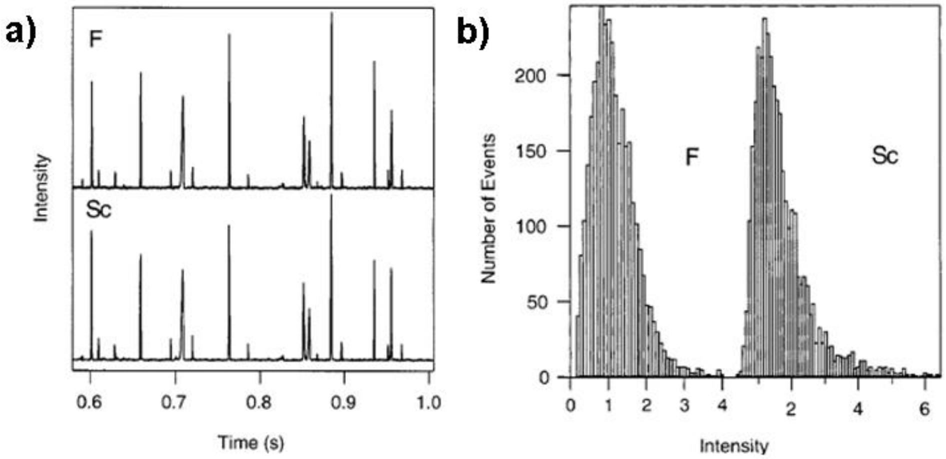

**Figure 1-27: Results from an E. coli bacteria counting application with a microchip-based flow cytometer device with free-space optical excitation and detection showing a) sample of the obtained signal during processing samples with fluorescent (F) and scattered (Sc) signals and b) plots of the histogram (right) obtained. *Source*: Reprinted from reference 40.**

Another device with a similar architecture of the above device but with improved performance is demonstrated below, in Figure 1-28.[52] This device had a microfabricated flow cell and used a free-space optical detection scheme to collect 2 parameters of interest: fluoresced and side scattered light. The device deomonstrated a 94.4% detection rate at a high throughput of over 350 cells/second. The results in Figure 1-28 show the raw data and the histograms generated from the detection of the two parameters from the E. Coli bacteria. There was excellent correlation between the two parameters, however some events were missed, like the one indicated by the small arrow on the plot. The formed histograms showed excellent population characteristics and demonstrate that the microfabricated flow cell is a suitable replacement for conventional flow cytometery.

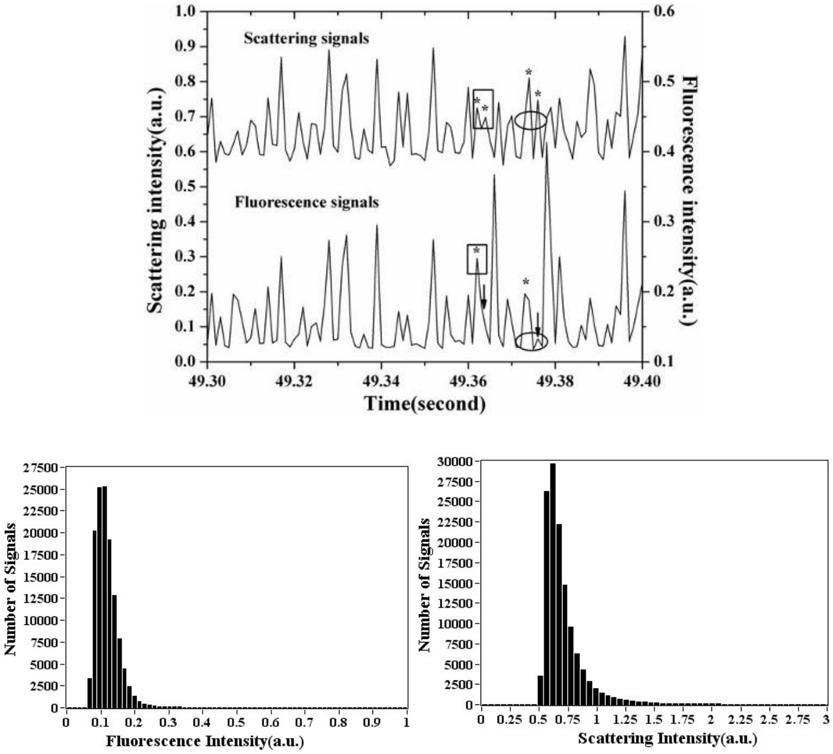

**Figure 1-28: Results showing a 0.1 s segment of the 300 s run of light scattering and fluorescence emission bursts for 5.0×106 cfu/mL FITC-labeled bacteria E. coli DH5α at an average particles throughput of 350 particles/s, the asterisk (*) indicates a event detected by peak algorithm, and the arrow represents a event missed by this algorithm. Histograms for fluorescence emission and light scattering intensities collected from FITC-labeled bacteria E. coli DH5α. *Source*: Reprinted from reference 52.**

A device that included a waveguide and a simple lens is shown in Figure 1-29a). This device was used in a simple scatter detection of blank polymer beads to try to detect a variety of sizes. The results, shown in Figure 1-29b), demonstrate the ability of the devices to resolve populations of the various sized beads. A range of particles from 2.8- to 9.1 μm in size were detected and decent CVs were detected – within the range of 25 to 30%.

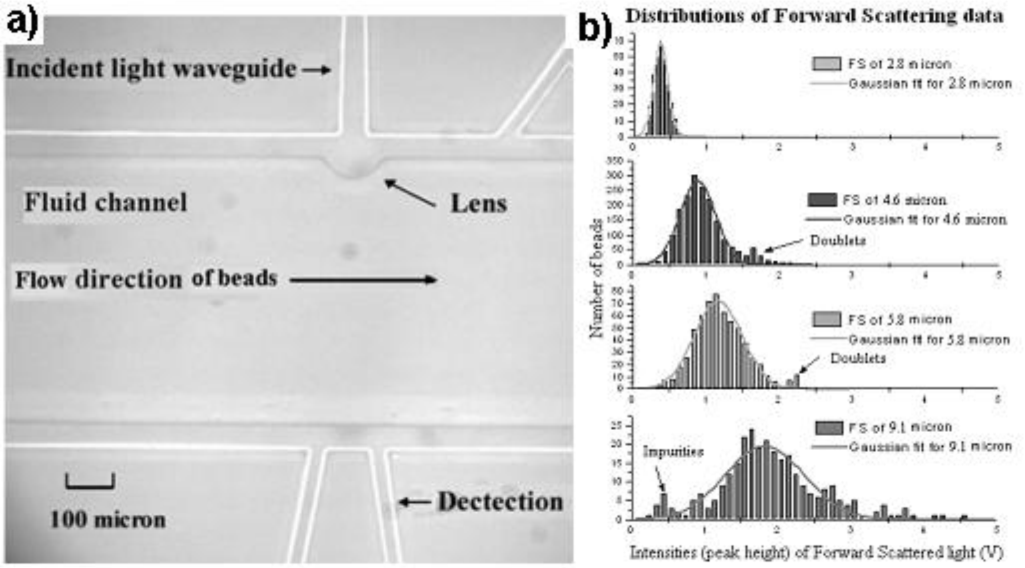

**Figure 1-29: a) Picture of a microchip-based device that incorporates waveguides for excitation and collection with a microlens for intensity improvement. B) Scatter histograms showing the performance of the device at different bead sizes – note the Gaussian fit and the double detections for larger sized beads and introduction of impurities. *Source*: Reprinted from reference 90.**

As the devices can reliably detect bacteria, they can be deployed in counting functions in conjunction with other devices. This has been demonstrated by the device shown in Figure 1-30.[47] The packaged device incorporates two flow cytometers located before and after an electrophoresis separation chamber. The devices incorporated inserted fibres for excitation and a simple free-space scheme for detection; it is clamped in order to provide a liquid-tight seal. The function of the flow cytometry units in the device’s overall function was to measure the efficiency of the on-chip electrophoresis chamber to sort yeast cells. Both units were able to differentiate between live and dead cells and log the events. Both flow cytometry units also provided a very simple detection, presence/absence decision and therefore, no need for high quality beam geometry. These units demonstrate a very rudimentary application, however, unless the detection reliability were increased – say through the addition of beam shaping on-chip – the devices would not suffice in higher level functionality or assay application.

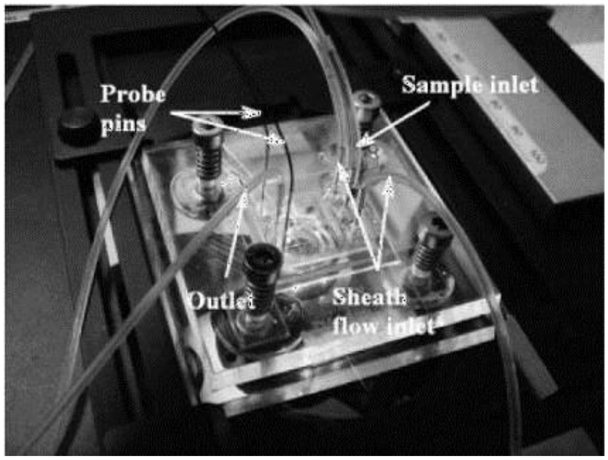

**Figure 1-30: Picture of a microfluidic chip with capillary tubes used as inlet and outlet tubes and inserted fibres for the flow cytometer excitation. A microscope objective is placed below the sample for detection and imaging purposes. *Source*: Reprinted from reference 47.**

Very high level and performance devices have been shown and have demonstrated the ability of flow cytometers for adequate performance in a microchip-based platform. Figure 1-31a) shows a device that incorporated the completely planar 3D hydrodynamic focusing method that was shown in Figure 1-19b) – with a modification that included inserted fibres for excitation and detection – as seen in Figure 1-31b).[99] This device was able to simulataneously collect 3 parameters: one fluorescence signal, and both the forward scatter and side scattered signals. The device was tested using three different microspheres sizes. Most importantly, this device utilized a high-quality single mode excitation source to control the divergence of the beam in the channel and limit the range of excitation intensities given to the specimens. Reliable detection at excellent SNR was observed, however it was noted that a large variance in detection intensity was caused by variation of the particles within the excitation beam – partly due to hydrodynamic focusing that could have been tighter. This work concluded that the performance could have been improved through tighter focusing of the sample, or a better beam quality. Tighter hydrodynamic focusing isn’t always possible due to the complexities of fluid flow.

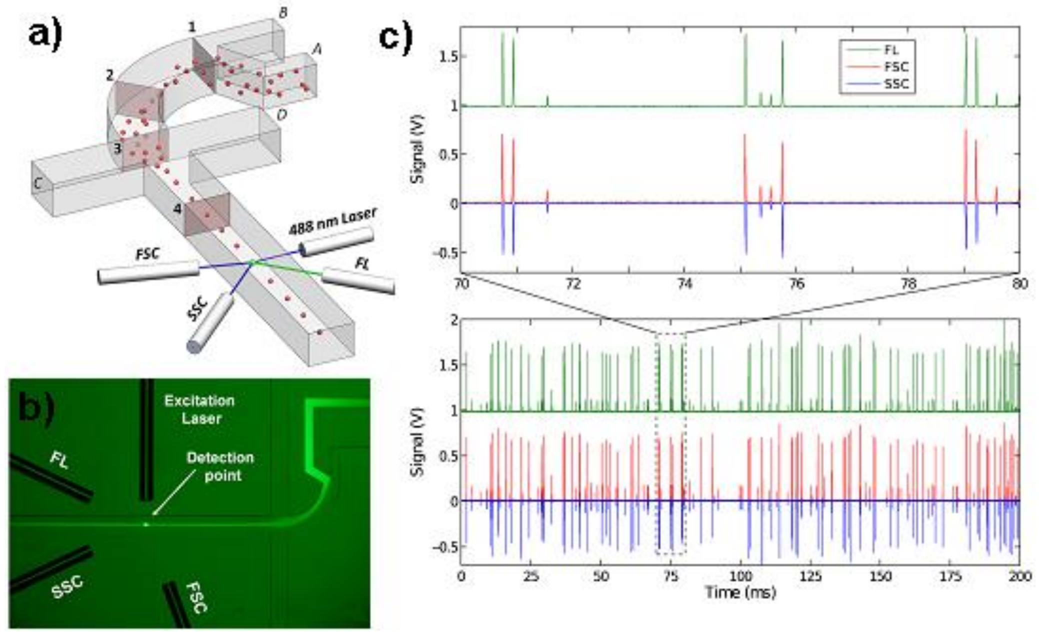

**Figure 1-31: a) Microchip-based device that incorporates 3D planar hydrodynamic focusing with inserted fibres for excitation and collection. b) Fluorescent image showing the focused stream of dye and inserted fibres. c) data from three simultaneous measured parameters: fluorescence, forward scatter and side scatter. *Source*: Reprinted from reference 99.**

One such microchip-based device has even been deployed to characterize several different species of marine algae. The device, shown in Figure 1-32a), has inserted fibres to excite with two different wavelengths: 532nm and 404nm.[75] This device also simultaneously collected the two wavelengths of fluorescent light from cellular structures containing phycoerythrin and chlorophyll. These two structures are naturally fluorescent and the specific quantities of fluorescent light will allow quantification of each of the cellular structure within, and thereby, conclusions can be made of the particular species and its relative characteristics of the cell within that population. Results depicted in Figure 1-32b) shows scatter plots for four different species of algae based off the quantities of fluorescence. Each scatter plot is a type of signature that can be used to identify different species in future tests.

The architecture of the device allows quick testing. The fibres allow quick removal from lasers and detectors and to swap in a new chip if the old one happens to clog allowing a plug and play format. This device also used the micro-weir structures mentioned in Figure 1-19a) to help increase the reliability of detection. Again, single mode fibres and a high quality laser source was used to control the divergence and deterioration of the beam as it traversed the channel.

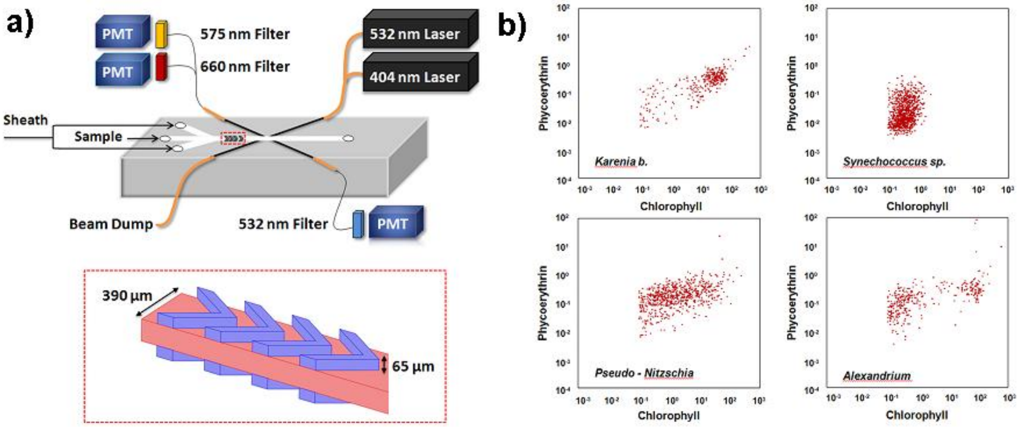

**Figure 1-32: a) picture of a microchip-based device with inserted fibres and a micro-weir structure for 3D hydrodynamic focusing. b) scatter plots comparing fluorescence from chlorophyll and phycoerythrin showing distinct populations for four different species of algae. *Source*: Reprinted from reference 75.**

Another practical application of a microchip-based device was the demonstration of the devices ability to detect a harmful bacterial species in milk samples.[100] A device was deployed to successfully detect lysteria monocytogenes using a commercially available microchip based system. This system was noted to have immediate application in safety and security monitoring and food quality inspections.

### 1.2.3.2 Point-of-care medicine

**Point-of-care (POC) medical applications have been cited as one of the most important and far reaching applications for LOC devices.[101,102,103,104] A study (review) was undertaken to show the applicability of mircofluidic flow cytometers as a portable haematology analyzer.[105] The proposed device should serve as a device that is able to perform a complete blood count (CBC) – ie. differentiate and count all the different components found in a sample of blood. CBCs are used to diagnose many conditions as seen in**

Table 1-2.

**Table 1-2: Type of CBC done and the diagnosis attributed to the count.**

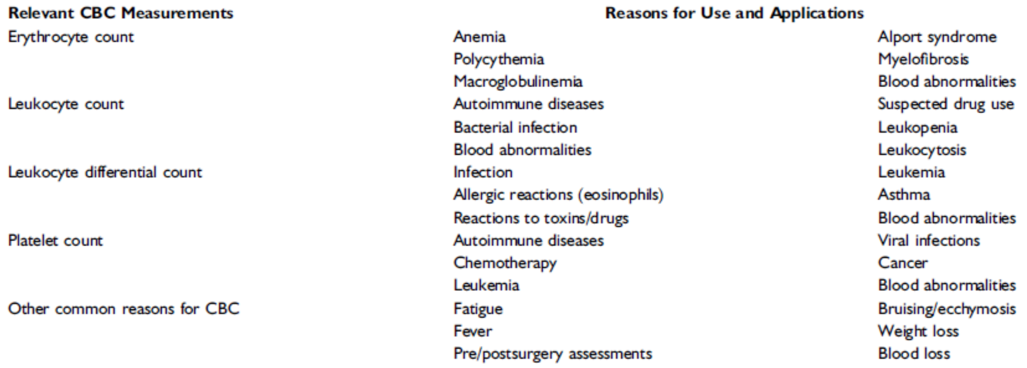

| Relevant CBC Measurements | Reasons for Use and Applications | |
|---|---|---|
| Erythrocyte count | Anemia | Alport syndrome |
| | Polycythemia | Myelofibrosis |
| | Macroglobulinemia | Blood abnormalities |
| Leukocyte count | Autoimmune diseases | Suspected drug use |
| | Bacterial infection | Leukopenia |
| | Blood abnormalities | Leukocytosis |
| Leukocyte differential count | Infection | Leukemia |
| | Allergic reactions (eosinophils) | Asthma |
| | Reactions to toxins/drugs | Blood abnormalities |
| Platelet count | Autoimmune diseases | Viral infections |
| | Chemotherapy | Cancer |
| | Leukemia | Blood abnormalities |
| Other common reasons for CBC | Fatigue | Bruising/ecchymosis |
| | Fever | Weight loss |
| | Pre/postsurgery assessments | Blood loss |

This study also pointed out that all patients in an emergency room (ER) undergo at least one CBC test via a bulky and expensive machine. This is a cumbersome and time sensitive procedure that is not best suited for the environment typically found in an ER. The ability to analyze blood samples with little to no preparation in an inexpensive and portable device is of immense value to medical professionals – in an ER or otherwise. A fast readout and immediate diagnosis at the patient's side would revolutionize the quality of care and the effectiveness of treatments.

Other specific POC applications, such as CD4 T-lymphocyte counting,[106] would enable a valuable tool to help to control could provide the necessary tool to help eliminate HIV in areas where it is an uncontrolled epidemic. Such a portable and inexpensive device would also serve to increase the level of treatment in developed countries. Ths work indicated that the technology is making the applications possible, however there has only been one success to date.[107]

A device that facilitates flow cytometric based immunopheontyping would allow immediate and constant monitoring of states of leukemia.[108] This would be of immense value in cancer treatments as it would facilitate continuous and inexpensive monitoring of residual disease – an important feature of effective cancer treatment. An up-to-date and exact picture of the state of the immune system, as provided by a flow cytometric analysis, would help medical professionals target treatments to ensure effective and efficient treatment.

Numerous other POC applications exist and have been proposed that range from clinical diagnostics, immunoassays, proteomics, and DNA sequencing and analysis.[35]

#### 1.2.3.3 Global Health Applications

Microchip-based flow cytometry, due to the portability and inexpensive potential, have far reaching possibilities and application for revolutionizing health care in developing countries. Currently, controlling the aids epidemic in Africa relies upon diagnostic methods based upon Polymerase Chain Reaction (PCR) methods, but real-time cell CD4 counts and determining the current viral load are very important details required for determining the most effective treatment options.[109] PCR-based methods are time-consuming, require large capital investment in equipment, and require trained operators to process and interpret results. A microchip-based flow cytometer would provide the analysis capabilities desired while eliminating the roadblocks that are keeping current cytometers out of such applications.

Current flow cytometer options for developing nations ravaged by epidemics have costs that are approximately $10 USD or more per test plus an initial investment of over $20,000 for a dedicated flow cytometer machine that could perform about 250 tests/day.[110] Operating parameters like these are a step in the right direction for creating a feasible machine – and are well within the affordable metrics by North American standards - however, these machines are still very expensive, not portable, and also require a skilled and dedicated technician – all options that are not always feasible in resource-poor settings.

Recently a study concluded that a cheap and efficient method for diagnosing communicable diseases would have the largest effect on the health of individual in developing nations.[111] This study also listed ten other technologies that would have a significant impact on the health of individuals in these resource-poor nations. The capabilities of flow cytometery or a microchip-based version would be applicable to six of the ten technologies listed. No doubt that a photonic integrated microchip-based cytometer has the potential to meet the needs of global health needs with a device that drastically reduces costs while allowing a portable and durable device. Such a device would be simple to use and allow plug-and-play capabilities with specificity of detection on-chip, thus reducing the costs of any initial capital expenses. The are no such devices functioning in these applications as of yet as the reliability of detection from the on-chip optics has not been demonstrated to serve as a reliable means of detection that can rival conventional methods.

#### 1.2.3.4 On-line Sensing and Monitoring

Environmental-based applications of microchip-based flow cytometers has been mentioned earlier in this work, however the devices that served these applications were laboratory based operated by a skilled technician. A real advantage to environmental applications would be a device that could be easily deployed in the field and operated remotely. If the function of the device is run in a continuous manner, and if the data were fed to a central command station, then these devices could create new applications allowing very powerful on-line sensing or monitoring functions. The small size of devices would ensure they could fit in small areas such as in water pipes or air ducts. The small size of the device also ensures the power consumption is reduced meaning that battery power is feasible – a necessity for in-the-field deployment. Monitoring real-time would allow timely and effective decisions to be made to locate the source of a potential problem and apply an efficient remedy before it develops into a large scale problem.

## *1.3 Research Objectives*

The overall goal of this research was to expand the current level of functionality of microchip-based flow cytometer devices to a point where they have reliable enough analysis capabilities to actually be used in POC or remote applications.

Through careful simulation, design, and fabrication, integrated optics are developed for introducing excitation light and achieving a beam shaping function on-chip to develop a system that is compact, low-cost and reliable.

As many of the devices described above did not deploy beam shaping on-chip this was one area that was defined early on as an avenue which would allow improvement of the operation of the devices. The lens systems used up until this work was proposed only served a simple function: to increase intensity at the point of interrogation or minimize losses of the beam and increase efficiency of the optics. However, conventional cytometry has long used beam shaping as a key element that allows the CV's of conventional cytometers to be extremely low and thus, allow accurate population-based conclusions to be drawn.

Many of the devices cited in the literature have focused on the 'tuneability' or flexibility of devices. Essentially much effort has been on creating a device that is able to perform many functions or assays in a device that is reuseable. These devices still rely on high-quality beam from single-mode sources – a direct barrier to many LOC and POC applications as it incurs large costs - something that goes against the niche of POC and LOC devices. Furthermore, a reusable device is a completely unnecessary function with the current manufacturing technology – economies of scale allow many devices to be made very inexpensively thus allowing many one-time use units that will lower the cost/test and eliminate problems should one fail or clog.

With this in mind, the aim of this work was to boost the reliability of detection, and thus performance of devices, by using on-chip integrated optics to tailor the beam to a particular optical geometry that leads specimen interrogation to excellent detection reliability. Furthermore, the device's reliance on a high-quality source must be relieved as POC and LOC based applications will demand low-cost and low energy components – especially for remote and on-line applications.

This work will attempt to apply integrated optics to collect testing signals to further create a compact the system, reduce system's costs and operation costs via a completely alignment-free design, and make the system completely portable.

It is this low reliability of detection that has kept optically-integrated devices in simple counting and presence/absence applications in laboratory and bench-top settings and it is this gap from the current technology to the desired performance that this work will seek to bridge

### 1.3.1 Proposal

This work attempts to solve some major technical problems concerning integrated optical designs. Through the integration of an input waveguide with a complex lens system into the same planar structure containing microchannels, the device will easily introduce an on-chip beam shaped excitation source of light into the channel for specimen interrogation. The integrated on-chip lens system will be fabricated in a planar fashion with the microchannel allowing 2D control of the beam geometry. These lenses will be designed to form different beam geometries in the channel; the geometries will form narrow beam waists in the channel to control the "time-of-flight" of particles and limit the double detections. Simultaneously, the lenses will tailor the intensity profile to form a uniform region of intensity in the flow direction – through the entire beam waist - and in the direction perpendicular to the flow in the plane of the chip; controlled through the system's depth of focus. This uniform intensity will ensure uniform excitation and more reliable detection shifting the cause of signal variance away from the system and to the specimen.

This work will attempt to succeed in moving the optical functionality of detection analyses to an on-chip platform in a seamlessly integrated fashion with the microchannel. Through the integrated excitation optics, the proposed devices will remove the dependence on free-space components for excitation allowing simpler testing and function of devices. Device designs will also allow a low-quality source to be used and achieve similar functionality to a device that uses a conventional single-mode beam as a source. Through integration of waveguides into the device – in addition to those used in conjunction with the beam shaping function – devices will be able to achieve signal collection on-chip. This further removes the devices dependence on free-space collection optics. As a final device improvement, the designs will integrate a novel method for on-chip forward scatter detection with the inclusion of on-chip excitation optics that serve a beam shaping function. This is an entirely new method for completing on-chip forward scatter collection.

### 1.3.2 Focus

The design of a microchip-based device are better suited for applications discussed above and will help the current level of devices achieve the next step to fill this application void. The proposed optical lens systems will take great care to form a beam geometry whose intensity profile has been optimized for reliable detection. This work will take into account the size of the specimen and target the beam – and application of the device - to that particular specimen. As device designs have an emphasis towards applications that require devices that are cheap and disposable, designs were of a one-time use format and have this end use in mind. Furthermore, miniaturization will allow many interrogations or analysis steps to be performed sequentially on one chip in one flow allowing multiplexing of analysis on chip. Designs allow a low quality source, and reshaped this beam to better optical illumination intensity.

The work herein tuned the fabrication procedure to produce the best quality devices possible for applications. Quality of devices was further improved through testing a more feasible and realistic packaging method to withstand the high pressures generated during operation.

Design of the device in this work approached the problem from a first-principles based method. Device design was broken up to consider each component separately and integrate them one-by-one after simulation and understanding of the most optimal deployment and configuration of the device with other components.

## 1.4 Contents of the thesis

This thesis has been broken down into five chapters. The first chapter – the current one – is an introduction to flow cytometry and microchip-based forms of flow cytometry and the applications and technical challenges and current gaps in this field. The next three chapters contain the work performed to accomplish the proposed idea divided up into the logical compartments from conception to realization and evaluation. Chapter 2, Device Design and Simulation, contains the simulations of the various designed devices and the resulting optimized device designs as well as covering the theory necessary to lead the reader through the logical progression of simulations to final device form. Chapter 3, Device Fabrication and Testing, contains a summary of the work that lead to the details necessary to properly fabricate and test the devices while the methodology of analysis for evaluating devices is also presented. The fourth chapter, Devices and Device Performance, contains the details and quality assurance inspections of the fabricated devices and the data obtained from the various testing and the evaluation of the data followed by a comparison to other similar devices listed in the literature. The last chapter draws some conclusions, proposes improvements, and outline possible future work.

# 2 Device Design and Simulations

The goal of this thesis is to produce a microchip-based flow cytometer that can mimic the functionality of a conventional cytometer – albeit for only a limited and specific function. As such, the optical systems should be fabricated on the device and optimized to work in the new integrated planar fashion. This ensures complete functionality of a portable device without sacrifice to analytical capabilities. This chapter discusses the theory behind the basic components used to create the device and then uses the theory to build these basic components and integrate them together in a logical order. The components are simulated one-by-one to understand performance and allow optimal integration together. Final simulations are used to guide the overall design and function of the devices.

## *2.1 Theory*

The theory presented here will give the reader an intuitive understanding of the function of the device's components. This treatment is by no means exhaustive; a full understanding of optical theory is not necessary to understand the device function and to make connections between device structure and performance. However, with a greater understanding of optical theory comes a greater optimization and understanding of device function.

### 2.1.1 Waveguide propagation

When an electromagnetic (EM) wave encounters a discontinuity in the refractive index of a medium the wave reflects and transmits according to the Fresnel relations. In the geometric ray approximation, we don't need to consider the polarization of the light, as the distances covered from propagation are many wavelengths in length. Thus, the light is represented by a straight line called a ray.

At the interface of an index discontinuity, the transmitted ray angle is governed by Snell's law, which depends on the indices of the two medium and is given in Equation 2-1.

$$n_1 \sin\theta_1 = n_2 \sin\theta_2$$

**Equation 2-1: Snell's Law.**

Figure 2-1 illustrates this situation where a ray is incident at a discontinuity and shows the two resulting rays: the reflected (black) and transmitted (red) ray. In this case the initial index, $n_1$, is greater than the outside index, $n_2$. Figure 2-1a) shows that the incident ray has a reflected component with an angle equal to the angle of incidence. The transmitted ray's angle is determined by Snell's Law - also shown in Figure 2-1a). At a certain angle – dubbed the critical angle – the solution to Snell's Law shows a transmitted angle of 90º. This situation is shown in Figure 2-1b). The critical angle, $\theta_c$, is given by Equation 2-2.

$$\theta_c = \sin^{-1}\frac{n_2}{n_1}$$

**Equation 2-2: Equation to find the critical angle.**

At angles of incidence above this angle, there is no transmitted ray and all the incident light is confined within the incident material. This situation is depicted in Figure 2-1c) and is called total internal reflection (TIR). Note that this situation only occurs if the initial material has a higher index than the second material.

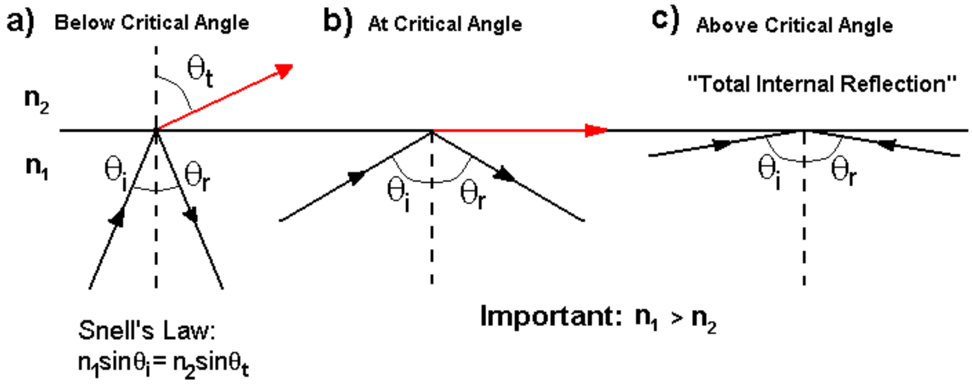

**Figure 2-1: Diagram showing a light ray incident at a discontinuity and illustrating Snell's law and the total internal reflection at: a) below the critical angle, b) at the critical angle, and c) above the critical angle.**

By sandwiching a slab of a high index material between two lower index materials a beam of light that is initially incident above the critical angle will be confined within the material as the light will bounce back and forth between the high index material's boundaries. Due to a portion of the ray vector pointing in a direction parallel to the boundary, this will cause the light to propagate down the material as a result of the light bouncing back and forth between boundaries. This structure is called a waveguide. This high index material that confines the beam is called the core of a waveguide while the flanking lower index regions are called the cladding. The configuration of a planar slab of material sandwiched between two planar cladding layers forms a waveguide that confines the light in one dimension, due to the light only being confined within a plane, but it can easily be extended to a two dimensional confinement by forming a one dimensional strip of material to confine the light in a line. This is the structure that is the basis that forms all optical fibres and waveguides.

#### 2.1.1.1 Multi-Modal Propagation

Just because a ray has an angle of propagation that will mean the angle of incidence is above the critical angle at the core's boundaries does not mean that the ray will propagate in the waveguide. In fact, not all rays are allowed to propagate within a waveguide, they must meet a criterion. As many rays are bouncing around inside the core, many will cause destructive interference. Setting up a boundary value problem will derive solutions of the wave equation that will specify the intensity profiles of the allowed with the waveguide. The solutions, called modes, form all the wave solutions to the boundary value problem with the index profile specified by the geometry of the waveguide. There are typically many solutions – especially if the waveguide width is much larger than the wavelength of light – and each solution is one of a typical Eigen value problem. Each mode consists of a collection of rays that form a stable intensity profile of propagation, ie. the rays that define a specific mode interfere to form a steady state intensity profile that then propagates down the length of the waveguide. The lowest Eigen value is the fundamental mode of the waveguide and forms the simplest solution, usually forming a two dimensional Gaussian profile. Any other modes that form solutions of this boundary value problem indicate that the waveguide is multimodal in nature and will have a much more complicated intensity profiles.

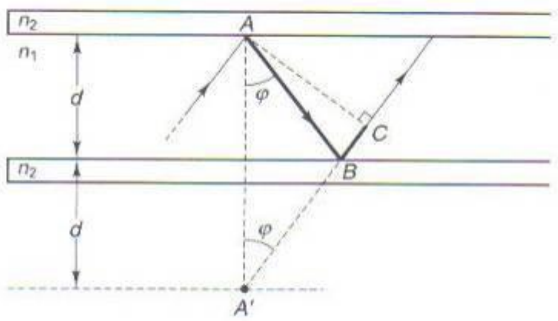

**Figure 2-2: Picture showing the condition that propagating rays must satisfy in order to form a mode. The rays must constructively interfere to form a stable image within the guide. *Source*: a) Reprinted from reference 112.**

From a geometric optics point of view, the condition to form a mode is much simpler. The picture shown in Figure 2-2 depicts a ray of light propagating within a simple slab waveguide. This ray is incident at the top surface, at A, and propagates to the bottom surface at B, where it reflects and propagates to the top surface again in a direction that is parallel to the path that it traveled before it was incident at A. If a line is drawn perpendicular from the propagation direction, a wavefront is represented by a plane wave that propagates in the waveguide. This wavefront is represented by the line segment AC. This wavefront must be maintained in order for a stable propagation of light down the waveguide.[112] This means that the round trip from ABC must be an integer value of 2π of the wavelength. This forms a stable image – called the beam intensity profile - in the waveguide. This formed image then propagates down the waveguide. The higher the order of the mode, the higher the angle of propagation in the waveguide. Any rays that don’t meet this criterion are not coupled into the waveguide because they will destructively interfere with one another and are thus considered losses. If the waveguide can accept many modes this means that more light rays that can be accepted into the waveguide and thus a higher power of light can be carried within the waveguide. As single mode waveguides only accept first mode – the fundamental mode - this means that they have a very selective coupling condition due to the restriction on acceptable ray angles. Therefore, the waveguide will have a high coupling loss.

Given that many different beam profiles are combined to form a beam image within a waveguide, a multimodal beam has a very unpredictable and messy beam intensity profile. Figure 2-3a) shows a couple of mode profiles for a cylindrical coordinate system. The ‘l’ and ‘m’ values are the Eigen values of the wave equation solutions for the angular and radial coordinates, respectively. Note that the solutions are periodic in the direction of the coordinate. Ie. the Eigen value indicates the number of oscillations that occur over the coordinate’s direction in the sinusoidal wave solution. An ‘m’ value of 2 means that there are two rings; whereas an ‘l’ value of 2 means that there are 4 lobes. Figure 2-3b) shows mode profiles in a rectangular coordinate system from a rectangular waveguide. Again, the numbers in the subscripts represent the number of zero crossings in the cosine intensity profile solutions. So, efficient coupling between a fibre and waveguide would require mode profiles to match; any mismatch is a significant source of loss in the coupling from one waveguide to the other.

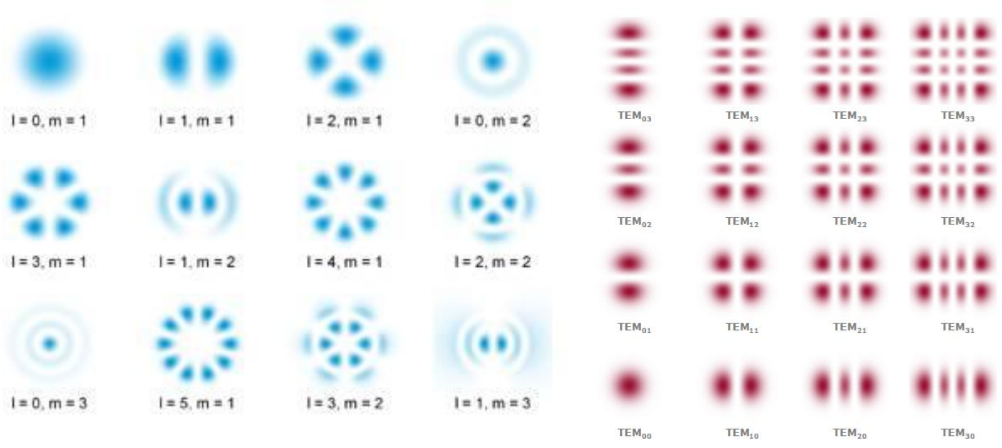

**Figure 2-3: Mode profiles for a) cylindrical waveguide geometry, and b) rectangular waveguide geometry. *Source*: a) Reprinted from reference 113, b) reprinted from reference 114.**

As mentioned earlier, a single mode beams will have a two dimensional Gaussian profile; ie. a very intense central region with diminishing intensity as the distance from the centre increase. The combination of many higher order modes will form profile that is approximated by a Super Gaussian. The equation that describes a typical super Gaussian profile is given by Equation 2-3.

$$I(r) = I_o \exp\left[-2\left(\frac{r}{\omega_b}\right)^N\right]$$

**Equation 2-3: Equation describing the intensity profile for a Super-Gaussian profile.**

$I_o$ is the on-axis intensity, r is the radial coordinate, $\omega_b$ is the waist at $1/e^2$ intensity, and N is the order of the Super Gaussian. Note that if N = 2 then a normal Gaussian curve is obtained. Typically with a multimodal structure, N is greater than 10. For an actual multimodal intensity profile, however, the intensity curve will not be as smooth as the prediction given in Equation 2-3.

### 2.1.1.2 Numerical Aperture

The numerical aperture (NA) is defined as the ability of the waveguide to accept divergent rays. It is a parameter that describes the largest angle of ray that is accepted by the waveguide facet based on the conditions of TIR within the waveguide. A schematic of this is depicted in Figure 2-4. To calculate the NA, one must first find the critical angle in the waveguide and translate it to the maximum acceptance angle at the facet of the waveguide. This is now the maximum angle at which a ray can be incident on the waveguide facet and still be confined within the waveguide. This angle in fact defines a cone of ray that can be accepted given that the waveguide has cylindrical symmetry. Equation 2-4 shows how to calculate the NA of a waveguide.

$$NA = \sqrt{n_{core}^2 - n_{clad}^2} = n \sin \Theta$$

**Equation 2-4: Definition of the numerical aperture of a waveguide**

The NA can be calculated from only the knowledge of the indices of the core, $n_{core}$, and cladding, $n_{clad}$, materials. The NA is an important parameter on the input side of a waveguide as it defines the acceptance angle, but it is also important on the output side as well. The NA defines the divergence of the beam as it exits a waveguide. The larger the NA, the more divergent the beam as it exits the waveguide. Typically, this divergence is the same as the beam that is injected into the waveguide given that the waveguide properties do not change.

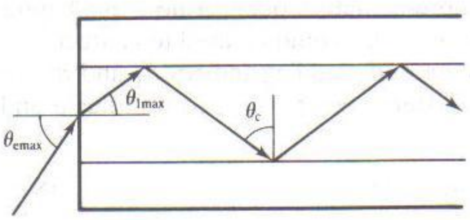

**Figure 2-4: A drawing showing the definition of the NA for a waveguide. The angle of the acceptance cone of rays is determined by the critical angle between the index difference of the core and cladding. *Source*: Reprinted from reference 115.**

### *2.1.1.2.1 Solid Angle*

When discussing a divergent beam, it is useful to discuss the solid angle that this divergence sweeps out in free-space. The cone of divergent rays from a waveguide is approximated by assuming the divergent beam originates from a single point. The solid angle defines how much of a solid sphere the beam covers assuming the ideal beam propagates as an isotropic spherical wave. The solid angle is the 3D extension of how an angle defines a portion of a circle in 2D. The solid angle is derived from the differential volume element in spherical coordinates with all proportionality to the radius removed. The solid angle doesn't change as one move closer/further from the origin given that the divergence angle of the rays doesn't change. Calculating the solid angle is done via the definition given by Equation 2-5, where θ is the azimuth angle and φ is the polar angle relative to a fixed zenith (typically the optical axis). The limits of the azimuth angle are between 0 and 2π while the limits of the polar angle are between 0 and π

$$\Omega = \int_{\vartheta_1}^{\vartheta_2} \int_{\phi_1}^{\phi_2} \sin\phi d\phi d\vartheta$$

**Equation 2-5: Definition of solid angle.**

Using the maximum limits, the maximum value of the solid angle, ie. the solid angle of a solid sphere, is 4π, indicating complete filling of free-space.

#### *2.1.1.2.2 Collection Waveguides and Collection Efficiency*

The solid angle can be used to describe a cone of rays emanating from a point while the NA defines the maximum cone of rays that can be collected by a waveguide. The NA of a waveguide can be expressed as a solid angle if the maximum angle of acceptance defined by the NA is used as the limits of integration in Equation 2-5. This solid angle is called $\Omega_{NA}$. The location of the point source can affect the collection efficiency – as indicated by the picture in Figure 2-5. Assuming a point source is emitting a cone of rays defined by some maximum angle, $\Omega_x$, the cone of rays will spread according to the angle as it propagates and increases the surface area the beam covers. If the surface area of the light is smaller than the waveguide facet, all rays can be coupled to the waveguide. A maximum distance is reached, at the point indicated A in Figure 2-5, where the surface area of the cone of rays is equal to the waveguide facet dimensions. By matching the cone of rays with the geometry of the waveguide facet one can ensure complete collection of the all emitted rays. Any longer of a distance between the waveguide and the point source, say at B in Figure 2-5, the cone of collectable rays is larger than the facet and the coupling efficiency will be decreased. This is due to rays that are within the confines of the definition of the NA and not being coupled due to them physically missing the waveguide facet – as given by the yellow portion of the cone in Figure 2-5.

Now, point A is defined by the source or the NA of the waveguide, depending on the solid angle of each. If $\Omega_{NA}$ is less than $\Omega_x$, then the cone of rays emitted from the point source is larger than the cone of rays that is collectable by the waveguide – leading to unavoidable losses due to the limited NA of the waveguide. The coupling efficiency is not source limited and can only be controlled through increasing the NA of the waveguide through a larger index contrast, if possible. The point source must be within the distance A which is defined by the NA of the waveguide; even if the surface area of the emitted rays is smaller than the facet dimensions, significant losses will still be sustained through losses from rays not meeting conditions for TIR. In the other case, where $\Omega_{NA}$ is greater than $\Omega_x$, then the cone of rays from the source is smaller than the cone defined by the waveguide's NA. This means that collection is source limited meaning that the point source is the determinant of how much light is collected. Increasing the waveguide's NA won't increase collection efficiency. The maximum point, A, is defined by the distance where the diverging source will match the waveguide facet's geometry. This example should clearly show how the smaller cone of rays will indicate which feature will limit the efficiency. Obviously, at a large enough distance, one will be beyond the maximum defined distance, A for both the waveguide definition and source definition.

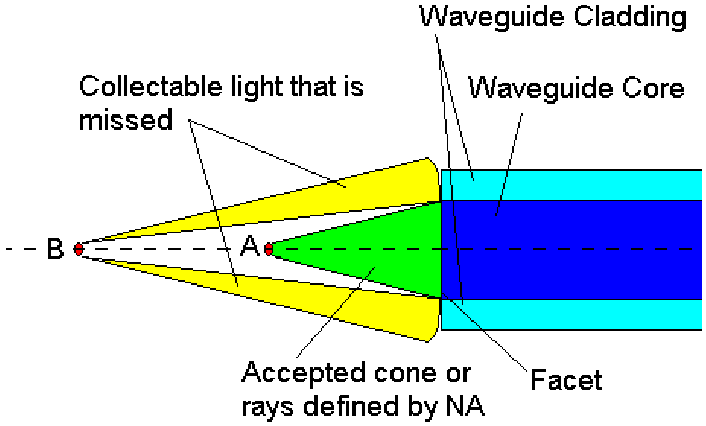

**Figure 2-5: Picture showing how a point source's position relative to the waveguide facet can affect the collection efficiency at the maximum distance, A, and an inefficient distance, B.**

To define the collection efficiency, one must divide the solid angle of collected light by the solid angle defined by source. One should use the solid angle of the collected light as it may be smaller than the solid angle defined by the NA of the waveguide. This is the typical situation when $\Omega_{NA}$ is greater than $\Omega_x$. This value is expressed as a percent and indicates the capability of the device to collect all the available light.

## 2.1.2 Refractive Optics

Using a curved surface allows for focusing effects of the light to be possible as the refraction at each point along the curved surface is controlled to send the light to a common point. Using lenses allows normally divergent light from the output of the waveguide to be focused to a common point. This at least allows for control of the beam divergence defined by the waveguide's NA.

### 2.1.2.1 Lens Equations

The focusing effect of a lens is described by the thin lens equation after a few approximations are made. The first is that the distance that the ray propagates is much larger than the wavelength of the light. The second approximation is that the lens is thin enough that any propagation through bulk material of the lens system can be ignored - with respect to normal propagation distances, ie. the ray exits the lens at the same radial position as it entered. Lastly, and most important, is that the majority of rays are paraxial, ie. close to the beam axis. As the beam makes an angle, θ, with the lens normal three approximations can be made: sinθ as θ, cosθ as 1, and tanθ as θ. This is only true if θ is small.

The thin lens approximation leads to a simple equation to relate the image distance and object distance to the focal length of the lens, given in Equation 2-6a). The full definition relating the radii of the curved surface and the index of the material is given in Equation 2-6b).

$$\text{a)}\ \frac{1}{s}+\frac{1}{s'}=\frac{1}{f} \qquad \text{b)}\ \frac{1}{s}+\frac{1}{s'}=\frac{n_2-n_1}{n_1}\left(\frac{1}{R_1}-\frac{1}{R_2}\right)$$

**Equation 2-6: a) Thin lens equation. b) Full equation for lens consisting of different radii on each side.**

From the equations in Equation 2-6, $s$ is the object distance to the lens, $s'$ is the image distance to the lens, $f$ is the focal length of the lens (system), $n_1$ is the ambient index (commonly air, so equal to 1), $n_2$ is the index of the lens material, $R_1$ is the radius of the front surface of the lens, and $R_2$ is the radius of the second surface of the lens.

A typical thin lens is depicted in Figure 2-6 where a simple object, RO, forms an image RI. The object has simple rays departing it and they are traced through the lens. The focal points are depicted along with the image and object distances. The focal length of a lens is defined as the image distance of an object at an infinite distance to the lens.

Again, much like a waveguide, a lens can be described by its NA. A lens actually has two NAs; one each for the input and output side. The input NA describes the maximum divergence of the light that can be collected by the system, and thus the collection efficiency. The image NA describes the divergence of the cone or rays that are emitted by the lens system. The definitions of the NA can be reversed if the direction of the rays through the system is reversed.

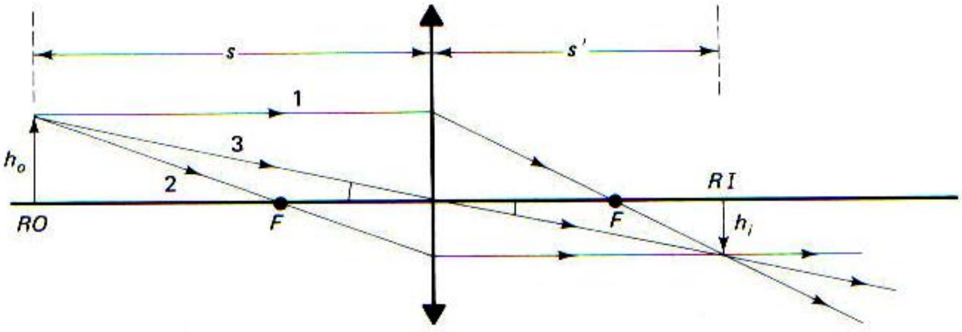

**Figure 2-6: Simple schematic of a thin lens showing how rays propagate through from the object, RO, and form an image, RI. *Source*: Reprinted from reference 112.**

### 2.1.2.2 Compound Lens Systems

When one or more lenses are used in very quick succession, it is cumbersome to constantly use either of Equation 2-6a) or b). Furthermore, the process becomes very complicated due to the sign convention attached with the relative position to the object and image with respect to the lens. A simplified method, called the matrix method, allows a quick analysis of lens systems' effect on propagating rays though the entire system. The system has the ability to describe every ray in the system by the radial component, y, and the angular component, α. The generalization of describing these rays is shown in Figure 2-7; every ray can be described the same way. A single radial and angular component provides a description for a group of rays in one direction or originating from the same radial location.

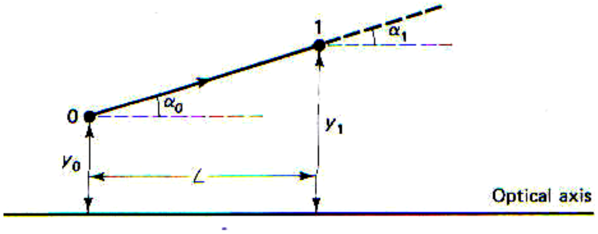

**Figure 2-7: Picture showing how a ray is depicted by the radial angular components for the matrix method. *Source*: Reprinted from reference 112.**

With the rays described by the two-component matrix, the rays then can have operations preformed on them that alter the ray components based on the individual refractive components in the system. Each surface element can be described by a subsequent matrix, called the ray transfer matrix. The multiplication of the input rays and the matrix produces a new ray matrix that describes the altered rays. As each subsequent ray transfer matrix multiplies with the previous ray transfer matrix and the ray matrix before that, a single ray transfer matrix can be formed for an entire system by multiplying the ray transfer matrix for each surface element. A simple example of this process is shown by Equation 2-7a).

$$M = \mathcal{R}_2 \mathcal{T} \mathcal{R}_1 \qquad \text{a)}$$

$$M = \begin{bmatrix} 1 & 0 \\ \dfrac{n_L - n'}{n' R_2} & \dfrac{n_L}{n'} \end{bmatrix} \begin{bmatrix} 1 & t \\ 0 & 1 \end{bmatrix} \begin{bmatrix} 1 & 0 \\ \dfrac{n - n_L}{n_L R_1} & \dfrac{n}{n_L} \end{bmatrix} \qquad \text{b)}$$

$$M = \begin{bmatrix} 1 & 0 \\ \dfrac{n_L - n}{n R_2} & \dfrac{n_L}{n} \end{bmatrix} \begin{bmatrix} 1 & 0 \\ 0 & 1 \end{bmatrix} \begin{bmatrix} 1 & 0 \\ \dfrac{n - n_L}{n_L R_1} & \dfrac{n}{n_L} \end{bmatrix} \qquad \text{c)}$$

**Equation 2-7: a) Matrix method for the propagation through a thick lens with b) the detail matrices for a thick lens and c) the approximation for the thin lens. *Source*: Reprinted from reference 112.**

A translation matrix, where the ray does not pass through any refracting elements, is the simplest matrix to describe. This matrix is described by the initial y and adding to it the angle multiplied by the distance travelled; the angle remains unchanged. An example of this matrix is given by the middle ray transfer matrix in Equation 2-7b). Again, this assumes very small angles of propagation as per the approximations made in 2.1.2.1. The refraction of the rays at a curved surface are found by splitting up Equation 2-6b) and separately applying it for the front and rear surfaces. The y component remains unchanged, but the angle is altered. The resulting matrices are shown as the first and last matrices in Equation 2-7b) and c). The entire process from Equation 2-7b) is for a thick lens, as the two refractive surfaces have a translation matrix inserted between them. Equation 2-7c) gives the complete description for a thin lens as the translation equation is for a distance of zero, as the value for t is zero.

The situation of a ray propagating through a thick lens is described pictographically in Figure 2-8. As indicated in Equation 2-7, there are two matrices required for each spherical refracting surface, each sandwiching a translation matrix.

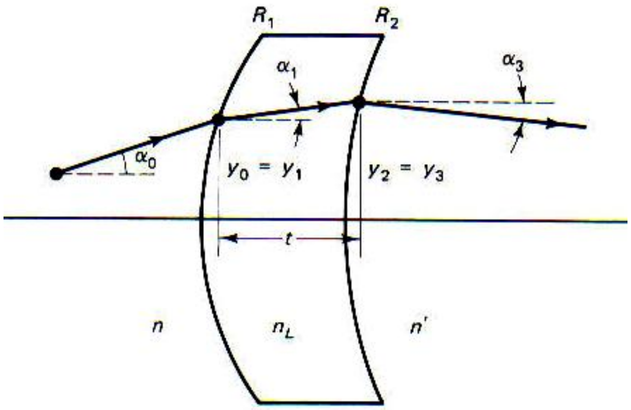

**Figure 2-8: A ray propagating through a thick lens. The parameters concerned with the matrix method are shown in the figure. *Source*: Reprinted from reference 112.**

### 2.1.2.3 Aberration Considerations

The lens equations discussed earlier were derived using the approximation that the rays were paraxial; ie. the angle between the ray and the lens surface normal is small. Outside of this paraxial regime this approximation and the corresponding lens equations break down and the predictions are inaccurate. Figure 2-9 depicts the difference between the emerging wave fronts from a lens system; one produced from the ideal paraxial approximation and another from the actual situation. As expected, near the optical axis the two wave fronts are approximately the same. The further away from the axis, the more deviation that appears between the prediction and actual situations. The outer radial rays are outside of the paraxial approximation. The resulting deviation from the two points on the wave fronts, A from the ideal and B from the actual wave front, is a shift in the lateral dimension of the formed image, from I to S.

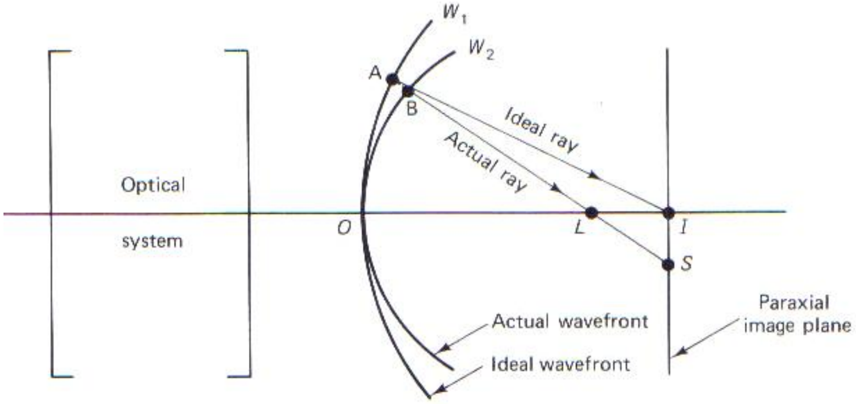

**Figure 2-9: Picture depicting how the prediction of a refracted wave front breaks down outside of the paraxial approximation.**

These deviations from the predicted performance of the lens equations are know as image aberrations. Of the five aberrations that exist, this work will only be affected by two: coma and spherical aberrations.

#### *2.1.2.3.1 Spherical Aberration*

Spherical aberrations are caused by non-paraxial rays and the break down of the approximation in the lens equations above. Spherical aberrations are unique in that they do not depend on the height position in the object plane meaning that spherical aberrations exist even for objects on the optical axis. A schematic of spherical aberration is shown in Figure 2-10 indicating that the aberration is due to the extreme rays forming an image that is shifted along the optical axis. Extreme rays at the edges of the lens are focused at a point E instead of at the ideal point I. At some point, M, there will be a ‘best focus’ where the blur from the rays meets some sort of minimum tolerance.

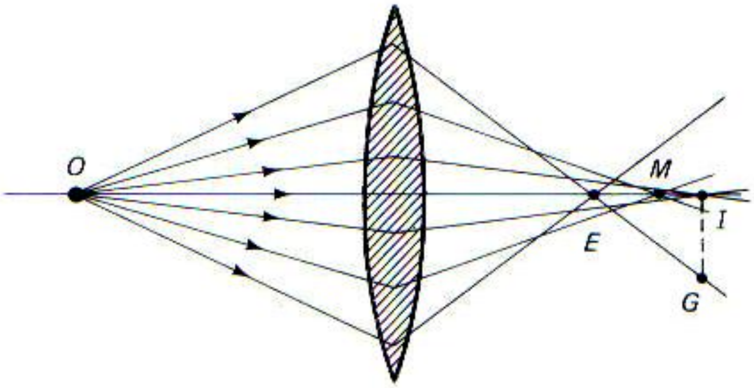

**Figure 2-10: Spherical aberrations due to non-paraxial rays and the shift along the optical axis of the image point from ideal, I, to M and E. *Source*: Reprinted from reference 112.**

A typical solution to spherical aberration is adjusting the curvature of the lens at the larger radial coordinates. This changes the lens from spherical, to elliptical, to parabolic, or hyperbolic. This effectively changes the angle of incidence for extreme rays to allow the refraction to shift the ray so that they are bent to focus at the image spot.

$$z = \frac{cr^2}{1+\sqrt{1-(1+k)c^2r^2}}$$

**Equation 2-8: Warping the sag, z, of the lens profile via a conic constant, k.**

Commonly, and as is done in ZEMAX, a warping factor is included in the lens profile equation. The lens surface then isn’t just expressed by a radius and thus allows other forms to be created. The equation that is used by the lens design software ZEMAX is given in Equation 2-8. The curvature is defined by *z*, the sag of the lens, and is essentially the lateral distance between the lens surface and a plane that is normal to the optical axis at the point where the lens intersects the optical axis. The parameter *r* is the radial coordinate; the distance perpendicular from the optical axis. The curvature of the lens is defined by *c* and describes the underlying spherical nature of the lens. The warping factor, *k*, is the conic constant, and is responsible for warping the surface away from the normal spherical nature. The value of the conic constant and the effect it has on the shape of the lens is given in Table 2-1.

**Table 2-1: Value of the conic constant and the shape of the lens surface.**

| Value of the conic constant | Surface shape |
|---|---|
| $k < -1$ | Hyperbolic |
| $k = -1$ | Parabolic |
| $-1 < k < 0$ | Elliptical |
| $k = 0$ | Spherical |
| $k > 0$ | Oblate Ellipse |

Proper deployment of Equation 2-8 allows specific lens shapes to be deployed that can completely eliminate spherical aberrations. In the case where it isn't necessary to eliminate all aberration, it allows the control of the aberrations. Now, a design can direct these extreme rays to a different part of the image.

### *2.1.2.3.2 Comatic Aberration*

Comatic aberrations are caused by the angle of the rays that intersect the lenses. As demonstrated in Figure 2-11a), the fan of rays that are focused by the lens have varying image points depending on the radial zone at which they intersect the lens. The rays from this fan should all be focused to the point defined by the chief ray (the ray the passes through the centre of the lens). As is evident from the figure, the further out the rays are from the centre of the lens, the higher the shift in the image point in the plane perpendicular to the beam axis. In Figure 2-11b) the effect comatic aberrations have on the image is described. This image is for a 3D lens system that has spherical lenses. Each circle is the image formed by a different radial zone of the lens. The top of each circle is formed by the tangential rays – shown in Figure 2-11a) – while the bottom of the circle is formed by the rays from the sagital plane – the plane that intersects the optical axis but is perpendicular to the plane shown in Figure 2-11a). All other rays along the radial circle that links the tangential and sagital planes form these comatic circles in Figure 2-11b). However, since this work will only deal with cylindrical lenses, only the tangential plane needs to be considered. This still cases a smearing of the focal point of the rays in the image of Figure 2-11b).

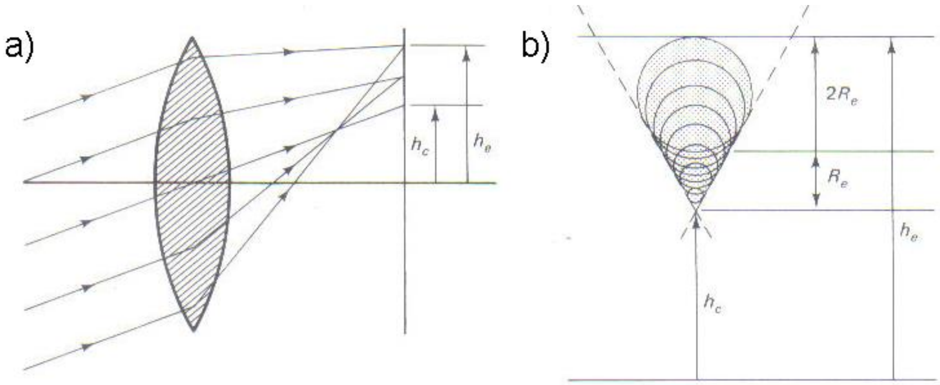

**Figure 2-11: a) Comatic effect from a lens. b) The image formed from each zone of the lens formes a comatic circle; the top is from the tangential rays (in the plane of incidence) while the bottom of the circles are from the rays in the sagital dircetion (perpendicular to the plane of incidence in a)). *Source*: Reprinted from reference 112.**

Comatic aberrations seem to have a demagnification effect as the extreme radial zones of the lens are considered – as evident by the increasing circle size of each comatic circle shown in Figure 2-11b). This can be controlled by bending the extreme portions of a lens to fix the magnification. Fortunately, comatic aberrations can be fixed in nearly the exact same way as spherical aberrations are fixed. In simple systems, the aberrations are identically controlled by the same warping of the lens.

### 2.1.2.4 Beam Width

A propagating beam is typically described by two parameters: intensity, and the width. Beam width has two common definitions: Full-width-at-half-max (FWHM), and $1/e^2$. The FWHM is the width of the typically Gaussian profile between points where the intensity is at half the max value. $1/e^2$ width is measured from the points on the typically Gaussian profile where the intensity drops to $1/e^2$ (or 0.135) of the maximum intensity. Either definition will work depending on the application's requirements.

When focusing a beam, the focused region is not an infinitesimally small region; it is an image of the beam with a contracted waist. The waist is the width of the beam, but in the narrowest region. This is shown Figure 2-12 as a beam is in the process of being focussed. The beam parameters are given as: $w_0(z)$ is the beam width as a function of the axial position, $z$, $w_0$ is the beam width at the point where the beam is most narrow, $d_0$ is the position of the waist, $z_R$ is the Rayleigh range, and $\theta_0$ is the beam divergence - the angle of the cone of rays in the far field. The Rayleigh range is defined as the distance from the beam waist where the beam area doubles in size. This is an important parameter when the beam has a Gaussian profile.

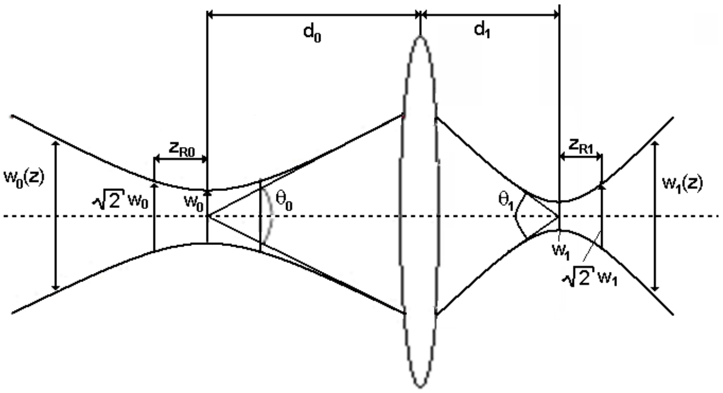

**Figure 2-12: Picture of a lens (system) focusing an input beam. Important parameters are given.**

After focusing – with large demagnification - one can see that the beam waist is compressed along with the depth of focus. Also, the divergence increases and the distance to the lens decreases. These relations can be described by the magnification of the system, M – which is defined by the image distance divided by the object distance. The parameters of the new beam related to input beam's parameters is summed up in Equation 2-10.

a) $M = d_1/d_0$ b) $w_1 = M \cdot w_0$ c) $\theta_1 = \theta_0 / M$

**Equation 2-9: a) Definition of the Magnification, b) relation of the object and image beam waists, c) the relation between the object and image divergence angles.**

When the input is from a waveguide, the waist is assumed to be the width of the waveguide while the divergence is defined by the NA. The image formed would be an image of the waveguide facet. The relation of the beam waist is given in Equation 2-10 as a function of the focal length of the overall lens system and the input parameters. Again, the focal length of the lens system is the image distance for an infinite object distance.

$$w_1^2 = \frac{f^2}{z_{R0}^2 + (d_0 - f)^2} w_0^2$$

**Equation 2-10: Relation of the output beam waist with the input parameters and the focal length of the lens system.**

#### 2.1.2.5 Depth of Focus

In the previous section, the depth of field was noted as twice the Rayleigh range, $z_R$. The depth of focus is a parameter that has various definitions depending on the requirements of the imaging system. Typically it is the distance over which the rays from a single point on the object will be within a defined area from one another in the image space. Since rays won’t converge at an infinitesimally small point for imaging systems, this area is defined by a single pixel size or detector area. $z_R$ is commonly quoted as the deptho of field because of the useful information that the beam area doubles over this distance. As this work will not be as concerned with image quality, but instead forming a uniform region of intensity, the depth of focus will be defined as the length along the beam axis where the beam intensity is within 5% of the maximum beam intensity. This forms a useful parameter as the only concern is forming a region where the intensity is uniform.

### 2.1.3 Diffractive Optics

Up until now, the optical theory presented has assumed that the distances the rays travel are much larger than the wavelength of the light. This is a fair assumption as the lens system's dimensions are large. Real EM waves have a wavelength and therefore are prone to interference effects. This typically happens when the Airy disks from two adjacent points are too close to differentiate. This is displayed in Figure 2-13 where the minimum allowable distance between two points is defined by the separation of the Airy discs. This minimum distance can be calculated by the Rayleigh resolution criteria given by Equation 2-11. This typically happens when the diameter of the aperture is comparable to the size of the wavelength.

$$x_{\min} = f\theta_{\min} = f(\frac{1.22\lambda}{D})$$

**Equation 2-11: Rayleigh resolution criteria.**

This equation uses the focal length of the image system, *f*, the divergence of the minimum resolvable points, $\theta_{min}$, the wavelength of the focused light, $\lambda$, and the diameter of the lens system, *D*.

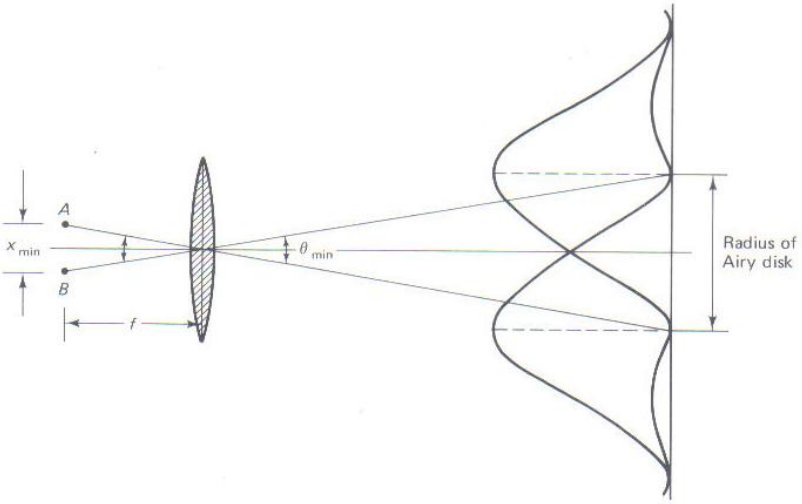

**Figure 2-13: The resolution of a lens system showing the resolution criteria based on the separation of the Airy disk. *Source*: Reprinted from reference 112.**

### 2.1.4 Particle dynamics

The interaction of light and matter is of paramount importance when considering optical interrogation in a flow cytometric application. Each different specimen's characteristics will interact with the light differently. Being able to detect this certain specific interaction will allow unique conclusions about specimens to be made; ie. the specific optical signature is unique to the specific specimen.

### 2.1.4.1 Scattering

Scattering is the process where light is reflected off of a specimen's features due to the index differences. As the surface of such a small particle is not a plane surface, but instead a fractured, granular texture, there are many different points of reflection. The resulting scattered light field appears random. Scattering is a complex process that needs to account for all the different index contrasts in a specimen, and the different surface directions. There are a couple of theories that use approximations to accurately describe the scattering of light.

Scattering is divided into two main categories based on the direction of the scattered light: forward and side scatter as depicted in Figure 1-11 and Figure 1-12. Two theories exist to describe scattering: Rayleigh and Mie. As Rayleigh scattering is only applicable when particles are very small, it is not applicable for flow cytometric functions. Mie scattering is simplified in this work as the only consideration was the bead size, thus the scattering is approximately propotional to the size. The geometry of the beam, the direction of the rays, and the size of the specimen will have an effect on the amount and angle of scattered light.

### 2.1.4.2 Fluorescence

Fluorescence was briefly discussed earlier in section 1.1.2.1. It is the fluorescence from a molecule with a specific absorption band that is attached to a specimen via a selective binding process. Fluorescence light is generated via the electron relaxation through emission of a specific band of light. As the fluorescence is only dependent on the intensity of the light that the particle is in, any slight deviations in the intensity of the emitted light will be directly proportional to the variation of intensity in the excitation field. This leads to two main issues with fluorescence: saturation and bleaching. Photon saturation occurs when the intensity of the beam is so high that every molecule of the fluorochrome is currently excited due to the finite lifetime the fluorochrome spends in the excited state. Saturation is dependent on the relaxation time constant, $\tau$. An increase in the fluoresced intensity is only possible through the use of more fluorescent molecules or molecules with a shorter lifetime. Thus, the maximum useful intensity of the excitation beam is found by:

the number of fluorochromes/area * $\tau$ / $\eta$ = # of photons/area/s

Where $\eta$ is the quantum efficiency ie. the probability of a photon being absorbed and resulting in a fluorescent emission. Note: the photons must be of sufficient energy to promote the electron of the fluorochrome to an excited state. Thus, saturation sets an upper limit on the fluorescence intensity and thus, the useful excitation intensity; any increase in excitation intensity will not result in a further increase to fluorescence intensity. This can be thought of as a maximum intensity to use and will allow for efficient operation as no wasted energy is placed into the excitation beam.

Photobleaching is when the fluorochome undergoes a destructive relaxation process whereby the chemical bonding of the fluorochome is changed and therefore, the molecule is no longer able to experience any excitation/relaxation cycles. This is a statistical process where the more cycles the molecules experience, the more likely a photobleaching event is to occur. Control of photobleaching is done through the length of exposure. In a flow cytometric application a specimen typically spends too short of a time in the beam to undergo enough cycles to photobleach and thus, is typically not a concern in flow cytometry.

In contrast to scattering, when detecting fluorescence, it is not necessary to take the collection angle into consideration. This is due to the direction of the light emitted being isotropic in nature and thus any collection angle on the chip should receive the same amount of light. This is akin to setting a point source's solid angle to $4\pi$.

## *2.2 Device Design and Simulation*

To create a portable microchip-based flow cytometer the components for optical excitation and collection must be integrated onto the chip along with the microfluidics. This included a waveguide to guide the light to the channel and a lens system to tune the beam shape in the channel. For efficient and functional device operation careful consideration must be taken into the design and architecture of the device to ensure proper device function.

### 2.2.1 Microchannels

Devices incorporate a standard 3-branched structure for the microfluidic channel incorporating a sample inlet flanked by two sheath inputs to allow for 2D hydrodynamic focusing. All fluids are removed from the chip via a single waste port. Figure 2-14 shows a cartoon of the simple planar design. This replaces the conventional flow cell and allows fluid handling for a free-space optical detection scheme.

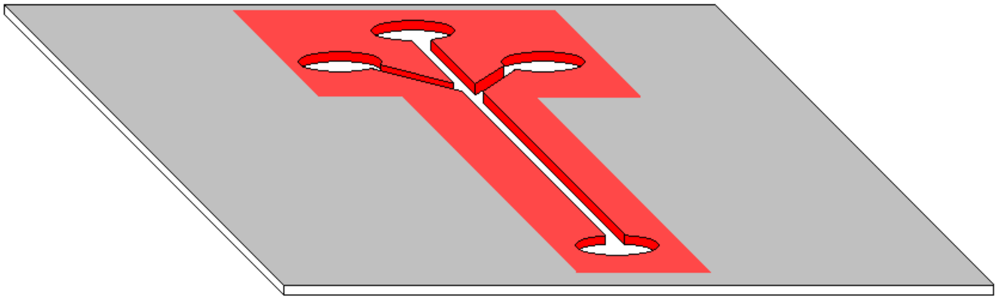

**Figure 2-14: Cartoon of a planar microfluidic channel network for hydrodynamic focusing of a sample fluid for flow cytometric analysis.**

### 2.2.2 Waveguide Introducing Excitation Light

It is a necessity to deliver the light from an external source to the exact point of interrogation in the microchannel. Typically, free-space optics are used to focus the light to the microchannel (see 1.2.1.2). Integrating a waveguide on-chip with the channel, as shown by the red shaded area in Figure 2-15, allows a guided optical beam to be coupled onto the chip to ensure exact and precise optical alignment with the channel that is permanent, portable, and sealed from external interference.

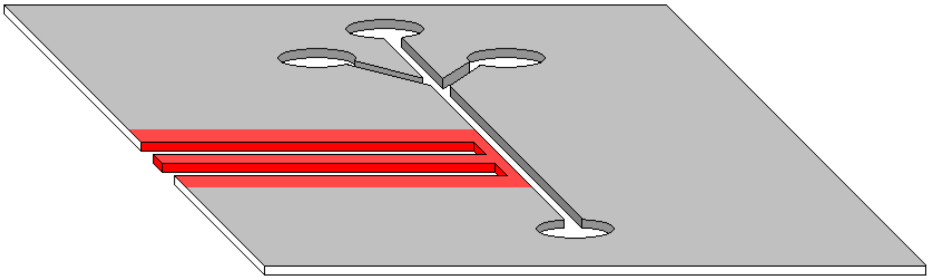

**Figure 2-15: Cartoon depicting a waveguide integrated next to the planar microfluidic channel for on-chip light delivery to the samples.**

### 2.2.2.1 Waveguide

When designing a waveguide it is important to take into consideration the multimodes and the NA situation described in sections 2.1.1.1 and 2.1.1.2. In order for device in this work to remain simple and practical, devices are designed to use the same material to fabricate both channel wall and waveguide cores while using air as a side cladding for the waveguide. A large index contrast between the SU-8 and air will ensure a large degree of optical confinement. This will also create a large NA and very multimodal propagation. For design purposes, an optical adhesive is considered as a cladding material. This will improve structural stability and will help with sealing devices. The adhesive is assumed to have an index of 1.52. Assuming a second material for the cladding will also prove the flexibility and usefulness of the design process used herein. Any combination of materials can be used for device structure given that the simulations and calculations presented from here on out have the indices of refraction updated and other design rules taken into account.

Coupling between the input source and waveguide must be efficient and simple to allow easy integration with a separate source. A better overlap integral is possible between a fibre and waveguide if the intensity profiles of both sources are heavily multimodal. The heavily multimodal profiles in both structures will ensure a large coupling efficiency due to a much larger overlap of allowed intensity profiles, as discussed in section 2.1.1.1. The large multimodal signal will also ensure a large input power.

To explore the coupling efficiency between the fibre and the waveguide, simulations were performed using beam propagation software. This software is designed to propagate an input beam down a structure whose index profile can be set depending on the designed parameters. By dividing the structure of the waveguide and surrounding up to a small grid, the software solves the wave equation at each point and uses solutions to solve for the next set of points step-by-step. This software keeps track of the phenomena generated by wavelength and polarization effects as the light propagates down the waveguide; specifically logging the interference effects of the many waves of light that are propagating in the waveguide simultaneously.

Figure 2-16 shows the simulation results using BeamPROP software from Rsoft. This simulation explored the efficiency of the coupling between a fibre and a waveguide. The program propagated light from a cylindrical waveguide and measured the amount of light that is coupled to a rectangular waveguide 50 μm tall by 50 μm wide. The results plot the coupling efficiency from the first mode of the fibre to the first mode of the waveguide, n. The simulation also tracked the coupling efficiency from the $n^{th}$ mode of the fibre to the previous, n-1, and next, n+1, modes in the waveguide. The results shows that the coupling from the $n^{th}$ mode in the fibre to the $n^{th}$ mode of the waveguide drops as the mode number increases - due to the increasing mismatch of the geometry of the mode profiles between the fibre and waveguide. The overall coupling efficiency, however, is maintained near perfect due to the neighbouring modes coupling the parts of the mode that do not overlap. This simulation did not account for reflection losses at the facet interface, but they can be minimized via an index matching fluid.

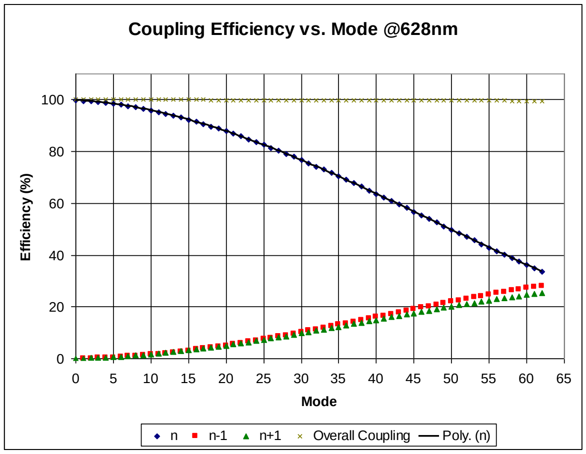

**Figure 2-16: Simulation results of the coupling efficiency from a circular fibre profile to a rectangular waveguide profile. The diameter of the fibre matches the dimension of the waveguide. Coupling is lost from one mode, n, into the neighbouring modes n-1 and n+1.**

As seen from the simulation results, this is a very relaxed coupling condition as the flexibility of the intensity profiles allows lots of options for the light to couple into. This will relax the coupling condition from a testing stand point to allow practical coupling and thus reduce the need for a high quality light source.

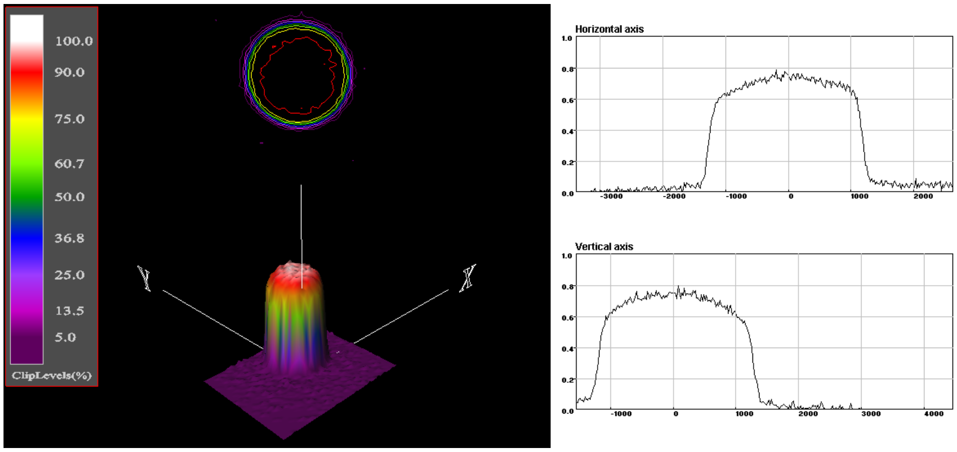

**Figure 2-17: Beam profile from the output of the pigtailed laser diode. Cross-section plots show the super Gaussian nature of the beam; a shape that is preserved within the channel.**

All these conditions on the waveguide are necessary as they will allow simple function with a low quality source. However, a low-quality source – such as an input from a multimodal source – can have an uneven intensity distribution. The cross-section measurement of the intensity profile from the multimodal laser source used in this work is shown in Figure 2-17. The beam shape is approximately the shape of a super Gaussian beam, however, it has a much more uneven intensity profile. This is a problem that some previous groups have encountered, the solution to which will be discussed in detail later in section 2.2.3.

#### 2.2.2.2 Waveguide Integration with Microchannel

Due to the multimodal nature and large NA of the waveguide, the beam will spread as it hits the channel wall due to the loss of the lateral confinement from the lack of the cladding layer, and again as it enters the channel. The width of the wall and channel will allow the divergent beam to spread even further depending on the overall length. The calculated NA of the SU-8/air core/cladding waveguide is 1.24 and means the waveguide will eject a beam with maximum divergence half angle of 51.2° and 68.8° in the SU-8 and then in water, respectively. This also means that the waveguide should confine any light incident on it in an ambient of air - even glancing angles. This means that as the light exits the waveguide and propagates to the excitation point, it will be very large.

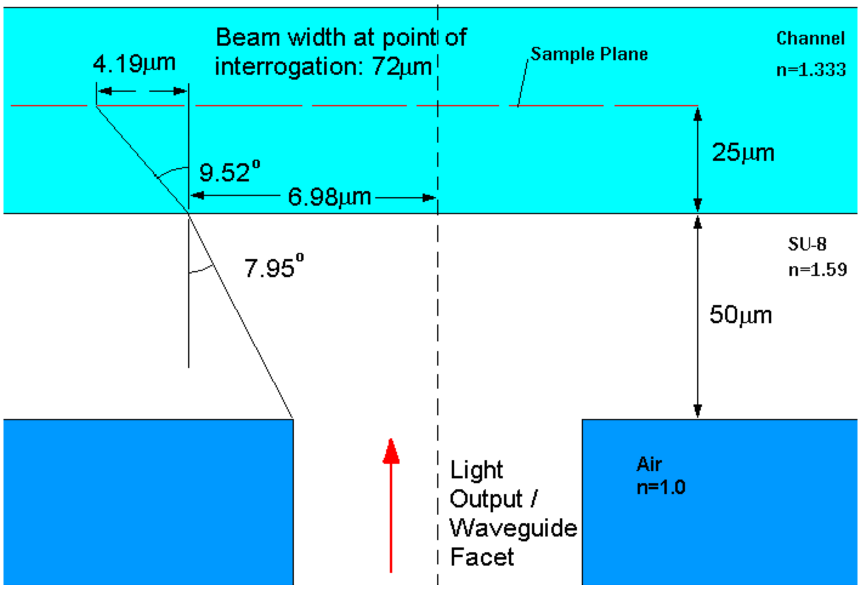

**Figure 2-18: Beam spreading from the waveguide. The beam diverges significantly as it propagates to the channel.**

This situation is shown in Figure 2-18 as a schematic depicts a beam exiting a high NA waveguide. For this work, a beam with an NA of 0.22 is injected to the waveguide as that is the NA of the waveguide that is coupled from the source used in this work. The beam spreads according to the angle specified by the NA of the beam. Figure 2-18 only depicts the very extreme rays that would be ejected from such a waveguide; all other rays will propagate in a similar fashion, but this work is only interested in the space in which the beam can be confined, thus only the extreme rays should be considered. The beam diverges with a half angle of 7.95° in the SU-8 using Equation 2-4, and then it refracts to 9.52° in water – according Snell's law in Equation 2-1. At these angles, the beam will spread approximately 11 μm in each direction; 7 μm in the SU-8 and 4 μm in the water. Once the 50 μm wide waveguide facet is included, the beam will span 72 μm at the point where the beam crosses the sample stream (the sample plane in Figure 2-18).

This can be problematic for detection due to an uneven beam profile that occurs as the intensity spreads. A wide intensity profile also drastically increases the rate of double detections due to the larger area covered by the beam. The intensity of such an injection scheme will be poor for performance as such a small portion of the beam is used for excitation at any given moment leading to much smaller detection intensity. One could limit the divergence or beam width by employing a single-mode beam for excitation. A single-mode beam will still diverge but allows a smaller core waveguide. Use of the single-mode beam for exication is desireable to avoid for reasons stated in section 1.3. Essentially, devices for LOC and POC application need to use a lower quality source.

Using a device that employs a narrow wall and channel width can limit the amount of beam divergence, however these widths are constrained. The minimum requirement for a channel wall width exists in order to allow for sufficient material to form a channel wall to allow for fluid confinement and sealing. The mimimum requirement for a channel width is needed to allow for a sufficient channel cross-section to prevent clogging due to particles being jammed in the sample flow.

### 2.2.3 Lens Systems

Conventional cytometry uses a single mode beam and narrow hydrodynamic focusing to ensure that optical excitation of particles is uniform. As explained in 2.2.2.2, the input from a waveguide allows almost no control over the geometry of the beam. Therefore, design of the microfluidic chips must have an integrated method that will increase the uniformity of optical geometry for excitation. Furthermore, the goal of these devices is to ensure functional device operation with a simple and inexpensive low quality source. A complex lens system of 2D lenses can be integrated with the waveguide at the channel wall to ensure optimal delivery and beam control in the channel, as shown via the substituted red shaded region in Figure 2-19.

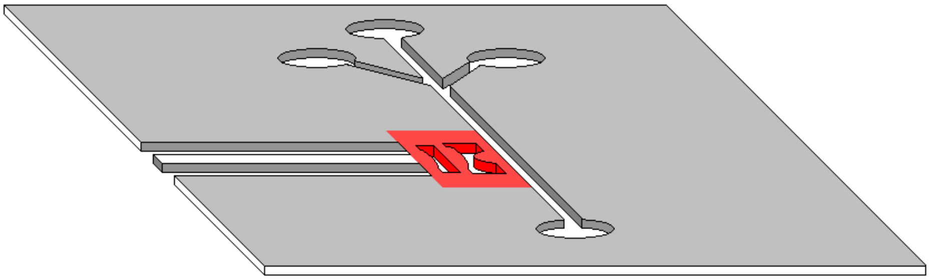

**Figure 2-19: Cartoon showing the intergration of a lens system with the waveguide to control the beam in the channel.**

These designs were accomplished using ZEMAX - software that is used to simulate and design complex lens systems that can use many different materials and structures. The simulation of rays through the lens design relies on geometric optics but does not make the paraxial approximations discussed in section 2.1.2.1 that are used to form lens equations in Equation 2-6. This means that the aberrations discussed in section 2.1.2.3 appear and ZEMAX allows the user to alter the lens designs to correct or control these aberrations. The ZEMAX simulations can deviate slightly from actual results due to diffraction, and, at the length scales typical in microfluidics, the diffraction limit can become an issue that ZEMAX will have to account for.

#### 2.2.3.1 Particle-Beam Interaction

The importance of beam shaping has been stated many times so far in this work. While a waveguide can precisely deliver the light to the channel, a lens system can shape it to a geometry within the channel that can improve the detection reliability.

When shaping the beam it is necessary to form a region of intensity that will provide uniform excitation to particles regardless of position in the channel. Furthermore, the goal of beam shaping is to form a region of uniform width to ensure that the detected pulses from the particles have a uniform width. With a reliable pulse duration, a second parameter is available to be measured; the area under the pulse. Pulse area is a more reliable parameter to measure than the intensity, though it requires much more computation capability to perform analysis.

Lens designs should strive to form an area of illumination that has equal intensity and width spanning the entire channel width – ideally forming a table top profile. Of course, this is not possible with a Super Gaussian input and refractive optics, as discussed in section 2.1.2.4 and described by Equation 2-10. As divergence is a necessary outcome from focusing the beam it is pertinent to control the depth of focus to stretch the uniform region across the channel.

Uniform intensity across the sample stream will ensure that any variation in fluorescent intensity is from the specimen and not from the device. Scatter detection will also become a more reliable parameter as it will homogenize the interaction of the light and the specimen.

#### 2.2.3.2 Beam Geometry

A range of beam geometries will be designed to be deployed via the integrated on-chip lens systems. This is done to test several things. The first is to see if there is a dependence on beam geometry and specimen size. The second is to determine how the formed region of intensity is affected by the different magnifications of the lens systems. Third, how much flexibility is there in the depth of focus and beam waist for a given lens system magnification. The last feature to explore is how small of an image can the lens systems produce before they are impeded by diffraction effects and fabrication limitations.

Figure 2-20 shows two simulations from two designs to fabricate 3.6 μm and 10 μm beam waists. As seen from the ray trace and lens detail on the left of the figure, the 3.6 μm has a much smaller input NA than the 10 μm lens system. This means less light is collected overall and results in less light to use for excitation. However, as the lens system focuses the light to a smaller point, so there is also a greater power density. Furthermore, the depth of focus appears smaller for the smaller beam waist. Careful control to the depth of focus was possible by tuning the non-paraxial beam redirection through warping the lens at its extreme edges via the conic constant presented in Equation 2-8.

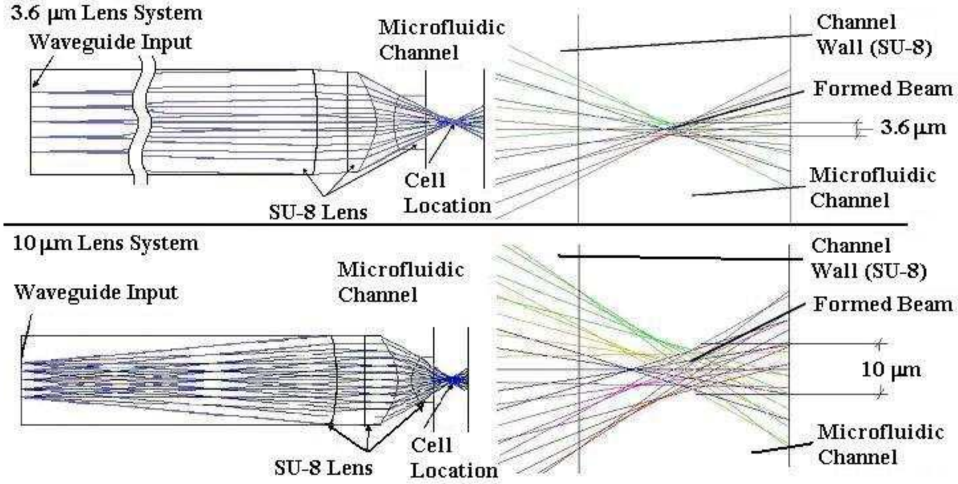

**Figure 2-20: Simulations for 3.6 μm lens system (top) and 10 μm lens system (bottom) with details of the formed spot (right). *Source*: Reprinted from reference 121.**[*]

There are a couple constraints in the design of the lens system that will limit performance. First, there is a minimum distance which must separate the lenses

---

[*] This figure is from the author's published work in reference 121.

in order to remove all the material from between the lenses. This means that normal conventional designs where lenses of different materials touch are no longer feasible. A second constraint is that there is a minimum thickness of lenses that can be made. This is to ensure that there is enough lens material present to allow the structures to adhere to the substrate. These minimum parameters are 15 μm and 10 μm for the clearance and thickness, respectively. These parameters were determined from experience working with various preliminary designs done in conjunction with work published by Thomas Kowpak.[116]

#### 2.2.3.3 Simulated Beams

By changing the lens parameters slightly, it was possible to change the beam waist. The most significant change between each lens design was the collection ability of the lens system via the input NA. As smaller beam waists have a smaller magnification, this would demand a lower divergent input beam. As Equation 2-9c) predicts, the divergence of the image is inversely proportional to the input. With a small magnification, the divergence in the image will be much larger and this means that the image of the beam will be formed very close to the injection surface side of the channel. To form the beam image at a larger distance from the channel wall, the divergence of the image formed must be kept small – meaning that the divergence of the input beam must be kept small if the magnification stays constant. To do this, the distance between the lens system and the wavguide facet is increased to allow the more divergent light to miss the lens system. As discussed earlier, this means that smaller lens designs will miss more input light from the waveguide and result in larger inefficiency.

Figure 2-21 shows the simulation results for designs that form five different beam waists. It is easy to see that as the designs progress from the smallest beam width to large widths, the object NA of the lens system is increased. Input of the 1.5 μm lens system in Figure 2-21a) is nearly collimated, while the largest beam width, 12 μm in Figure 2-21e) has the ability to collect nearly all of the full cone of rays ejected from the waveguide (with a half angle of ~8º). The last two designs have a large enough magnification of the image that the lens systems retain the ability to collect enough light that they are placed in relatively close enough proximity to the lenses that they can be seen in the simulations from Figure 2-21 d) and e). The collection efficiency of the waveguide light is above 80% for each lens system.

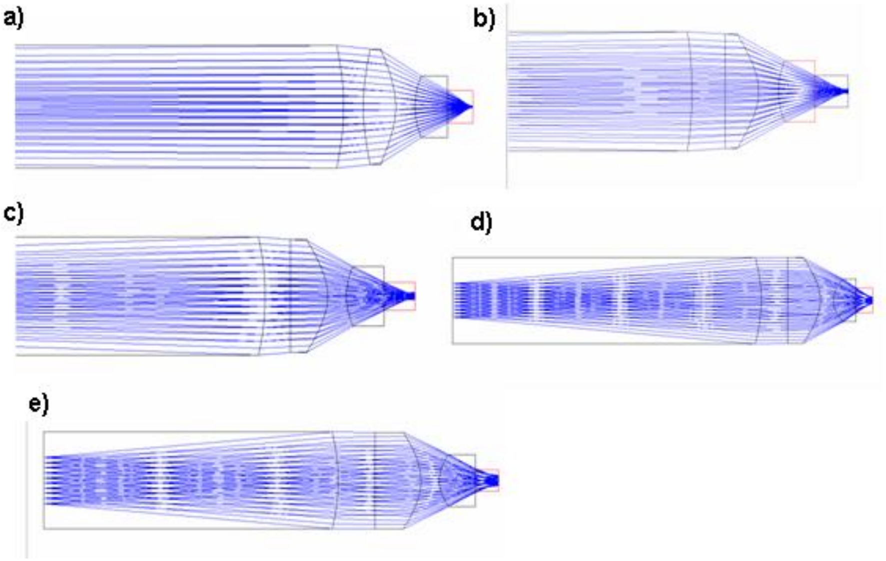

**Figure 2-21: ZEMAX simulation results for lens systems producing a) 1.5-, b) 3.6- c) 6.0- d) 10.0- and e) 12 µm spot sizes. The object NA of the systems decreases with the designed spot size.**

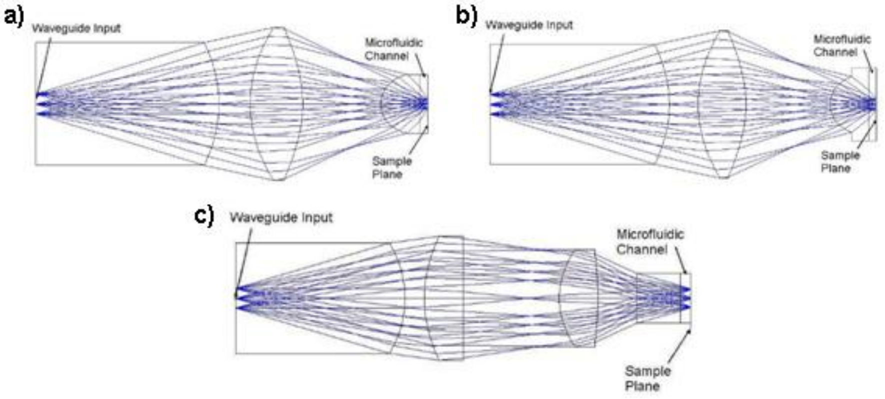

**Figure 2-22: ZEMAX simulation results for lens systems producing a) 25-, b) 30-, and c) 50 µm spot sizes.**

Larger spot sizes were created, as shown in Figure 2-22, and the lens systems were designed to form 25-, 30- and 50 µm beam waists. The designs were able to collect all of the light from the waveguide facet. As will be dicussed in detail later in section 4.2.1, for smaller small particles, the interaction with these larger beam geometries will be quite poor as the regions of intensity are too big. The large width will cause double detection of the small particles that are typical in flow cytometric functions and the formed intensity region will subject the paricles to varying levels of excitation intensity.

### 2.2.3.4 Lens Parameters

Parameters to create the lens systems from the simulation results shown in Figure 2-22 are listed in table, Table 2-2. Each parameter controls a specific feature from the input requirements in the ZEMAX simulation software. The parameters listed are broken up by each surface that they form. The radius is the underlaying basic spherical radius of the surface, the thickness is the distance between surfaces from the points on the optical axis, the semi-diameter is the radius of the lens or the clear aperture of the lens (in this work it can be interpreted as the radius of the beam), and the conic constant is the warping factor of the lens radius of curvature given by Equation 2-8.

**Table 2-2: Parameters from ZEMAX simulations used to create lens systems to form 25-, 30-, and 50 um beam widths.**

| Lens | Surface | Radius | Thickness | Semi-Diameter | Conic Const. |
|---|---|---|---|---|---|
| | Object | Infinity | 440 | 25 | 0 |
| 50 µm | 1 | -275 | 50 | 144.0 | 0 |
| | 2 | 325 | 100 | 160.5 | -1.5 |
| | 3 | Infinity | 250 | 154.8 | 0 |
| | 4 | 200 | 100 | 126.7 | -0.75 |
| | 5 | -750 | 100 | 114.9 | -50 |
| | 6 | Infinity | 115 | 64.8 | 0 |
| | Channel | Infinity | 25.3 | 33.0 | 0 |
| | Sample | | | 24.6 | |
| | Object | Infinity | 470 | 25 | 0 |
| 30 µm | 1 | -310 | 75 | 156.5 | -1.50 |
| | 2 | 320 | 125 | 192.2 | -1.2 |
| | 3 | -325 | 220 | 190.1 | -4 |
| | 4 | 70 | 100 | 73.1 | -0.2 |
| | Channel | Infinity | 20 | 96.0 | 0 |
| | Sample | | | 14.0 | |
| | Object | Infinity | 470 | 25 | 0 |
| 25 µm | 1 | -320 | 80 | 156.8 | -1.5 |
| | 2 | 315 | 135 | 195.0 | -1.2 |
| | 3 | -325 | 200 | 192.3 | -4 |
| | 4 | 68 | 100 | 74.6 | -0.2 |
| | Channel | Infinity | 20 | 43.2 | 0 |
| | Sample | | | 12.0 | |

The designs used to form the smaller beam waists designed in Figure 2-21 from the ZEMAX simulation software have the surface parameters listed in Table 2-3. These parameters are for the same features described in table Table 2-2.

**Table 2-3: Parameters from ZEMAX simulations used to create lens systems to form 1.5-, 3.6-, 6.0-, 10-, and 12 µm beam waists.**

| Lens | Surface | Radius | Thickness | Semi-Diameter | Conic Const. |
|---|---|---|---|---|---|
| | Object | Infinity | 2500 | 25 | 0 |
| 1.5 µm | 1 | -160 | 15 | 46.8 | -16 |
| | 2 | 150 | 25 | 44.1 | -13 |
| | 3 | -68 | 15 | 42.9 | -4.1 |
| | 4 | 120 | 25 | 25.2 | -0.8 |
| | Channel | Infinity | 27 | 15.2 | 0 |
| | Sample | | | 0.8 | |
| | Object | Infinity | 1100 | 25 | 0 |
| 3.6 µm | 1 | -290 | 25 | 44.1 | 0 |
| | 2 | Infinity | 25 | 42.3 | 0 |
| | 3 | -40 | 15 | 42.0 | -3 |
| | 4 | 60 | 27 | 22.7 | -0.6 |
| | Channel | Infinity | 25.2 | 11.7 | 0 |
| | Sample | | | 1.8 | |
| | Object | Infinity | 600 | 25 | 0 |
| 6um | 1 | -210 | 20 | 56.0 | 0 |
| | 2 | Infinity | 30 | 53.8 | 0 |
| | 3 | -43 | 15 | 53.4 | -3.11 |
| | 4 | 70 | 32 | 27.5 | -1.5 |
| | Channel | Infinity | 25 | 13.6 | 0 |
| | Sample | | | 3.1 | |
| | Object | Infinity | 470 | 25 | |
| 10um | 1 | -210 | 40 | 65.3 | -6 |
| | 2 | Infinity | 50 | 64.8 | 0 |
| | 3 | -60 | 20 | 64.6 | -2.5 |
| | 4 | 40 | 34 | 32.2 | -0.4 |
| | Channel | Infinity | 25.6 | 18.7 | 0 |
| | Sample | | | 5.1 | |
| | Object | Infinity | 400 | 25 | 0 |
| 12um | 1 | -150 | 50 | 59.1 | -5 |
| | 2 | 2200 | 60 | 56.5 | 0 |
| | 3 | -65 | 22 | 55.0 | -4 |
| | 4 | 60 | 42 | 34.7 | -0.8 |
| | Channel | Infinity | 25 | 18.3 | 0 |
| | Sample | | | 6.5 | |

In the two tables of parameters, the input beam is from the surface labeled ‘Object’ while the beam images is formed on the surface labeled ‘Sample’. Values in the ‘Semi-Diameter’ column are interpreted as the beam waist and show how the beam is altered through each surface.

### 2.2.4 Waveguides for Signal Collection

To fully alleviate the dependence on free-space optics, the collection should be integrated onto the chip as well. Figure 2-23 shows the addition of a waveguide –

shaded in red - that has been integrated with the previous optical features and will allow efficient collection due to close proximity to the sample.

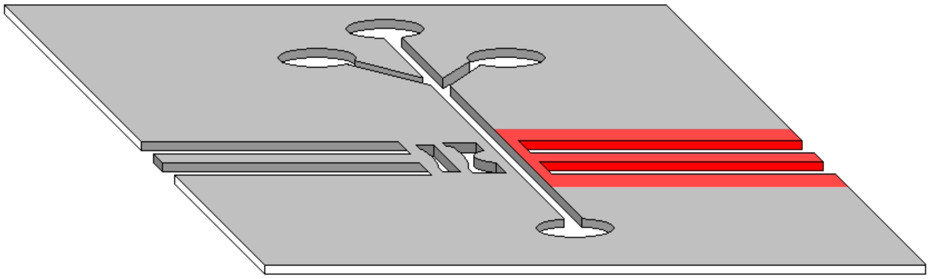

**Figure 2-23: Cartoon depicting the addition of a waveguide to collect light from the channel after on-chip optical interrogation.**

As explained earlier, placing a waveguide next to the channel can increase the collection sensitivity due to the close proximity of the collection facet to the interrogation region. However, care must be taken to consider the solid angle of collection and the NA of the waveguide as outlined in section 2.1.1.2. If the waveguide is placed too far away, it will collect less light due to a decreasing solid angle – as long as the facet remains the same size. Often the facet is recessed from the particle by just the distance of the channel and channel wall. Simulations were undertaken to determine the effect of the channel wall thickness and channel thickness on collection efficiency. Simulations were specifically constructed to determine the effect of the solid angle of collection of a waveguide through various channel and wall widths.

### 2.2.4.1 Wall width

Using wave propagation software, BeamPROP by RSoft, the wall width was varied with a channel half-width of 20 μm. A varied wall width effectively moves the waveguide further away from the source point. By varying the divergence of a source point located in the middle of the channel, the waveguide's collection efficiency was measured based on the amount of beam diverged as it propagated through the channel and wall width. A combination of the channel and wall width will eventually be reached where the maximum distance is surpassed for full collection – as demonstrated by point A in figure Figure 2-5 - and enter the regime described by point B in Figure 2-5. Results from the simulation are shown in Figure 2-24. The collecton efficiency refers to the amount of light emitted from the point source that is collected by the waveguide.

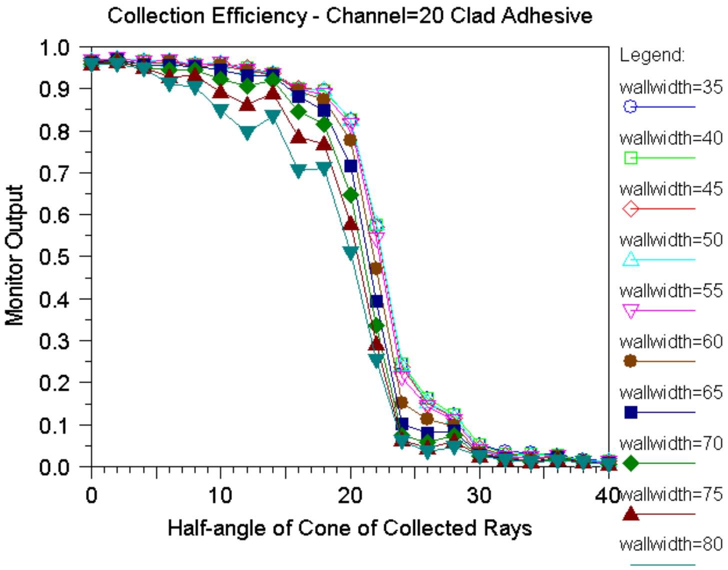

**Figure 2-24: Plot from simulation of the collection efficiency of a waveguide vs. varying wall widths. These results plot the efficiency of the waveguide collection (Monitor Output) from a cone of rays. An adhesive material is used as cladding.**

During this simulation, a cladding material of adhesive is assumed. The simulation propagates a 1 μm wide source to approximate the point source. By varying the divergence of the source the simulations can record how well each device's architecture collects the light. The simulation is run repeatedly to scan a range of the two parameters: first it is run multiple times to scan the complete range of divergence angle in the cone of rays, then the wall width is changed and the divergence is scanned again.

As seen from the results, several wall widths have the same collection efficiencies. A channel width of 20 μm in combination with wall widths from 35- to 55 μm has the same performance recorded. These architectures efficiently collect a cone of rays with up to approximately a 20° half angle. This is as predicted as the maximum cone of rays collectable from a waveguide with a cladding layer – as given by calculating the NA using Equation 2-4 with a cladding index of 1.52 – yields an NA with an angle of 20.53°. Increasing the wall width further puts the source further away and decreases collection efficiency as evident by the maximum cone of collectable rays from the different device architectures shifting to smaller angles.

The simulation was repeated for a waveguide with an air cladding material. A similar plot of the results was generated and is shown in Figure 2-25.

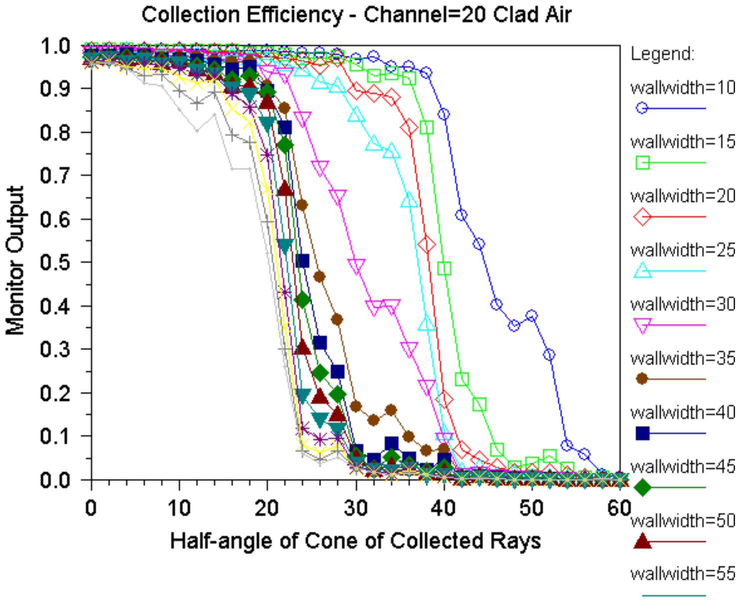

**Figure 2-25: Plot from simulation of the collection efficiency of a waveguide vs. varying wall widths. These results plot the efficiency of the collection (Monitor Output) from a cone of rays. Air is used as the cladding material.**

The NA for an SU-8 waveguide with air cladding is 1.24 and thus the angle of collection in water is approximately 68°. The smallest combination of channel and wall width used in the simulation could not even simulate this maximum as a wall width smaller than 10 μm is not feasible for fabrication. There is an obvious advantage to an air cladding due to the collection ability.

### 2.2.4.2 Channel width

Simulation from the previous section were repeated but instead varied the channel half-width to determine its effect on collection. The simulations assumed a wall width of 25 μm as it is a value that will provide enough surface area to facilitate strong bonding to hold fluid pressures and provide effective sealing. Figure 2-26 shows the simulation results from a configuration where the channel half-width (labelled channelwidth in the simulation) was varied. The collection waveguide employed an adhesive for cladding, and again, the obvious maximum collection collection efficiency at a divergence half angle of 20° was observed. Several channel half-widths from 25- to 50 μm put the waveguide facet within the maximal distance for efficient collection defined in Figure 2-5.

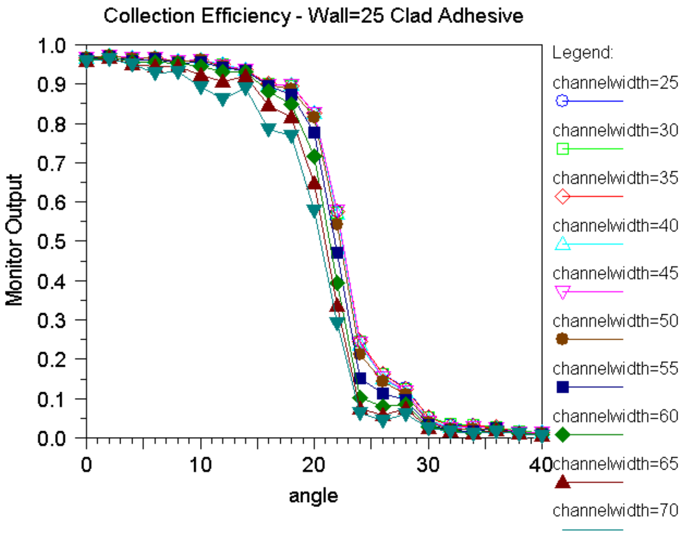

**Figure 2-26: Plot from simulation of the collection efficiency of a waveguide vs. varying channel half-widths. These results plot the efficiency of the collection (Monitor Output) from a cone of rays. An adhesive material is used as cladding.**

Figure 2-27 shows results from the same simulation except where air was used as the cladding material. A much smaller channel half-width was explored as the waveguide has a much larger NA. Still, the theoretical maximum collection angle of 68º was not observed as the wall width was too thick to facilitate this.

It should be immediately obvious from the previous four simulations that an air cladding waveguide has a better confinement and larger collection abilities. For this reason the adhesive idea was dropped from further consideration. Furthermore, it was observed that it would complicate device fabrication and was not necessary to enhance device sealing. The inclusion of the adhesive material was done to prove the usefulness of the design method with any combination of materials, as mentioned earlier.

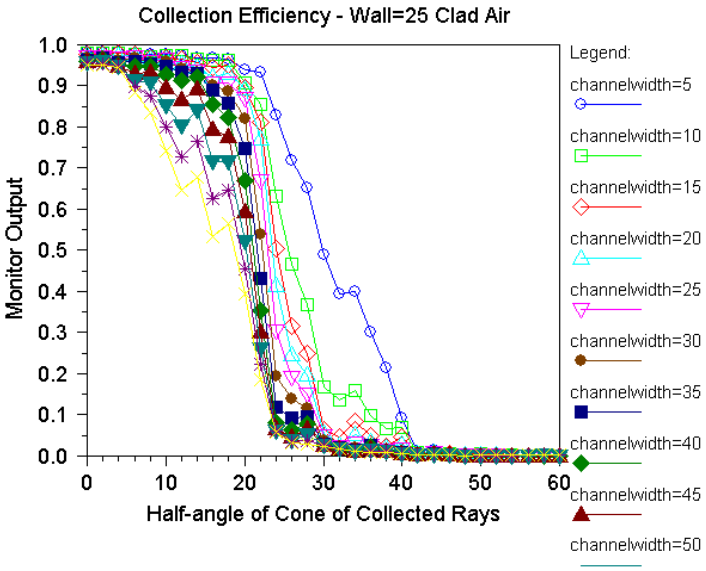

**Figure 2-27: Plot from simulation of the collection efficiency of a waveguide vs. varying channel half-widths. These results plot the efficiency of the collection (Monitor Output) from a cone of rays. Air is used as the cladding material.**

### 2.2.4.3 Optimal Wall and Channel Combinations

To fully understand the collection ability of the waveguides, calculations were performed to determine the collection efficiency using solid angle considerations. The collection ability of the waveguide was divided into its two components: lateral collection in plane of the chip, and transverse collection in the plane perpendicular to the chip. The simulations performed in the previous section only considered the lateral collection ability as the devices were assumed to have equal dimension and architecture in each direction. However, in practical devices, the transverse collection will have less confinement due to the substrate and sealing layers having a lower index.

The first step in the calculations was to project the facet of the waveguide onto the channel wall. This is shown in Figure 2-28 by assuming a point source in the middle of the channel. The extreme rays that refract to through the channel wall and are incident at the extreme edges of the waveguide are the only rays considered – again, as this work is only concerned with the confinement of the beam. These rays are depicted by the red rays in Figure 2-28. To calculate where these rays intersect the channel wall is not a straight forward calculation – an iterative solver must be run to simulataneously find the cone of rays that will connect the source with the facet corners while intersecting the channel wall at an angle so that Snell's law in Equation 2-1 holds. With this projected geometry one can then calculate the solid angle of collection of the waveguide by interpreting this cone of rays and comparing the solid angle of the cone to that of the waveguide given by the NA. Ideally, the designs should be selected that will have the calculated solid angle from the projected geometry greater than the solid angle dictated by the waveguide NA. This will ensure maximal collection efficiency as explained in the situation depicted in Figure 2-5.

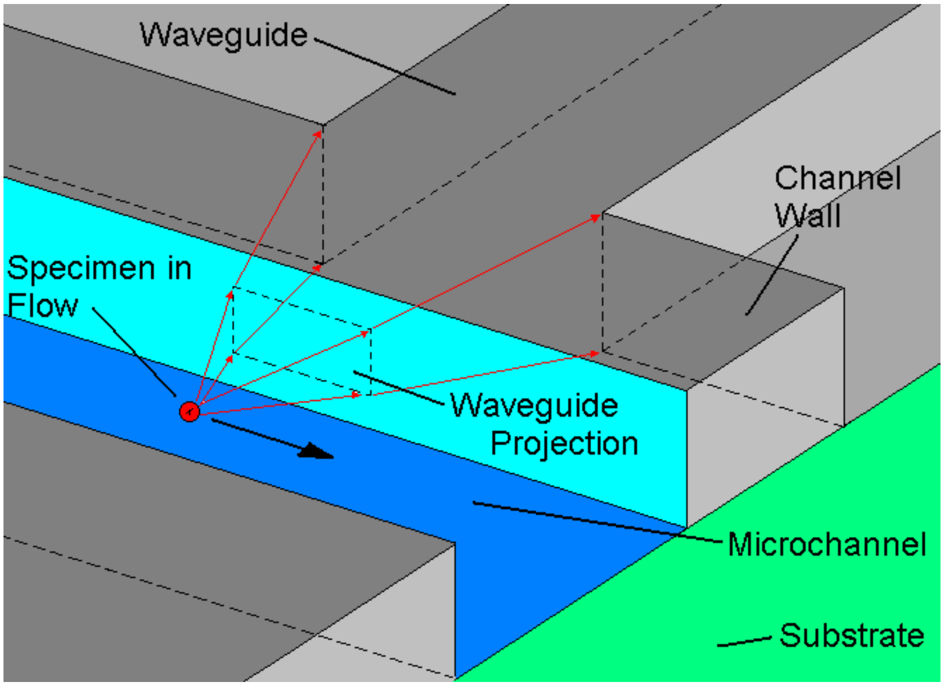

**Figure 2-28: Picture showing the collection of light by a waveguide. The collected light can be determined by the projection of the waveguide facet on the channel wall.**

These calculations simulated waveguides 25 μm thick with air and adhesive claddings. The results of all these calculations can be found in Appendix A and

Appendix B for both the air and adhesive cladding cases, resectively. A summation of the results is shown in Figure 2-29. This plot shows the percentage of light collected from a point source that emits light in a perfect sphere; ie. it is the percentage of the sphere that is collected. Each line represents a different wall width and cladding material plotted vs. the channel width. It is easy to see the maximum collection available from the two cladding materials: air cladding has much better collection for many different configurations.

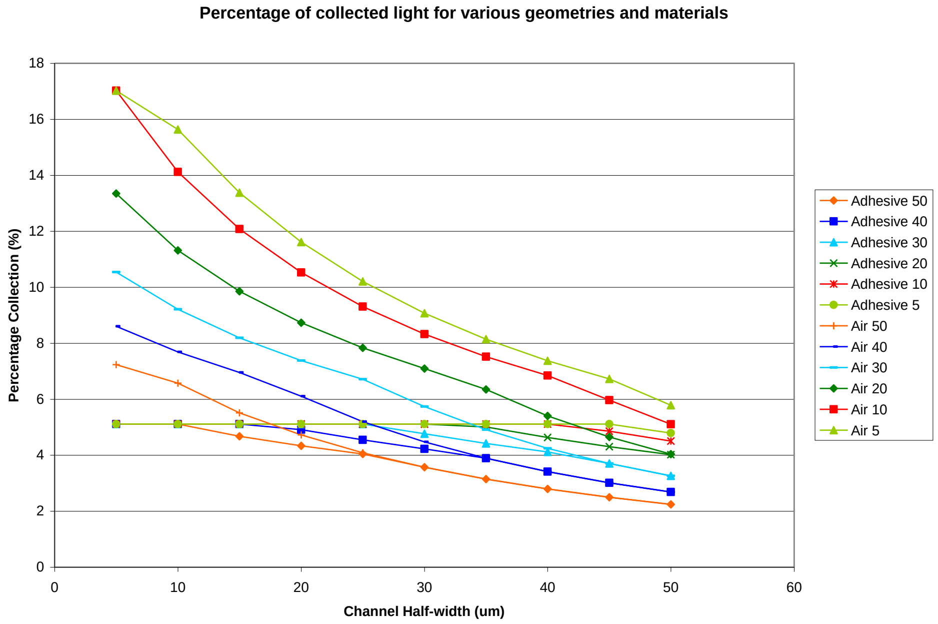

**Figure 2-29: Plot showing the percent collection capability from a solid sphere of excitation for different device channel half-width (x-axis) and wall width (different curves) for both adhesve and air cladded waveguides.**

Figure 2-29 shows the results of the calculations except expressing the total percentage of collection from an entire sphere of isotropic radiation. A more useful visual of the efficiency of the device architecture is shown in Figure 2-30. This shows the collection efficiency for various channel half-widths and wall widths but instead, plots the efficiency of the waveguide to collect the amount of light that is collectable by the waveguide NA. The calculations assumed NAs of 1.24 in the lateral direction and 0.60 in the transverse direction (using an index of 1.474). This is a more useable interpretation as it indicates if the device architecture is being used to its full potential to collect the maximum amount of light possible given the waveguide properties. Efficient use of device architecture would be employing channel and wall thicknesses that enable collection efficiency of 100% at the point where the efficiency just reaches 100%.

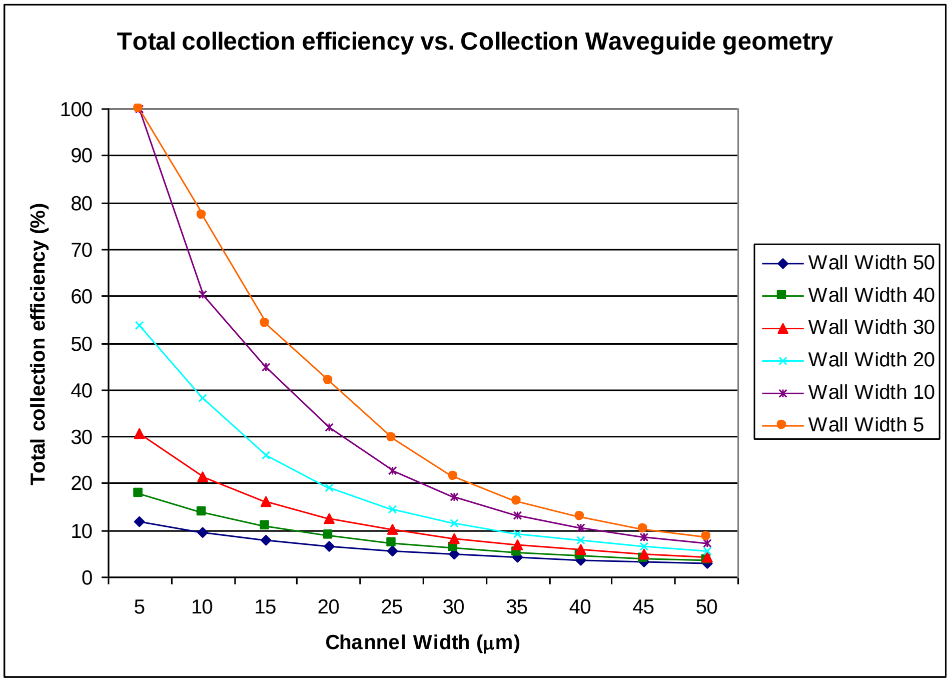

**Figure 2-30: Plot of the collection efficiency of waveguides of varying architecture with an air cladding.**

### 2.2.4.4 Angled waveguides

Signals collected from a waveguide directly across from the lens system will obviously suffer from large noise as light from the input will be coupled directly to the collection waveguide. By simply angling the collection waveguide, as demonstrated via the addition depicted by the red shaded region in Figure 2-31, one could reduce the amount of noise seen on the output.

These designs must be carefully deployed as they must take into account the refraction at the interface between the channel and channel wall. Tilting the waveguide requires that designs not just align the centre line of the waveguide with the interrogation point, but account for refraction using Snell’s law. The cone of collectable rays will be altered – some more than others as one extreme ray will be closer to normal incidence while the other will have a much more extreme angle and will also have a longer distance to travel in the water medium within the channel. This is depicted pictographically in Figure 2-32a) showing the introduced kink in the centre line of the configuration due to refraction at the wall/channel interface.

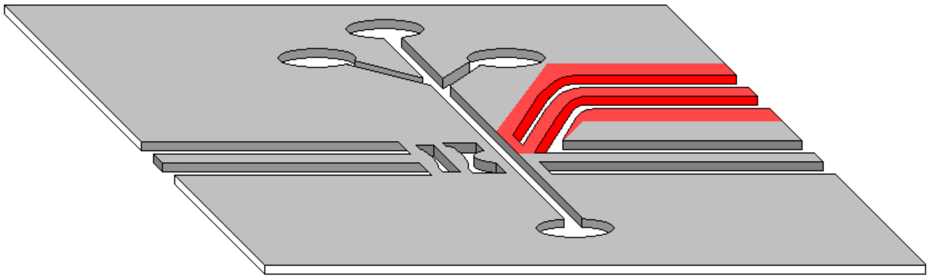

**Figure 2-31: Cartoon showing the addition of an angled waveguide for collection to limit the amount of noise coupled from the input.**

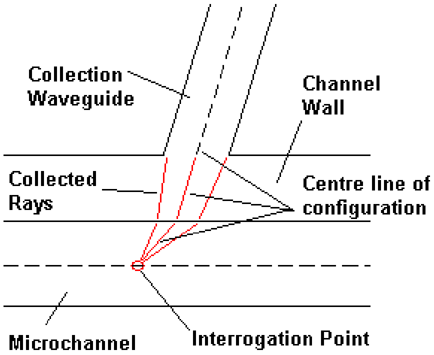

**Figure 2-32: Schematic showing how a waveguide can be tilted to collect rays and the affect at the interface that refraction has on the cone of collected rays.**

A simulation was run to show the amount of light that is coupled into an angled waveguide. The simulation was done in BeamPROP and was setup to have the light input injected from a 50 µm waveguide with an NA of 0.22. The channel width was set to be 50 µm wide while a wall width of 50 µm was used. The power was measured in the collection waveguide, as well a measurement was conducted to detect the power in the channel in a 50 µm wide region; this measurement to shows how much power stays concentrated in the channel as the angle will increase the propagation distance and therefore will allow the beam to diverge more.

An array of collection waveguides, spaced on-centre 125 µm apart, was placed across the channel to determine the coupling to many waveguides in potential parallel detection schemes. Simulation results indicate that as the collection waveguides are angled, the collection from the input beam decreases. The angle used in the simulations is the angle measured between the channel and waveguide; 90° is a perpendicular collection waveguide. Decreasing the waveguide angle with respect to the channel increases the angle between the waveguide and injection light.

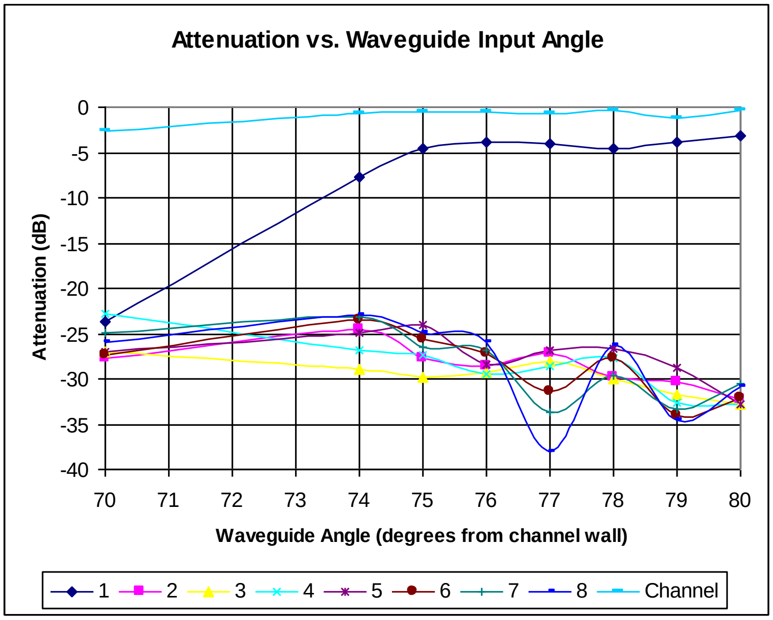

**Figure 2-33: Plot showing the simulation results where the angle of the collection waveguide is varied.**

Figure 2-33 shows the results from this simulation. A plot is constructed that depicts the power in the channel in a 50 µm wide region along with the collection from waveguide 1 – the waveguide directly across from the input – and shows the expected decreasing power collection as the angle of the collection waveguide decreases. Furthermore, the power in the 50 µm wide region in the channel shows decreasing power as the increased propagation distance allows spreading of the light – but only slightly. As the waveguide approaches 90° coupling across the channel will be maximized at a value close to 1.0 due to losses sustained because of the divergence of the beam as it traverses both channel walls and the channel. At any angle below 70° there is no significant coupling observed between the input and collection waveguides. This is ideal and will not be repeated in application due to scattering and other effects – however, these sources of noise should remain low enough that they won't cause large detrimental effects to detection. The further neighbouring channels do not collect any significant amount of light and thus an angled waveguide should not interfere with any parallel detection schemes.

#### 2.2.4.5 Multiple Outputs

Multiple waveguides can easily be added to the chip without affecting the other collection waveguides. Figure 2-34 shows the addition of one more waveguide – again, shaded in red - to allow a chip with the possibilities for multi-parameter simultaneous detection.

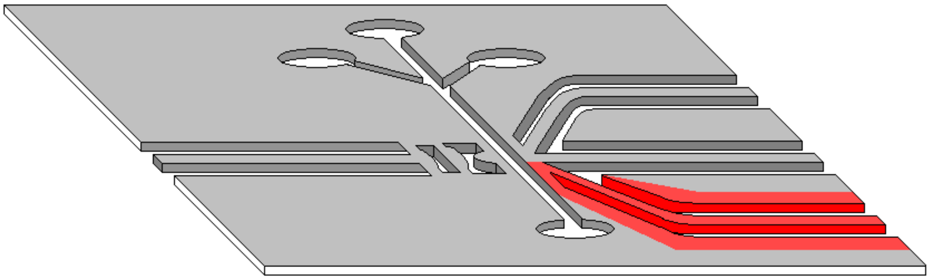

**Figure 2-34: Cartoon depicting multiple collection waveguides at a single point of interrogation.**

When designing such devices, all the parameters discussed thus far must be taken into account: the NA, channel width, wall width, and to make sure that all rays are accounted for. The addition of a lens system does complicate matters as it makes the rays divergent and thus the angled waveguides may be able to pick some up excess light. Figure 2-35 contains a simple illustration where multiple waveguide have been designed into the device.

Carefully using the design principles laid out earlier, the designs can be expand to incorporate multiparameter detection. The placement of waveguide will have different amounts of light associated with them that are based on the scatter properties associated with the particle. With this work, microspheres are used, so the particles are uniform and thus, side scattering will be quite uniform. The side scatter waveguide will be aligned from 30º to 90º. The forward scatter picked up by the aligned waveguide is a more difficult parameter to discriminate from the background noise as it needs to be nearly in-line with the injection waveguide. Fluorescence detection only has proximity dependence as it has an isotropic radiation field. When placing the waveguides so close to one another, the size of the facet can be a problem as they can interfere with each other's functions. However, a large facet is needed to maximize collection and it is also necessary to have close proximity to the source. This is problematic as outlined in 2.2.4.3.

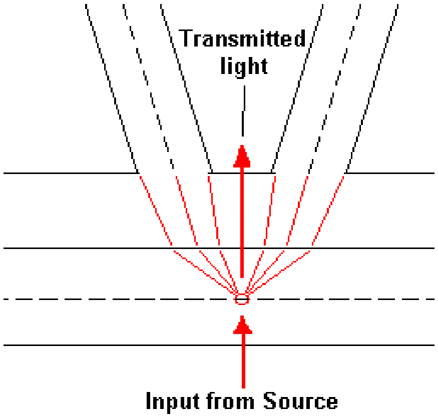

**Figure 2-35: Using Figure 2-32 as a base unit, a complicated architecture can be constructed using repeating units. This specific design collects two angles while allowing transmitted light to escape for low noise detection.**

Using Figure 2-32 as a building block, more complex units are built. The device was mirrored about the interrogation point to show two angle collections while the transmitted light is mostly allowed to propagate straight through and not show up on either collection waveguide – so long as the image beam is not too divergent. The presence of the input light is reduced on both collection waveguides and results in a higher SNR. Placing a waveguide in the gap between the two waveguides is also possible as there is plenty of room to fit an additional waveguide facet. Transmitted light is a useful property to measure through the extinction of the light.

#### *2.2.4.5.1 Advanced Architecture*

Just angling the collection waveguides is not the only option to improve the designs. As side scatter is very sensitive to the excitation signal due to the fact they are the same wavelength, this can lead to direct noise on the collection signal. Device configuration of the lens system can limit the background signal on the scatter collection waveguides. The input lens systems can be angled in much the same way the collection waveguides were angled in previous sections. A picture of this idea is depicted in Figure 2-36 by the red region. This angled input will reduce the noise on the perpendicular waveguide and thus create a very low background signal for upper waveguide. Now there is an optimal orientation of 90º between the collection waveguide and the input waveguide axis.

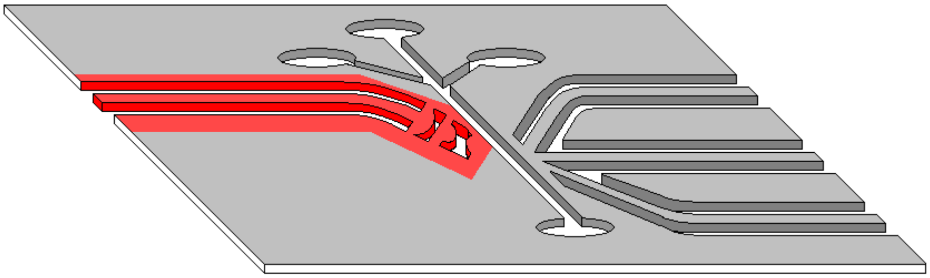

**Figure 2-36: Cartoon depicting the angling of the lens system to allow more complex interrogation and lower SNR on collection.**

With an angled input, there is room to fit another collection waveguide on the same side as the channel as the input system. This is shown by the added red region in Figure 2-37. A waveguide at an angle of 30 degrees from the channel combined with an input lens system aligned at 60º to the channel means a 90º collection angle. This allows a very low SNR possibility. This waveguide can be used to collect a large side scatter parameter or weak fluorescence detection.

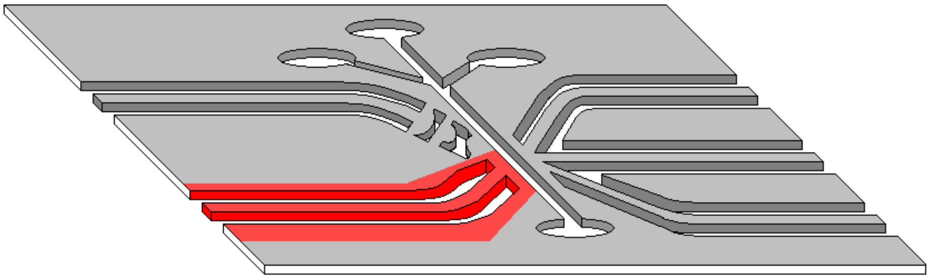

**Figure 2-37: Cartoon depicting a collection waveguide on the same side of the channel as the input made possible by the angling of the input.**

### 2.2.5 Device Integration

These simulations have served to determine the performance of the optical components necessary to perform a cytometric function. All of these optical components will be seamlessly integrated into a single layer with the microchannel to form a portable and inexpensive cytometer. With all the devices in a single layer it is necessary to consider the substrate, sealing, and interconnection of the device with external components. The resulting sandwiched device shown in Figure 2-38 should allow seamless and efficient function of the optical and fluidic components. The device has transparent sealing, device, and substrate layers.

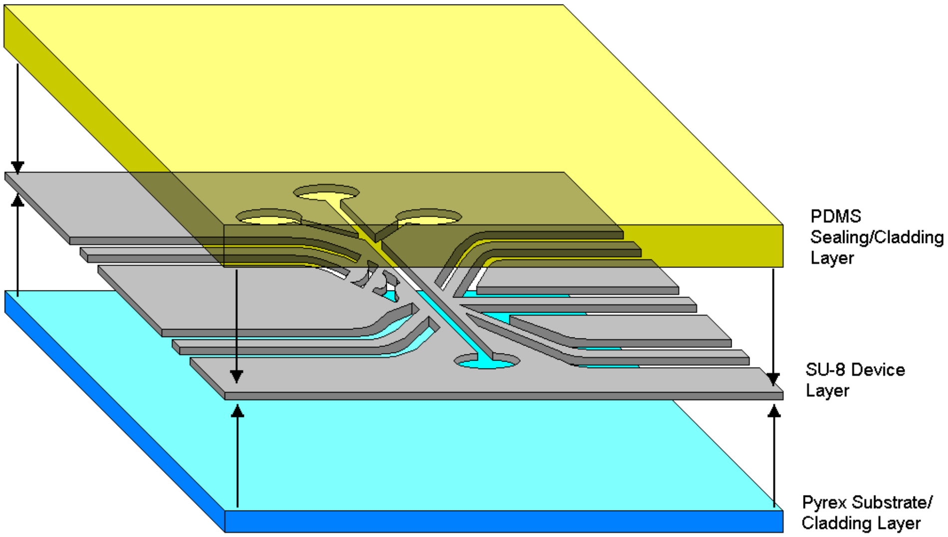

**Figure 2-38: Cartoon depicting the assembly and integration of the device in planar fashion. The top sealing layer is transparent, hence the device layer is visible through it.**

### 2.2.5.1 Waveguide and Microchannel Integration

Using SU-8 as the device layer is for design, fabrication, and functional purposes. SU-8 allows one layer designs via a one-shot processing procedure.[44] Integrating the waveguide and the channel together does necessitate the need to take into consideration the waveguide/channel wall and the effect on the beam spreading discussed earlier in this chapter. Voids are easily formed in the layer to fabricate the channel can also to define the waveguide region via an air cladding. SU-8 forms a transparent layer in the same spectrum as that used for many biological detection schemes. SU-8 forms rigid structures so that it will not deform once fabricated. Deformation during operation is due to fluid pressure warping the optical structures and the optical devices and will cause incorrect optical function. The index of SU-8 is also sufficiently high to allow confinement between substrate and sealing layers.

### 2.2.5.2 Upper and Under Layer

A Pyrex substrate serves a dual purpose of sealing and providing optical confinement from the top. The substrate provides good bonding to the device and is transparent in the spectrum of interest for biological detection.

A PDMS cover slip can provide a completely conforming seal and allows easy interface of the fluidic components via punching holes in the soft elastomer layer. The chemical reaction between the PDMS and SU-8 allows a very strong bonding mechanism to provide strong bonding and good sealing of devices. PDMS is also transparent in the same optical spectrum as many biological assays require. The index of PDMS has a lower index than the SU-8 to allow optical confinement from the top.

### 2.2.5.3 Fluidic and Optical Interconnections

The fluidic sealing of devices must be simple, rugged, and reusable if possible. This is done through the top PDMS layer as it is very flexible and allows for holes to be made through simply punching the elastomer. A glass substrate would require drilling and complicate fabrication. The elasticity of the PDMS will allow some sealing though pressure between the PDMS and the inserted metal interconnecting pins. The interconnection must be able to handle high fluid pressures common in microfluidics. A new method was developed to handle this, and will be discussed later.

The final device design structure is shown in Figure 2-39. The picture has the construction of the device exploded and separated layer by layer. This clearly shows the device layer sealed via the substrate and PDMS sealing layer. The waveguide facets are formed via the photolithographically defined vertical edge. The sealing of the device is done by bonding glass pads, with adhered metal pins, to the PDMS surface – as will be discussed in detail in chapter 3.

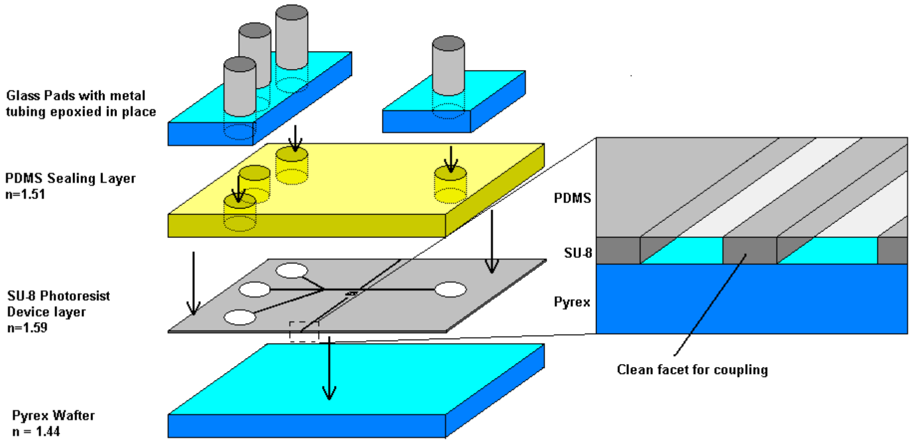

**Figure 2-39: Explosion of the device showing the individual layers used to construct the device. Details (zoom region) of the device layer where the waveguide facet is formed.**

### 2.2.6 Integrated System for Forward Scatter

So far, the designs have considered multiple collection angles for fluorescence and scatter, and no focus has been on the forward scatter. The forward scatter is very susceptible to background noise due to the fact that the forward signal and transmitted excitation signal are very nearly coincident. When a divergent beam is used, as is with beam shaping, the divergence of the transmitted light compounds this problem.

It is necessary to have as much functionality on-chip to mimic the functionality of a flow cytometer. Forward scatter adds a layer of complexity due to the need to distinguish between transmitted light and the forward scatter light. A method must be deployed that would allow on-chip collection and cause no detriment to the function achieved by beam shaping. Figure 2-40 depicts this simple change to the device by the shaded red area. This device modification must eliminate the transmitted portion of the beam while allowing the slightly deviated light to propagate through to the detection waveguide.

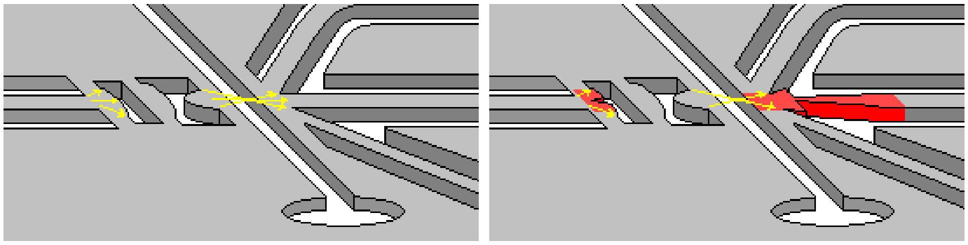

**Figure 2-40: Cartoon depicting minor changes that can be made to the lens system and collection waveguide to allow a large SNR on forward scatter collection.**

### 2.2.6.1 Motivation

If a divergent beam is used, much of the forward scattered rays will overlap with other transmitted rays. The more divergent the beam, the more noise can potentially appear as the side scatter signals will eventually overlap with the forward scatter light. This is shown in Figure 2-41a). The light from ray 1 produces some forward scattered light – given by the green rays. The transmitted portion of 1 is distinguishable from the forward scattered rays. However, in a divergent beam another ray, 2 in this case, has a transmitted portion that will be coincident with the forward rays from 1. This will constitute as noise on the forward scatter signal. In a heavily divergent beam the side scatter from 2 will overlap with forward scatter from one. A large enough intensity will completely obscure the forward scatter signal. To get a clear signal, many designs forgo the use of a largely divergent beam.

Conventional cytometery typically focuses the input beam to a very fine beam stop on the opposite side of the channel as depicated in Figure 1-11b) and c).

This is a tricky design to accomplish in a planar configuration as it will complicate fabrication. Conventional cytometry also uses a beam stop in the input side, as shown in Figure 2-41b). This forms a dark spot in the image. As the image of the beam and the image of the beam stop are not coplanar, the beam shape is not affected by the beam stop. This allows the device to form a bright spot at the interrogation and a dark region at the detection waveguide. Conventional cytometery blocks enough of this light to open a window that will allow a large amount of forward scattered light to be detected.

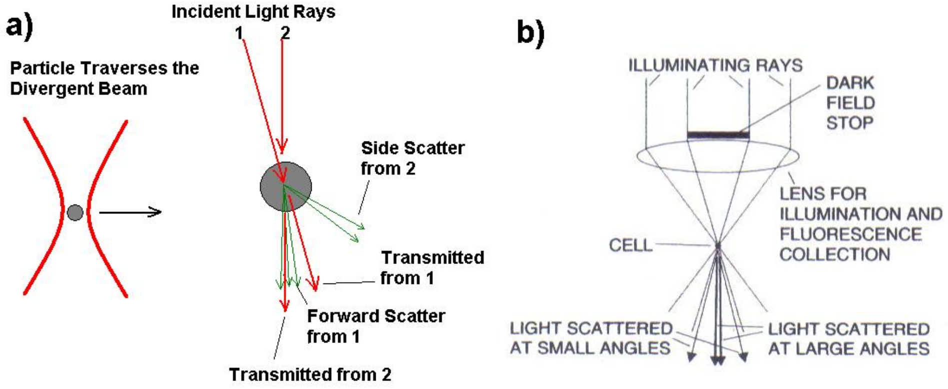

**Figure 2-41: a) A particle in a focused beam causes forward scattered light to be obscured by transmitted light and large scattered light. b) Conventional techniques use an obstruction on the input to create a shadow in the image plane. *Source*: a) reprinted from reference 124[†], b) reprinted from reference 3.**

### 2.2.6.2 Notched Design

The conventional method shown in Figure 2-41b) can be adapted to a planar design. It is only a matter of inserting a dark field stop, or "obscuration" in the lens design. The planar design limits the ability to manufacture many solutions, such as some that insert ink, that also require a complex fabrication procedure to produce the multilayer design.

Designs here use a notch in the first surface of the lens system. The notch is shown in Figure 2-42 on the second surface of the simulation – on the first curved surface in the lens design. Figure 2-42a) shows a detailed image showing how the

---

[†] This is from the author's work in reference 124.

axial rays from the simulation are deflected via the notch. They are eliminated from the ray trace and manifest themselves as a dark spot in the formed image. The removed rays don't affect the formed beam geometry in the channel - as shown in Figure 2-42b). The image plane of the first surface has a large gap formed by the notch. A waveguide can be placed in the dark spot formed and any rays collected by the waveguide are refracted to this spot scattered by a small angle compared to the input light. Rays scattered here are only deflected by a small angle – only 1 to 5º.

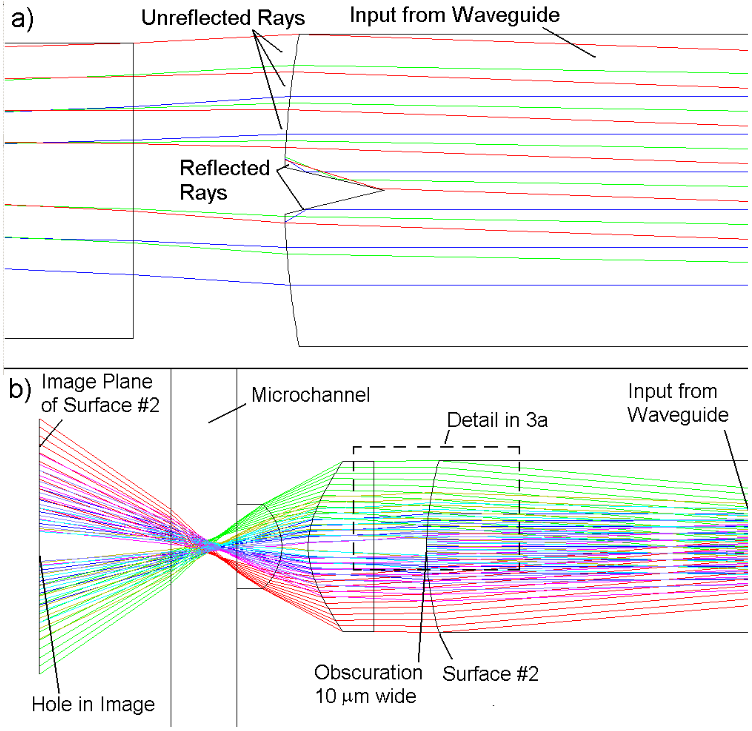

**Figure 2-42: a) Simulations showing the proposed lens modification where a notch is inserted into surface 2 of the lens system that will b) generate a hole in the formed image where the collection waveguide will be located. *Source*: Reprinted from reference 124.**[‡]

This design allows an all planar solution that allows beam shaping. The shape of the beam is not affected by the missing segment of rays. The ZEMAX simulation allows a spot analysis in the channel, shown in Figure 2-43. As ZEMAX performs these simulations in 3D, the lenses are spherical in nature and the focused light fields are circular due to the focusing in both the x and y axes.

---

[‡] This figure is from the author's work in reference 124.

The obscuration is a circle in the simulation, as noticed via the obscuration in the formed spots in Figure 2-43. For a microchip-based design, designs must assume focusing only in the plane of chip – the y axis. Spot images would then have the obscuration form a slot that extends the entire spot width in the x-direction. The spot diagram in Figure 2-43 shows different formed images based on the angle of rays entering lens system. Spot shapes clearly show that the missing rays from the hole are spread out over the formed image. The missing rays won't have a cumulative affect in any one spot in the beam.

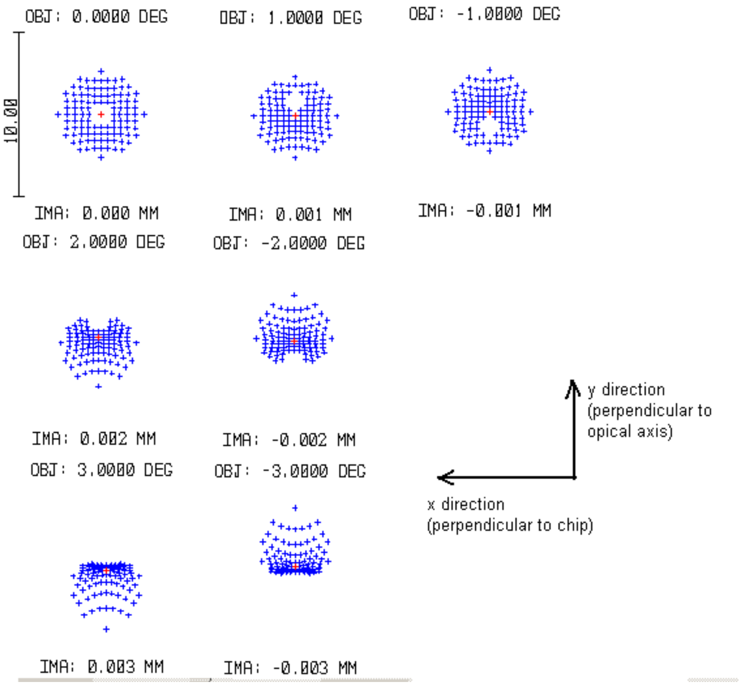

**Figure 2-43: Spot diagram of the beam at the point of particle interrogation with obscuration on lens surface 2. The missing intensity is spread out over the lateral direction.**

With an adequate solution, designs were made for each of the previous beam width designs from Figure 2-21. Three samples of the simulations are shown in Figure 2-44 - for spot sizes of 3-, 6-, and 12 μm beam widths.

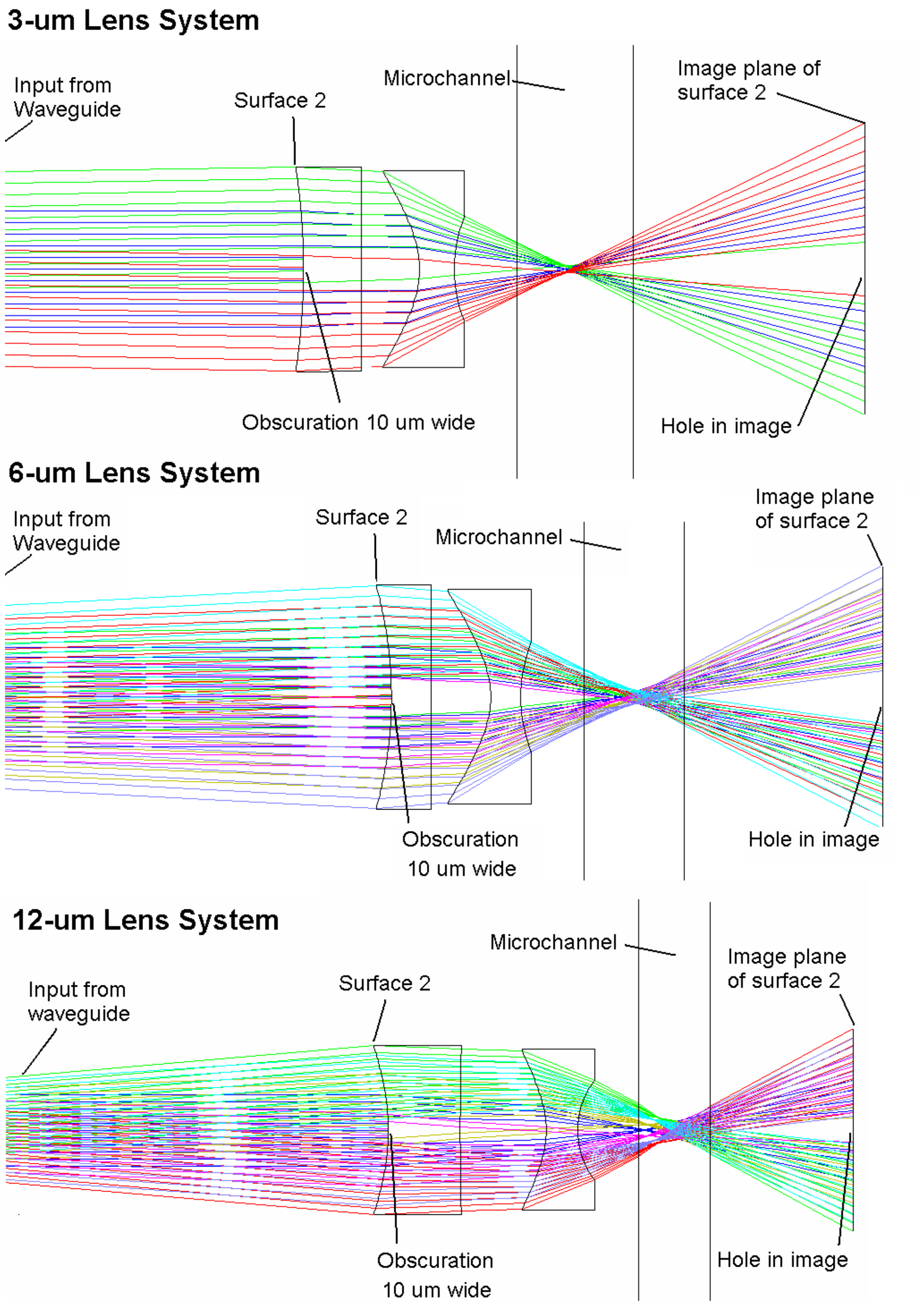

**Figure 2-44: Simulations for three lens designs that incorporate the notch for forward scatter capabilities: 3, 6, and 12 µm.**

### 2.2.7 Photomask Designs

With all the simulations and theory in mind, several devices exploring various designs were fabricated. In total, 4 masks were made – all designed by the author of this work. The first – shown in Figure 2-45 - was a very simple mask that was used solely in Thomas Kowpak's thesis work to determine the limits of fabrication with SU-8. It consisted of various waveguide thicknesses and spacing, various channel widths, wall widths, waveguides angles, and even simple lenses.

The second mask – shown in Figure 2-46 - employed the lens systems to form the larger beam shapes designed in Figure 2-22 as well as some simple waveguide architectures. Smaller beam waists were designed in the next iteration of devices, shown in Figure 2-47, as well as some geometries that explored the waveguide configuration and general device architecture. These designs even included some trial designs that integrated lenses on the collection waveguide to try to increase the collection angle.

Figure 2-48 shows the last photomask design. It includes revisions to lens designs to improve the performance of the beam shapes, the new forward scatter designs, angled lens input designs, and multiple collection waveguides. Furthermore, this design tried to make the fabrication process more efficient by manufacturing multiple devices on a single microchannel to increase the yield of fabrication. Lastly, this design has the waveguide facets spaced so that they align with the spacing from a fibre array block that contains 8 50 μm core diameter fibres space 125 μm on-centre. This allows quick integration of multiple source/collection fibres.

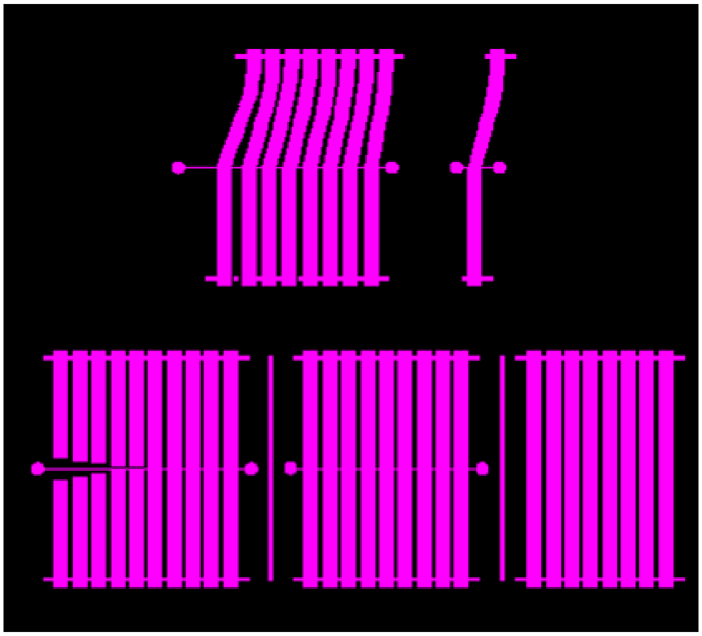

**Figure 2-45: 1st Photomask. Designs explored waveguide angle, channel width, wall width, waveguides width and spacing, and simple lens structures.**

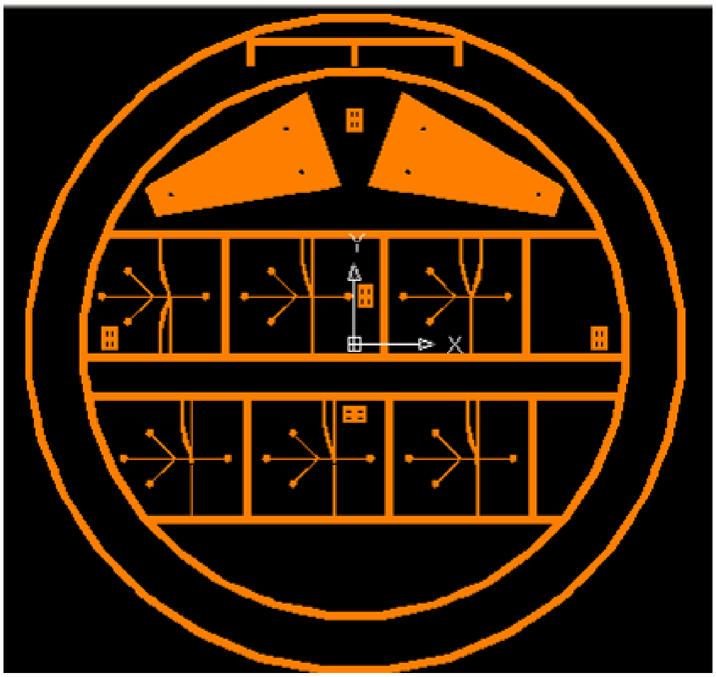

**Figure 2-46: 2nd Photomask. Device on the bottom are 25-, 30- and 50 µm beam shapes. Devices in the middle explore different waveguide architecture. Top two structures are not related to this work.**

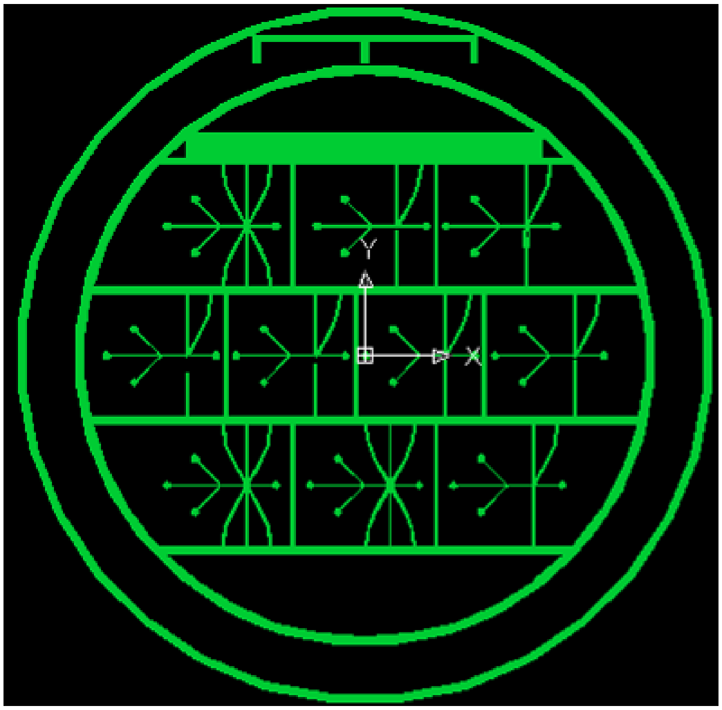

**Figure 2-47: 3rd Photomask. Designs included 1.5-, 3.6-, 6.0-, 10.0-, and 12 μm lens designs (middle four devices and bottom right device). Also includes several designs using multiple angles and collection optics to increase the angle of collection.**

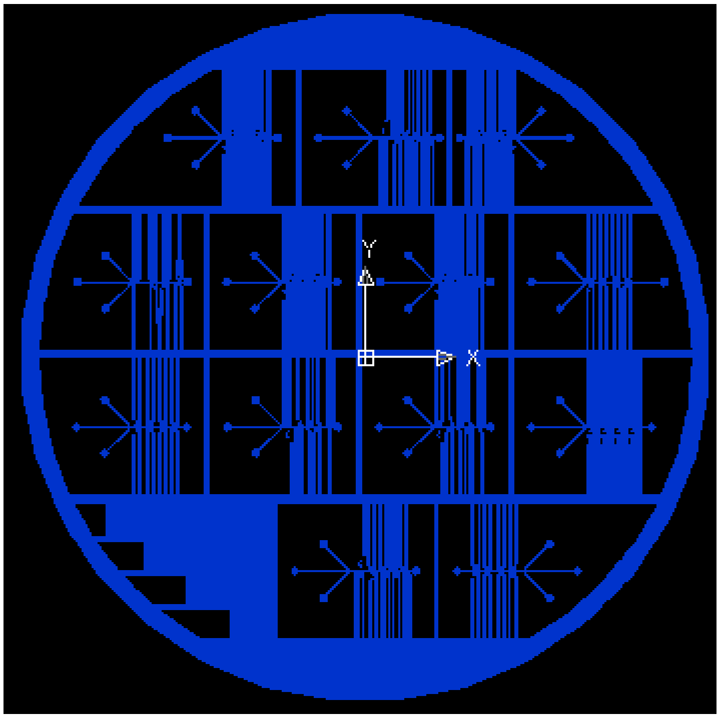

**Figure 2-48: 4th Photomask. Multiple devices per channel. Revised lens designs are used. Forward scatter and multiparamter and device operation are incorporated to the designs.**

#### 2.2.7.1 Microchannels

Microchannels are a simple 3-branched structure common in microchip-based flow cytometers that allow simple 2D hydrodynamic focusing between two sheathing fluids. Channels are 50 μm wide to facilitate a range of particle sizes from 1 μm to 10 μm to eliminate the chances of clogging and to facilitate hydrodynamic focusing within a feasible pressure range.

#### 2.2.7.2 Excitation Waveguides

Excitation waveguides are 50 μm wide to match the core diameter of the input waveguide. The wide core width allows a very heavily multimodal nature of propagation within the waveguide as shown in Figure 2-3. This will relax the coupling condition between the source and the waveguide as noted in the simulations results shown in Figure 2-16, and facilitate easy alignment of the fibre to the device.

#### 2.2.7.3 Lens Systems

Devices based on the simulations in Figure 2-21 are incorporated to a photomask. Parameters used in ZEMAX were used to create very precise curved surfaces in the photomask. The end of the waveguide facet was placed where the ZEMAX source was specified in simulations. The lenses are shown in Figure 2-49 and are a sample from the 4th photomask design. By tilting the waveguide and lens, and by taking into account the refraction due to non-normal incidence and the adjustment to the length of the optical axis, several designs for an angled input were created, as shown later.

These lenses shown in Figure 2-49 also incorporate a light blocking structure that blocked the stray light missed between the waveguide and the lens system. This is a design revision applied from results from testing initial lens designs and will be discussed later in 4.2.1.4.

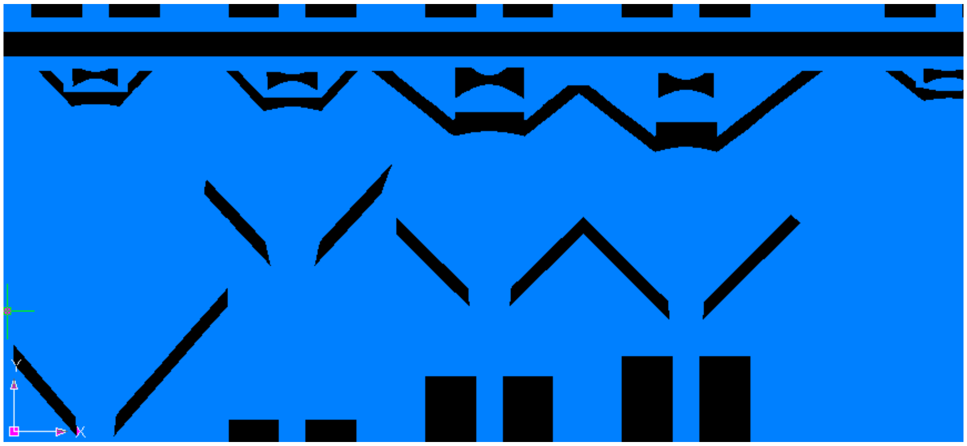

**Figure 2-49: Designs for multiple simple devices on a single microchannel. Devices have an input, lens system, and single collection waveguide.**

### 2.2.7.4 Collection Waveguides

Single, multiple, and opposite side collection schemes for 2, 3, and 4 parameter detection capabilities are designed according to simulation results from section 2.2.4.5. The waveguides are designed with regular spacing to ease integration to a fibre array block to allow easy multiple coupling capabilities to the multiple parameters collected by the waveguide. The mulitple waveguides are integrated with the lens systems, angled input and multiple inputs – each carefully placed to limit the cross-coupling from the input side to the output in order to reduce the noise on the outputs. In the case of any fluorescence parameter, the reduction of noise on the output waveguide is not necessary as an optical filter is already necessary to remove the scattered light.

Figure 2-50a) shows a sample of the series of devices designed from the 4th photomask. These devices integrate a lens system (10 μm lens system in this case) while the opposite side of the channel has collection from three waveguide angled to different degrees: 5°, 30° and 70° to the beam axis. These specific devices could be used to perform to simultaneously detect 2 different fluorescent signals plus a large angle side scatter parameter. These designs are only feasible with a single input – unless two light sources are coupled to the same waveguide to form overlapping excitation regions.

Figure 2-50b) shows the same device as in a) but with the input angled at 20° from the normal to the channel. The output waveguides are now at angles of 0°, 45°, and 90° to the input beam axis. This architecture will allow transmission or fluorescence measurement along with another waveguide that could allow measurement of another fluorescence or side scatter parameter. The side scatter will have very low background noise as collection is at 90 ° to the input beam and thus, a very low amount of light will be coupled into the waveguide.

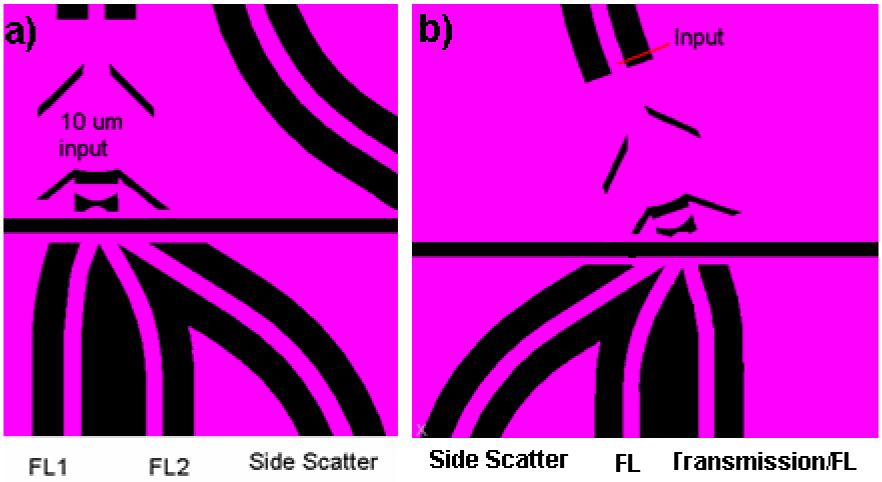

**Figure 2-50: a) Design for a 10 µm input lens system and three collection waveguides for two fluorescence collections (FL) and one side scatter collection. b) Design for an angled 10 µm lens system input and three collection options.**

Expanding design architecture further, the next logical step would be to try to incorporate two excitation sources into the same interrogation point. This would allow multiple colour inspection or two simultaneous beam widths in the same interrogation point. Figure 2-51a) shows a device whose design included two inputs, one from each side of the channel. Due to the angled input from each side of the channel there is only enough room to efficiently integrate a single waveguide on each side. This waveguide’s large angle allows for either a large angle side scatter collection or low angle scatter or fluorescence detection – depending on if the collection waveguide is on the same side as input, or the opposite side, respectively. This device architecture has the same lens system on each input – the 10 µm in this case.

Figure 2-51b) shows the same design except different lens designs on each side. This would expand the flexibility of the device by allowing different excitation spot sizes with different colours. Specific detection of two specimens or two different features from a specimen via simultaneous excitation from two different wavelengths would be possible.

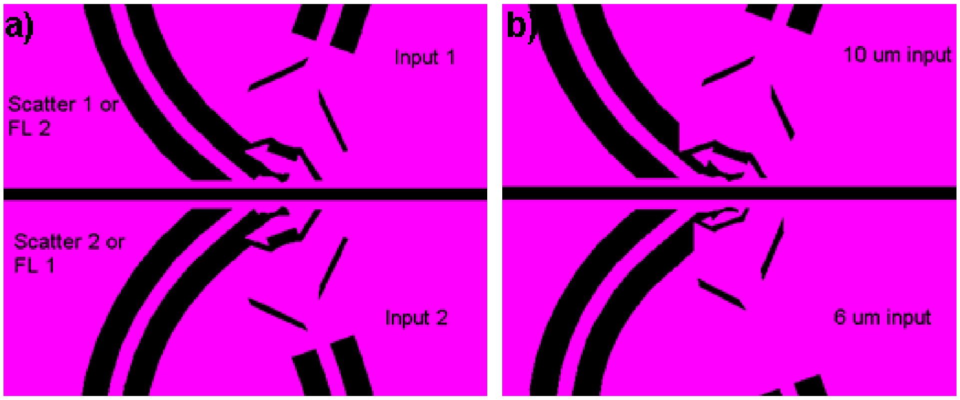

**Figure 2-51: a) Designs for a device with dual inputs from two angled lens systems and one in-line or 90° collection option. b) Design for a device with dual angled different lens system (10 µm and 6 µm shown here) with in-line or 90° collection options.**

### 2.2.7.5 Forward Scatter Collection On-chiph

Designs to reduce the noise on the forward scatter colletion in an integrated on-chip fashion with beam shaping capabilities with the on-chip were incorporated into designs with multiple collection waveguides. The designs of these devices are shown in Figure 2-52a), using the same architecture as the straight input design from Figure 2-50a). The narrow waveguide for forward scatter collection is the only addition outside of the notch in the lens surface. Placement of the waveguide does not interfere with the collection waveguides already in place due to the very narrow facets. Figure 2-52b) angles the input waveguide and lens system similar to the design presented in Figure 2-50b). In this design, the forward scatter collection uses one of the collection waveguides already in use in the design from Figure 2-50b). The only modification – other than the notch – is that the one waveguide was narrowed to perment selective coupling necessary by the waveguide facet.

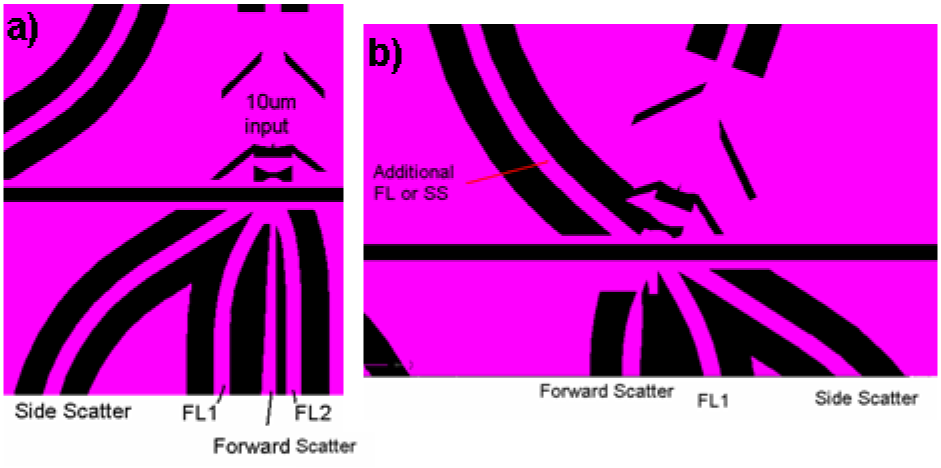

**Figure 2-52: a) Designs for a device with a 10 µm focused beam with notch design to block stray light for forward scatter collection on the narrow waveguide; also with capability for three other collection parameters. b) Design for an angled input 10 µm lens system with notch design to block stray light for forward scatter collection on the narrow waveguide; also with capability for three other collection parameters.**

# 3 Device Fabrication and Testing

Devices designed with various beam shapes and optical components for collection of forward scatter need to be realized and the operation of which has to be evaluated and confirmed in order to validate designs and the design method. Fabrication of the designs must ensure device construction is realistic and that the designs are functionally feasible and workable. With physical devices, rigorous testing can confirm the accuracy of simulations and confirm the expected operation of the designs. Analysis of data obtained in actual experiment situations will allow testing to confirm the level of performance, the adequacy of the results, and allow improvements to be made to new designs.

## *3.1 Fabrication*

### 3.1.1 Materials

The rational for the choice of materials used to construct the designed devices is given in section 2.2.5. The materials' properties will be summarized here so as to confirm the criteria.

The chosen material for a substrate is a Borosilicate wafer. Early work referred to this wafer by the brand name 'Pyrex'; the two work are synonymous and will be used interchangeably in this work. The wafers were purchased from Plan Optik. These wafers have an index of refraction of 1.471, and a low surface roughness of <1.5nm – ideal for the fabrication of devices as this smooth interface will provide less scattering during optical function. The borosilicate glass has a low coefficient of thermal expansion (CTE) ~ $3\text{x}10^{-6}$/°C) which will make the wafer less susceptible to thermal shock – a benefit given the large temperatures used in processing.

The device layer is fabricated from SU-8 2025, a positive epoxy-based photoresist developed by and purchased from MicroChem Inc.. SU-8 has an index of refraction of 1.582 at 635nm, 1.59 at 660nm. The material's dispersion is negligible over this range so an index of 1.59 was used throughout this work.

The intermediate layer between the SU-8 device layer and Pyrex substrate was developed primarily to facilitate bonding between the two materials. Another positive epoxy-based photoresists was used; SU-8 3015 from Microchem Inc. This particular series of SU-8 was specially formulated to adhere to glass substrates. The index of this material was deemed irrelevant in this work as the layer used was kept very thin; enough so that it was unable to support any propagating optical modes – lossy or not.

To formed the devices in the photoresist layer a developer was purchase to remove the regions of unwanted SU-8 2025 from the device layer. This developer was purchased from MicroChem Inc. NOTE: other manufacturers' developers will not produce satisfactory devices, as noted later in section 3.1.3.1.

To seal the devices a layer of Poly(dimethylsiloxane) was used. PDMS was purchased from Dow Corning as a Sylgard 184 elastomer kit that contains the monomer and curing agent. The index of refraction of the PDMS is 1.4 for the wavelengths of interest in this work.

The glass pads used for interconnection are generic soda lime glass that can be found in large quantities around a typical lab. The only conditions for correct device manufacturing is that the glass is a silicon based material.

Metal pins that served as fluid interconnects were purchased from Instech Laboratories Inc. The pins were 22 gauge stainless steel (model No. SC22/15) and had an original function as catheter interconnects.

During device manufacturing, several chemicals are used. Analytical grade isopropyl alcohol (IPA) from Sigma Aldrich and analytical grade Acetone, again, from Sigma Aldrich, were purchased for use in the various device manufacturing steps. A common photoresist, 1813 photoresist from Shipley, is used for the encapsulant during device dicing. The bonding step during device fabrication requires nitrogen gas ($N_2$) from Praxiar, to ensure proper PDMS activation. This gas was of very high purity (greater than 99.9995%) as to ensure excellent bonding, as will be discussed later in section 3.1.3.4.

### 3.1.2 Equipment

Various equipment is used during the fabrication – much of which is standard for any photolithography-based fabrication. Furthermore, due to the micro-scale nature of the device features, as much of the fabrication as possible should be done in a cleanroom at all steps until the devices are packaged. This is to eliminate contamination issues – as will be discussed in 4.1.1.2.3. In this work, a class ISO 5 or ISO 6 cleanroom was used to for substrate work to form the device layer, while a class ISO 7 or ISO 8 cleanroom was used during the bonding and packaging steps.

A model WS-400A-6NPP/LITE spinner from Laurell Technologies was used for applying the SU-8 (and 1813) photoresist layers to the substrate. This spinner unit allows many programmable steps that allowed custom spin speeds and durations during each step. Very uniform and repeatable layers can be produces from this spinner. A hotplate with a controlled rate for cooling and heating was used in this work. The capacity of the hotplate to reach 265ºC was necessary for the first step of the device fabrication procedure. An exposure machine from ABM Inc. with a 365nm exposure wavelength was used to transfer the photomask pattern to the device. A sonicator mixer with low-speed capabilities was used and is highly recommended to agitate the devices and developer solution during the development step.

A nitrogen vacuum oven from Diamed (SHL 1407) with a 0.6 cubic feet capacity was used during the pre-bonding steps. To free the waveguide facets, a dicing saw, the MicroAce Series 3 from Loadpoint Ltd., was used to precisely cut the substrate with little chipping.

A custom-made hole punch for creating holes to facilitate fluid interfacing through the PDMS was fabricated from a blunt tipped syringe. The inside of the syringe tip was filed down very slightly to help form a sharpened outer edge and ease the cutting of the PDMS. A generic oven for heating devices and curing the PDMS was used with the capability of achieving temperatures of up to 150ºC. The PDMS mold used to manufacture covers slips was fabricated in-house from extra silicon and glass substrates to ensure that the bonding surface of the PDMS (to the SU-8) was extremely flat and free of structural defects. To bond the devices, a nitrogen/oxygen capable plasma bonder from Harrick plasma was used.

### 3.1.3 Procedure

In order to realize the new device designs it is necessary to follow a 5 part fabrication procedure that breaks the manufacturing of the devices down to the major processes. The five segments are as follows: SU-8 device fabrication, PDMS cover slip fabrication, device dicing, device sealing, and device packaging. Fabrication consists of pattering device structures in a layer of photoresist though selectively removing material. These devices are then sealed via bonding a prepared PDMS cover slip to the patterned devices after they have been diced to free waveguides. After bonding, interfacial connections for fluidic control are made and completes the packaging of the device. The groundwork for this fabrication procedure was done in conjunction with Thomas Kowpak and can be found in his publication in reference 117 and in his thesis work in reference 116. The fabrication process contained within this work is an adaptation of the process in references 117 and 116 to optimize for the designs within this work. Furthermore, the bonding procedure was developed jointly with Thomas and is summarized in reference 118 while a simplified bonding procedure was developed in conjunction with Zhiyi Zhang, found in reference119.

Figure 3-1 shows a flow chart depicting the five main segments of fabrication, and how they relate to each other sequentially. Each segment contains a sequence of steps to create a major part or accomplish a major change to the device; bringing these fabricated or modified parts together forms the fully functioning unit. Details of the steps for each major fabrication segment have been optimized through a trial and error process based on the inspection of the quality of the resulting devices. The following sections contain the exact recipe for the fabrication of each segment of the device and the process to integrate them together.

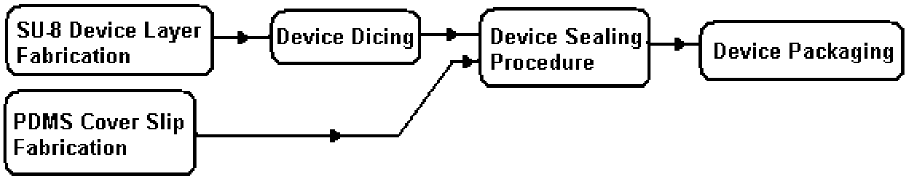

**Figure 3-1: Flow chart showing the 5 main segments of the fabrication procedure.**

### 3.1.3.1 SU-8 Device Layer Fabrication

A flow chart of the process to develop the SU-8 devices on a Pyrex substrate is shown below in Figure 3-2. Basic photolithography techniques are used and it is most important that this segment of fabrication is done in a cleanroom. This ensures proper quality and formation of devices free from debris and chemical contamination. Again, this work was based off preliminary done in conjunction with T. Kowpak.[116,117,118]

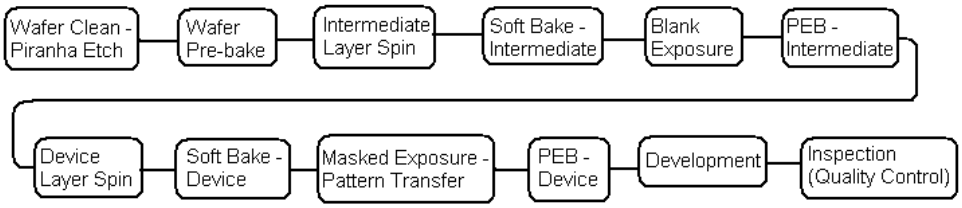

**Figure 3-2: Flow chart depicting the steps necessary to form the SU-8 based devices on a Pyrex substrate.**

The following is a very detailed description of the steps necessary to form the SU-8 device on the Pyrex substrates.

- <u>Wafer clean/Piranha etch</u>: devices are cleaned via a combined solution of sulphuric acid and peroxide. This step removes any organic substances that may be on the substrate surface that would interfere with bonding or device formation.

- Wafer Pre-bake: devices are baked at 265$^{O}$C for 3 hours in order to ensure that all water molecules are removed from the wafer surface as any water present will interfere with bonding and device formation.
- Intermediate Layer Spin: A 30% weight solution of SU-8 3015 in the corresponding developer is poured onto the wafer and then spun in a stepwise sequence using the following conditions:
    - 500rpm for 7 seconds
    - 1500rpm for 5 seconds
    - 3000rpm for 30 seconds
    - 1000rpm for 3 seconds
    - 500rpm for 3 seconds

  These conditions result in a layer approximately 600nm thick as per Thomas Kowpak's work revealed.[116,117] A solution containing 10% weight SU-8 3015 can also be used and results in a much thinner layer – approximately 133nm thick.
- Soft Bake - Intermediate: immediately after spinning, the wafer is placed onto a hot plate set at 95$^{O}$C for 5 minutes to drive out the developer solvent.
- Blank Exposure: The wafer is placed in the exposure machine and is exposed for 5 seconds under a full-field exposure at any intensity.
- PEB – Intermediate: The exposed device is placed on a hotplate set at 95$^{O}$C for 5 minutes to initiate cross-linking in the layer.
- Device Layer Spin: The wafer is then coated with SU-8 2025. A portion of SU-8 about an inch in diameter is carefully poured onto the centre of the wafer in order to avoid any bubble formation. The wafer is tilted and rotated to ensure that the entire surface - save for the outer ~2mm of the wafer - is coated before spinning. The wafer is spun in a stepwise fashion using the following conditions
    - 100rpm for 5 seconds
    - 500rpm for 15 seconds
    - 750rpm for 10 seconds
    - 1000rpm for 15 seconds
    - 1250rpm for 15 seconds
    - 1500rpm for 15 seconds
    - 1750rpm for 90 seconds
    - 1500rpm for 10 seconds

  - 1000rpm for 10 seconds
  - 500rpm for 10 seconds
  - 300rpm for 10 seconds

  The resulting layer should be ~28µm thick. During the 5th and 6th steps in the spin, a syringe should be introduced to the spinner. The tip should hover over the wafer by about 2-3 mm. The syringe slowly dispenses developer to the outer 2-3 mm of the wafer for the duration of the 5th and 6th steps and for half of the 7th step. This will remove the thick bead that is present on the wafer.

- Soft Bake – Device: the coated wafer is placed onto a room temperature hotplate (20$^{O}$C) and is set to ramp up to 95$^{O}$C at 100$^{O}$C/hour. Once the hotplate reaches 95$^{O}$C, it is immediately set to ramp down to 20$^{O}$C at 25$^{O}$C/hour. This step drives out any solvent in the SU-8. Heating and especially cooling must be done slowly to ensure that the bonding is maintained otherwise the SU-8 layer will result in delaminating, as will be discussed in 4.1.1.1.

- Mask Exposure – Pattern Transfer: the mask aligner's intensity is set to 3.5mW/cm$^2$. The application of optically dense filter sheets may be necessary in order to get the intensity this low. The device is then placed into the mask aligner and the mask is aligned to be centred over the wafer. Gentle contact is then made between the mask and wafer with a completely conforming contact the ideal results of contact. With the filter sheets in place, the exposure is cycled on an off; typically in 9 seconds on/5 seconds off intervals. This is to ensure a relaxation of the Lewis acid production and avoid results similar to over exposure – as discussed in Thomas Kowpak's work.[116,117] A total value of exposure of 190mJ/cm$^2$ is done. It is found that the machines intensity and the total number of intervals are parameters that provide some flexibility to fabrication without serious detriment to the device quality - as long as total exposure is constant.

  Eg. 9 seconds on * 6 cycles * 3.5mW/cm$^2$ = 189mJ/cm$^2$

  OR 9 seconds on * 10 cycles * 2.1mW/cm$^2$ = 190mJ/cm$^2$

  These two exposure conditions will produce no noticeable difference in device quality.

- PEB – Device: The exposed wafer is placed onto a room temperature hotplate (20$^{O}$C) and is set to ramp up to 90$^{O}$C at 100$^{O}$C/hour. Once the hotplate reaches 90$^{O}$C, it is immediately set to ramp down to 20$^{O}$C at 25$^{O}$C/hour. This step drives the cross-linking of the SU-8 epoxy molecules and will form the rigid structures required. Heating and especially cooling must be done slowly to ensure that the bonding is maintained otherwise the SU-8 layer will results in delaminating.

- This step is one of two (along with the exposure step) that can be adjusted depending on the final device quality. Too many cracks and poor resolution are both affected by these steps. It is VERY important that these two steps be optimized.

- Development: Immediately after the PEB the wafers must be submersed in the appropriate developer. As mentioned earlier in section 3.1.1, the MUST be from Microchem as other manufacturers' developes do not work as well and will leave a white film that will ruin the device. The wafer should be agitated for 5 minutes via the vortex mixer on a low setting – or by hand if a mixer is not available. After sitting in the developer, the wafer must be removed and rinsed with a stream of clean IPA (Isopropyl-alcohol), and then dried under a nitrogen stream. Some pointers for development are as follows:
  - If any material remains (usually will turn white after IPA rinse) the wafer can be re-submersed in the developer and agitated for another 5 minutes. This is not advisable as the device quality at this point will be poor.
  - Remaining material can be removed with acetone (it is a very powerful SU-8 developer), however this can cause lots of cracking in the cross-linked sections due to material swelling (via uncross-linked SU-8) in the middle of the formed regions and destroy the device's quality.
  - The device must be developed very soon after the PEB as leaving them too long (eg. Overnight) will serious degrade device resolution.
- Inspection (QC): With formed devices on a wafer, they can be inspected to determine the quality of formed structures. Notes are made about any point defects in any of the optical structures or where a complete and conforming seal will be difficult and a decision can be made whether to continue with fabrication or to scrap the device.

#### 3.1.3.2 PDMS Cover Slip Fabrication

PDMS cover slips must be prepared separately and in parallel with the SU-8 devices. These cover slips must be formed and have holes punched in them prior to bonding to the SU-8 devices. Figure 3-3 shows a flow chart of the relatively short and simple process to prepare the cover slips. The most important step in this process is the inspection step as the quality of the punched holes can affect the bonding and thus, the sealing of the devices. Work was adapted from preliminary work done with T. Kowpak.[116,117,118]

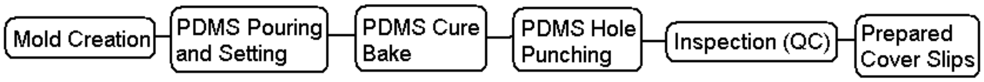

**Figure 3-3: Flow chart of the PDMS cover slip fabrication process.**

Steps to prepare the PDMS coves slips are described below.

- Mold Creation: Suitably sized cover slips are created via a mold. The mold should consist of a very clean and flat surface that will insure a bonding surface that is clean and free from defects. Molds can be reused but should be cleaned before each use.
- PDMS Pouring and Setting: PDMS is mixed from the suitable kit in a ratio of 10:1 for monomer and curing agent solutions. Once mixed the solution is poured into the mold and left to set for 24 hours. Enough mixture should be poured into the mold to form a layer ~2-5 mm thick. This ensures enough material exists to form a press-seal on the pins that are inserted later in fabrication.
- PDMS Cure Bake: After sitting, the mold containing the PDMS is placed into an oven and baked at $110^{O}$C for 1 hour. The mold is promptly removed and, when cool, the cover slip can be removed by carefully cutting around the mold's edge and carefully peeling from the surface of the mold.
- PDMS Hole Punching: Cover slips are placed onto a dummy device. This dummy device is created via the procedure outlined in section 3.1.3.1 except with a thicker layer and on a silicon substrate. A pre-drilled glass cover plate - drilled with holes matching the reservoir placement on the device - is aligned overtop of the reservoirs as viewed through the PDMS cover slip. Once aligned, holes are carefully punched through holes in the glass plate over channel reservoirs. Care must be taken to ensure that material is completely removed from the punched hole as any particles or 'flakes' can drop into the reservoir and become clogs later when fluid connections are made.
- Inspection (QC): With punched cover slips, the PDMS can be inspected to ensure a clean and defect free surface with cleanly punched holes.

### 3.1.3.3 Device Dicing

Dicing the devices is performed solely to provide access to the waveguides for optical coupling. As such, it is important to cut as close to the facet as possible to allow butt-coupling without destroying the fine quality of the photolithographically formed the facet surface. As the dicing is performed outside of a clean room an encapsulation procedure was developed to protect the SU-8 layer from damage and contamination. Washing away this encapsulant washes away any contamination picked up while outside of the clean room and during the dicing procedure. A process flow is shown in Figure 3-4 while a picture depicting where to cut is shown in Figure 3-5.

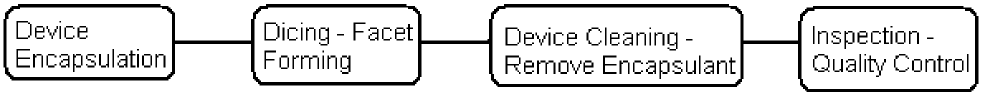

**Figure 3-4: Flow chart of the steps necessary to dice the device for waveguide facet formation.**

Steps describing the dicing procedure are as follows:

- <u>Device Encapsulation</u>: To protect the devices from debris during the dicing of the wafer, the wafer is encapsulated with a sacrificial layer that will prevent debris from contacting the SU-8 devices. Shipley Photoresist 1813 is applied to the entire surface of the device and spun at 250rpm for 20 seconds. The wafer is then immediately placed onto a hotplate set at 95$^{O}$C for 5 minutes.
- <u>Dicing - Facet Forming</u>: Devices are diced using the precision dicing saw mentioned in 3.1.2. Cuts are made as close to the formed waveguide facets as possible without touching them. This ensures a facet smoothness defined by the photolithography procedure. Dicing instruction details with figures illustrating the cut locations are found in Figure 3-5 below.
- <u>Device Cleaning – Remove Encapsulant</u>: Devices have the encapsulant removed by placing them under a stream of acetone. Debris is washed off with the photoresist. Do not submerge the devices in acetone as it will cause more cracking of the SU-8 layer. Once all photoresist is removed rinse the devices in developer and then with IPA. Dry the device under a nitrogen stream. Further clean devices by placing under a stream of highly filtered de-ionized water. Rub gently with a gloved finger in order to dislodge any further material. Dry under a nitrogen stream.
- <u>Inspection (QC)</u>: Devices can be inspected again to ensure that waveguide facets are clean, intact, and that the devices are clean of debris. Any issues that may affect device quality can be address or the device can be scrapped at this point.

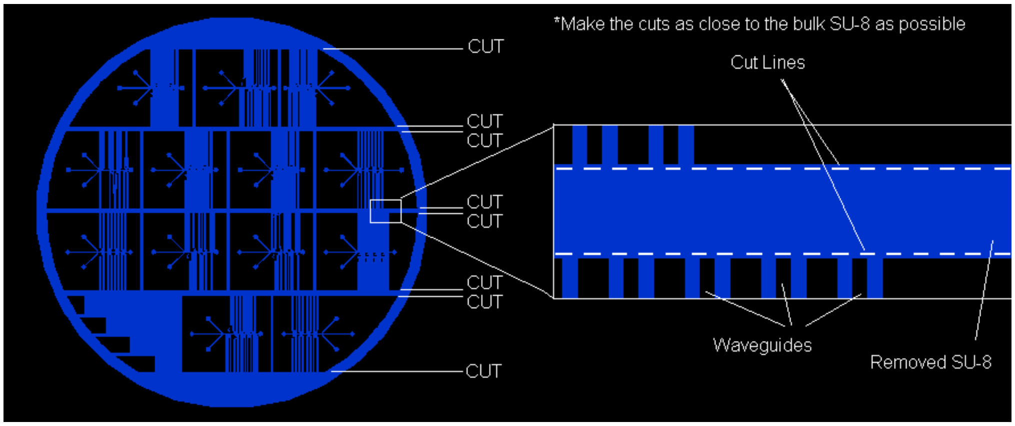

**Figure 3-5: Picture describing on the photomask exactly where the dicing is to take place.**

### 3.1.3.4 Device Bonding with PDMS

A flow chart of the bonding procedure is shown in Figure 3-6. Bonding of the devices originally was performed with an APTMS coated surface of oxygen plasma activated PDMS developed by Thomas Kowpak.[116,117,118] Although a suitable method for bonding microfluidic devices, a simpler procedure for achieving the exact same bonding was developed by Zhiyi Zhang and tested on numerous devices – including those described in this work.[119] The bonding is achieved by aminizing the silanol groups on the PDMS surface via a nitrogen plasma. These amine groups can then react with the residual epoxy groups on the SU-8 surface. This process is shown schematically in Figure 3-7a) while the details of the chemical reaction are shown in Figure 3-7b).

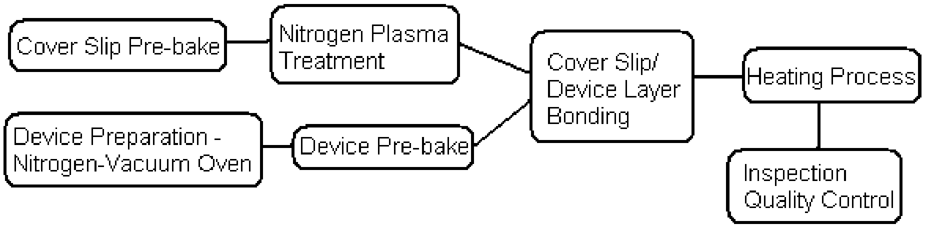

**Figure 3-6: Flow chart showing the steps necessary to bond the SU-8 device to the PDMS cover slip.**

Steps to complete the bonding are described below. Note: the next two steps must be performed in parallel with the two steps following them as the timing of the final steps of the bonding procedure depends on the components.

- Cover Slip Pre-bake: PDMS cover slips are placed in an oven and baked at 150 $^{O}$C for 24 hours. The devices must **not** be more than 30 minutes removed from the heat source before the next step.
- Nitrogen Plasma Treatment: The baked cover slip is put into the plasma bonder and the chamber is closed. Air is removed from the chamber and flooded with the very pure (>99.9995%) nitrogen. This purge and flood step is repeated ten times to ensure a very pure nitrogen atmosphere inside the chamber. Purge steps should achieve pressures of 150mTorr at first, with the final few purges reaching pressures of 30-50mTorr. After ten purging steps, the pressure within the chamber is set at 200 mTorr and the bonder is turned to the 'high' setting. The plasma treatment is left to run for four minutes. After four minutes the device is removed and brought to the prepared SU-8 device.

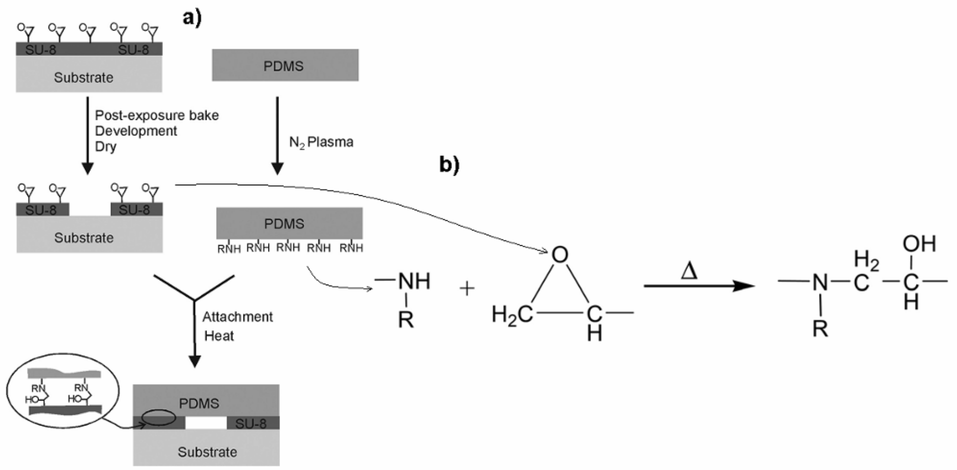

**Figure 3-7: Diagram showing the chemical bonding procedure between the SU-8 and PDMS interface and the chemical reaction details. *Source*: Reprinted from reference 119.**

Again, the next two steps must be performed in parallel with the previous two steps to ensure proper timing for the bonding procedure.

- Device Preparation – Nitrogen/Vacuum Oven: Cleaned SU-8 devices are put in the nitrogen/vacuum oven. This maintains a negative pressure with a constant supply of nitrogen entering the chamber. The devices must remain in this environment for 21 hours.
- Device Pre-bake: Heat is then applied to the devices for 5 hours. The temperature is set at 65$^{O}$C. After 5 hours, devices are removed and await a PDMS cover slip. Devices are stable for a couple hours after removal from the nitrogen vacuum oven.
- Cover Slip/Device Layer Bonding: Plasma treated PDMS cover slips are immediately brought into contact with the SU-8 devices. Care must be

taken to properly align punched holes with the reservoirs on the devices. Contact between the PDMS and SU-8 can be made, broken, and reapplied several times without detriment to the bonding. Application of PDMS to SU-8 should be done within 2 minutes of the PDMS plasma treatment otherwise the activated amine groups on the PDMS surface are passivated and bonding is no longer possible.

- Heating Process: Once satisfactory alignment and contact are made, devices are put into an oven at $100^{O}$C to activate and drive the bond. Pressure may be applied to the device to force a conforming contact between the PDMS and SU-8.
- Inspection (QC): The sealed devices can be inspected to ensure that there is a complete and conforming contact across the entire area of the device.

### 3.1.3.5 Device Packaging – Fluidic Connection

Due to the tiny size of the channel and the surface tension of the liquids in the channel, the sealing of the devices needs to be able to withstand very large fluidic pressures. Simple press-punch sealing can handle large pressures but was found to be susceptible to fracturing if there were any small tears formed during the punching process. A new method to seal the devices was subsequently developed in conjunction with C. Mu that would handle large pressures.[§,120] Figure 3-8 show a flow chart of the steps necessary to complete the interconnection method.

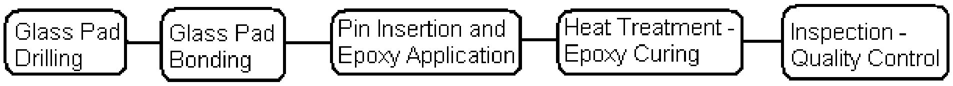

**Figure 3-8: Flow chart showing the process steps to form the fluidic interconnects and complete the device packaging process.**

The packaging procedure steps are preformed as follows:

- Glass pad drilling: Glass pads are drilled with holes precisely placed so that they align with the punched holes in the PDMS and the reservoirs on the SU-8 devices. The diameter of the hole is large enough to accept a 22-guage pin.
- Glass Pad Bonding: Glass pads with drilled holes are bonded to the top surface of the PDMS of the sealed device via an oxygen plasma treatment.

---

[§] My contribution consisted of taking the developed bonding method and expanding it to handle multiple inputs in a single glass pad to allow device integrated to be scaled up. Many devices were created and demonstrated that the alignment with multiple inputs is not an issue. Demonstration of a functioning device was also reported.

Glass pads and PDMS are exposed to an oxygen plasma for two minutes under a pressure of 150mTorr. Within one minute of the conclusion of the plasma treatment, the pads and PDMS are forced into contact to ensure the holes in the glass pad are aligned with the punched holes. Metal pins may be inserted into the punched holes prior to the device entering the plasma bonder to guide the placement of the glass pads on the device and ensure exact alignment. Devices are then place in an oven at $100^{O}$C for one hour to drive the bonding. Pressure can be applied to force a complete and conforming contact.

- <u>Pin Insertion and Epoxy Application</u>: Metal 22 guage blunt pins are inserted into the punched holes. Care must be taken to ensure that no debris is pushed into the SU-8 reservoir during pin insertion. Devices are then placed in an oven at $120^{O}$C and left to heat for 30 minutes. Epoxy is applied to the hot pins - just a tiny drop will suffice - and is allowed to run down the pin to fill the void between PDSM, glass hole, and pin.
- <u>Heat Treatment – Epoxy Curing</u>: Devices are left in the oven at $110^{O}$C for one hour to react the epoxy.

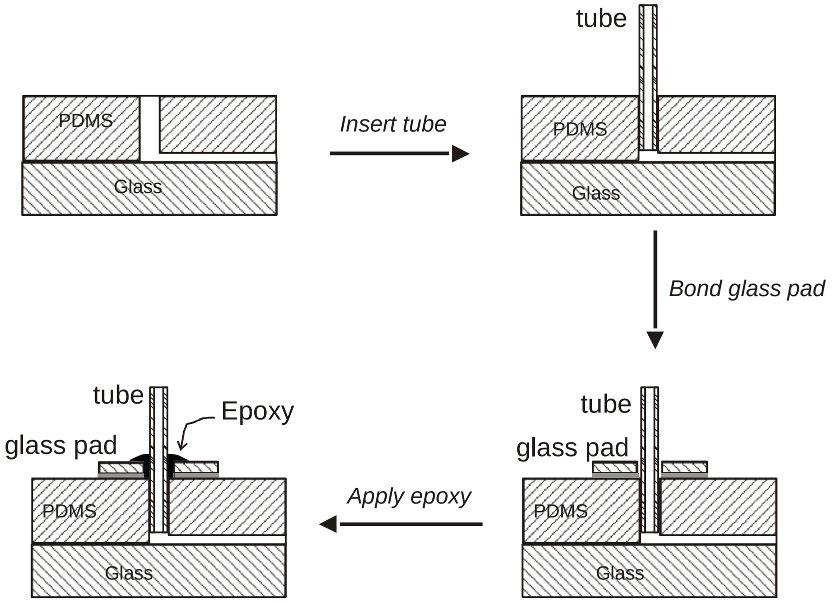

**Figure 3-9: Interconnection method developed that increased the bonding area to increase fluidic pressure capabilities. *Source*: Reprinted from reference 120.**

### 3.1.3.6 Fabrication Flow Chart

The entire fabrication process can is summed up below in Figure 3-10 as a detailed flow chart showing each step necessary to fabricate the device and the major segmentations and the steps involved with them.

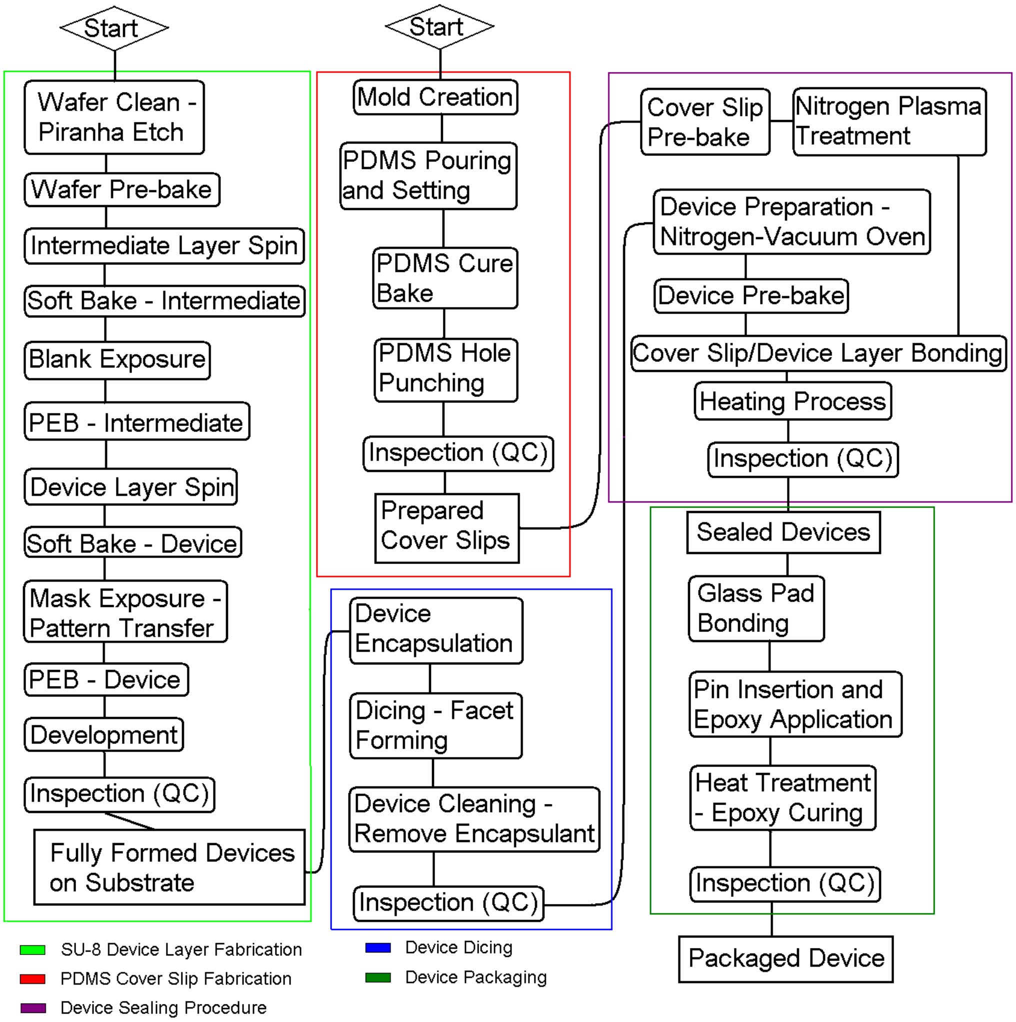

**Figure 3-10: Flow chart of the fabrication process showing the five main segments of fabrication and each step necessary within that segment.**

## 3.2 Testing

To validate the performance of the created designs, the following sections describe the apparatus and materials used to do such testing and generate acceptable data. Two types of testing had to be performed outside of the general qualitative quality control inspection of devices. The first procedure was taking an image of the beam in the device through the excitation of a fluorescent dye in the channel. This image was then analyzed to determine the beam properties and conclusions about the formed lens system and designs could then be made based on the analysis. The second testing procedure was a standard bead counting test used in standard conventional cytometric machine calibration. Microbeads – blank and fluorescent – were flown through the microchannels and gave off a specific optical signature based on the interaction with the formed beam in the channel. Analysis of device performance allowed comparisons of device designs. Testing procedures have been briefly described in publications produced from this work,[91,98,118,121,122,123,124] but are presented in detail here.

### 3.2.1 Materials

To produce an beam in the channel that is capable of having its image captured, the beam's wavelength is converted using fluorescent dye from Exciton Inc. This is a high efficiency laser dye - Nile Blue 690 Perchlorate that has an excitation max of 630 nm and an emission max of 660 nm. The dye, normally in a solid form, is dissolved in ethanol at a concentration of 0.1 Mol.

Tests to perform a cytometric counting application used microspheres as the interrogated specimens to provide a uniform source to quantify the performance of the device. The fluorescent beads were purchased from Invitrogen. Two different bead sizes were purchased in order to test the device's performance dependence on specimen size. AlignFlow 2.5µm diameter microspheres with a 630 nm excitation peak, and a 660 nm fluorescence peak were purchased. These beads had a manufacturer calibrated CV of 3%. The larger bead used was the AlignFlow Plus 6.0 µm diameter microspheres, also with a 630 nm excitation peak, and a 660 nm fluorescence peak. The manufacturer calibrated CV for these beads was 5%

To perform scatter detection tests, blank microspheres from Polyscience Inc. were purchased. Three different sizes were used to determine any dependence of the device's performance based on the bead size: Polybead 1µm diameter blank polystyrene spheres, with a calibrated size CV of 3%; Polybead 2µm diameter blank polystyrene spheres, with a calibrated size CV of 5%; and Polybead 5µm diameter blank polystyrene spheres, with a calibrated size CV of 8%. All bead suspensions were prepared by mixing the beads into filtered de-ionized (DI) water. DI water also doubled as a sheath fluid to hydrodynamically focus the sample bead suspension.

### 3.2.2 Equipment

The excitation sources for both the beam geometry imaging and bead interrogation and counting experiments was done with a 50 μm core diameter fibre pigtailed 250mW variable power 635 nm laser diode from Meshtel; model MFS-635-50M. Early prototyping work done to image formed beams was done with a 8mW HeNe laser from SpectraPhysics. This source was abandoned early once the Meshtel unit arrive for reasons discussed earlier in section 1.3.

To image the beam in the channel a camera and accompanying software were purchased from Lumenera Inc. The camera used was an Infinity 2-3C, a CCD-based sensor with 3.3 megapixels with colour capabilities. The software used to run the camera and perform some analysis was Lumenera Infinity Capture and Analyze, also from Lumenera Inc. For beam geometry imaging an objective lens from Mitutoyo, with a magnification of 10 and a long working distance was used in series with a Navitar 12x zoom lens. This configuration allowed flexible imaging of the beam.

Bead experiments used PMTs for photon detection purchased from Newport. Two separate units manufactured by Oriel were used – one for each wavelength – model 77343 for 635 nm detection and model 77341 for 660 nm detection - due to the different sensitivity range of each unit. The power supply to both units was provided from a dual PMT power supply from Newport capable of supplying up to 2000V. Coupling fibres to provide the excitation and collection of optics signals to the device was accomplished using multimodal fibres with a core of 50 μm. These fibres have large losses around the range of spectrum of interest, 635 nm, and therefore, very short length were used to minimize these loses. For accurate positioning of coupling fibres, miscellaneous 3- and 5 axis micro-positioning stages for precise optical alignment were used.

Signals obtained from the PMTs were converted to voltages using an I-V amplifier from Keithley, model 428. A DAQ-card from National Insturments, NI-USB-6211, that allowed up to 8 voltage-based analogue inputs was used to digitize the signals to be further analyzed. A computer with LabView software from National Insturments with a custom written program was used to further analyze signals and to perform the necessary criteria for peak detection.

To force beads into suspension, a Sonicator Mixer was used to put the mixture into a vigorous vortex. The solutions were prepared through the accurate measurement of bead and diluting solutions to create the desired concentrations via a MicroPipet from VWR International. These pipettes provided a range of volumes – from 0.5-10µm and 20- 200µm volumes.

Optical detection was aided through wavelength selection optics. Band pass filters to select only the light from the excitation band were purchased from Newport, model number 10BPF10-630, which had a 10 nm wide pass band centred on 630 nm to ensure the removal of any fluorescent or extraneous light. The band pass filter for light within the fluorescent band was purchased from Omega Optical, model number 660DF20, which had a 20 nm wide band pass with very sharp cut-on/cut-off edges of over OD6 in magnitude to ensure that excitation light is reduced by over six orders of magnitude.

### 3.2.3 Setup

Two very similar setups were used for both the beam imaging and bead detection experiments. For beam imaging, the device was set on a stage with the area of interest hanging in free-space. This allows for a clear window for imaging, one that is free from artefacts or noise. Furthermore, this configuration allows for a light to be placed above the device to enhance the contrast of the image. A mirror placed blow the device allows the deflected image to be collected by the objective and zoom lens to be focused on the camera sensor. A colour filter placed between the mirror and the objective to filter out all but the fluorescent light during beam imaging. The configuration of the camera connected to the large working distance objective and zoom lens allows an easy working distance and provides a range of magnifications and imaging options. Formed images on the camera sensor were digitized and sent to the computer to be analyzed. A 5-axis stage next to the device on the input side allowed for precise alignment of the excitation fibre. Precise alignment was accomplished through the control of the x, y, and z coordinate positions, plus the angular alignments from yaw and pitch control. Roll control was obviously not necessary due to symmetry of the fibre. A schematic of the beam imaging setup is shown in Figure 3-11a).

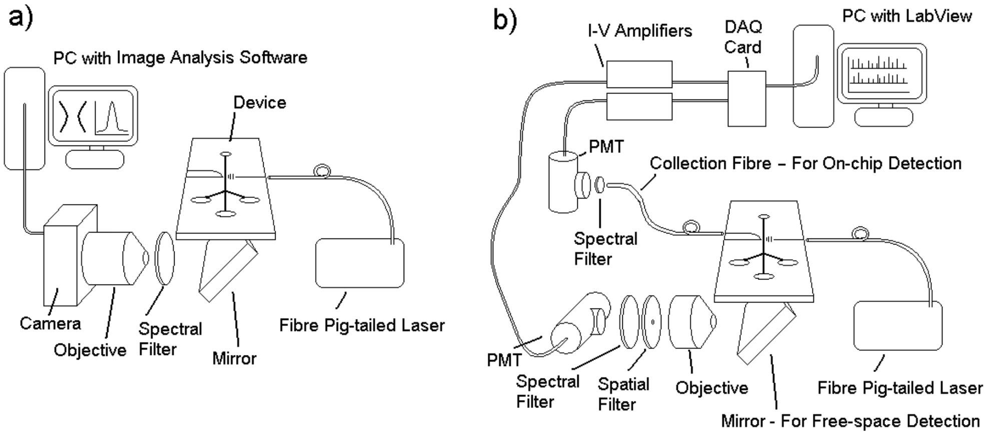

**Figure 3-11: Schematic showing the testing setups for a) beam image acquisition, and b) bead detection and collection; both showing input fibre coupling to the device. In b) the output collection fibre may be substituted for a fibre array block when necessary. *Source*: Reprinted from reference 123.**

For bead testing, the experimental setup again requires the device is set on the same stage with the area of interest hanging in free-space. This allows camera to be used again for alignment purposes. The source light is coupled into the device in the same manner as for the beam imaging process, from a carefully aligned fibre to the device’s edge. For experiments that require the free-space optical collection scheme, a mirror deflects light to the collection objective where the image is formed on the input of a PMT after passing through a colour filter (selected for either fluorescent or excitation band pass depending on fluorescent or scatter detection) and a spatial filter. For alignment purposes, the PMT could be replaced by the camera until satisfactory alignment of the waveguides are obtained. For experiments that test the device's on-chip collection waveguides, another 5-axis stage is placed near the output side of the device to allow for precise alignment of a single fibre - or a fibre array block if multiparameters are to be measured. Signals from the fibres are directed onto PMTs to amplify and convert the photons to an electrical signal. A schematic of the bead detection setup is shown in Figure 3-11b).

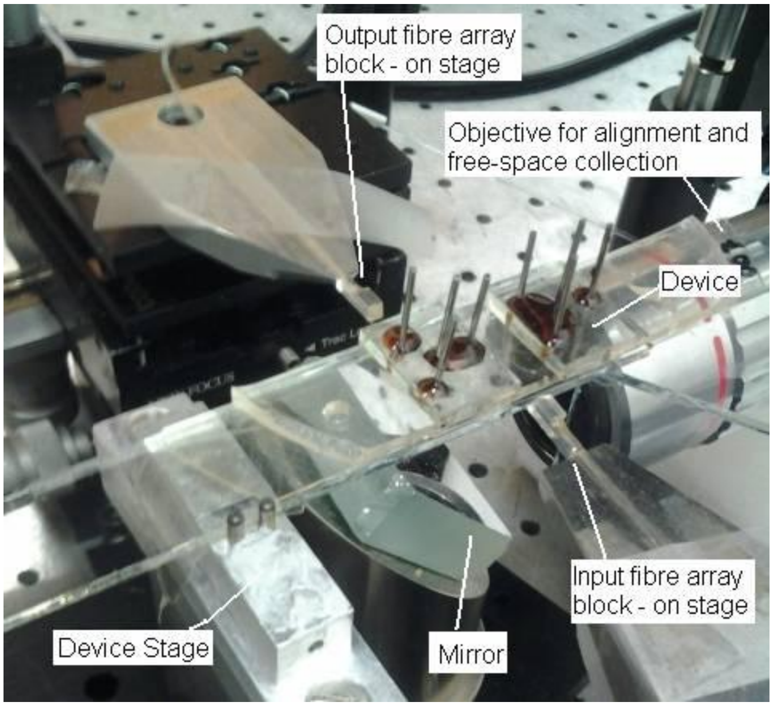

**Figure 3-12: Picture showing the testing setup for image acquisition. This setup will allow both imaging and bead setup via swapping the camera with a PMT at the end of the objective. *Source*: Reprinted from reference 123.**

A picture of the setup is shown in Figure 3-12. This clearly shows the input and output fibre array blocks and the stages they sit upon. It also shows the device above the deflection mirror and the objective lens directed at the mirror for image acquisition. At the end of the objective are the zoom lens and the mounting for the camera or the filter and PMT combo to allow switching between beam imaging and bead detection (free-space.)

## 3.2.4 Procedure

### 3.2.4.1 Beam Imaging

The entire procedure for capturing beam images for analysis is summarized in the flow chart in Figure 3-13. A detailed description follows.

- Device Seating: the device is placed on the stage and positioned so that the objective lens can be positioned to obtain an image from anywhere on the device – from the channel to the waveguide facets.
- Attach Fluidic Tubing: capillary tubes containing the fluorescent dye are slid overtop of the metal fluid interface tubes.
- Set Field of View – Beam Location: The position of the lens is adjusted and the magnification is altered so that enough of the channel and lens system are present. The focus is adjusted until the image is sharp. Adjust the exposure time, gain, and brightness setting in the camera capture software until good image contrast is obtained.
- Set Field of View – Input Waveguide Facet: Move the lens so that the field of view is on the end of the device and the waveguide facet is visible.
- Align Fibre: Adjust the position of the input fibre so that it is visibly aligned with the waveguide and almost touching the waveguide facet.
- LASER ON: Connect the laser fibre to the fibre being aligned. Turn on the laser. At this point, the reflection from the facet may be visible and the fibre can be repositioned to ensure better alignment.
- Set Field of View – Beam Location: Move the lens so that the field of view is back on the microchannel where the lens system injects the beam. One should be able to see scattering from the channel walls, lens system walls, and scattering from other defects in the device layer.
- Align Fibre – Fine Positioning: Using the scatter from the input light that is visible adjust the fibre so that the brightest amount of scatter is visible off the lens system walls and as little is observed in the channel.
- Inject Fluorescent Dye: Inject dye into the microchannel until it is filled.
- Align Fibre – Best Intensity: The beam should be visible in the channel. Adjust focus, gain, exposure time, and brightness until good contrast is obtained. Reposition the fibre until the brightest possible beam is visible in the channel. This is the best coupling obtained with the fibre. Moving

the fibre back and forth horizontally, one should be able to see the intensity of the beam shift back and forth from one extreme side of the beam to the other.

- Set Region of Interest: Adjust the magnification until the beam takes up a significant amount of the field of view without sacrificing clear contrast. Readjust focus and camera parameters for best contrast.
- Acquire image: Take several images to ensure that at least one is obtained where vibrations are minimized and not obscuring image clarity.

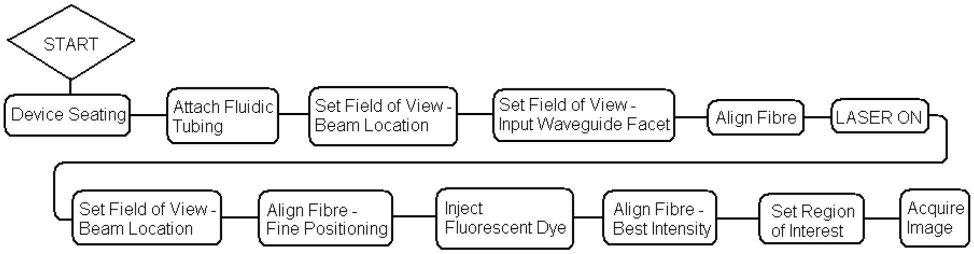

**Figure 3-13: Flow chart depicting the procedure to acquire beam shape images.**

### 3.2.4.2 Bead Detection

The experimental procedure to test the bead detection is a process that is very similar to the beam imaging process, but with a passivation step added before the device is seated and many steps added on instead of injecting a fluorescent dye. The passivation step changes the surface chemistry of the SU-8 and the PDMS in the channel. Normally, PDMS has $CH_3$ groups terminating the surface making it hydrophobic.[48] It was found that exposure to air plasma for 1 minute will oxidize the surface to Si-OH groups. This surface is hydrophilic and the surface will hold this surface chemistry as long as it is in contact with water.[48] The surface chemistry of SU-8 is normally hydrophobic as well, however, this can be changed via an oxygen plasma as well. Treatment for 2-8 minutes was found to effectively passivate the SU-8 to a hydrophilic nature – though this oxygen plasma treatment does have detrimental effects to the surface roughness after repeated treatments.[125]

This passivation step is necessary as hydrophobic channels can trap air, causing sticky side walls and create very strong back pressure forces due to capillary forces; sometimes they are strong enough to cause the bulk PDMS material to fracture.

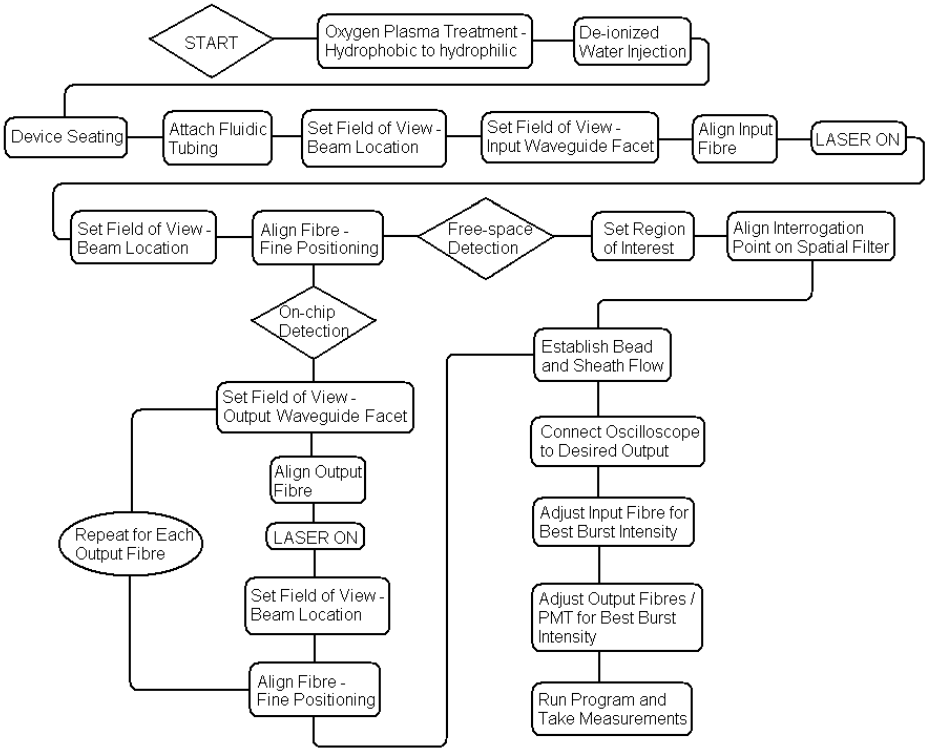

**Figure 3-14: Flow chart depicting the steps to perform the bead flow testing for both free-space and on-chip collection schemes.**

The entire procedure to perform the bead testing is given in the flow chart presented in Figure 3-14. Details of the procedure are described below.

- Oxygen Plasma Treatment – Hydrophobic to Hydrophilic: the device is placed inside the plasma bonder and the chamber is evacuated to a pressure of 150mTorr. The chamber is turned onto high and left for 6 minutes. The plasma bonder is switched off and the chamber is returned to atmospheric pressure and the device is removed from the chamber. This changes the surface of the PDMS and SU-8 to a hydrophilic state.
- De-Ionized Water Injection: To keep this hydrophilic state, the channel is filled with water. At the same time the device is inspected under a microscope to ensure there are no leaks that flood the voids forming the lens systems and thus will render the devices faulty.
- Device Seating: the device is placed on the stage and positioned so that the objective lens can be positioned to obtain an image from anywhere on the device – from the channel to the waveguide facet

- Attach Fluidic Tubing: capillary tubes containing the sample and sheath fluids are slid overtop of the metal fluid interface tubes. A tube to collect waste is also fitted. Just prior to attaching the sample tubing, the liquid should be thoroughly agitated via the sonicator to ensure good suspension of beads.
- Set Field of View – Beam Location: Adjust the position of the lens and adjust the magnification so that enough of the channel and lens system are present and adjust the focus until the image is sharp. Adjust the exposure time, gain, and brightness setting in the camera capture software until good image contrast is obtained.
- Set Field of View – Input Waveguide Facet: Move the lens so that the field of view is on the end of the device and the waveguide facet is visible
- Align Fibre: Adjust the position of the input fibre so that it is visibly aligned with the waveguide and almost touching the waveguide facet.
- LASER ON: Connect the laser fibre to the fibre being aligned. Turn on the laser. At this point, the reflection from the facet may be visible and the fibre can be repositioned to ensure better alignment.
- Set Field of View – Beam Location: Move the lens so that the field of view is back on the microchannel where the lens system injects the beam. One should be able to see scattering from the channel walls, lens system walls, and scattering from other defects in the device layer.
- Align Fibre – Fine Positioning: Using the scatter from the input light that is visible to adjust the fibre so that the brightest amount of scatter is visible off the lens system walls and as little is observed in the channel.

At this point, if the experiment is to test the on-chip collection of signal, then the next few steps should be performed. If no on-chip collection is being used, then the procedure skips over the next five steps to the free-space collection procedure.

- Set Field of View – Output Waveguide Facet: Move the lens so that the camera captures the output waveguide facet.
- Align Output Fibre: Adjust the position of the fibre (or array block) so that the fibre is visibly aligned with the waveguide facet.
- LASER ON: Connect the laser fibre to the fibre being aligned. Turn on the laser. At this point, the reflection from the facet may be visible and the fibre can be repositioned to ensure better alignment.
- Set Field of View – Beam Location: Move the lens so that the field of view is back on the microchannel where the lens system injects the beam.

One should be able to see scattering from the channel walls, lens system walls, and scattering from other defects in the device layer.

- Align Fibre – Fine Positioning: Using the scatter from the input light that is visible adjust the fibre so that the brightest amount of scatter is visible off the lens system walls and as little is observed in the channel.

Repeat the previous five steps for each fibre in the array block or for each parameter that is being measured for the on-chip collection scheme. One can reconnect the laser to each fibre to ensure that alignment is preserved for previous fibres.

If the experiment demands the collection of a parameter via a free-space collection scheme, the sequence picks up at the next step. Otherwise, the next two steps can be skipped.

- Set Region of Interest: Move the lens so that the camera captures the interrogation region. Remove the camera and place a white surface in the project light to form image.
- Align Interrogation Point on Spatial filter: Adjust the position of the PMT and spatial filter/bandpass filter so that the point of interrogation is incident on the hole in the spatial filter. The hole should be sufficiently small so as not to collect stray light from the channel was but large enough to not block any light from the specimens. Adjust focus to sharpest image contrast possible.
- Establish Bead and Sheath Flow: Turn on the syringe pumps so that the correct flow conditions are achieved. One may have to wait a few minutes. Do not push on syringe plungers manually, this creates large pressures that take a long time to dissipate in the device and will create incorrect flow conditions until the pressure does relax.
- Connect Oscilloscope to Desired Output: Connect the leads to the output from the I-V amplifier to monitor the signal quality. Flow conditions can be adjusted until bursts are visible or occur at the desired frequency.
- Adjust Input Fibre for Best Burst Intensity: Adjust the input beam fibre until the bursts are of maximum intensity and of best quality.
- Adjust Output Fibres for Best Burst Intensity: Adjust the output fibre (array) until the bursts are of maximum intensity and of best quality.
- Run Program and Collect Data: Start the LabView program and perform multiple runs. The oscilloscope can be used for real-time monitoring to

check quality of signals and flow within the channel (indirectly through the quality of the signal).

The testing setup contains many devices that can allow for tuning so as to fine the best quality signal. After much trial and error the basic settings that are typically used for all the equipment are: a PMT voltage of between -500 V and -900 V, and I-V amplifier gain of 1e4 to 1e7, and I-V amplifier filter of 30 μs to 100 μs, and a sampling rate in LabView of 50 μs. Slight deviations from these values can allow best signal quality to be achieved.

Signal detection and peak recognition in LabView software should be adjusted on a run by run basis. In LabView, the baseline signal should be set at the signal intensity observed where laser is on in the absence of bead flow. The threshold for a signal should be set to 2x the baseline value to ensure the minimum SNR.

Flow conditions during testing are kept low enough so that the flow rate of the sample solution could be kept constant at 20 μL/hr to ensure constant throughput for all tests. To alter the sample flow width the sheath flow was varied according the empirical relation in Equation 1-1.[52] The flow conditions used and the calculated sample stream widths are summed up in Table 3-1.

**Table 3-1: List of sample stream widths and the flow conditions necessary to achieve them.**

| Sample Stream Width (μm) | Sample Flow Rate (μL/hr) | Stream Flow Rate (μL/hr) |
|---|---|---|
| 1 | 20 | 646 |
| 2 | 20 | 313 |
| 3 | 20 | 202 |
| 5 | 20 | 113 |
| 6 | 20 | 91 |
| 10 | 20 | 46 |

When monitoring the signal quality, it should be noted that clogs will cause very messy bursts with very long burst durations of over 1 ms. If a messy burst is noted then the device should be backwashed by forcing a surge of sheath fluid. If that does not return flow to normal, the device should be removed and backwashed from the waste port. If that doesn't fix the clog, then the device is deemed scrap. A diminished signal intensity likely means misalignment of the input or output fibres and thus a quick adjustment of fibres will usually work even while the experiment is being run – though the LabVIEW program should be restarted to ensure uniform intensity throughout the entire run.

#### *3.2.4.2.1 Reproducibility*

Multiple devices are tested to ensure that the batch-to-batch processing is produces uniform devices that can function exactly the same. This is also done to eliminate the possibility that an individual result isn't an outlier and that the observed performance is indicative the actual designed devices. The same devices are also tested day-to-day and run back-to-back to ensure the repeatability of the testing procedure.

## *3.3 Data Analysis*

The method for analyzing the performance of the devices was created especially for this work. The criteria for specifying the beam geometry was developed based on predictions about ideal beam/bead interaction. Performance of devices had standards set for bead flow detection that are similar to that used in conventional cytometry and which are applicable for different POC and LOC geared assays. These methods have been disclosed in publications generated from this work,[91,98,118,121,122,123,124] however, details are provided here.

### 3.3.1 Beam Profiling

The first step in analyzing the beam geometry is to convert the acquired images to a 2D matrix of integer values based on pixel intensity. To facilitate this, a vision analysis software, ATS SmartVision from ATS Automation Inc., was used to run a simple procedure to convert a region of interest (ROI) in the direct vicinity of the beam to a matrix of integer values. The program is a sequence of tools that each perform a specific function that allow some flexibility based on user input. A C-code based script was written to integrate the tools together to perform the desired function. The code to operate the tools is shown in Appendix C A description of the code's function is given below.

First, a calibration factor is determined to give a pixel size that relates to a real-world distance. This value, a distance/pixel will allow accurate distances to be lifted from the analyzed image. To get the calibration factor, the script first locates the microchannel edges from the formed beam. This is a fairly tricky procedure due to the blurring of the edge from the long depth of field necessary to image through the entire depth of the channel. The script finds the length between channel edges in pixels. As the channel was designed to be 50 μm wide, therefore conversion factor is calculated from 50 μm / # of pixels between channel edges. Using this distance between channel walls, the script then sets a region of interest (ROI) around the beam with the extreme top and bottom of the ROI aligned with channel wall at the top and bottom of the beam. The width – the distance along the channel – of the tool is set to be approximately 50 μm wide. This is a suitable value for the width of the ROI as the beams are typically longer then they are wide. The script then moves through the image pixel-by-pixel and takes the pixel intensity, converts it to an integer value and then stores the value to a text file. Each text file the particular conversion factor attached to it. The intensity values ranged between 0 – for fully dark – and 255 – for fully saturated.

With the converted values the analysis is then performed row by row in the matrix. One row is considered a slice across the beam in the direction of bead flow. These slices are beam profiles and are therefore the change in intensity that a particle would experience as it traverses the beam. Obviously a specimen has a much larger size the a single slice so the entire intensity profile that a particle experiences would actually be a collection of these narrow slices. Each row should have an intensity profile of a specific formed shape that is approximately Gaussian in nature. A fit curve to this profile allows analysis of the profile to be assessed from the curve parameters.

A Gaussian curve is fit to the data through a simple reduced chi-squared analysis. This method tries to find a solution that will minimize the chi-squared parameter, and a sample of analyzed data is given in Figure 3-15. To do this analysis, an error for the measured pixel value is determined by taking the square root of the measured value. A guess of the Gaussian curve that would fit this specific row is determined through the basic parameters shown in Figure 3-15; the mean value (sigma), the standard deviation (mu), the amplitude (A), and the vertical offset or baseline (B). The difference between the value of the Gaussian fit value and the measured value is then recorded. This is called the residual. The chi-squared value is found by dividing the square of the residual by the square of the measured error. A sum of all these values is then recorded, as shown in Figure 3-15. The solver command is then executed in the spreadsheet and values for the fit Gaussian are changed until the sum of the chi-squared values are minimized. A sample of a single row with the fit Gaussian is shown in Figure 3-16. From this fit curve, the FWHM is calculated from the values of the standard deviation by multiplying it by 2.354. The FWHM is taken to be the width of the beam.

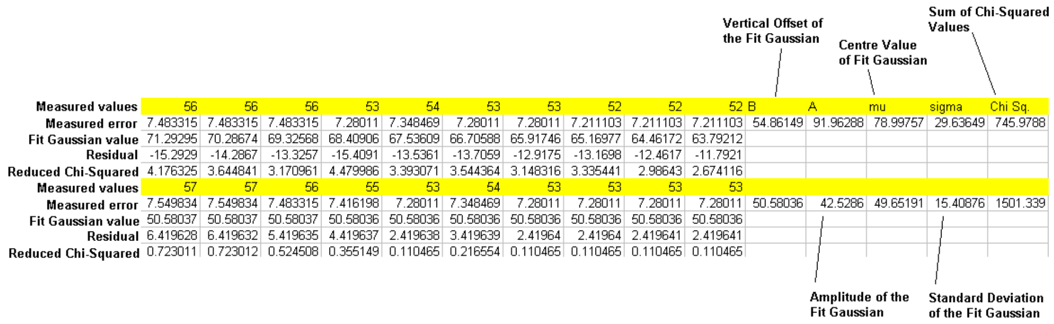

| | | | | | | | | | | | | | | | |
|---|---|---|---|---|---|---|---|---|---|---|---|---|---|---|---|
| **Measured values** | 56 | 56 | 56 | 53 | 54 | 53 | 53 | 52 | 52 | 52 | B | A | mu | sigma | Chi Sq. |
| **Measured error** | 7.483315 | 7.483315 | 7.483315 | 7.28011 | 7.348469 | 7.28011 | 7.28011 | 7.211103 | 7.211103 | 7.211103 | 54.86149 | 91.96288 | 78.99757 | 29.63649 | 745.9788 |
| **Fit Gaussian value** | 71.29295 | 70.28674 | 69.32568 | 68.40906 | 67.53609 | 66.70588 | 65.91746 | 65.16977 | 64.46172 | 63.79212 | | | | | |
| **Residual** | -15.2929 | -14.2867 | -13.3257 | -15.4091 | -13.5361 | -13.7059 | -12.9175 | -13.1698 | -12.4617 | -11.7921 | | | | | |
| **Reduced Chi-Squared** | 4.176325 | 3.644841 | 3.170961 | 4.479986 | 3.393071 | 3.544364 | 3.148316 | 3.335441 | 2.98643 | 2.674116 | | | | | |
| **Measured values** | 57 | 57 | 56 | 55 | 53 | 54 | 53 | 53 | 53 | 53 | | | | | |
| **Measured error** | 7.549834 | 7.549834 | 7.483315 | 7.416198 | 7.28011 | 7.348469 | 7.28011 | 7.28011 | 7.28011 | 7.28011 | 50.58036 | 42.5286 | 49.65191 | 15.40876 | 1501.339 |
| **Fit Gaussian value** | 50.58037 | 50.58037 | 50.58037 | 50.58036 | 50.58036 | 50.58036 | 50.58036 | 50.58036 | 50.58036 | 50.58036 | | | | | |
| **Residual** | 6.419628 | 6.419632 | 5.419635 | 4.419637 | 2.419638 | 3.419639 | 2.41964 | 2.41964 | 2.419641 | 2.419641 | | | | | |
| **Reduced Chi-Squared** | 0.723011 | 0.723012 | 0.524508 | 0.355149 | 0.110465 | 0.216554 | 0.110465 | 0.110465 | 0.110465 | 0.110465 | | | | | |

**Figure 3-15: Sample of the data to perform a Gaussian fit through a Chi-squared analysis.**

As discussed in section 2.1.2.5, the depth of focus determines the area of near uniform intensity in the direction perpendicular to flow in the plane of the chip. Again, this is the distance over which the bead could deviate in the stream flow and still receive same excitation. Section 2.1.2.5 noted that for this work the depth of focus would be defined as the distance over which the intensity of the beam varies by less than 5% of the maximum intensity. The maximum intensity is determined by using an averaging filter of a 3x3 pixel area to ensure that any outliers are removed.

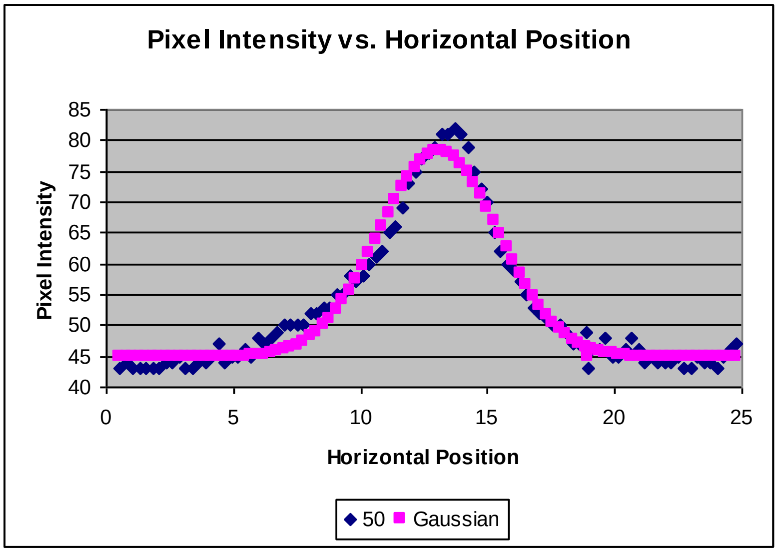

**Figure 3-16: Sample of a fit curve to a sample of a row of matrix data. the data shows a slice of the beam intensity in the direction of fluid flow.**

With the maximum intensity determined, horizontal slices of the matrix are then analyzed using a 3x1 wide filter again to average the profile and remove any outliers. The filter scans across the region and determines the positions in the beam perpendicular to fluid flow where intensity is above 95% of max. There should be two of these positions; where the beam intensity initially increases past this value on the injection side, and where the beam decreases past this value on the collection side. These two points determine the depth of focus. Within these two points, the matrix is further scanned to collect the two positions laterally in the flow where the beam crosses this 95% threshold. This is a sort of width that is defined by the 95% criteria. One last scan is performed through all the rows and collects the points on the beam that are defined by the FWHM. The code to perform this scan is given in 0

With points collected by the 95% definition, a contour plot of the beam can be overlaid with these points. An elliptically-shaped area will be traced out with the major axis coincident with the beam axis and the minor axis parallel to bead flow. An example of this is shown in Figure 3-17. The overlay in green shows the

FWHM of the beam while the near-uniform region defined by the 95% criteria is overlaid in red.

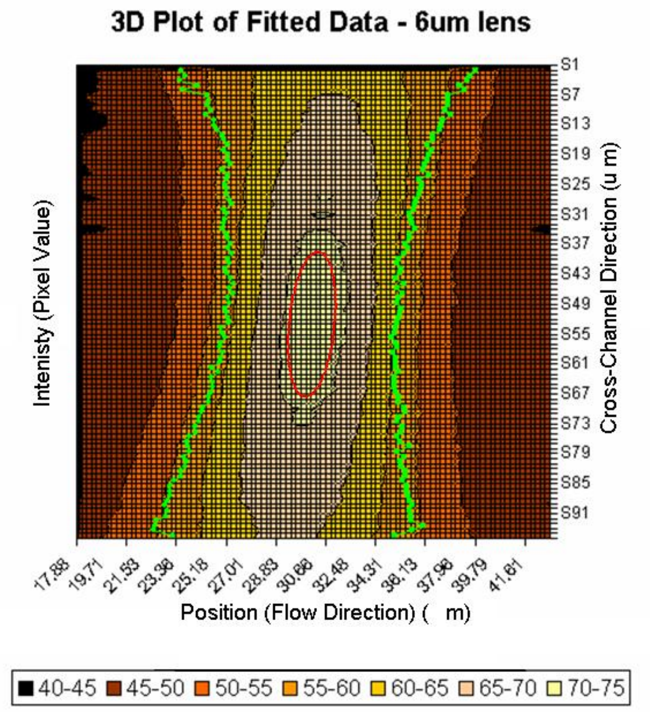

**Figure 3-17: Contour map of a formed beam shape with an overlay of the FWHM (green) and the area of near-uniform illumination (red).**

### 3.3.2 Bead Detection

Data logging is done by a custom LabVIEW program that determines if a peak occurred. A peak is deemed an event if the intensity of the peak is above a threshold level, and if the value from the previous peak has returned below the baseline. This program was originally written by Feiling Zhang for work by Canjun Mu, but was adapted to suit this work. A text file that logged all the raw data and the histogram points (without a time-stamp) were created at the conclusion of the program. Two channels could be logged with this program allowing for simultaneous two parameter detection.

This LabVIEW program had a bug that couldn't be fixed within the program. In some tests it was noticed that a secondary peak was detected; possibly due to slight misalignment or diffraction effects from the free-space optical setup - the spatial filter to be exact – or from saturation effects on the dye. This secondary peak artefact can be seen in the sample of raw data plotted in Figure 3-18a). Some peaks have the artefact; some do not, though the artefacts seem to occur with peaks of larger intensity. This would support the saturation explanation. A secondary peak artefact caused the LabVIEW program to detect two peaks - despite a direct violation of the peak detection criteria. Furthermore, data files did not contain any timestamp for any of the data points – raw data and histogram. Lastly, the histogram file only recorded the peak intensity; no log of the data points forming the peak was done completely eliminating any possible analysis by pulse shape.

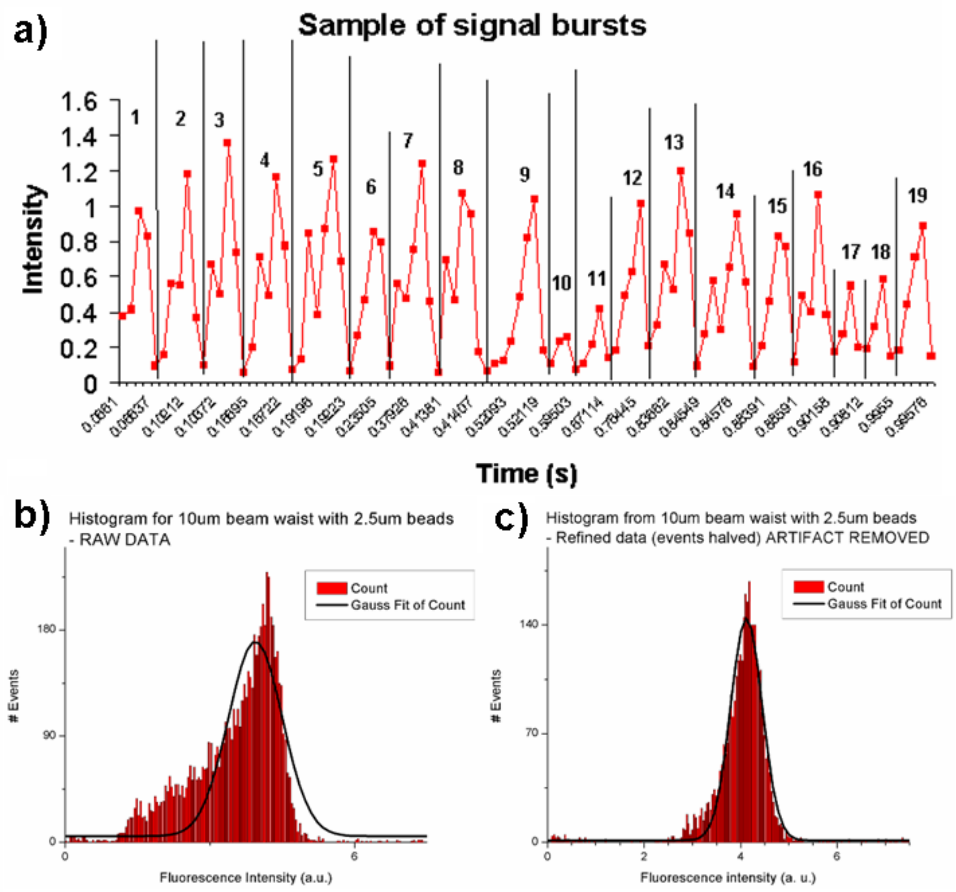

**Figure 3-18: The secondary peak artefact and the effect on detection and analysis. a) Plot of the raw data (with intermediate data removed) showing many pulses with and without the secondary peak artifact, b) histogram of a run without the secondary peaks removed, and c) the same histogram with the secondary peaks removed.**

The problem with secondary peak detection is easily shown in Figure 3-18b) and c). The histogram of the data inFigure 3-18b) has a large tail on the lower intensity side due to these smaller peaks. The fitted Gaussian is a poor fit and analysis of this Gaussian would indicate poor performance based on the large CV that would be calculated from the curve. Removal of these secondary peak artifacts shows the true performance of the device, as shown in Figure 3-18c). This histogram has the small bump on the lower intensty side removed and the fitted Gaussian is much better and would yield a much better CV more indicative of the actual device performance.

To remedy this, a C-code script was written to run after the fact to re-analyze the raw data files to remove the secondary peak artifact and collect all data points above threshold so that the full burst shape is recorded. Furthermore, the script would add a times stamp to all data. This script is shown in Appendix E Essentially, the script opens the data file and reads through the raw data point-by-point to detect peaks and record entire burst. The entire burst shape is needed to make conclusion about particle velocity and the area under the burst can be used instead of peak intensity to give a more reliable measurement.

With the processed and corrected files, the data was then analyzed in Origin data analysis software. The intensity values are binned and a histogram is formed. This histogram has a Gaussian curve fit to it using the in-house fitting tool in Origin. Using this fit Gaussian's parameters, the CV can be calculated from the centre value and the standard deviation and the SNR of the test can be calculated from the centre value and the baseline used in the test.

Double detections are events that will typically have twice the intensity of a single event. Therefore, there should be a small number of events on the histogram at approximately double the main histogram peak value. To log these events, the the centre value of the histogram is multiplied by 1.5 and any events above this value are logged as double (or multiple) detections.

When analyzing multiparamters, the data files should be combined as separate files are cumbersome to deal with. As the LabVIEW program was not written to do this, a custom script was written to perform this off-line after the data files had been obtained. This script is an expansion of the script to record the entire pulse shape given in Appendix E with the modification that the script opened two raw data files and ran through both data files simultaneously searching for peaks. This modified and greatly expanded script is given in Appendix F The script writes a new file that contains the pulses for both parameters; if one pulse is missing for one of the paramters, zeros are inserted. With the new files analysis can be performed in Origin where the histograms are analyzed and raw data can be correllated.

A custom script was written to provide a quick analysis tool to determine the reliability of the on-chip detection technique by comparing it to the simultaneous free-space collection data. This script is given in Appendix G and a sample of the printed data analysis is shown in Figure 3-19. This readout shows that the on-chip events coincided with the free-space events 99.4% of the time, while the free-space events were accompanied by on-chip events 89.6% of the time.

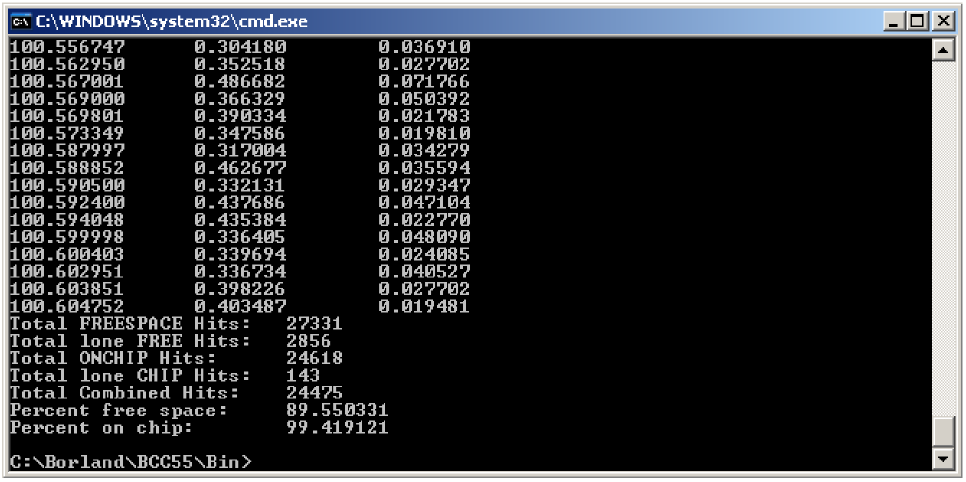

```
100.556747      0.304180        0.036910
100.562950      0.352518        0.027702
100.567001      0.486682        0.071766
100.569000      0.366329        0.050392
100.569801      0.390334        0.021783
100.573349      0.347586        0.019810
100.587997      0.317004        0.034279
100.588852      0.462677        0.035594
100.590500      0.332131        0.029347
100.592400      0.437686        0.047104
100.594048      0.435384        0.022770
100.599998      0.336405        0.048090
100.600403      0.339694        0.024085
100.602951      0.336734        0.040527
100.603851      0.398226        0.027702
100.604752      0.403487        0.019481
Total FREESPACE Hits:   27331
Total lone FREE Hits:   2856
Total ONCHIP Hits:      24618
Total lone CHIP Hits:   143
Total Combined Hits:    24475
Percent free space:     89.550331
Percent on chip:        99.419121

C:\Borland\BCC55\Bin>
```

**Figure 3-19: Screen shot of the readout of completed data analysis to determine the coincidence rate of the on-chip collection.**

# 4 Devices and Device Performance

Fabrication methods outlined in the previous chapter allowed feasible device fabrication. The procedure described is the result of fine-tuning to produce the best quality possible. Quality of devices was monitored and problems outlined in this chapter allowed changes to be made until the recipe allows fabrication of excellent quality devices. Testing high quality devices in a cytometric function is demonstrated and the performance is evaluated. Device designs are confirmed through quantifying uniformity of the formed ideal beam geometries to ensure that they accurately replicated the intended beam geometries. With confirmed beam geometry the operation of the devices in a flow cytometric function – both in fluorescence and scatter detections - is compared to other state of the art devices. Most of the results within this chapter have been disclosed in various publications (references 98, 118, 121, 122, 123, and 124) with extra data inserted to provide a more comprehensive presentation of the performance measured by devices.

## *4.1 Devices and Quality Control*

### 4.1.1 Device Quality Control

Proper device fabrication is essential to efficient and optimal performance, therefore, periodic inspections of the quality of the devices was done to ensure good device formation while proper changes were made to the fabrication process to correct for any poor performance or poor quality devices. Several fabrication issues were identified as solutions were developed for each.

#### 4.1.1.1 Intermediate Layer

As mentioned earlier in section 3.1.3.1 bonding SU-8 to glass is extremely difficult due to the large difference in the CTEs. The CTE for SU-8 is 52ppm/K while the Pyrex substrate has a CTE of 3.25ppm/K. After the PEB step the device is cooled from 95°C and this temperature change causes features to not adhere to the substrate. This delaminating of the device layer is clearly shown in Figure

4-1a) where the waveguides are warped due the broken bond to the substrate.[116] In extreme cases, this can result in the entire layer of SU-8 delaminating from the substrate even though the features are properly formed, as shown Figure 4-1b).[116] This problem was solved though that application of a very thin (~600nm) layer of SU-8 photoresist. As mentioned earlier, SU-8 3015 is a special blend that is specially designed for better adhesion to glass. What was found out from this work in conjunction with Thomas Kowpak's work was that this intermediate layer serves as a sacrificial layer that will ease the stresses generated between thermal expansion differences. The layer is kept thin enough that it would not affect the guided waves in the devices above. This work was published in reference 117.

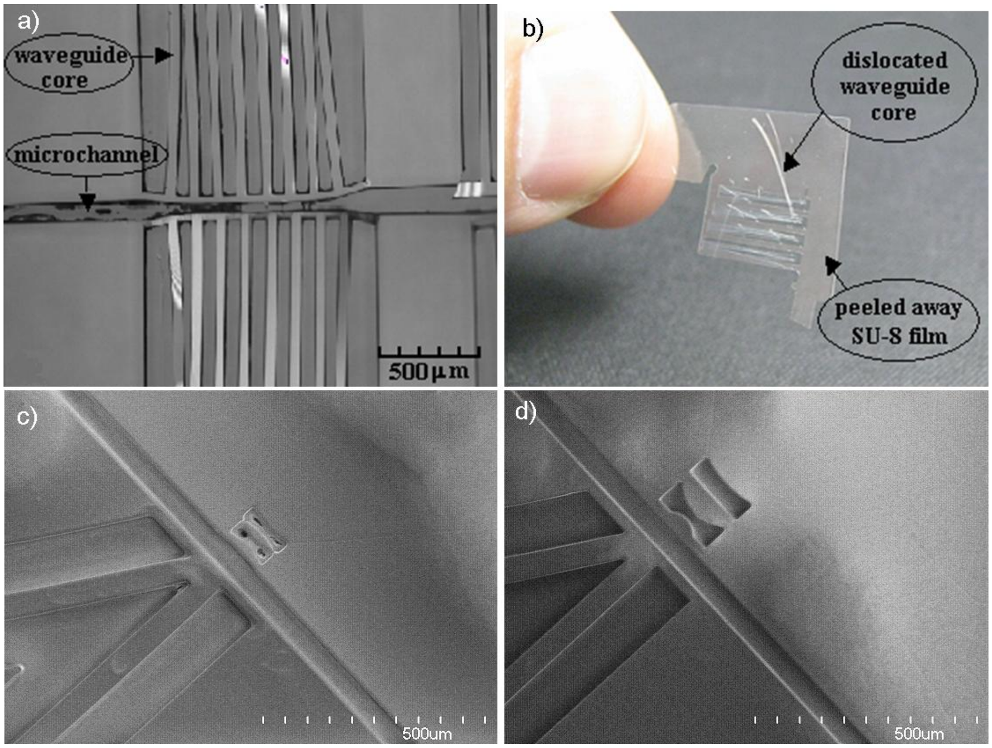

**Figure 4-1: The thin intermediate has a dramatic affect on the SU-8 bonding. a) A device with a the absence of the intermediate shows SU-8 structures that are not fixed to the substrate, b) the entire SU-8 layer can be easily peeled from the Pyrex substrate. c) A device with the intermediate layer shows good bonding with poor resolution, d) a device with proper bonding and resolution. *Source*: a) and b) reprinted from reference 116.**

With the addition of the intermediate layer, the proposed conditions for fabrication had to be changed. Initially, the procedure used followed the manufacturer's suggestions. Figure 4-1c) shows a device manufactured under the suppliers suggested instructions and the poor resolution and improper removal of material. There is obvious material still in the lens areas and the microchannel is partly filled with SU-8. Excess material was due to improper exposure conditions and had to b changed to reflect the extra surface that was now applied underneath. Also, there are extra chemistry considerations to remove all the material. The fabrication procedure was modified until satisfactory devices were manufactured and the recipe listed in section 3.1.3.1 resulted. Figure 4-1d) shows a device where the intermediate layer was deployed on the device with the tuned manufacturing conditions to allow proper formation of devices.

### 4.1.1.2 Device Resolution

Resolution of the devices is one of the most important defects to control in the manufacturing of devices. It involves the correct transfer of the designs to the devices and proper formation of all the features with few flaws that could affect performance. These include cracking, pattern transfer, and cleanliness.

#### *4.1.1.2.1 SU-8 Cracking*

Cracking of the SU-8 device layer is a persistent issue in the fabrication of devices; evidence of cracking can be seen in all SEM images presented in this work, and is especially prevalent at very corners of devices. Cracking is caused by one of two things. The first is a low exposure dose that does not properly form the Lewis acids necessary for polymerization throughout the entire layer, the result is a layer with a larger degree of polymerization at the surface – where light is preferentially formed. Developing of the layer will cause the inside under-polymerized material to swell and thus crack the surface. The second cause is from a high exposure dose that forms a large amount of Lewis acids. This creates a large degree of polymerization and large amounts of cracking in the baking step follows due to the large thermal expansion in the now rigid and brittle device layer. The solution to solve one issue leads to problems with the other. Raising the exposure dose to reduce cracking due to swelling causes more cracks to form due to layer brittleness. This work found that one can play with the PEB temperature to help control the cracking, however, this again presents a trade-off between the two issues causing cracking. The solution is to find a combination of exposure dose and PEB temperature that yields the lowest amount of cracking.

As mentioned earlier, the cracking generally starts only at the corners of the formed devices. Some formed devices have eliminated cracks that spontaneously appear in the middle of the bulk surface, however to eliminate cracks in future devices, designs should have rounded corners to eliminate this nucleus for crack formation.

##### *4.1.1.2.2 SU-8 Pattern Transfer Resolution*

Transferring the pattern to the device layer accurately is accomplished through careful exposure. As mentioned in section 3.1.3.1, the contact of the device layer with the mask if of paramount importance. During fabrication it was noticed that if the mask made good contact on one side, the resolution of devices was excellent, while the other side had a very poor pattern transfer resolution. Figure 4-2 show such a device where it is obvious that all material has not been removed. It is especially obvious as the intended pattern transfer is visible as a faint outline. This will be an obvious detriment to performance due to different lens curvature and poor surface quality. The poor pattern transfer is specifically due to the fact that poor contact causes light to diffract and expose areas that are supposed to remain dark and visa versa. This results in a partly exposed region that has low level of cross-linking and is therefore difficult to develop away completely. This explains the film of material left around device edges in Figure 4-2.

Using a 4 inch wafer, it is difficult to achieve complete conforming contact throughout the entire wafer. The bead of thicker amounts of SU-8 that accumulates at the layer edges during the spinning step make resolution poor in the middle as it creates a gap between mask and layer. The bead removal procedure mentioned in section 3.1.3.1 was developed to remove this thicker material to allow for better contact throughout the entire device. Even with the edge bead of thicker SU-8 removed it was found it necessary to place dark tape on the underside of the exposure machine in the middle of the device to force the middle to make contact. Furthermore, careful levelling of the substrate with respect to the mask was done to ensure conforming contact across the entire surface. Figure 4-3a) and b) show properly formed devices where good mask contact was established and the correct areas were exclusively exposed.

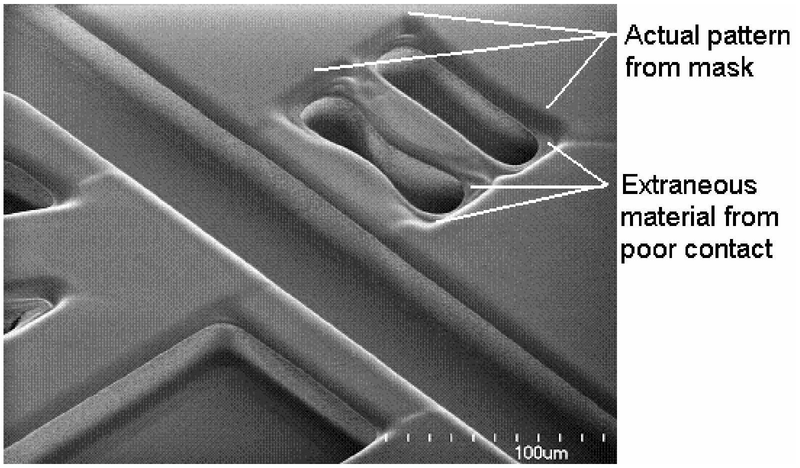

**Figure 4-2 SEM of a device with a 3.6 µm lens system showing poor resolution from poor device-photomask contact. The intended pattern can be seen as a 'film' outline of un-removed material.**

Figure 4-4 shows two devices that both include the new design that incorporates the notch to reject noise on the forward scatter waveguide, as discussed in section 2.2.6. The notch in Figure 4-4a) is poorly formed as residual material blocks most of the notch. It was noticed that in some cases it was a skin of material on the top of the notch; this would still have limited functionality. After tuning the fabrication procedure the resolution of the notch in Figure 4-4b) was drastically improve and is of excellent quality. A very well defined notch will allow very good removal of the paraxial light that is crucial to the proper performance of these designs. It should be noted that a 'perfect' notch is impossible as an infinitely sharp point is impossible to form, however, this notch is the smallest feature of all the designs in this work and is a fine example of the resolution abilities of the formed fabrication procedure.

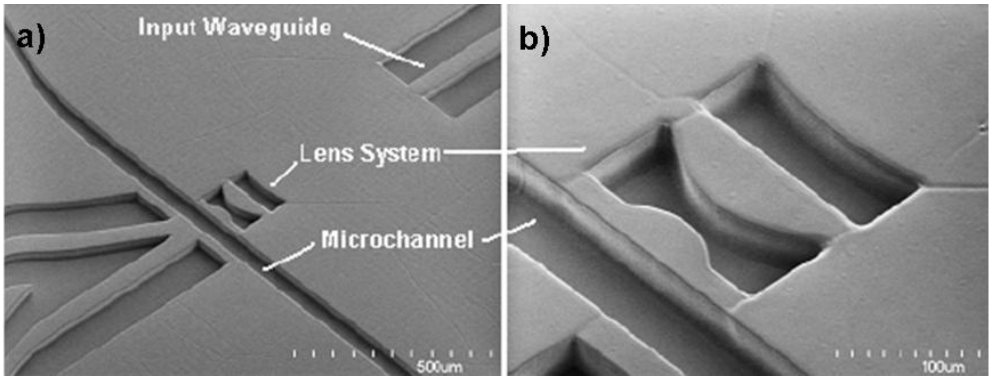

**Figure 4-3: SEM images showing a) device and b) high magnification of interrogation area where the side walls are smooth, voids are clear, and there is limited cracking. *Source*: Reprinted from reference 121.**[**]

The resolution discussed above focused on the quality of the surface edges formed during the exposure step of photolithography in the lens system areas. It is obvious that there is little room for error with the optical components in these designs. The affect of poor contact resolution on waveguide facets is less severe. As shown in Figure 4-5a), a waveguide of poor quality has obvious extraneous material at the corners of the waveguide and the sidewalls are not as vertical as is formed in an optimal fabrication. A higher magnification SEM image in Figure 4-5b) with a different viewing angle shows the poorly formed facet. This waveguide would still be useable; however, the coupling losses would be larger.

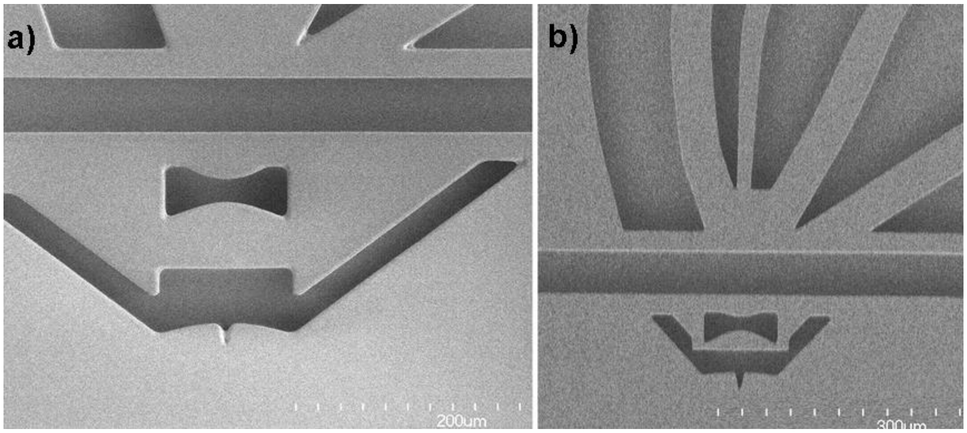

**Figure 4-4: The effect the pattern transfer resolution has: a) the notch is poorly resolved and thus filled with material, b) the notch's resolution is excellent as all material is removed.**

---

[**] This figure was from the author's work published in reference 121.

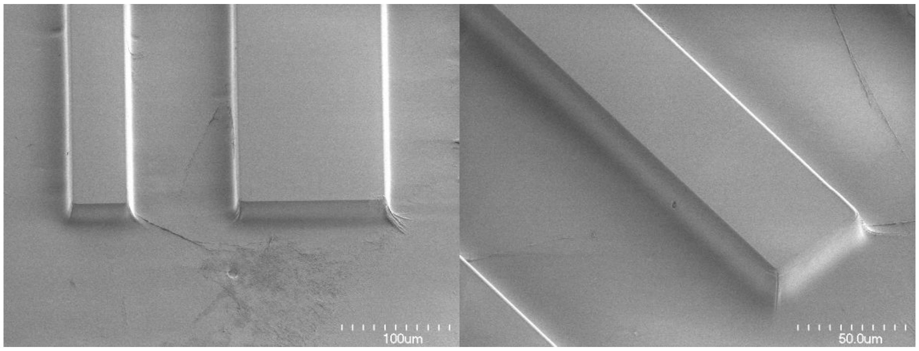

**Figure 4-5: a) SEM image of a poorly defined waveguide. b) High magnification SEM shows the poorly defined edges and non-vertical walls on the waveguide.**

### *4.1.1.2.3 Cleanliness*

The cleanliness of the devices is one of the hardest sources of defects to control. Contamination on a device is largely rather innocuous, however, particles in the device layer – if situated properly – can cause defects. Figure 4-6 shows a particle that just happened to coincide with the edge of a device. The particle causes an obvious rippling on the formed surface and would cause scattering of light and degrade the optical function of the device. This is an extremely rare occurrence if proper clean room procedures are followed.

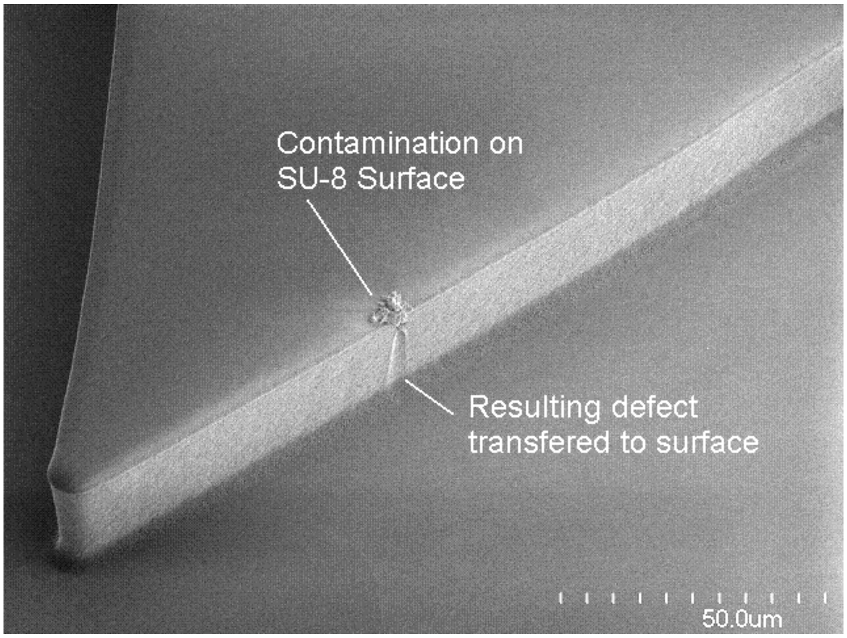

**Figure 4-6 SEM image showing a contamination particle and the effect it has on the transfer of the photomask to the SU-8.**

A more salient concern about contamination is effect it will have on the bond and subsequent sealing of the device and thus, problems with containing fluids. Such a device with a large amount of contamination is shown in Figure 4-7 with the obvious debris near the branched structure of the microchannel. None of these particles happen to lie on an optical feature, and thus the optical performance of the device would not suffer. However, when bonding the PDMS to the SU-8, this debris will prevent complete and conforming contact. Voids in the immediate proximity of the contamination will appear and the size of the void is proportional to the height. and more generally the size, of the particle. If the location of the contamination, and thus the void, are spatially coincident with the channel and a device structure, the void can overlap both features. This will allow a direct leak to ruin the performance optically and can also ruin hydrodynamic focusing within the channel.

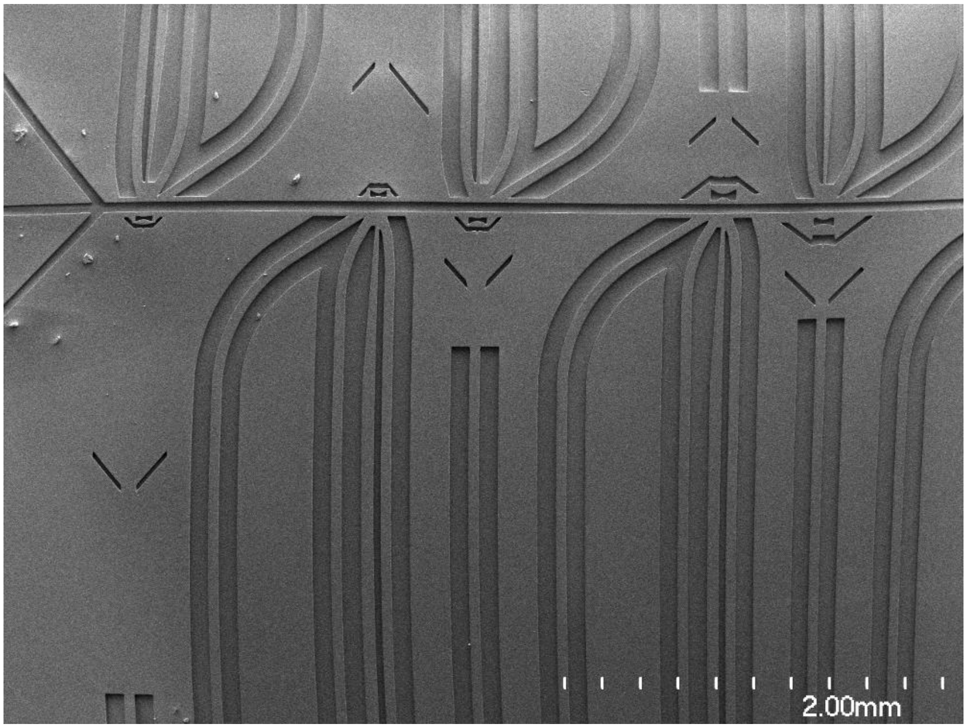

**Figure 4-7: Large contamination issue on the surface of the device in the upper left of the SEM image will cause leaking problems around the first device next to the branched channel.**

#### 4.1.1.3 SU-8/PDMS Bonding

Early devices produced incorporated an oxygen plasma bonding method developed by T. Kowpak.[116,117] This process involved coating an oxygen plasma activated PDMS surface with APTMS. This aminized the PDMS surface and allowed strong bonding with the residual epoxy groups on the SU-8 surface. The performance is summarized as Thomas' contribution to the author's publication in reference 118.

More recent devices switched to a nitrogen plasma bonding method developed by Z. Zhang et al.[119] As mentioned in section 3.1.3.4, this is a much simpler procedure and produces the same resulting bond as the previous method developed by Thomas Kowpak. This was briefly discussed previously in section 3.1.3.4 while the chemical bonding was shown in Figure 3-7. The results and performance from devices formed using this bonding method are summarized in the publication in reference 119. The authors contribution to this work showed excellent bonding and completely conforming seals despite complex device design and a very strong bonding as the bulk material fractures before the bond yields.

#### 4.1.1.4 Packaging

Early devices using press-fit seals allowed feasible devices to be fabricated, as shown in Figure 4-8a). The press-fit sealing method – although sufficient in some testing - was abandoned shortly after the first few batches of devices were fabricated as seals were found to be inconsistent and often could not hold a sufficiently high fluidic pressure common in these microfluidic devices. The seals were found to be prone to leaking and furthermore, slight defects in manufacturing – tears from the hole punching, for example – were found to easily fracture under modest fluid pressure and permanently ruin the seal and devices for further testing. Repeated insertion and removal of interconnection pins was found to also cause seals to rapidly fail and was therefore deemed a sealing method that was inconsistent with the requirement of a feasible device. The press-fit seals are visible in Figure 4-8a) as a simple hole punched in the centre of the thickened PDMS areas.

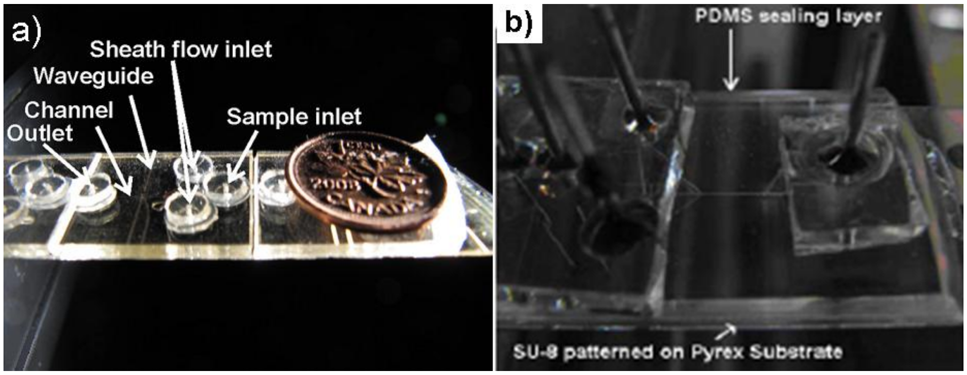

**Figure 4-8: a) Early device fabrication with PDMS glued on top to form a press seal. b) Picture of the fabricated device with strong interfluidic connection method. *Source*: a) Reprinted from reference 119[††] and b) reprinted from reference 118[‡‡].**

A new sealing method developed by C. Mu et al. – as outlined in section 3.1.3.5 - was applied to devices and found to allow fabrication of excellent quality devices and, through this work, was shown to be able to be expanded to a multiple port-per-pad format as shown in Figure 4-8b). Contrasted to the press-fit seal method, this method has metal pins permanently fixed to the device so that the only wear from repeated use occurred on the capillary tubing – a component that is cheap and easily replaced, sparing the devices from ruin.

### 4.1.2 Quality Devices

With the fabrication issues solved as discussed above, quality devices were regularly fabricated. Proper fabrication conditions yielded devices of excellent quality; Figure 4-9 shows several SEM images of a device that has a lens system to focus a multimodal input to a 10μm beam waist in the channel with perpendicular views, a) and a close-up in b), and 30º tilted angle view, c) and a close-up in d). Excellent resolution of the device's features and good transfer of designs from photomask to the device layer is evident as seen in Figure 4-9a). The complete removal of unexposed areas can be seen in Figure 4-9b). Clear,

---

[††] This figure represents the author's contribution to the published work in reference 120.
[‡‡] From the authors published work in reference 118.

smooth, and defect free side walls that allow for low scattering losses during optical function are evident, as shown in Figure 4-9c) and d).

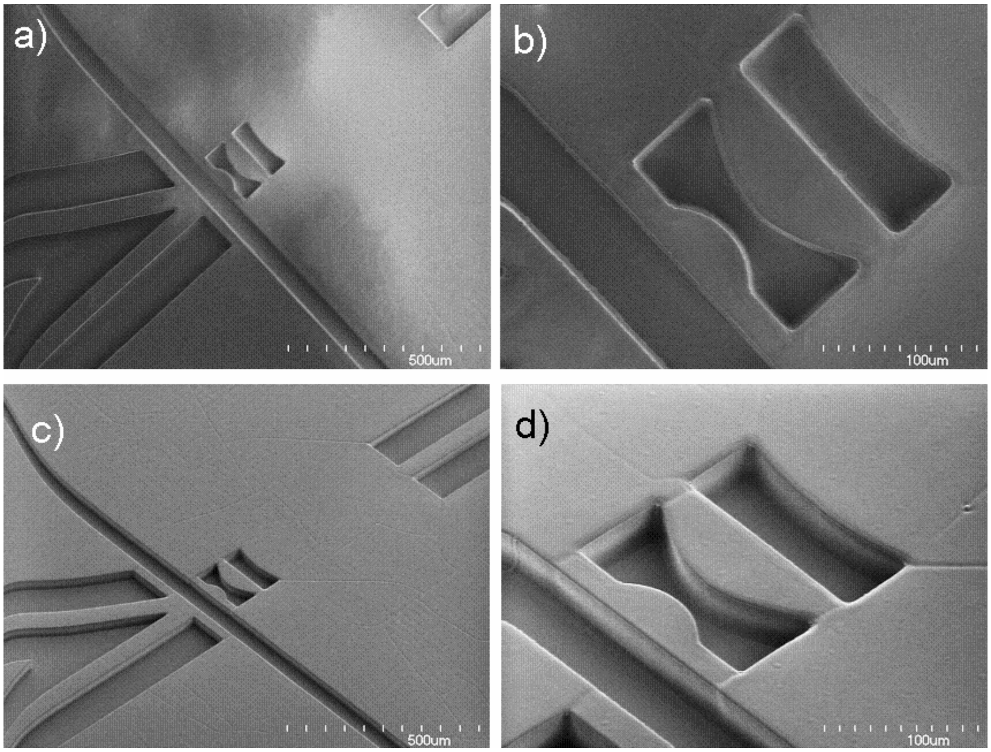

**Figure 4-9 SEM images of a device with a 10um lens system. a) normal view and b) close up of the lens system. c) 30 degree skewed angle and d) a close-up view of the lens system revealing surface quality.**

Waveguide facets were replicated very well and the excellent quality will allow relatively low propagation losses. The sidewall and facet quality are confirmed by the SEM image in Figure 4-10. Figure 4-10a) shows the waveguide next to some bulk material showing a clean cladding area on either side of the core, as well as excellent defined edges. The magnified SEM image of the waveguide end in Figure 4-10b) shows excellent facet resolution that is smooth and defect free. Again, the device has well defined vertical edges and excellent replication of the 50 μm designed width.

The optical coupling ability of the device is shown in shown in Figure 4-11. The waveguide is clearly visible through light that escapes along the length of the waveguide vial the leaky modes. A fair bit of excess light is evident at structures light the channel and the opposite end primarily due to the physical mismatch between the 50 μm core cylindrical fibre geometry and the 30 μm by 50 μm rectangular waveguide geometry. There is a very intense spot is the interrogation region indicating that much of the light propagates to the interrogation region. The brightness of this spot is provided by scattering from the lens surfaces and channel walls.

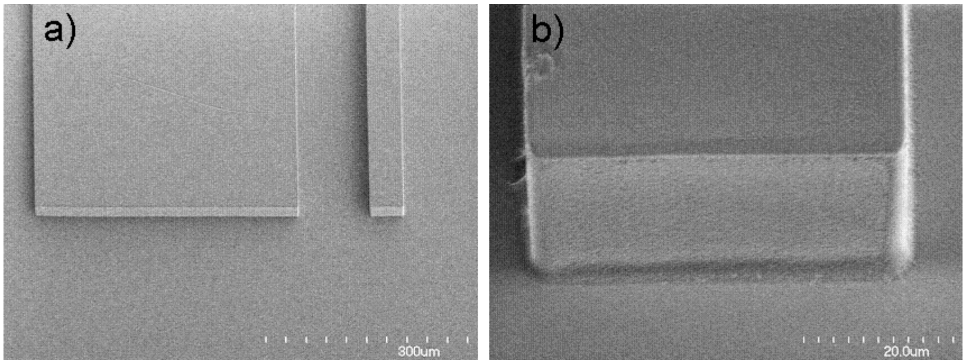

**Figure 4-10 a) SEM image of a waveguide facet and adjacent bulk material and b) a close-up of the waveguide facet showing excellent facet quality.**

Propagation losses were not measured for these devices, instead the well established and reported value of 1.3dB/cm @ 630nm was assumed.[44] The scattering that is visible along the fibre is due to leaky modes escaping from the uneven removal of protective polymer sheathing. Note that the amount of light that is coupled across the channel into the collection waveguide and the slightly less amount of light that is coupled into the angled collection waveguide. Also of note in this image are the bright defects and artifacts in the SU-8 and PDMS layer. The scattering from artifacts in the PDMS layer are because of light that is coupled into the top PDMS layer from the core fibre as it is larger than the 30 μm waveguide height. The scattering in SU-8 layer is because of light that is coupled into the bulk material from either the top PDMS layer or from leaky light that escaped from the waveguide. Most of the errant light along the channel is from stray light due to the mismatch of waveguide NA and lens NA as discussed will be discussed later in section 4.2.1.4.

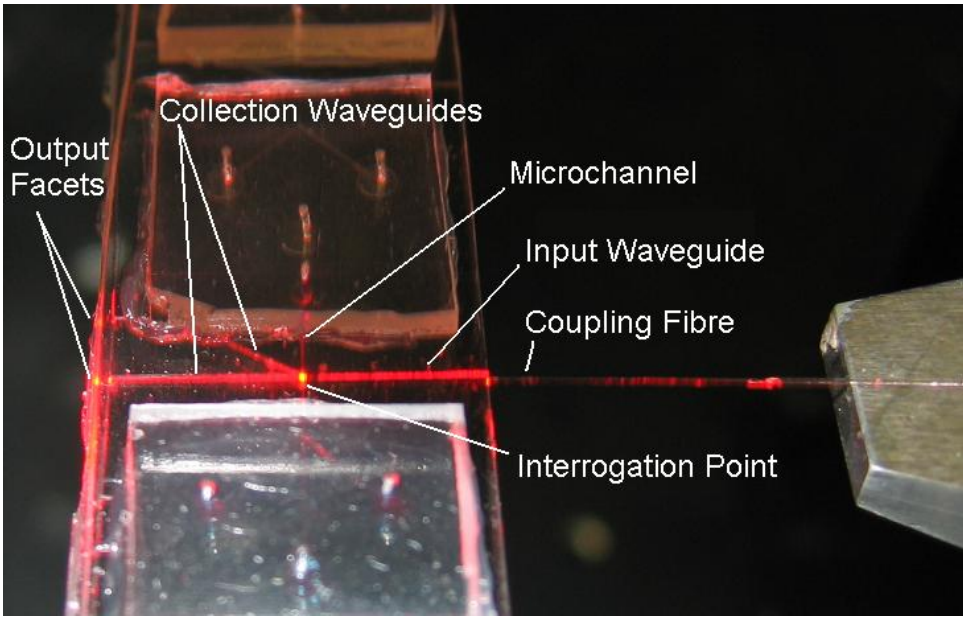

**Figure 4-11 Picture showing the coupling to the device. Note the amount of light that is cross-coupled into the straight output waveguide as opposed the angled waveguide.**

An image of the device near the interrogation region is shown in Figure 4-12a) showing quality of the formed structures and the conforming bond between the SU-8 and PDMS as evidenced by the lack of voids and bubbles where material has separated. Figure 4-12b) shows a picture of the detailed cross-section of the device shown in a) showing the excellent resolution, clean waveguide facet, voids that are completely removed of material, and a completely conforming bond between the SU-8 and PDMS – even in narrow regions such as the 50 µm wide waveguide. Given that care was taken during the fabrication process, the bonding between the PDMS and SU-8 was found to be completely conforming even in the narrow regions between the lens system and channel. This small surface area of bonding – visible in Figure 4-12a) - was found to be strong enough to hold together even when the channel was under sufficient fluidic pressure.

New designs attempted to contain a much higher density of devices. Figure 4-13a) shows the replication of many devices on a single substrate from the designs shown in Figure 2-49. No interference between devices with respect to fabrication was observed. The larger device density results in a higher yield as a single defect will still allow many functional devices per substrate. The good resolution was able to remove all unwanted material as evidence by the high magnification SEM image of a device with a 12µm lens system shown in Figure 4-13b).

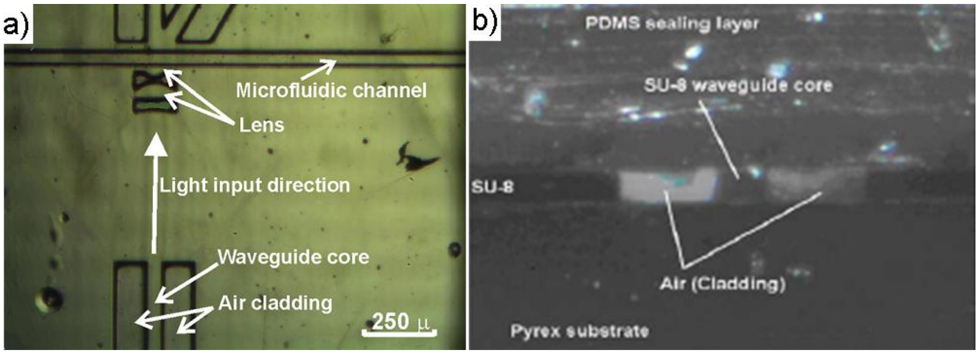

**Figure 4-12: a) image of the detailed area around the interrogation region. b) Image of the waveguide facet showing the layered structure and quality of the facet.**

The sealing of these devices was observed to be completely conforming over the entire surface of the wafer. The bonding was observed to hold the high fluidic pressure throughout the entire length of the channel, even along the sections that had a reduced wall width between the channel and the waveguide facets.

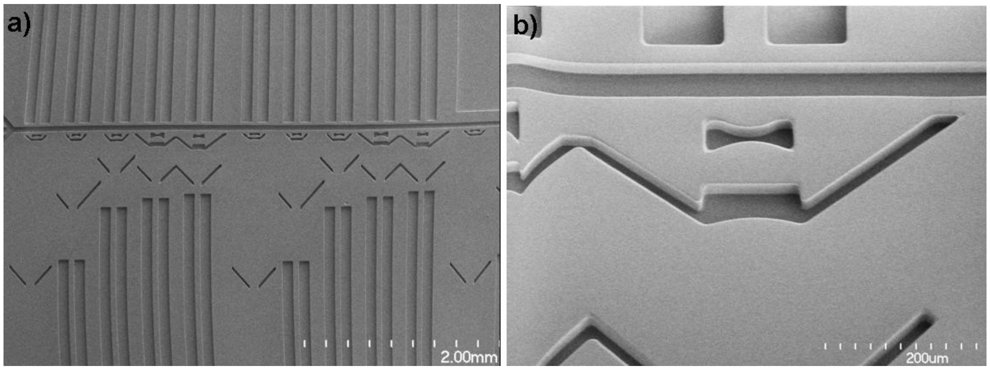

**Figure 4-13: SEM image of a device that forms many devices on a single microchannel. a) Shown are two sets of simple input, lens system, and straight collection waveguides for two sets of 1.5-, 3.6-, 6.0-, 10-, and 12µm lens systems. b) high magnification of a 12µm lens system.**

Fabrication of designs that incorporated the multiple collection waveguides with a single input of a normally incident lens system is shown in Figure 4-14a) from the single device design shown in Figure 2-50a). Again, each device has excellent resolution and the complete removal of material will allow low-loss operation of optical components. As shown by the high magnification SEM image in Figure 4-14b) there is no interference due to the close proximity of devices and the resolution is very good as it produces very sharp features. The sealing of the devices was observed to be sufficient and held pressures generated under normal operating conditions – even in the very narrow area between the channel and lens as observed in Figure 4-14b).

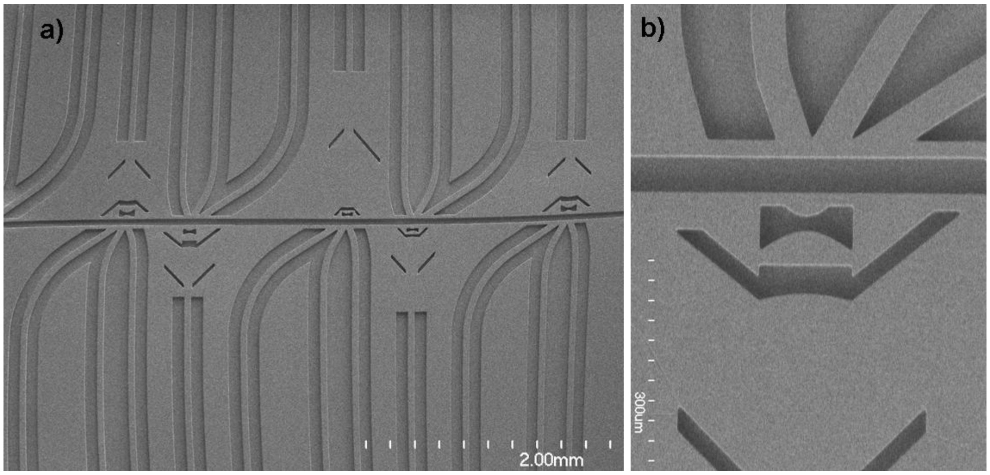

**Figure 4-14: a) SEM image of many devices each with a different lens system and multiple (3) collection waveguides. b) High magnification of a device with a 10µm lens system.**

Realization of a device designs with multiple collection waveguides and a focused angled input designs from Figure 2-50b) is shown in Figure 4-15a). This image shows just two devices of five that are formed along the length of the entire microchannel. Again, quality of the devices is excellent and sharp edges are formed and all material is removed, as evident in the high magnification SEM image in Figure 4-15b).

Device designs from Figure 2-51 where dual angled inputs from two different lens systems were fabrication and are shown in the SEM image from Figure 4-16. As discussed in section 2.2.4.5.1, the collection waveguides can provide a large angle (~90º) collection if the waveguide is opposite the channel from the corresponding input or a low angle collection (~20º) if the waveguide is on the same side of the channel as the corresponding input. These devices were easily fabricated and the proximity of devices did not interfere, and device material was easily removed from all areas. The bonding was observed to be sufficient to hold fluid in the channel even in the long narrow section along the channel where bonding surface is severely reduced.

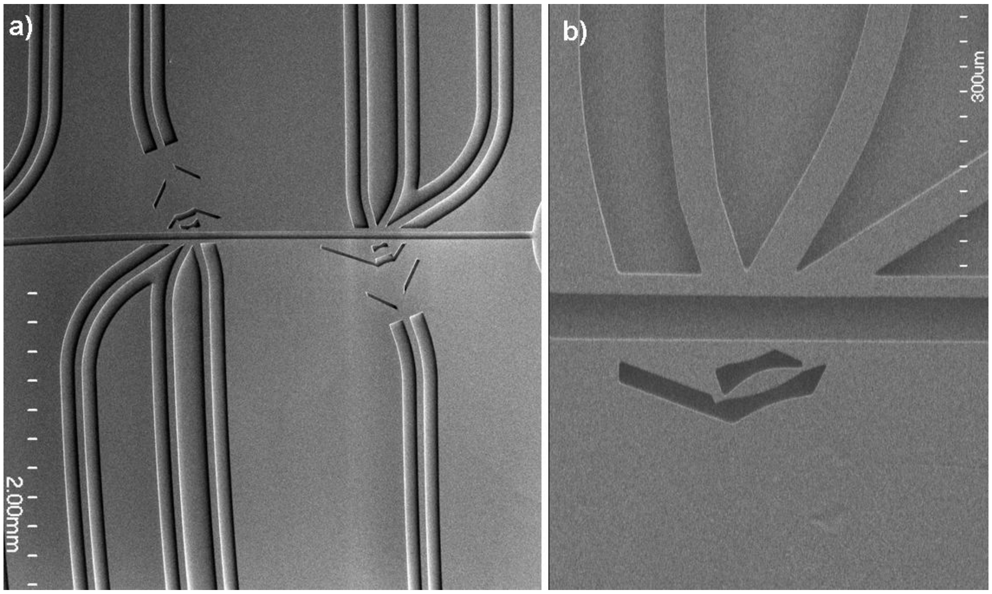

**Figure 4-15: a) SEM image of two (of 5) devices on a single microchannel with an angled input and multiiple collection waveguides. b) High magnification of a device that has a 1.5µm lens system.**

Forward scatter designs from Figure 2-52a) and b) – showing straight and angled inputs, respectively – are shown via the SEM images in Figure 4-17 and Figure 4-18, respectively. Figure 4-17a) shows the 10.0 µm lens system with the modified notch system and the narrow waveguide that will limit the collection of light. A modified 3.6µm lens system with the forward scatter notched design is shown in Figure 4-17b). Devices have very good resolution and the notch quality (inset of Figure 4-17b) is good. Figure 4-18a) shows the angled 10 µm lens design with the modified notch, while formation of the forward scatter design with a 6.0µm lens system is shown in Figure 4-18b) The notch details in the inset of Figure 4-18b) indicates good reproduction of the design. Notch resolution is not perfect in any of these devices; due to the limits of the fabrication procedure there will always be some difficulty removing material in the deepest part of the notch. The effect this has on device operation will be evaluated later in section 4.2.2.4. The notch is also a source of cracks as was discussed in 4.1.1.2. Again, any limitation do the device performance will be discussed later in section 4.2.2.4.

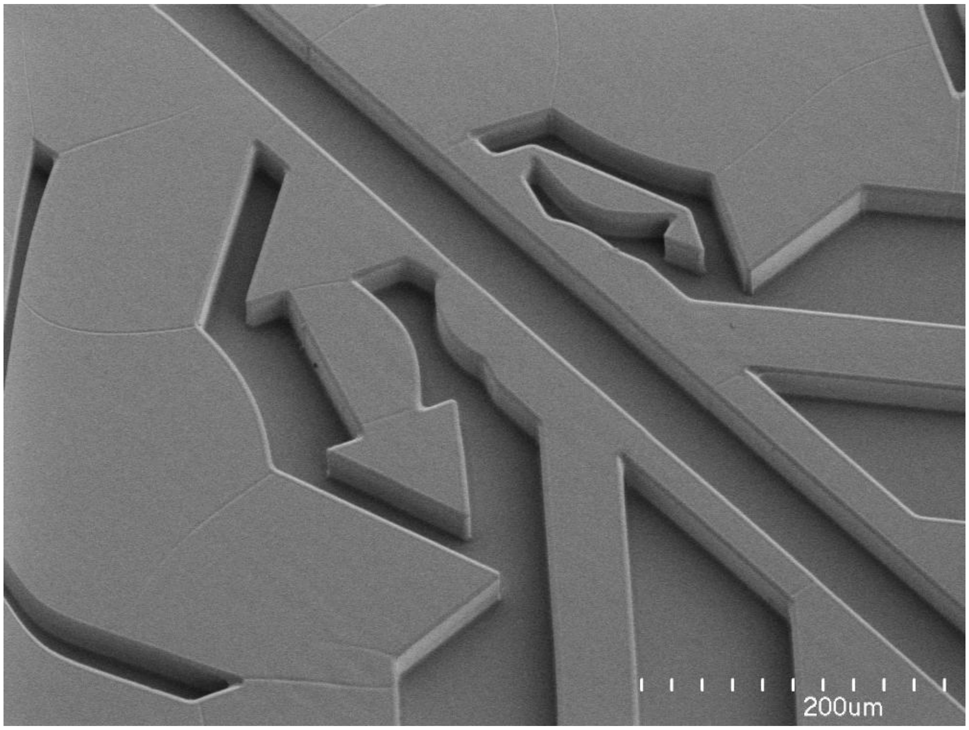

**Figure 4-16: SEM image of a device that has two different focused inputs from angled 1.5- and 12µm lens systems with an angled collection waveguide on each side.**

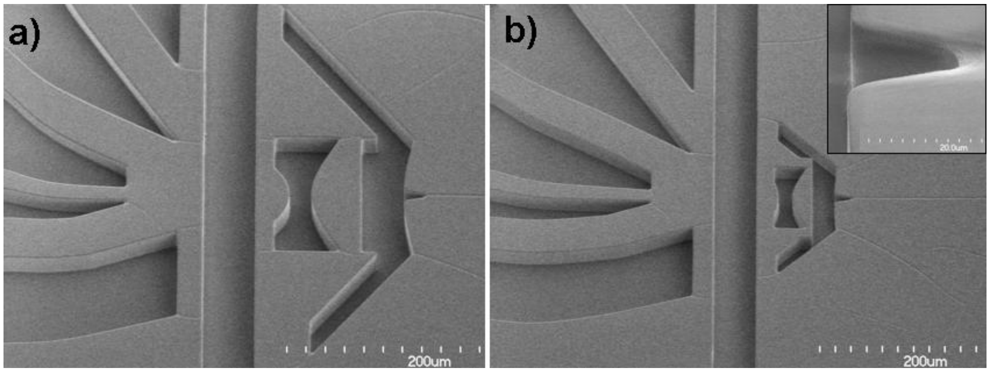

**Figure 4-17: SEM images of devices that form a) 10.0µm beam and b) 3.6µm beam with forward scatter design and high magnification of the notch (inset).**

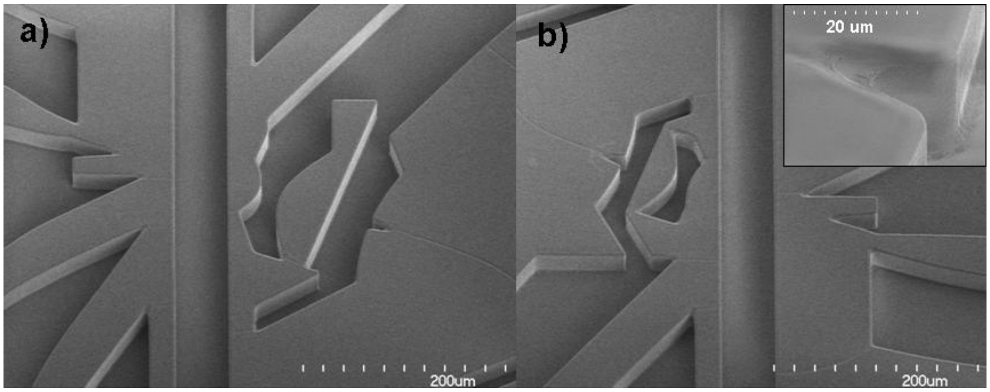

**Figure 4-18: SEM images of devices that form a) 10.0µm and b) 6.0µm angled beams with forward scatter design with a high magnification of the notch (inset).**

## *4.2 Device Performance*

With quality devices, the performance of the device is tested. The beam shapes formed in the channel are analyzed to form a large region of near uniform intensity – a region large enough to cover the entire sample flow with a low variation of intensity. This region of uniform intensity is defined to be where the intensity does not vary by more than 5% from the maximum intensity. With such ideal regions of excitation, the performance of the devices in a cytometric function is confirmed through determining the CV of each designed device with different beads. Device performance is found to have a dependence on the combination of the bead and beam sizes used – a straightforward one for fluorescence detection, but a vague one for scatter detection. Low CV values are desirable, and the flexibility of devices if found to be quite large due to the large regions of uniform excitation.

### 4.2.1 Excitation Beam Shaping

The ability of the fabrication procedure to accurately transfer the designs to the device layer is confirmed through quality inspections – as discussed in section 4.1.1 - and also through the testing of the devices. However, qualitative inspections cannot confirm the correct replication of device designs. Careful analysis of the formed excitation beams and comparison with simulations allow for a quantitative confirmation of proper design realization.

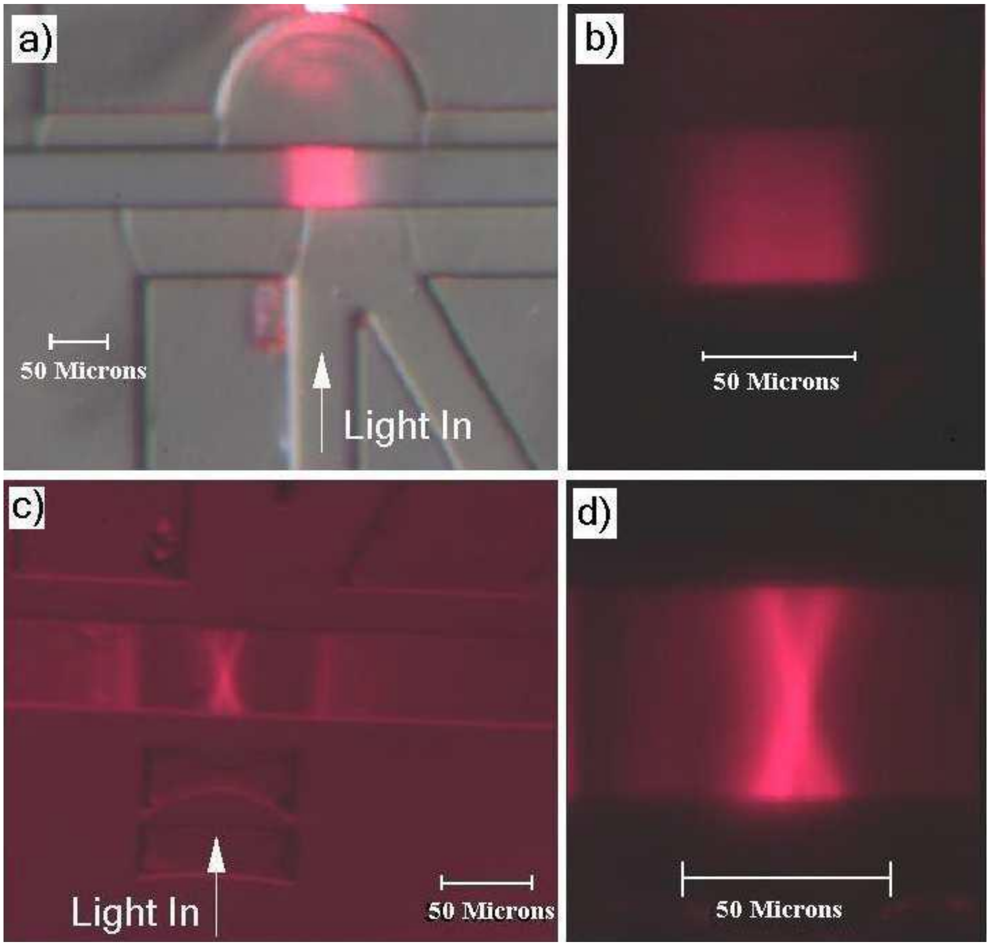

**Figure 4-19: Pictures of the device in simple use. a) Beam from a device with no lens system and b) a detailed image of the formed beam shape. c) device forming a 3.6um beam waist and d) a detailed image of the formed beam shape. *Source*: Reprinted from reference 121.**[§§]

An example of the fluorescence used to illuminate the beam is shown in Figure 4-19 highlighting the device's capturing the beam in the microchannel. To capture the beam, the channel is injected with the fluorescent dye and everything but the fluorescent light is filtered out to allow a clear beam image to be acquired. Figure 4-19a) shows the formation of a beam that does not pass through any lens system, with a backlight illumination to show the surrounding device structures. A detailed image with the backlight removed is shown in Figure 4-19b). It is obvious that the intensity of the beam decreases as it traverses the channel due to the divergence of the beam as it traverses the channel. Any particle that passes

---

[§§] This figure is from the author's published work in reference 121.

through this beam will get a varying dose of intensity while more than one particle could easily fit in the beam. These two features are very detrimental to detection capabilities of the device.

Applying a lens structure has a very dramatic effect on the beam, as shown in Figure 4-19c). This image shows a device that was designed to form a 3.6 μm beam waist with a backfield light applied and the band-pass filter in place. It was possible to use a filtered backlight with the 3.6 μm structure because the intensity of the focused beam is much greater than the device that did not employ any beam shaping . Figure 4-19d) shows a magnified image of the beam filtered and in the absence of the back light. The shape of the beam is an obvious ‘bowtie’ shape formed from the convergence of the beam in the centre of the channel. The useful uniform portion of the beam is in a narrow region in the centre of the channel.

#### 4.2.1.1 Raw Images

Images for all narrow designed beam waists whose simulations are shown in Figure 2-21 were obtained through the fluorescent imaging used to obtain Figure 4-19. An example of all these images is shown in Figure 4-20. This is the first iteration of these device designs. It is obvious that the increasing beam width corresponds to the intention of the designs. Furthermore, an increasing depth of focus was achieved with increasing beam width that allows for a larger region of uniform illumination.

Images show that the 3.6-, 6.0-, and 10.0 μm formed beam all appear to form a region of uniform intensity in the middle of the channel – as predicted by simulations. The 1.5- and 12.0 μm beams have the centre of the beam shifted quite significantly to the bottom of the channel – the injection side of the channel. This means that specimens in the flow stream will instead cut through the divergent portion of the beam and receive a varying intensity depending on the deviation in the sample stream. This was an error that was deemed to be corrected in the next iteration of device designs. Furthermore, there is a lot of extraneous light in the channel further up and downstream from the interrogation beam. As alluded to earlier in sections 2.1.2 and 4.1.2, this is due to the mismatch of NA from the waveguide and input NA of the lens system. The smaller the formed beam, the larger the image NA and thus, the smaller the object NA - as given by Equation 2-9. This means that a significant portion of the light ejected by the waveguide will misses the lens system entirely and end up propagating through the bulk material to the channel. This issues is discussed later in section 4.2.1.4 and design revisions to remove this light are shown in the schematics of Figure 4-39. The distance between the stray light and the beam increases with increasing beam waist due to the larger collection angle of the lens systems that form larger beam waists. The angle of the stray light also increases due to more extreme rays only being rejected. As can be noticed Figure 4-19b), the no lens beam does not have any stray light from this source as all light is guided by the waveguide to the channel. There is still some light evident but this is from scattering sources and imperfect coupling and is very dim.

Designs that formed larger beam waists, as shown via the simulation results in Figure 2-22, were created and sample images of the beams formed in the channel are shown in Figure 4-21. These formed beams had waists of a) 25 μm, b) 30 μm, and c) 50 μm. As mentioned earlier, these beams are much too wide to use with small particles, but were instead fabricated to demonstrate the flexibility of device designs. Note the lack of stray light in the channel: this is due to the designs being able to accept all light from the waveguide. This is because the input NA of lens system was greater than 0.22 – the value of the output NA of the waveguide. These lens systems therefore have a high efficiency as all injected light is used to form the illumination beam geometry. This is partly the reason why many other microchip device use single-mode beams for excitation: because very high efficiency of light makes it to the channel for illumination. However, as the beam is much bigger than the proposed specimens that are to be detected, the energy density of the beam is low and thus the specimen will only be illuminated by a tiny portion of the beam’s energy.

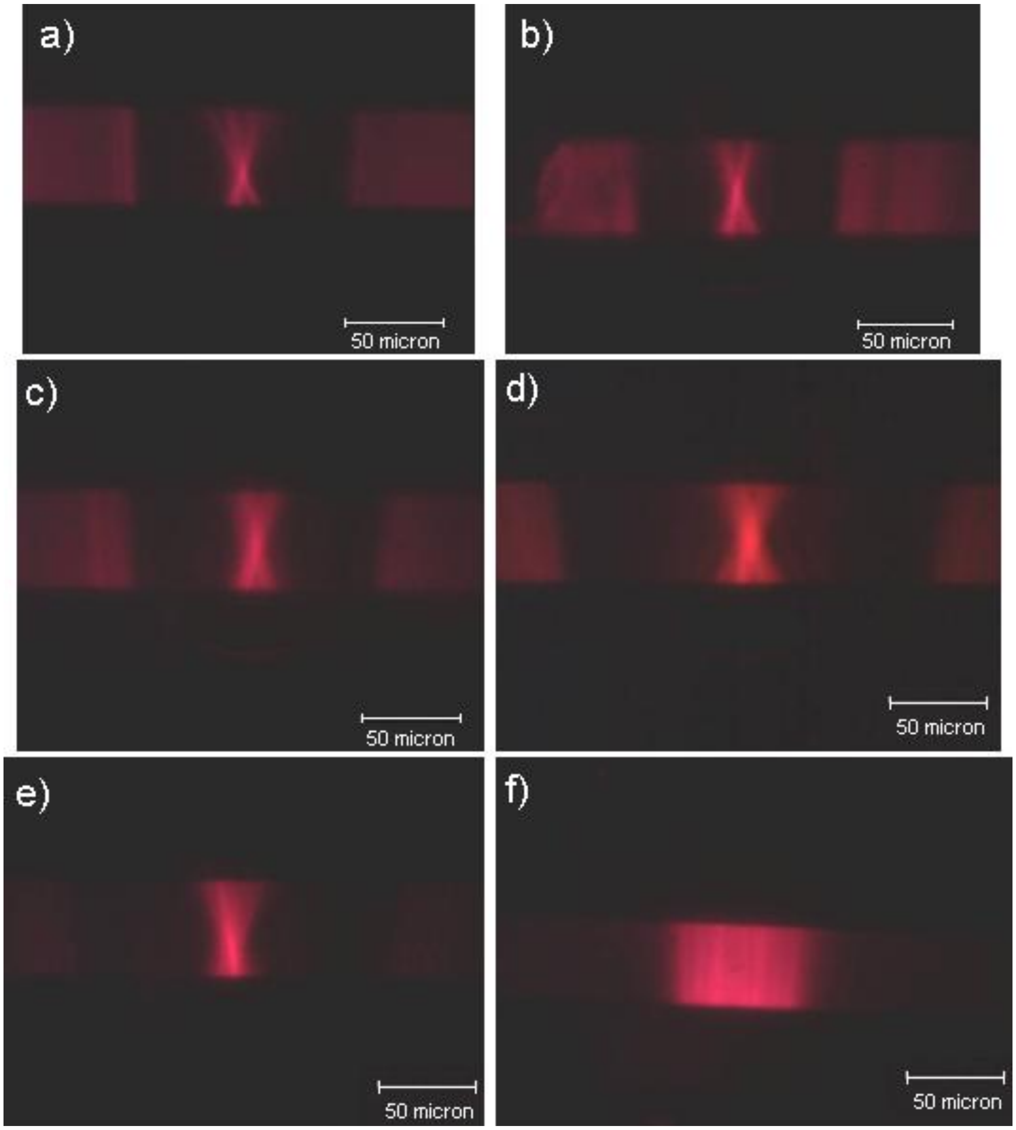

**Figure 4-20: Fluorescent images of the beam shaped formed in the channel for a) 1.5-, b) 3.6-, c) 6.0-, d) 10.0-, e) 12 µm and f) no lens system designs.**

Aside from the reason just given above, through a qualitative inspection of the beams shown in Figure 4-21 the conclusion was made that these beam would not provide very good excitation of particles. The uneven beam intensity in the direction of particle flow and the direction perpendicular to it will cause variation of excitation of specimens that will cloud the analysis of the detection signals. This variation is largely due to the multimodal nature of the beam; it has an uneven intensity profile. As the magnification of these beams are high - 0.5 for the 25 μm beam waist and 1 for the 50 μm beam waist - the uneven profile of the original beam is preserved. The smaller beams have these uneven regions overlap and average out to a desirable even beam intensity.

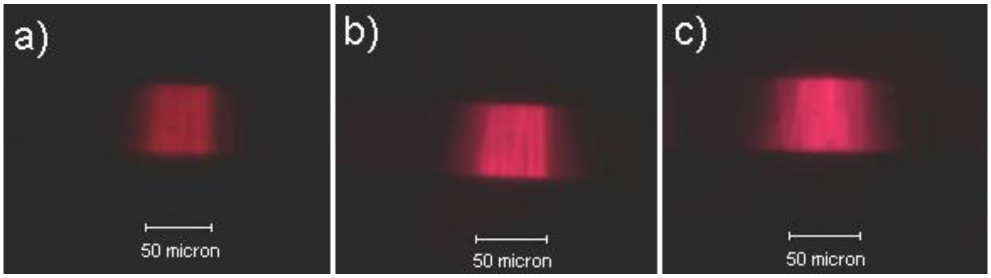

**Figure 4-21: Fluorescent images from designs to form larger beam waists. a) 25-, b) 30-, and c) 50 μm beam waists.**

For the purposes of this work these beams were deemed not relevant for bead detection for two reasons: the performance of the devices with small particles would not be close enough to mimic conventional detection, and performance with larger beads (20-50 μm), though possible better, is not applicable in this work due to the small channel size not being large enough to accommodate larger particles. Furthermore, biological applications are rarely concerned with particle sizes above 10 μm. Therefore, the bead detection tests are only performed with the beams formed in Figure 4-20.

#### *4.2.1.1.1 Device Repeatability*

To test the ability of the fabrication process to produce devices that are identical, beam imaging was performed on many devices. Figure 4-22 shows two images from each of the five main designs, 1.5-, 3.6-, 6.0-, 10.0-, and 12.0 μm beam waists. Each image is from a different device made during a completely separate fabrication run. The identical beams from each devices shows the reliability of the fabrication process to reproduce the intended designs repeatedly and with consistent quality. One of the images, from a device that forms a 10.0 μm beam waist, has a very dim image. This was found to be due to a poor waveguide facet quality from the dicing procedure. The coupling efficiency was poor and thus the beam intensity was poor. However, the formed beam geometry from both 10.0

μm devices are identical. Beam geometry is still the same shape as predicted meaning that the lens systems and the channel replication is consistent.

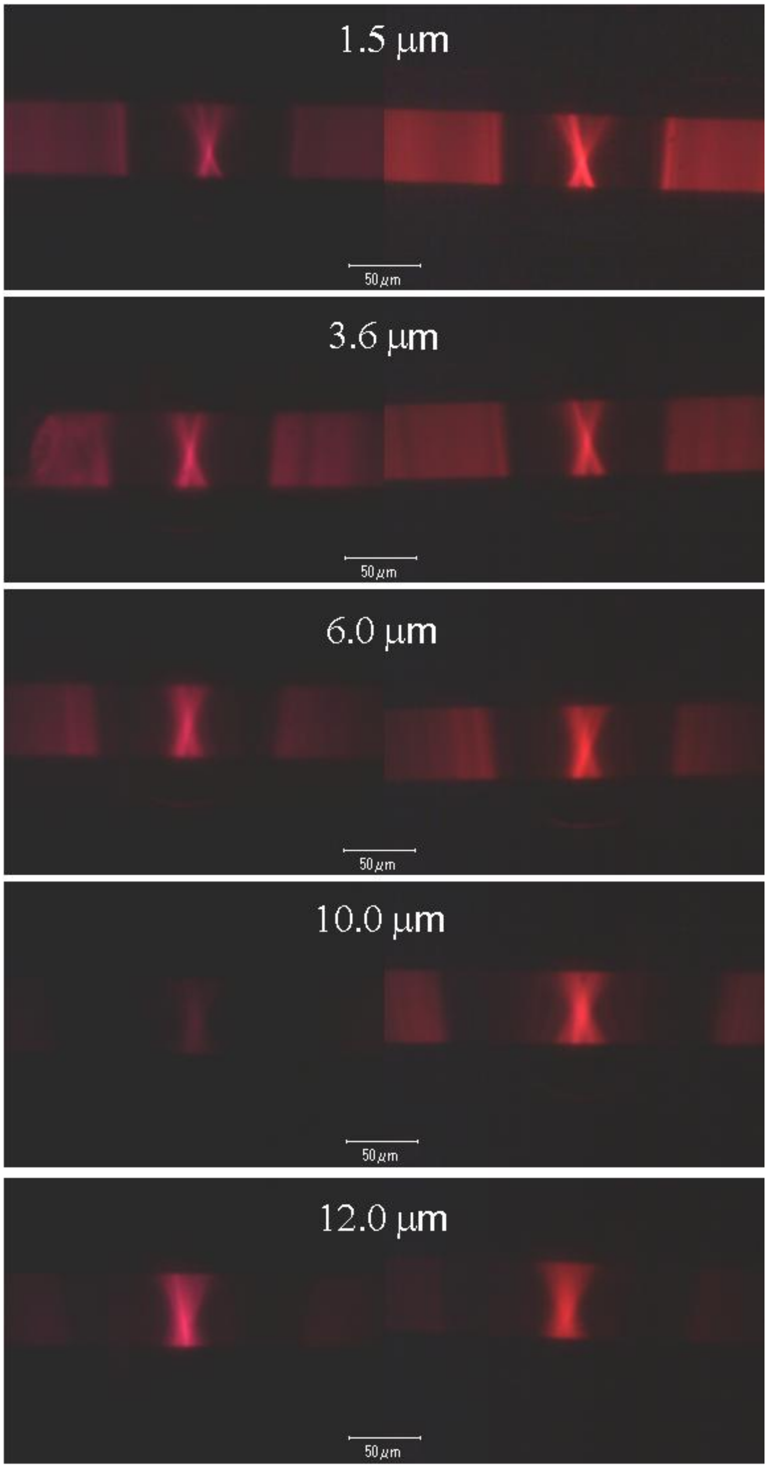

**Figure 4-22: Beam images of the five main designs from two different devices each.**

#### 4.2.1.2 Simulation Confirmation

Devices will only function properly if they accurately replicate the simulated designs, therefore, tested devices must have confirmation that the formed beams exactly conform to simulated beam shapes. Beams must form a well defined region of uniform intensity in the centre of the channel. As can be seen in Figure 4-23a), the simulated lens system for a 6μm lens system design closely fits the formed structures in the fabricated device. This figures is simply an overlay of the formed lenses plus the ray trace, but the overlay closely fits the structures formed on the image of the actual device and places the focused beam and region of uniform intensity right in the middle of the channel - as predicted. Figure 4-23b) shows the fluorescent image from a 6 μm beam formed in the channel. A qualitative inspection shows a region of uniform intensity in the middle of the channel stretching in the beam axis (perpendicular to flow) and a narrow beam waist over which the intensity is nearly uniform (in the direction of flow). Figure 4-23c) shows a coloured contour map of the beam in b). The beam's intensity is broken down into segments and the difference between baseline intensity and the maximum measured intensity is 73 (in arbitrary units) for this particular image. As the highest segment of intensity forms a region that is close to the definition of uniform intensity discussed in section 2.1.2.5, this region can be considered the formed region. This region measures approximately 9 μm long by 4 μm wide. The width, 4 μm, is smaller than the designed width because it is the width at 95% intensity whereas the FWHM is closer to 9 μm.

A better comparison to simulations is shown in Figure 4-24. The shape of the ray trace from the simulations corresponds very accurately to the formed beam in the channel. In this particular device the designed width is 10 μm, the FWHM was measured to be 10.5 μm. Although this method is quite a qualitative method, it is still is valid to perform it before moving on to apply the more rigorous analysis approach that is discussed in section 3.3.1. Any conclusions from the visual inspections need to be confirmed.

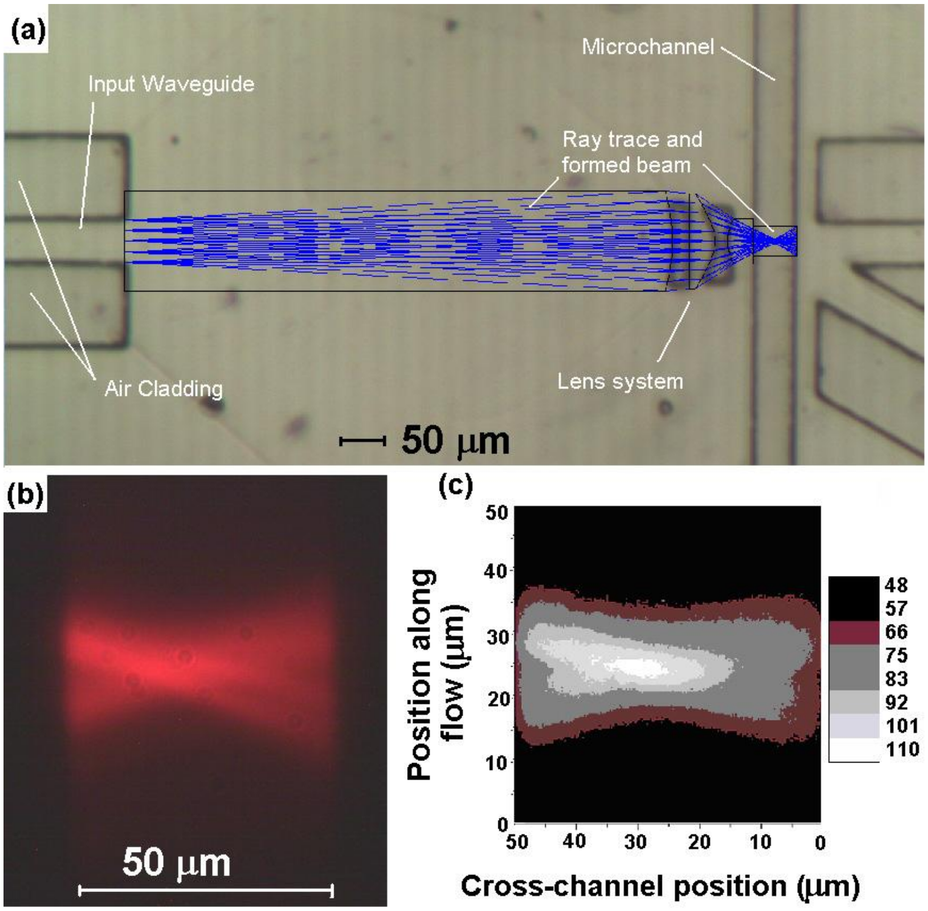

**Figure 4-23: Comparison of the formed device to the simulations. (a) Picture of the device with an overlay of the simulated ray trace indicates good device reproduction. (b) Image of a formed 6 um beam waist, and (c) a contour plot showing the uniform region in the middle where particle receive uniform optical excitation. *Source*: Reprinted from reference122.*****

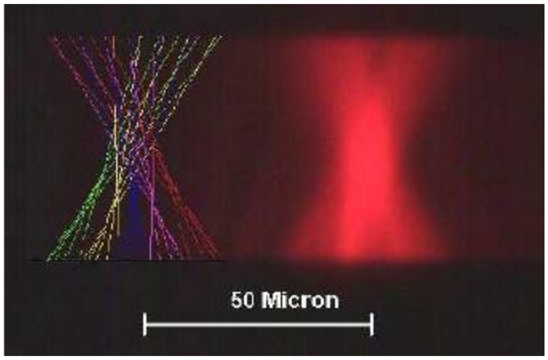

**Figure 4-24: An image of a formed 10um beam with the ray trace from simulations overlaid next to it. A good visual reproduction is obvious. *Source*: Reprinted from reference 121.†††**

---

[***] This figure is from the author's published work in reference 122.

[†††] This figure is from the author's published work in reference 121.

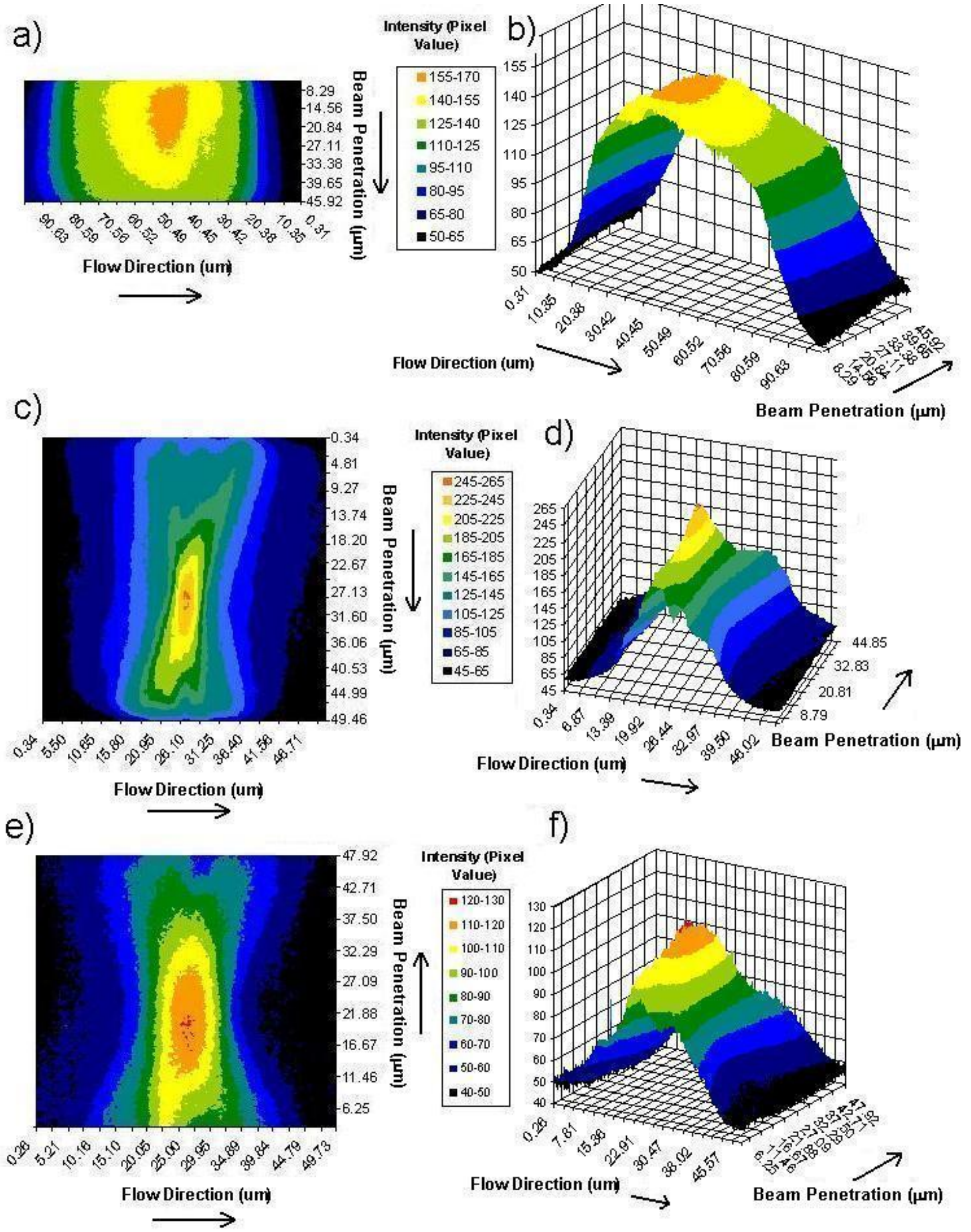

**Figure 4-25: False colour contour plots of a beams in the channel with a) no lens system, c) 3.6um lens, and e) 10um lens along with 3D representations of the beam intensity profiles for devices incorporating b) no lens, d) 3.6um lens, and f) 10um lens. *Source*: Reprinted from reference 121.**

Beam images from Figure 4-20 were converted to contour plots, two of which are shown in Figure 4-25 plus a contour plot for the no lens device. Figure 4-25a), c), and e) shows contour plots of beams formed by no lens system, a 3.6 μm lens system, and a 10 μm lens system, respectively, at a normal viewing angle. Figure 4-25b), d), and f) show 3D relief plots of the beams to give a better representation of the intensity profile that the particles will traverse. From these contour plots it is confirmed that the beam formed by no lens system in Figure 4-25a) and b) has a decreasing intensity across the channel as well as a very wide beam width not suitable for single particle detection. Comparing the contour plots of the formed 3.6- and 10.0 μm beams to the beam simulations in Figure 2-20 shows that the images are closely replicated.

### 4.2.1.3 Beam Geometry Parameters

Each beam was characterized according to the method outlined in 3.3.1. The row by row analysis of the beams - essentially planes parallel to the sample flow and perpendicular to the plane of the chip - is shown in the next series of figures. The first, Figure 4-26, shows the measured FWHM of the beam as a function of the propagation distance through the channel (channel position). As the curves indicate, each beam clearly narrows in the centre of the channel and some devices performed better than others. This plot confirms the previously made observation from section 4.2.1.1 that the worst performance is from the 12.0 μm device where the narrowest point of the beam is shifted very close to the channel wall on the input side. This means that particles will traverse the beam in the more divergent and wider area around the 25 μm mark in the channel position. This is obvious from the images in Figure 4-20e) and Figure 4-22. The plot also confirms that the 1.5 μm beam is also shifted closer to the input channel wall – around the 17 μm mark. Again, this was obvious from the images in Figure 4-20a) and Figure 4-22 - though less so than the 12 μm device.

Of the devices shown in the plot in Figure 4-26, the 10 μm device performed the best showing the narrowest FWHM - approximately 11.5 μm - very near the centre of the channel at 25μm. Furthermore, the narrow regions stretch over a significant portion of the channel; from the 20 to 30 μm positions across the channel the width varies by less than 5% of the minimum. This is part of the designed uniform region and ensures that specimens in the sample stream will be in the beam for equal amounts of time leading to uniform pulse generation.

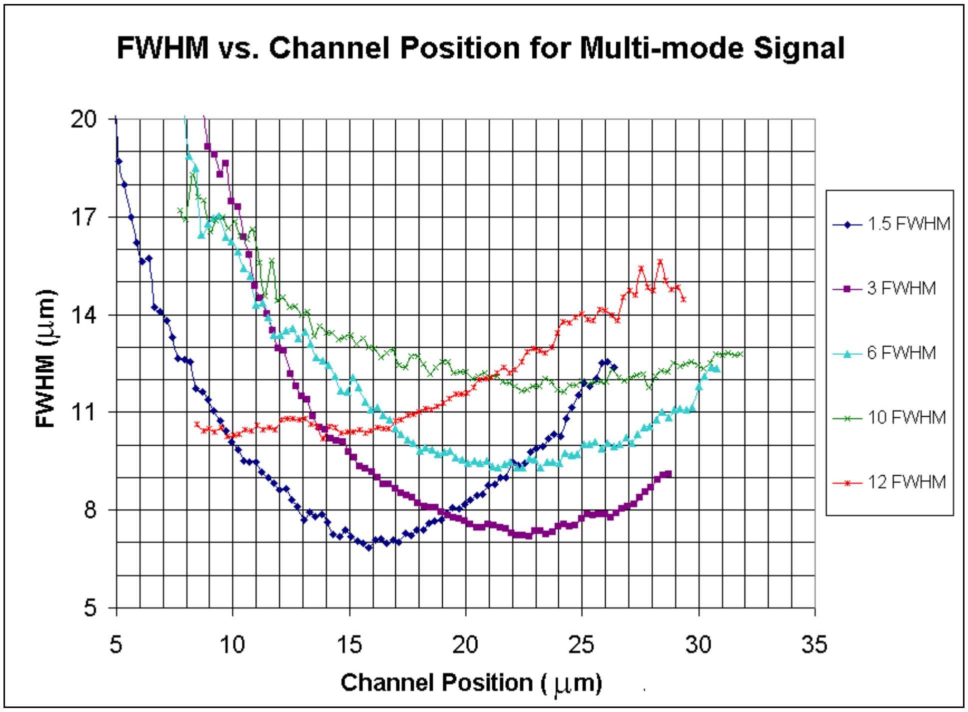

**Figure 4-26: Graph showing the measured FWHM for the 1.5-, 3.6-, 6.0-, 10.0-, 12.0 µm beams with input from the multimodal source.**

The 6 µm device formed a narrow FWHM of 9.1 µm at the 23 µm point in the channel. This beam covers positions 19 to 25 µm in the channel where the width varies 5%. The 3.6 µm device covers positions 21 to 25 µm with a minimum FWHM of 7.3 µm. This confirms the predicted performance from section 2.1.2: the narrower the beam, the narrower the region where the FWHM is controlled. With limited coverage this indicates that the beams must be properly deployed depending on the size of the specimen that the tests targets. Ie. too small of a beam size will cause particles to traverse divergent areas of the beam where the excitation will not be uniform or ideal; too large of a beam may have some negative consequences, however, that will be determined by results from bead testing.

The next plot further illustrates the beam geometry and allows comment on the usefulness of the beams. The maximum amplitude of the beam as a function of the position across the channel is plotted in Figure 4-27. The peaks of the curves coincide quite well with the minimums of the FWHM curves from Figure 4-26. There is a slight shift to the left towards the injection side of the devies as the absorption of the beam in the due to the dye will decrease the intensity of the beam as it propagates through the channel. Correcting for this would entail adding a small value to each point proportional to the distance from the injection side. The overall effect would slant the curve up on the right side.

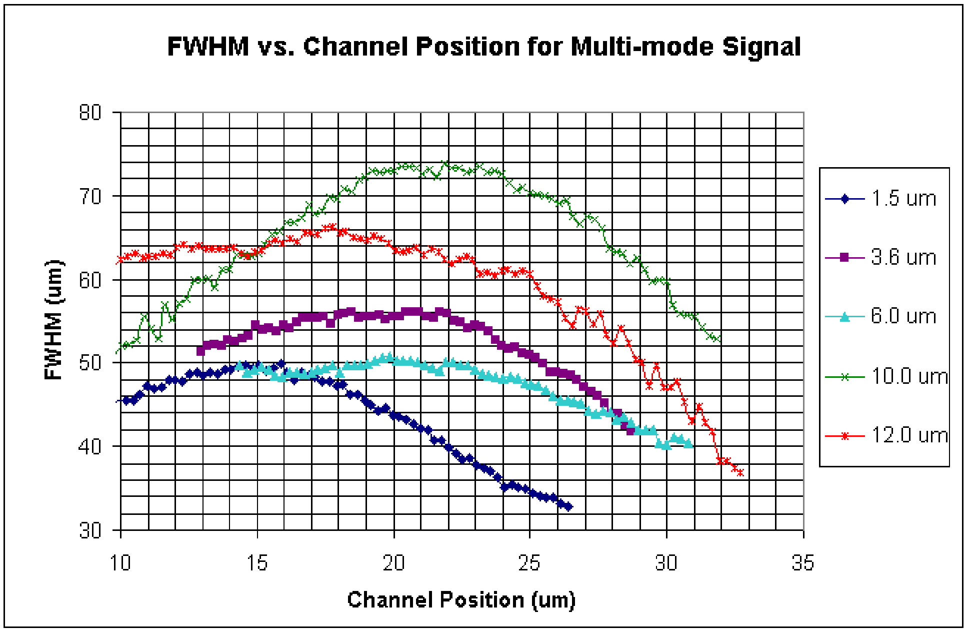

**Figure 4-27: Graph showing the measured amplitude relative to background intensity in the surrounding channel for the 1.5-, 3.6-, 6.0-, 10.0-, 12.0 µm beams with input from the multimodal source.**

Inspection of the curves again confirms that the worst performance is from the 1.5- and 12.0 µm designs. This suggests a design flaw in the simulations. Again, this was intuitively expected through the inspection of the beam images in Figure 4-20a) and e) and Figure 4-22. There is a trade-off that exists between the uniformity of the formed geometry and the beam waist: the smaller the beam waist, the smaller the formed region in the channel.

For a better comparison of two devices, the 3.6 µm and 10 µm FWHM and intensity plots are shown below in Figure 4-28 along with a plot for a beam with no lens system. The minimum beam width and maximum beam intensity both coincide very closely with the centre of the channel indicated good alignment. A much wider region of controlled beam width and intensity from the 10 µm device is possible, as expected. The comparison to the device with no lens is very dramatic. With no lens, the beam has a very stable beam width, however, it is much to wide to be useful for practical application. Furthermore, both the 3.6- and 10 µm device have much larger intensities at the point of interrogation due to the focusing of the beam. As discussed earlier in section 2.2.3, the very low magnification makes up for the loss of light due to any missed light due to the mismatch between the lens system NA and waveguide NA.

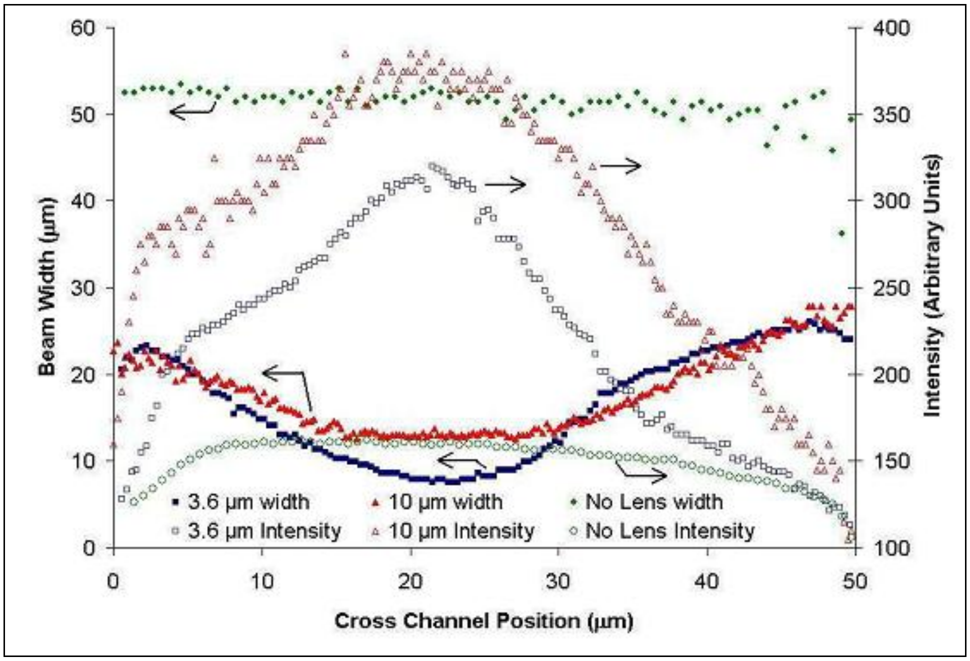

**Figure 4-28: Comparison of the 3.6- and 10.0 µm device with a device that utilizes no lens system.**

Early on in the work, testing was done with a HeNe laser as a light source instead of the multimodal fibre coupled source. Comparison between operation with a low quality multimodal source and a high quality laser source was possible by coupling this high quality beam into the device to test the lenses. Again, results are presented in the same form as in Figure 4-26 and Figure 4-27. The plot of the FWHM is shown in Figure 4-29 while the amplitude plot is shown in Figure 4-30. The results from the beam analysis with a single mode source closely match those with a multimodal beam. The single mode beam has a smoother profile – as expected due to the better quality input beam from the HeNe laser resulting in the lens systems focusing a single-mode beam with a Gaussian profile. This demonstration shows that the multimodal beam can be shaped into a profile that is of similar quality to that formed from a single-mode source.

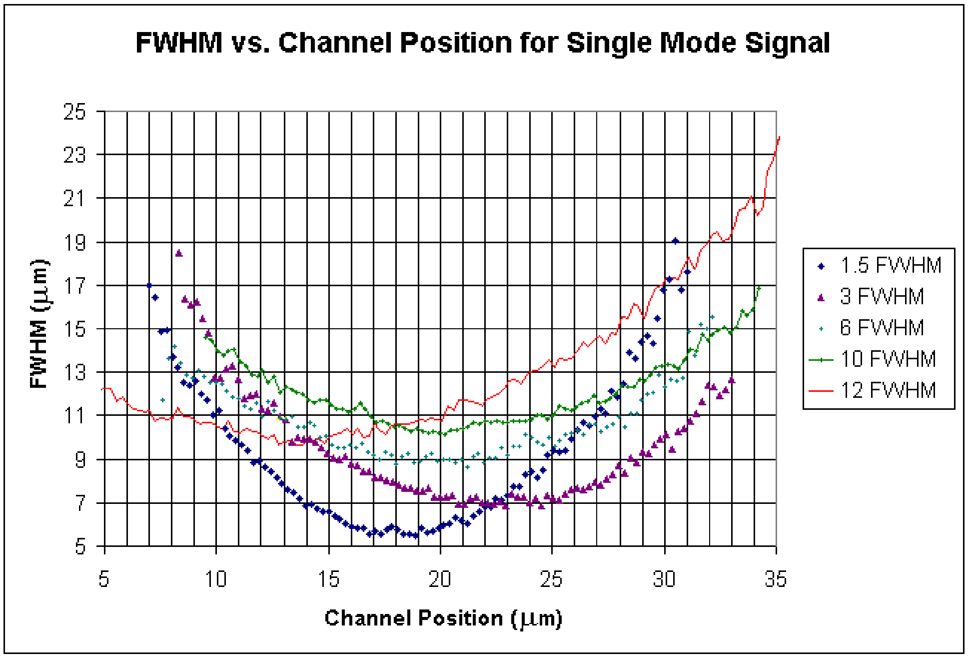

**Figure 4-29: Graph showing the measured FWHM for the 1.5-, 3.6-, 6.0-, 10.0-, 12.0 µm beams with a single mode input from a HeNe laser.**

Now, armed with an intuitive knowledge of where the beam geometry is located in terms of the FHWM and amplitude, analysis can now define the regions of uniform intensity. Figure 4-31 shows a contour plot similar to that in Figure 4-25e) with the defined region of uniform intensity clearly marked in red for the 10 µm design. The dimensions of this area were found through the procedure outline in section 3.3.1 using the script from Appendix D The area is defined where the intensity of the beam does not deviate by more than 5% of the maximum and forms an elliptical area with dimensions of 14.3 µm - in the beam axis (major axis) direction perpendicular to specimen flow - by 5 μm in the flow direction (minor axis). This creates a span across the sample flow that will ensure equal excitation of specimens and ensure equal signal for identical specimens. This will give the devices the ability to resolve tiny differences in specimen populations and increase the analytical ability. The design do need slight modification to shift the region so that it is perfectly in the centre of the channel, however, this shift could be from absorption of the dye that artificially decreases intensity in the latter half of the of the channel. Modifications to device designs would have to be very slight.

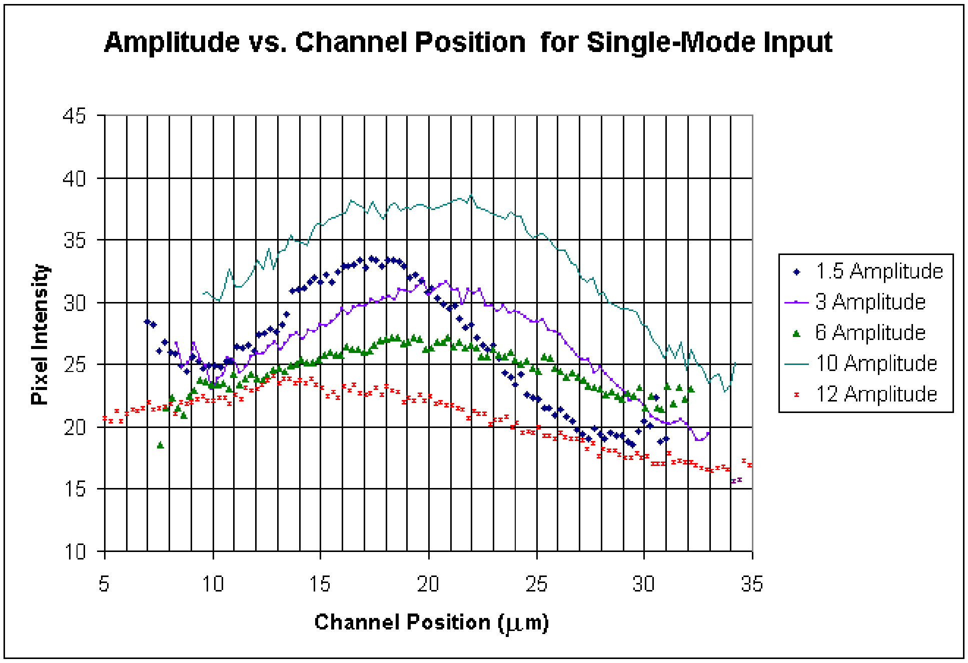

**Figure 4-30: Graph showing the maximum amplitude of the beam as a function of position across the channel for 1.5-, 3.6-, 6.0-, 10.0-, and 12.0 μm beam designs with a single mode input from a HeNe laser.**

Expanding the analysis from above to cover all the device designs results in Figure 4-32 which shows contour plots much the same as the plot presented in Figure 4-31 - except that it displays results from the four other device designs. Inspecting the contour plots from the smallest beam waist – 1.5 μm in Figure 4-32a) – to the largest beam waist – 12.0 μm in Figure 4-32d) – demonstrates that the dimensions of the uniform region grows with the beam waist size. This is an expected result due to simple geometric optics predictions from section 2.1.2.

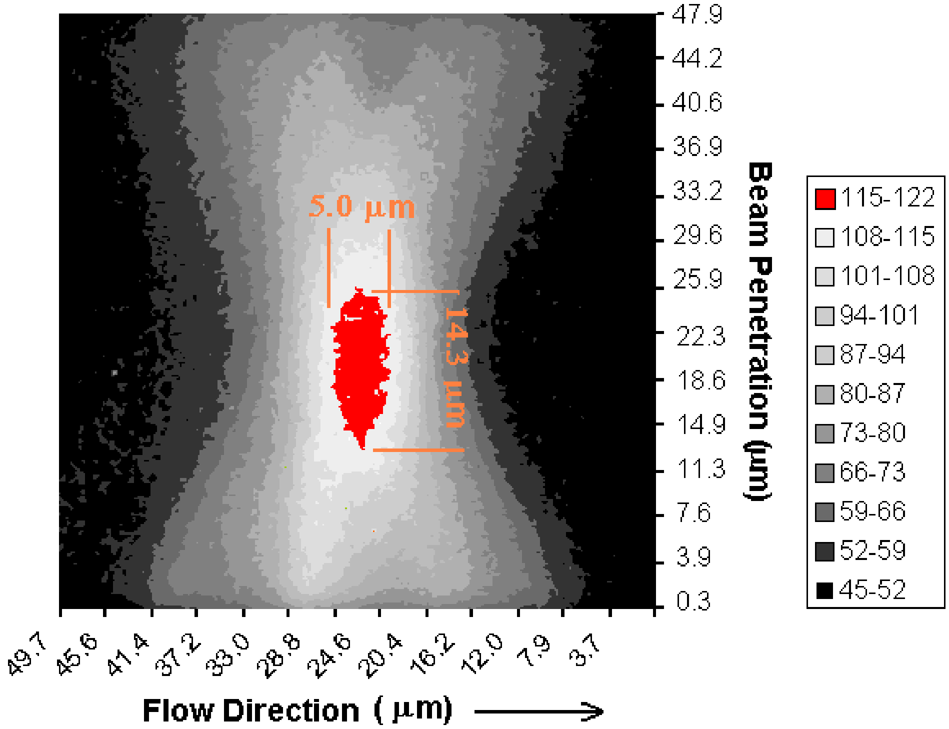

**Figure 4-31: Contour plot showing the defined uniform region (in red) and the dimensions.**

Table 4-1 contains a collection of the measured parameters from the beam data obtained from the contour plots in Figure 4-31 and Figure 4-32. The table shows the minimum FWHM of the beam, the dimension of the uniform region (the width and the depth), and also lists the position of the centroid of the uniform region in the channel with respect to the beam penetration in the channel; ie. 25 µm would be ideal as it is the centre of the channel. The uniform regions are confirmed to be quite large - larger than the intended beam width. This ensures that even large particles - close to the same size as the FWHM - will receive uniform excitation. The 10 µm lens system was the most accurately replicated as the region was centred in the channel at 23.0 µm, the FWHM was measure to be 10.9 µm - very close to the simulated width – and the depth of focus is very large so as to ensure very uniform excitation of specimens.

The 3.6- and 6.0 μm devices closely replicated the intended design, but need slight adjustments to the designs. Both need a smaller FWHM, while the 6 μm device needs to have the region be positioned closer to the channel centre. Both devices still produced very large depths of focus relative to the intended design width.

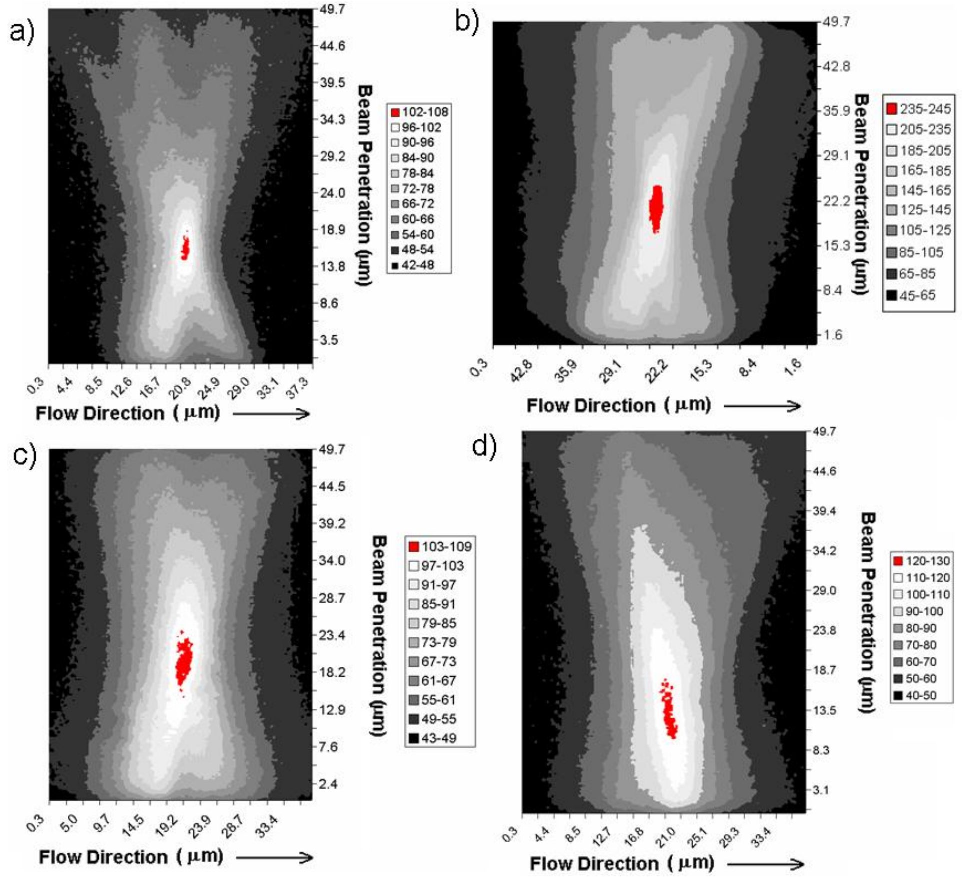

**Figure 4-32: Contour plots showing the defined region of uniform intensity for the a) 1.5-, b) 3.6-, c) 6.0-, and d) 12 μm device designs.**

The devices that formed 1.5- and 12 μm beam were way off the intended design and need major adjustments.

**Table 4-1: Collection of measured beam widths and depth of focus values.**

| Device | FWHM (μm) | Width (μm) | Depth of Focus (μm) | Position (μm) |
|---|---|---|---|---|
| 1.5 (μm) | 6.7 | 1.0 | 3.9 | 16.3 |
| 3.6 (μm) | 7.4 | 2.1 | 8.3 | 22.3 |
| 6.0 (μm) | 10.2 | 2.6 | 10.2 | 19.7 |
| 10 (μm) | 10.9 | 5.0 | 14.3 | 23.0 |
| 12 (μm) | 10.1 | 2.3 | 9.5 | 13.5 |

So far the demonstration of high quality devices has been shown. Device designs are accurately replicated on-chip in a single layer. These designs create devices that form well defined regions of intensity in the channel. Furthermore, these designed regions of intensity fit the simulated beam very accurately. The intended regions of uniform intensity are very large and should allow each beam width to enhance device performance through reliable results from specimens whose size is close to the same size as the FWHM of the beam. There will be an upper limit and lower limit to the devices in terms of acceptable specimen size – which is confirmed by the cytometry tests described later in section 4.2.2. A summary of the accomplishment and contribution of this work is shown in Figure 4-33 and demonstrates a marked difference and improvement to other examples of the state-of-the-art in the literature originally shown Figure 1-24. This figure has been expanded to show the contribution of this work, shaded in yellow. The beam formed by the conventional method, shown in Figure 4-33i), is the ideal situation. Injection from waveguide sees the beam spread and have an uncontrollable intensity region as shown in Figure 4-33ii), while early works have demonstrated some form of focusing, though with no effort towards beam shaping, Figure 4-33iii). This work clearly demonstrates the improvement and gap in microchip devices by tailoring a custom beam geometry on-chip through the use of on-chip integrated optics. This method allows the device to function with the input from a lower quality light source. These designs have a larger efficiency as it uses a large amount of the input beam to form the excitation region for the specimen leading to a larger detection signal, as opposed to the conventional method that wastes a significant portion of the beam, as discussed in section 1.1.1.2.1.

Overall, the 10- and 6 μm devices should have excellent performance in bead flow as the region of uniform intensity is centred around the middle of the channel and they provide very large and even regions of intensity to provide uniform excitation to all specimens despite deviation in the sample flow stream. A large efficiency of these devices is due to the designs allowing a large amount of coupled light from the waveguide to actually form the excitation region.

The 1.5 μm device in the original design is predicted to have the worst performance. Poor performance will be due to the formed geometry; it is so small that the slight miss-alignment is catastrophic to excitation. Specimens in the sample flow will miss the intended illumination region and instead be excited by the divergent portion of the beam subjecting the specimen to uneven illumination.

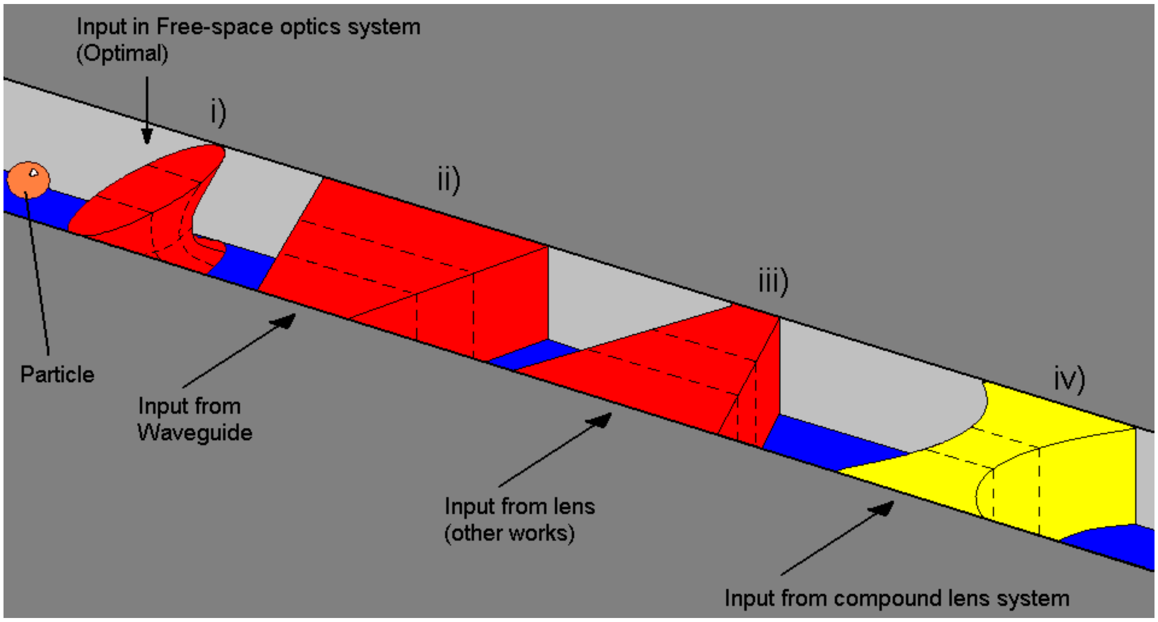

**Figure 4-33: New designs allow a new beam geometry in the channel iv) that closely mimics free-space methods i).**

Performance from the 12 μm device – despite a serious misalignment of the beam geometry - should have adequate performance, especially with smaller bead sizes. The designed uniform region is so large that it still overlaps the sample stream. Smaller sized beads are still excited by the defined region – though through the extreme edge of the formed region. Large sized specimens will suffer as a portion of them will traverse the divergent potion.

Design for the 3.6 μm device, despite good alignment in the channel, will still suffer some performance issues as beads will ‘clip’ the intended formed beam. The small size allows less room for error on the alignment of the beam in the channel. Essentially, specimens will traverse the beam half-in and half-out of the formed beam geometry.

#### 4.2.1.4 Revised Lens Designs

Before presenting results of the bead flow experiments with new integrated-photonic devices capable of beam shaping, work is first presented to show the iterative work done to take beam analysis results and apply them to fix designs. New device designs have modifications done to form a better beam shape in the channel based on the feedback obtained from beam analysis on the current devices. The iterative design process based on the optimization of individual components was part of the goals specified at the onset to be accomplished by this work.

These devices' short-comings in formed beam geometry are important to fix as they will lead to very uneven illumination and cause a severe degredation of the device performance. Figure 4-34 demonstrates this very clearly. This figure overlays the intensity profiles from Figure 4-27 onto beam images along with the the channel walls and an imagined sample flow 7 μm wide superimposed on the image. The imposed flow includes two different particle sizes 2- and 4.5 μm Figure 4-34a) shows the 1.5 μm beam and the intensity profile along the channel – in yellow. Any deviation of particles in the sample stream would mean that the particles receive a widely varying amount of excitation – up to almost 50% more. Smaller particles would have a greater variation in the stream and a greater variation in excitation and thus detection reliability. The 10 μm beam in Figure 4-34b) has the intensity profile centred over the middle of the channel and the sample stream. As this excitation is more uniform the specimen excitation will be more uniform and thus, lead to more reliable detection.

The most glaring fixes that need to be made are from the 1.5- and 12 μm lens systems. The 1.5 μm just needs adjustments so that the focused spot is shifted further into the channel to reduce the chance a particle traverses the divergent portion of the beam. This design error was due to the difficulty of moving the focused spot further into the channel while maintaining such a small spot diameter. A focused spot with a larger image distance requires a larger magnification, due to the lens properties discussed in section 2.1.2. Correction of this design was accomplished through a better understanding of the lens systems. Also, improvement to fabrication techniques allowed tighter tolerances leading to smaller lens spacing. Figure 4-35 shows the old simulation results and image for the initial 1.5 μm design and the revised design resulting in an improved beam image of the fluorescently captured beam. It is easy to see that the spot has shifted closer to the centre of the channel. This image shows that the beam is of much better quality with a smoother profile and has a large area of uniform illumination. The centre of the defined illumination regions still appears as if the image is off centre – but this is likely due to the absorption in the channel causing the beam to lose intensity from the injection to collection (bottom to top in the image) side of the channel. This is discussed in detail later in this section.

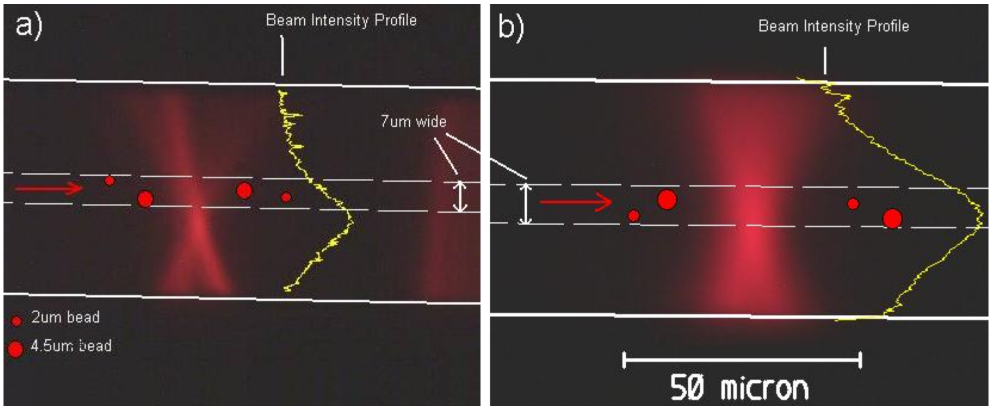

**Figure 4-34 Picture of a) 1.5 μm and b) 10 μm excitation beams with overlays of channel walls, sample fluid flow, and intensity profile showing how misalignment will lead to uneven illumination.**

Another important feature to note is the improvement to overall device quality and the effect it has on beam quality. The beam intensity profile of the old beam in Figure 4-35 in the divergent areas is very uneven and it appears as though one can see individual rays. The dark hole on the beam axis at the injection side (bottom of the image). This is due to poor quality of the lenses – in particular the surface quality. Excess material exists between lenses on the optical axis where lens surfaces are closer together due to early iterations of the fabrication process not being able to remove all this material. This material is on beam axis will block light in this central region. This missing light is only noticeable at the edges of the channel where the beam is spread out. The new beam has a full beam intensity in the divergent regions with a smooth beam profile indicating much better material removal in the lens structures.

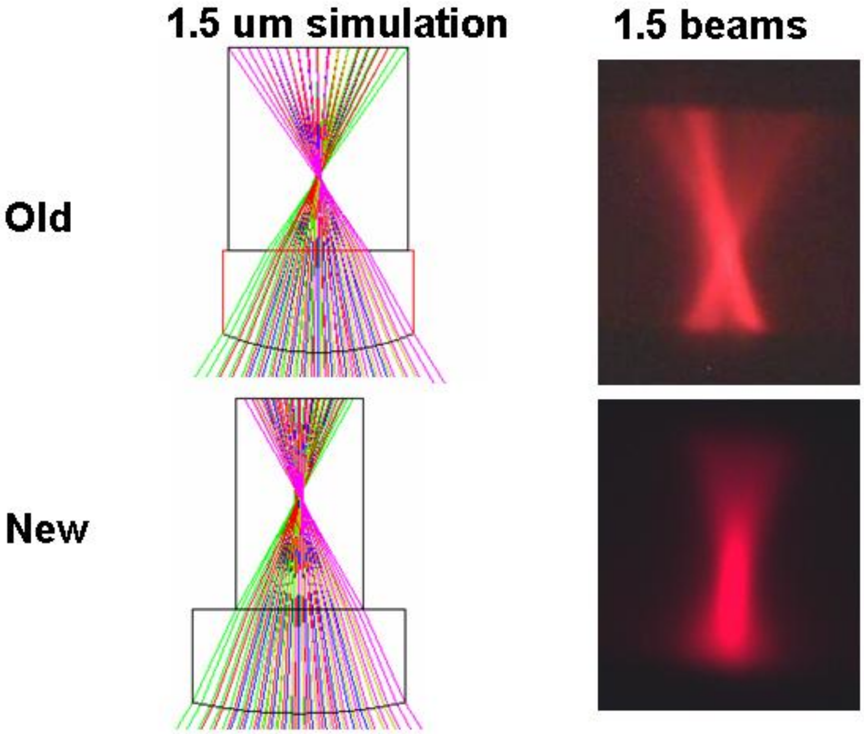

**Figure 4-35: Revised design of the 1.5-um lens design showing the old and new simulations and the resulting beam images.**

Whereas the first iteration of the 1.5 μm lens system was finalized knowing that it would be shifted slightly, the 12 μm lens system was finalized with the idea that the formed image would be adequate. Simulation of the old design in Figure 4-36 shows a focused spot in the centre of the channel. However, the different ray directions are focused near the injection side of the channel and diverge very quickly just before the intended beam waist. The result is that the beam is more diffuse on the latter half of the channel than on the injection side's half. The results is a dimmer more diffuse latter portion of the beam. The beam image of the old design in Figure 4-36 confirms this; the new design fixes this issue. As indicated in the new simulations in Figure 4-36, now each direction of ray is less divergent and the concentration of rays is fairly uniform on each side of the channel centre. A fluorescent image from the new design is shown in Figure 4-36 indicating that the new defined region is much improved as it is a more uniform region and the formation of the beam is closer to the centre of the channel.

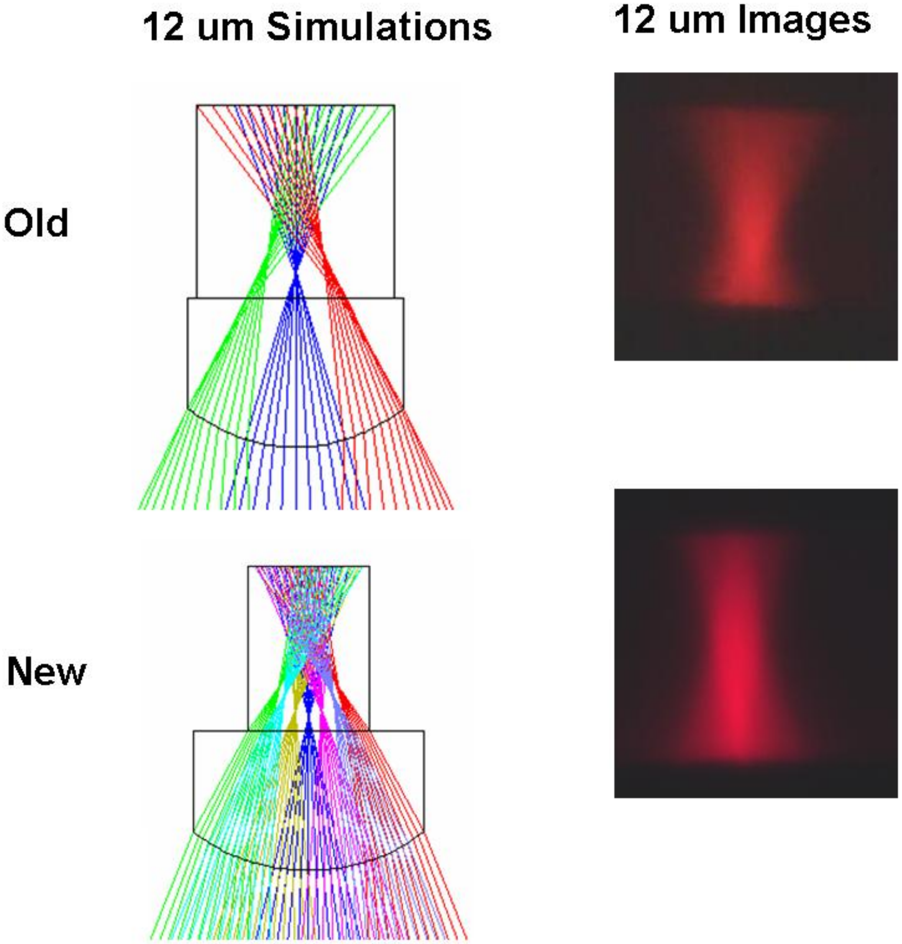

**Figure 4-36: Revised design of the 12-um lens design showing the old and new simulations and the resulting beam images.**

Repeating the beam analysis outlined in section 3.3.1 and demonstrated in section 4.2.1.3 with the first iteration of device designs the improvement of the new designs is confirmed via comparison of the parameters. New fluorescent beam images are digitized and the results are used to form contour plots to define the region of uniform intensity. The resulting contour plots from these new designs are shown in Figure 4-37. Improvements to the defined regions of uniform intensity can be immediately seen through simple inspection of the contour plots for the new 1.5-, 6.0-, and 12 μm beams, as shown in Figure 4-32. Improvement to the uniform regions was achieved through a greatly increased depth of focus and narrow region width. These three beams should have the most prominent changes as these three had the largest design revisions. The 3.6 μm had very slight modifications to adjust the beam waist and the 10 μm design was not changed.

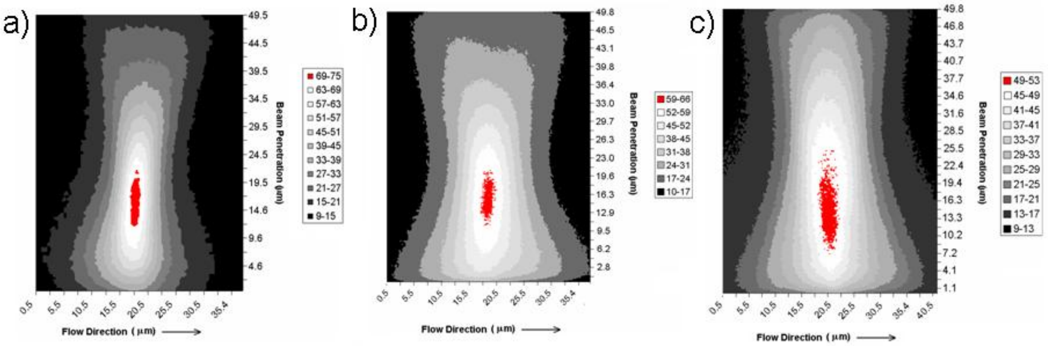

**Figure 4-37: Contour plots for redesigns of a) 1.5-, b) 6.0-, and c) 12 μm devices with improved uniform regions of intensity.**

Comparison of the new and old beams' parameters is shown in Table 4-2. Immediately evident from the new device designs is the drastic improvements to depth of focus. The 1.5- and 12.0 μm systems' depths of focus improved from 3.9 to 9.9 μm and 9.5 to 16.5 μm, respectively. This ensures a very wide region where uniform excitation will occur and allow for much better detection techniques. Improvement to the 6 μm device's depth of focus is only slight as the only change to design was to shift the beam to a more central region in the channel. The FWHM of all the beam didn't changed as the width wasn't altered in the simulations. The width of the 1.5 μm beam is likely limited due to the diffraction limit.

The biggest issue to correct was the position of the beam in the channel; shifting it so that it was more central in the channel to ensure particles traversed the designed beam and not the divergent parts. The old device designs had a range of different beam position in the channel, however, all of the new designs have the same beam position; centred around 16 μm from the injection side of the channel. As all the new designs are able to form geometries in the centre of the channel, the consistency of the device design between different beam widths is excellent. The position of the region's centre at 16 μm is a bit concerning, but the cause of this issue isn't with the design, but with the fluorescent dye used in more recent tests done with the new designs.

**Table 4-2: List of beam geometry parameters for old and revised lens designs.**

| Device (μm) | FWHM (μm) | Width of defined uniform (μm) | Depth of Focus (μm) | Beam Position (μm) |
|---|---|---|---|---|
| 1.5 (old) | 6.7 | 1.0 | 3.9 | 16.3 |
| 1.5 (new) | 6.5 | 1.5 | 9.9 | 16.6 |
| 6.0 (old) | 10.2 | 2.6 | 10.2 | 19.7 |
| 6.0 (new) | 10.2 | 3.4 | 11.1 | 15.8 |
| 12 (old) | 10.1 | 2.3 | 9.5 | 13.5 |
| 12 (new) | 13.3 | 3.5 | 16.5 | 16.0 |

Testing of the 3.6 μm lens system sheds some light on the beam position problem. As the 3.6 μm design was not altered to change the position it is expected that the beam shape should be in the same position as in the previous design. It is apparent from Figure 4-38 that the overall shape of the beam is the same. Figure 4-38a) is the original beam image from early tests while Figure 4-38b) is the results from a more recent test. The peak intensity uniform region is larger and shifted in the new design. Table 4-2 shows the beam parameters to make the effect more clear. In the new design the entire beam is shifted towards the injection side of the channel. The centre position of the new design has the beam position at 14.6 μm. As this position is approximately the same as the other new designs of the 1.5-, 6.0-, and 12 μm beam designs, and the new design of the 3.6 μm device did not have any alterations to the beam position, the position of the beam in the channel from the new designs is not a design issue. It is instead caused by the fluorescent dye.

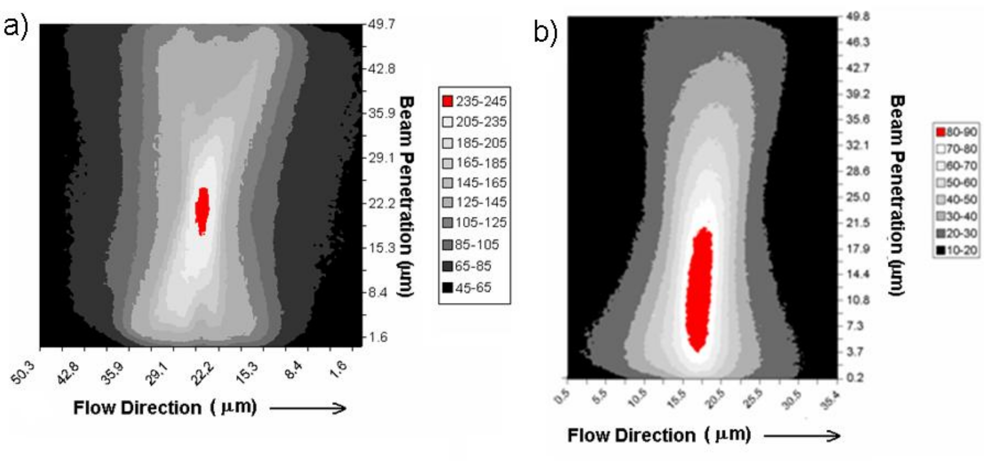

**Figure 4-38: Contour plots of the 3.6 µm device showing the defined uniform regions of intensity from a) an early run and b) a more decent run.**

The fluorescent dye was dissolved in ethanol. The time between when the original image and the new designed image spanned over a year and a half. As the bottle that contained the fluorescent dye was frequently opened – and as it wasn't perfectly sealed to eliminate the escape of vapours from the bottle – it is assumed that the concentration of the fluorescent dye within the bottle was much stronger when the second image was taken. As much as half the fluid was missing leading a much stronger dye concentration. This large dye concentration is the result of the shifting. The more concentrated fluorescent dye has a very strong absorption in the channel and will cause the beam to significantly diminish in intensity as it traverses the channel. This is obvious from comparison of equal intensity regions in Figure 4-38a) and b). The older image has equal intensity distribution at the input and output sides, whereas the recent tests have a much larger intensity at the injection side than at the collection side. A correction applied to the image in Figure 4-38b) would see the intensity profile shift further into the channel until it more closely matches the first image collected in Figure 4-38a). The dye concentration was tuned during initial testing to be concentrated enough to provide strong fluorescence while not disrupting the beam properties. Obviously, the more concentrated dye has a detrimental effect on imaging.

Unfortunately, this problem was only identified after the laser used for excitation broke making reacquiring the images impossible. However, from the trend noted between the two acquired images from the 3.6 μm device, with proper dye concentration, the uniform region should shift into the channel approximately 8 μm making the measured 16 μm values from Table 4-2 a more acceptable 24 μm. This confirms that the new designs are approximately centred in the channel. Furthermore, simulations have been shown to be accurately replicated during fabrication and means that new designs will be sufficient for cytometric performance.

**Table 4-3: Values for the uniform intensity region for the 3.6 μm device with a) early and b) recent results.**

| Device (μm) | FWHM (μm) | Width of defined uniform (μm) | Depth of Focus (μm) | Beam Position (μm) |
|---|---|---|---|---|
| 3.6 (old) | 7.4 | 2.1 | 8.3 | 22.3 |
| 3.6 (recent) | 9.3 | 3.9 | 14.0 | 14.6 |

Another effect of the dye is the change to the measured depth of focus parameter in Table 4-2. The drastic increase from 8.3 μm to 14.0 μm is not all from the simulation. From the best estimate of simulations the increase would have been to 12 μm, the remaining would be attributed to the absorption effect of the concentrated dye. This would affect the measured values in Table 4-2, changing them to approximately 6/7s their reported value.

A potentially serious performance issues with the old designs was the rather large amount of stray light in the channel outside of the beam image. As noted earlier in section 4.2.1.1, this stray light is from the low collection NA of the lens system. A mismatch of the NA of the input lens system and the output NA of the waveguide means that the lens system missed the most divergent rays. Small beam waists had lens systems that had smaller input NA and this resulted in more light in the channel and closer to the formed beam. This stray light can degrade the performance of the device by serving as another excitation point for other particles in the stream causing events to have early or late artifacts. To remedy this, a simple solution was instituted. Light blocking structures were introduced to eliminate this light, as shown via the photomask designs in Figure 4-39. An overlay (in yellow) shows the light rays that are missed by the lens system that show up as stray light. Through the introduction of voids in the device layer that form very large angles of incidence with these rays, the stray light can be deflected via total internal reflection. The stray light may enter the channel after it is reflect, however it will be far enough from the interrogation point that no negative effect is reasonably possible.

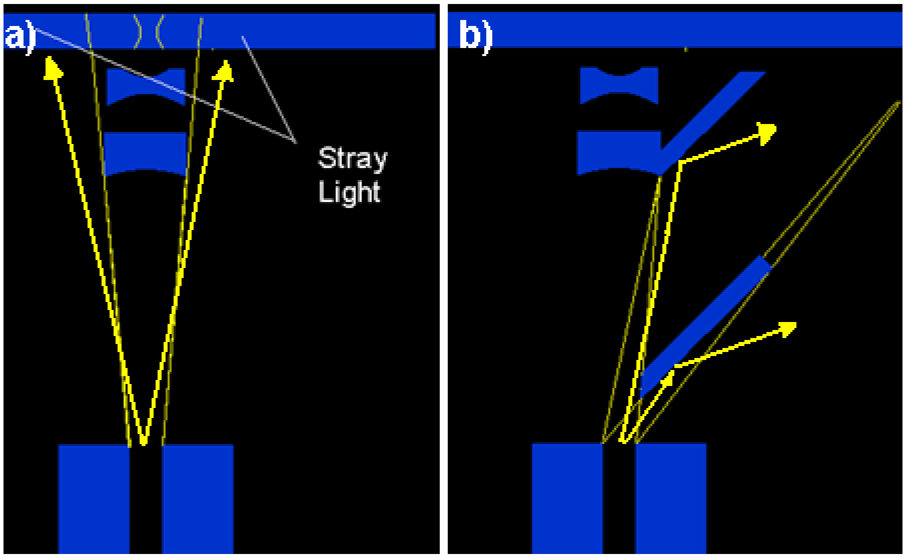

**Figure 4-39: Designs to eliminate stray light in the channel as determined by the input NA of the lens system.**

Deployment and function of the devices is shown in Figure 4-40a) where a bright-field image of the device with the realized light blocking structures is shown with the coupled input laser beam. Obvious scattering is seen off the structure. A dark field image of the exact same field of view from Figure 4-40a) is shown in Figure 4-40b). The absence of the backlight enhances the scattering and demonstrates that it is functioning at it is intended – however, there still appears to be a lot of scattering off the channel wall. This scattering off the channel wall is though to be from the scattering off the lens system and will not amount to much in the channel. Applying the fluorescent dye in the channel to visualize the stray light shows excellent blocking ability. Figure 4-41 shows fluorescent images from the 1.5- and 10 μm devices both with and without light blocking structures. The devices that employed the light blocking structures demonstrate a complete removal of this stray light.

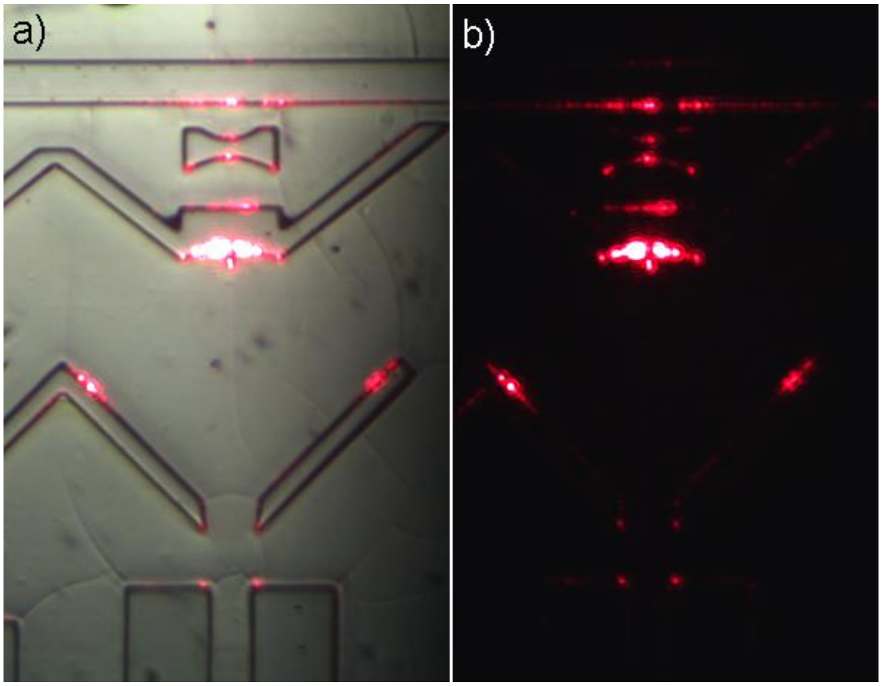

**Figure 4-40: a) Light field and b) dark field images with and input beam showing the operation of the light blocking structures. Scattering is still present at the channel wall from the lens surfaces.**

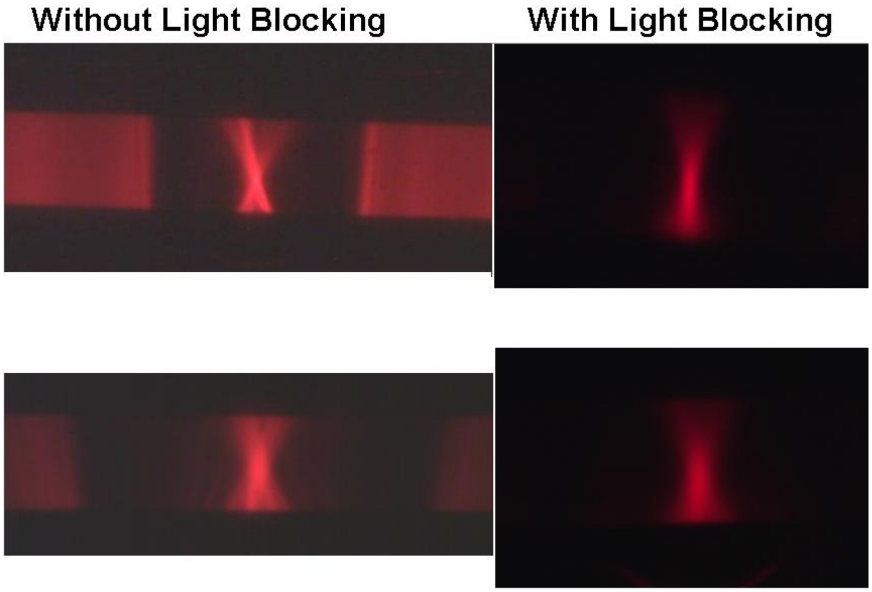

**Figure 4-41: Contrast of the effect of light blocking structures on the formed beams from 1.5- and 10 µm devices: without the structures (left) and with structures (right).**

### 4.2.2 Cytometric Function (Bead Flow)

With beam shapes characterized, the performance of the devices with beam shaping capabilities can be determined in a practical flow cytometric function. As the specimen size will have a different interaction with each beam geometry, it is necessary to test every beam with multiple bead diameters in both fluorescent and scatter detection situations. Proper deployment of these designs on a chip will allow fabrication of devices with a specific application in mind. Fabrication of multiple lens designs on chip in a parallel fashion would allow multiple detection analysis in a single run – however, the interaction with beam geometry must be characterized to ensure device designs suit device function.

#### 4.2.2.1 Fluorescence detection

To get a comparison for the improvement of placing a lens system on the chip, the first step is to characterize the performance from a device that instituted no integrated lens system deployed on-chip. This comparison will allow an immediate conclusion of whether the lens systems improves device performance.

The first experiment ran 6.0 μm fluorescent spheres through a device that had no beam shaping optics, the results of which are summarized in Figure 4-42[‡‡‡] The excitation in the interrogation region is from the injection of a multimodal beam from the on-chip integrated 50 μm core width waveguide. A sample of the collected raw data, along with an inset of the fluorescent beam image, is shown in Figure 4-42a). The bursts from the raw data have a rather uneven distribution of intensity. This is expected as the beam as shown in the inset has a very large beam width (~75 μm) with a diminishing intensity across the channel along with a variable intensity along the channel. This beam geometry, as has been mentioned several times within this work, is not ideal for flow cytometry application due to the large variation of specimen excitation. Indeed, this poor performance is confirmed from the histogram formed from the entire 100 second long test in Figure 4-42b). The shape of the histogram indicates how unacceptable the

---

[‡‡‡] This paragraph and analysis is from the author’s published work in reference 98.

performance is. There appears to be a very large instance of double detections – nearly twice the amount of single detections – as evident by the very large collection of events on the histogram that are approximately twice the intensity of the smaller population at the left of the histogram. Furthermore, as the populations are severely overlapping and partially indistinguishable, this would lead to an ambiguous conclusion or confusion when a sample population with non-uniform characteristics is analyzed, unlike the uniform microbeads used in this experiment.

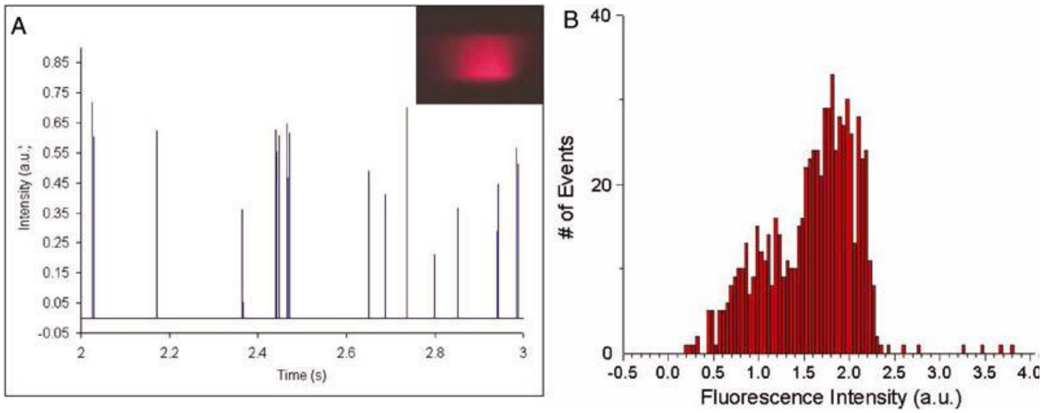

**Figure 4-42: a) Plot showing one second of raw runtime data from a counting test of 6 µm beads employing a device with no beam shaping and a sample image of the beam (inset). b) the associated histogram plot from an entire 100 second run showing a confusing population. *Source*: Reprinted from reference 98.[§§§]**

There are examples of devices that use the injection from a fiber and achieve a better performance than what has been observed here, but in these cases the optical input is from a high-quality single mode beam light source. Such a source is avoided in this device as it would add complexity to coupling and substantially increase the cost of the device and limit feasibility in remote and POC applications.

Now, the performance from a device with a lens system is analyzed to show the immediate benefit. A device with a 10.0 µm beam is used with the same fluorescent beads as in the previous experiment; the results are shown in Figure 4-43. A selection of two seconds of real time data is shown in Figure 4-43a) and

---

[§§§] This figure is from the author’s work published in reference 98.

clearly shows the fluorescence bursts are of a near uniform value with only a slight variation due to the uniform beam intensity formed across the interrogation region in the middle of the channel (inset). The histogram from the run is shown in Figure 4-43b) and indicates the overall performance of the device. All events are located around a central mean yielding a CV of 16.7% obtained from the fitted Gaussian curve (as outlined in the procedure given in section 3.3.2). There is a small bump at approximately 2× the histogram mean, 3.0, indicating a very small amount of double detections. The occurrence of these events is very small and represents less than 1% of total events and is negligible for most applications[****]

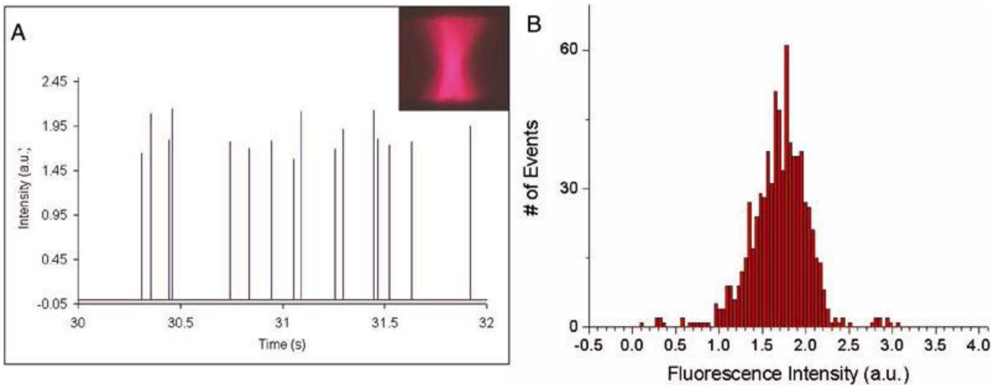

**Figure 4-43: a) Plot showing two seconds of raw runtime data from a counting test using 6 µm beads employing a device with a 10 µm beam waist and a sample image of the excitation beam (inset). b) Associated histogram plot for the full 100 second test showing a clean obvious population. *Source*: Reprinted from reference 98.**[††††]

A direct comparison of Figure 4-42 and Figure 4-43 clearly demonstrates the performance advantage gained from integration of the lens system on-chip. Performance is enhanced from the more uniform detection intensities from a population of uniform microspheres. With an obvious advantage of enhancing the detection performance from the integrated lens system it is important to test to see how the performance of devices – specifically the CV - varies with changes in deploy beam geometry via the different lens designs.

---

[****] This paragraph and analysis has been adapted from the author's published work in reference 98.

[††††] This figure is from the author's work in reference 98.

Previous tests we run once again, but this time with a smaller beam waist deployed on-chip. Figure 4-44 show results from a 1.5 μm beam deployed with 6 μm particles. A three second span of raw data shown in Figure 4-44a) shows excellent control of the variation of burst intensity – though not as good as the control from the 10 μm design. Degradation of the performance is mostly due to the bead being too large for the formed beam geometry. The 6.0 μm particle is much larger than the uniform region, as indicated by the parameters in Table 4-1, and thus, a significant portion of the bead will be outside this region. Furthermore, the shifting of the uniform geometry in the device towards the injection side means that the beads traversed the beam in the more divergent section of the beam just outside of the uniform region leading to variation in excitation intensity. Indeed, analysis from the histogram in Figure 4-44b) produces a CV of 21.7% for this device. The incidence of double detections is very low as the beam is too narrow to allow two beads in the beam simultaneously. The overall performance of the device is better than the performance from a device with no lens system, yet it is not as good as the performance from the design that deployed a 10 μm beam waist. This indicates an optimum deployment where the beam must be tailored to the specimen's size.

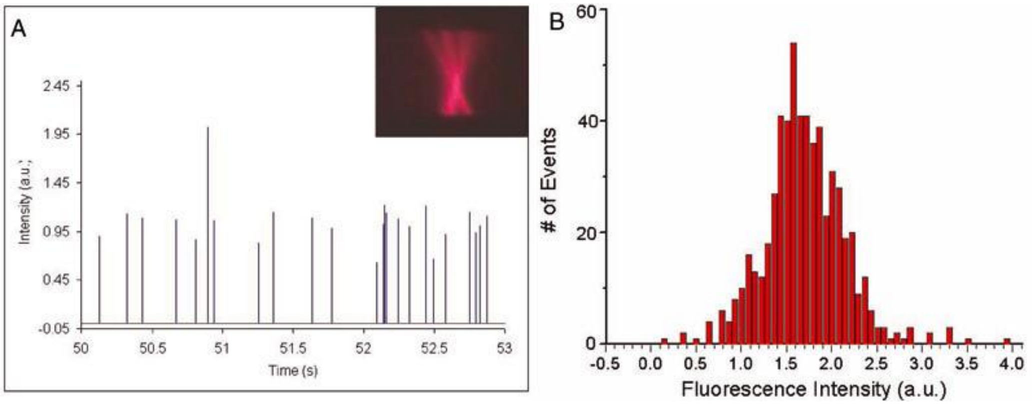

**Figure 4-44: a) Plot showing three seconds of raw runtime data from a counting test using 6 μm beads employing a device with a 1.5 μm beam waist and a sample image of the excitation beam (inset). b) Associated histogram plot for the full 100 second test showing a clean population. *Source*: Reprinted from reference 98.**[‡‡‡‡]

---

[‡‡‡‡] Figure from the author's published work in reference 98.

As changing the beam geometry in the channel affects the device performance, so too will the device performance change if the bead size in the sample stream is changed. Figure 4-45 shows histogram plots from two different fluorescence tests performed with 2.5 μm beads in two different devices. The device in Figure 4-45a) employs a beam geometry with a 3.6 μm beam waist, while the device in Figure 4-45b) forms a 12 μm beam waist. Both results are better than the performance from a device with no beam shaping as they form a distinct population, but it is obvious that the performance of the device with a 3.6 μm beam geometry is superior due to the more tightly confined population of events. Therefore, when designing a lens system into the device to improve device performance, it is imperative that the beam geometry be tailored to the characteristic size of the specimen in the biological analysis. This confirms the premise formed just above: that the device's performance is dependent on the combination of bead size and the beam geometry.

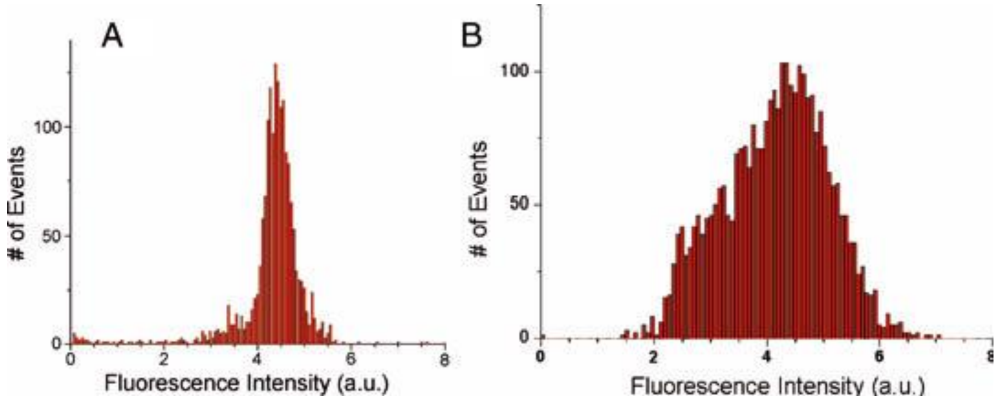

**Figure 4-45: Histograms from a 3.6 μm device (a) and a 12 μm device (b) using 2.5 μm beads showing much better performance from the 3.6 μm device. *Source*: Reprinted from reference 98.**

### *4.2.2.1.1 Performance Summary*

To determine the relationship between the beam geometry (specifically the beam waist) and the bead size, multiple devices with various beam waists were tested with both bead sizes while the CV was recoded. Tight hydrodynamic focusing was employed so that the sample stream was only slightly larger than the particle size. Table 4-4 contains the results from these tests. Different detection accuracies from employed beam configuration exist for each bead size: the best configuration is 3.6- and 10 μm beam waists for 2.5 and 6.0 μm bead particles, respectively. There is a range of acceptable beam geometries that exist for each specimen size, and given the analysis performance requirements, these could be within a deemed acceptable performance. Performance deterioration outside this range exists as beams too small or too large yield the worsening results. Beams much smaller than the particle size will result in the specimen being excited by the divergent areas of the beam outside the designed beam geometry, while beams much larger than the specimen size cause larger variation in detection; possibly due to the overlap integral between the bead and beam being more sensitive to beam intensity variation (an increasing phenomena as the magnification increases to 1 and the multimode's variation in intensity profile is preserved). Better CVs are obtained for the smaller beads, and this is expected as the manufacturer's data holds a tighter tolerance on the fluorescence CV for the 2.5 μm beads than for the 6.0 μm beads.[§§§§]

When designing the device with an integrated lens system, careful consideration must be made about the specimen(s) size and the lens system used to ensure reliable detection. Table 4-4 indicates optimal beam/bead combination but can also, as noted earlier, indicates a range of appropriate beam shapes given the performance requirement of the specific analysis. The SNR value of each fluorescent measurement was maintained at a high level for all the tests performed—ensuring accurate and obvious detection of fluorescent bursts. The 6.0 μm beads show much less then a 2× deviation from the optimal CV value over all the beam geometries used, while the 2.5 μm beads show a narrow range where the CV deviates less then 2× from the optimal value. For example: a 10 μm beam geometry could analyze both 2.5- and 6.0 μm beads despite the fact that better detection from the 2.5 μm beads could be obtained from a 3.6 μm beam geometry. If the slightly worse CV for the 2.5 μm beads is acceptable for the analysis being

---

[§§§§] This paragraph and analysis is from the author's published work in reference 98.

performed, then both populations could be done with one device – saving cost and allowing multiplexing on a single platform.[*****]

**Table 4-4: Collection of fluorescence performance parameters for different lens designs and bead sizes. *Source*: Reprinted from reference 98.**

| Beam | 2.5 um beads | | | 6.0 um beads | | |
|---|---|---|---|---|---|---|
| Waist (um) | CV (%) | DD (%) | SNR | CV (%) | DD (%) | SNR |
| 1.5 | 22.0 | n/a | 15.9 | 21.7 | 2.5 | 39 |
| 3.6 | 8.5 | 1.0 | 384 | 17.7 | 0.2 | 518.9 |
| 6.0 | 10.9 | 0.3 | 58.2 | 17.9 | 1.0 | 450 |
| 10.0 | 10.5 | n/a | 404 | 14.6 | 1.8 | 87.8 |
| 12.0 | 25.8 | 1.4 | 11.8 | 24.3 | 1.5 | 23.1 |

The very large SNR recorded for the tests are far above the ‘acceptable minimum’ for feasible deployment. The optimal SNR are the devices that form 3.6-, 6.0-, and 10 μm beams for both the 2.5- and 6 μm beads. As the beam is very concentrated with the 3.6 μm design, it has a very large energy density at the specimen, and thus a very large SNR. The SNR for the 6 μm bead is larger in this device as the entire bead is illuminated at once. The SNR is larger for the 6 μm beads because they generate a larger signal due to the much larger size of the particle.

The misalignment of the 1.5- and 12 μm beams have an obvious disadvantage as both have poor performance and low SNR – though still within an acceptable limit. The small SNR in the 1.5 μm device is because the beads traverse the lower intensity portion of the beam in the divergent region – the 6 μm have a larger signal partly because of the larger size (and therefore more fluorescent dye present) but also because the larger size means that part of the bead overlap with brighter section of the beam.

The values from Table 4-4 are from results with the original beam designs. The revised designs were tested – though only once. A summary of the newer design’s performance parameters are tabulated in Table 4-5. Not all devices were tested as the excitation laser used in testing malfunctioned before all the devices could be tested, most notably the 1.5 μm device with 2.5 μm beads.

---

[*****] This paragraph and analysis is from the author’s work in reference 98.

Obviously, the CVs are improved for the 1.5- and 12 μm lens systems – confirmation the that improvements to beam design will improve the performance of the device - while the double detections and SNR is quite unchanged, also as expected as the intensity and beam widths were not significantly changed. The CVs for the experiments with the 6 μm beads all improved slightly – this is likely due to the improved fabrication quality with the more recent devices. The SNR for the 1.5- and 12 μm are still quite low, this is because the design for the 12 μm beam spreads the intensity out a little too far while the 1.5 μm design loses a significant amount of light at the input of the lens system.

**Table 4-5: Collection of fluorescence performance parameters for revised lens designs.**

| Beam | 2.5 um beads | | | 6.0 um beads | | |
|---|---|---|---|---|---|---|
| Waist (um) | CV (%) | DD (%) | SNR | CV (%) | DD (%) | SNR |
| 1.5 | n/a | n/a | n/a | 8.9 | n/a | 37.8 |
| 3.6 | 6.6 | 0.8 | 69 | 9.0 | 0.2 | 611 |
| 6.0 | 9.0 | 0.5 | 41.5 | 13.9 | 1.3 | 554 |
| 10.0 | 7.3 | 0.8 | 400 | 10.4 | 2.0 | 113 |
| 12.0 | 12.6 | 1.6 | 11.6 | 10.8 | 1.4 | 56.7 |

Again, the best performance for the 2.5 μm beads is with the 3.6 μm beam design, though the highest SNR is with the 10 μm device due to large collection of input light. The 6.0 μm beads have much better performance for all beam designs and seems to have best performance from the 1.5 μm beam – in terms of the CV. Reasons for this are that the beam is focused to a very tight spot and has a much greater depth of focus allowing the 6 μm bead to have much better interaction with the beam - as noted in Table 4-2. All performance parameters are increased due to the increased device quality to fabrication, but also could be receiving some added benefits from less noise due to the stray light blocking designs discussed at the end of section 4.2.1.4.

### *4.2.2.1.2 Device Flexibility*

When trying to detect a population that contains two or more bead sizes careful deployment of device design must be taken. If a device were to be used to detect multiple specimen sizes simultaneously, the smaller specimens would have to exhibit acceptable performance from the device with a relaxed condition on hydrodynamic focusing as the larger specimen will determine the minimal sample stream width. Figure 4-46 shows histograms from successive bead flow tests using 2.5 μm beads in a device that forms a 10 μm beam waist while the hydrodynamic flow is relaxed to allow successively larger sample stream widths. Sample stream widths of 2, 3, 5, and 10 μm are shown in Figure 4-46a) through d), respectively. As can be seen, best detection accuracy occurs when a 3 μm sample stream is used, which is shown in Figure 4-46b). Very tight focusing, Figure 4-46a), shows slight deterioration in performance, while a relaxed condition where the sample stream is 2×, the bead diameter shows slight deterioration as well (Figure 4-46c). The large sample stream, 10 μm in Figure 4-46d), shows a very wide histogram, yet still a distinctive population.[†††††]

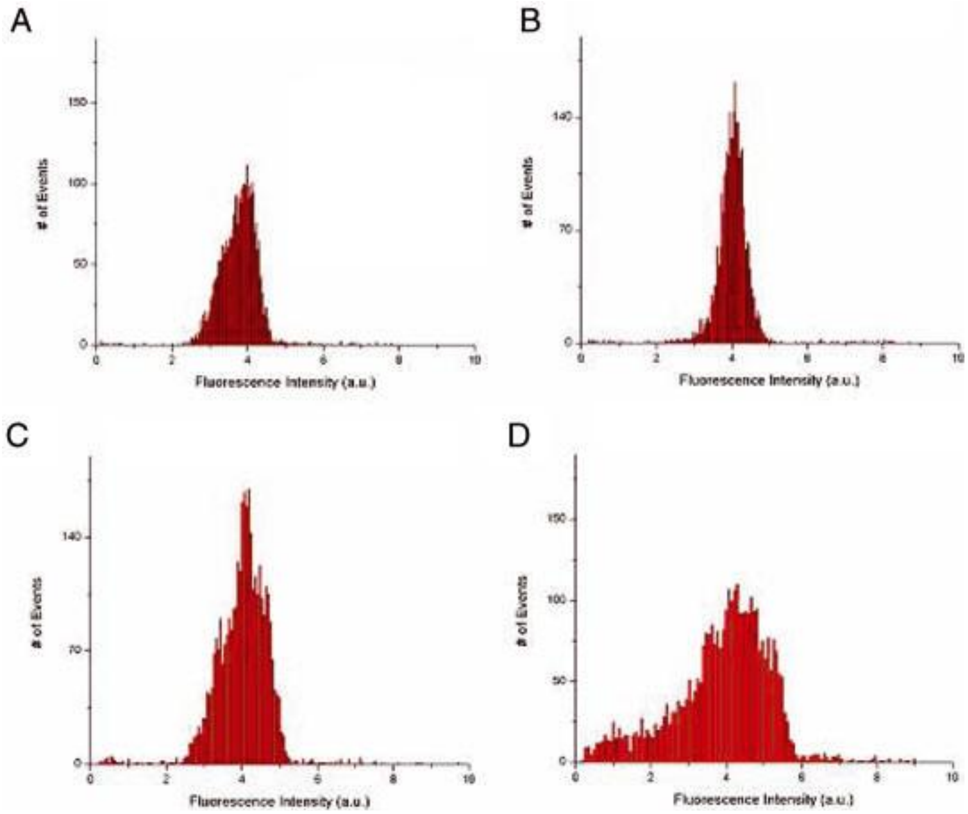

**Figure 4-46: Multiple histograms from fluorescence detection tests using 2.5 μm beads in a 10-um device with varying hydrodynamic focusing with sample stream widths of a) 2 μm, b) 3 μm, c) 5 μm, d) 10 μm. *Source*: Reprinted from reference 98.**

---

[†††††] This paragraph and analysis is from the author's published work in reference 98.

Table 4-6 summarizes the CVs from the histograms in Figure 4-46. Deviation of the CV from the optimal sample flow (3 μm stream) using tight flow focusing (2 μm stream) or relaxed flow focusing (5 μm stream) is slight, increasing less than 1.5×. The 10 μm sample flow—4× the beam diameter—shows a CV of 21.5%, a poor performance compared to an optimal configuration, but still allows proper conclusions. The larger number of low-intensity detections (at the expense of detections at the peak), in the histogram of Figure 4-46d) compared with Figure 4-46b), is due to the increased number of beads interacting with edges in the depth of focus. However, this beam has excellent designed uniform optical intensity along the beam as normally a relaxed flow condition is disastrous to the CV. The relaxed hydrodynamic flow condition increases sample throughput while allowing devices to be less complex. However, the increased sample stream width increases sample solution in the beam and increases the probability of double detections. A flow condition of 10 μm in this example would be a logical limit as the CV is increasing to a level that limits accurate conclusions while the double detections have started to increase significantly.[‡‡‡‡‡]

**Table 4-6: Collection of data from 2.5 μm fluorescent beads tested with a 10 μm device where the sample stream width was varied to show performance of the uniform excitation area. *Source*: Reprinted from reference 98.**

| Stream Width (um) | CV (%) | DD (%) |
|---|---|---|
| 2 | 11.6 | 1.24 |
| 3 | 9.5 | 1.29 |
| 5 | 13.9 | 1.18 |
| 10 | 21.5 | 2.15 |

Though multiple particle analysis is possible with an adequately shaped beam and relaxed hydrodynamic focusing, our designs also permit side by side placement of multiple optical components next to the channel and therefore allow multiple interrogation regions with specifically formed beam geometries all on one device in one manufacturing process. To accommodate this design, it would require introducing split light with a fiber array or directly integrating a well-know waveguide power splitter structure into the device. Nevertheless, if one

---

[‡‡‡‡‡] This paragraph and analysis is from the author’s published work in reference 98.

optical interrogation can fulfill the analytical needs then there is no need to over-engineer the device.[§§§§§]

#### 4.2.2.2 Free-Space Scatter Detection

As noted in section 2.1.4.1, scattering is a much different phenomena than fluorescence. Much as for the fluorescent detection just discussed, there is a need to determine the correct way to deploy lens systems on chip when scattered light is considered. The main goal is to determine the performance of the device with on-chip integrated excitation optics and compare results to conventional methods. The devices were deployed in a single parameter free-space side (90°) scatter free-space collection. The secondary goal is to determine the relationship (if any) of the beam geometry and bead size has on the device performance – also similar to the fluorescence detection just discussed.

Figure 4-47 shows results from an experiment that ran 2 μm beads through devices that deployed designs to form 6.0- and 12 μm beam waists in the channel. Figure 4-47a) and b) shows samples of the raw data from the tests with each device. Histograms in Figure 4-47c) and d) confirm there is a difference in performance depending on the beam geometry used – the narrow population from the 6.0 μm device has better performance.

The burst intensities from the 6 µm device show much more uniform bursts than those from the 12 µm device. Figures 4c) and d) show the histograms from the full 100 second runs shown in a) and b). Much better performance was obtained from the 6 µm device based on the much narrower histogram. The CV for the 6 µm device was calculated at 11.0% while the CV for the 12 µm device was calculated to be 19.1%. There was also a low incidence of double detections recorded in each device as evident by a small number of events outside the main population.[******]

---

[§§§§§] This paragraph and analysis is from the author’s published work in reference 98.

[******] This paragraph and analysis are from the author’s work in reference 123.

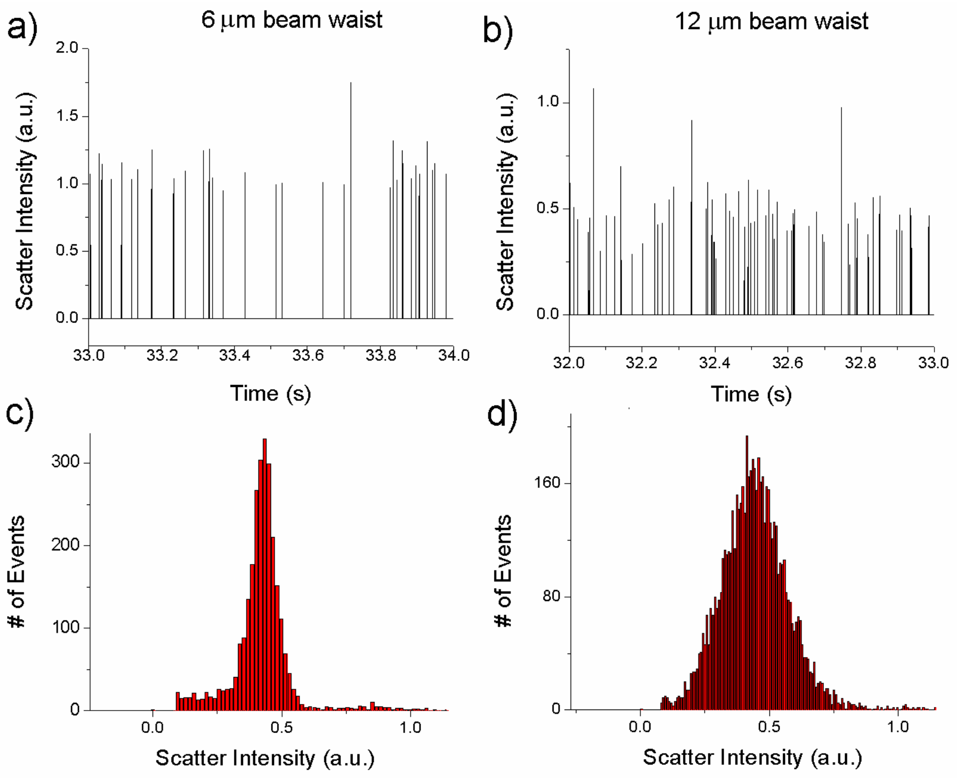

**Figure 4-47: Raw scatter data from (a) 6 μm device and (b) 12 μm device with 2 μm blank beads. The histograms for the (c) 6 μm and (d) 12 μm devices indicate a relationship between bead size and beam width with respect to device performance. *Source*: Reprinted from reference 123.**

The above tests were run again with the same devices, but instead with 5 μm beads. The results are shown in Figure 4 47. Figure 4 47a) and b) show samples of raw data from runs using 6 μm and 12μm devices, respectively. The bursts are clear and easily identified from others. There is noticeably better uniformity of burst intensity from the 6 μm device, though there is less of a difference in burst intensity between the two devices using the 5 μm beads than the 2 μm beads. Figure 4 47c) and d) are histograms obtained from the full 100 second tests which are represented in a) and b); again with adjusted horizontal intensity axes. As noted before, better performance is obtained from the 6 μm device as evident by the narrower histogram. The CV calculated for the 6 μm device was 12.5% while the CV for the 12 µm device was 16.5%. As with the 2 µm beads, a low incidence of double detections was observed.[††††††]

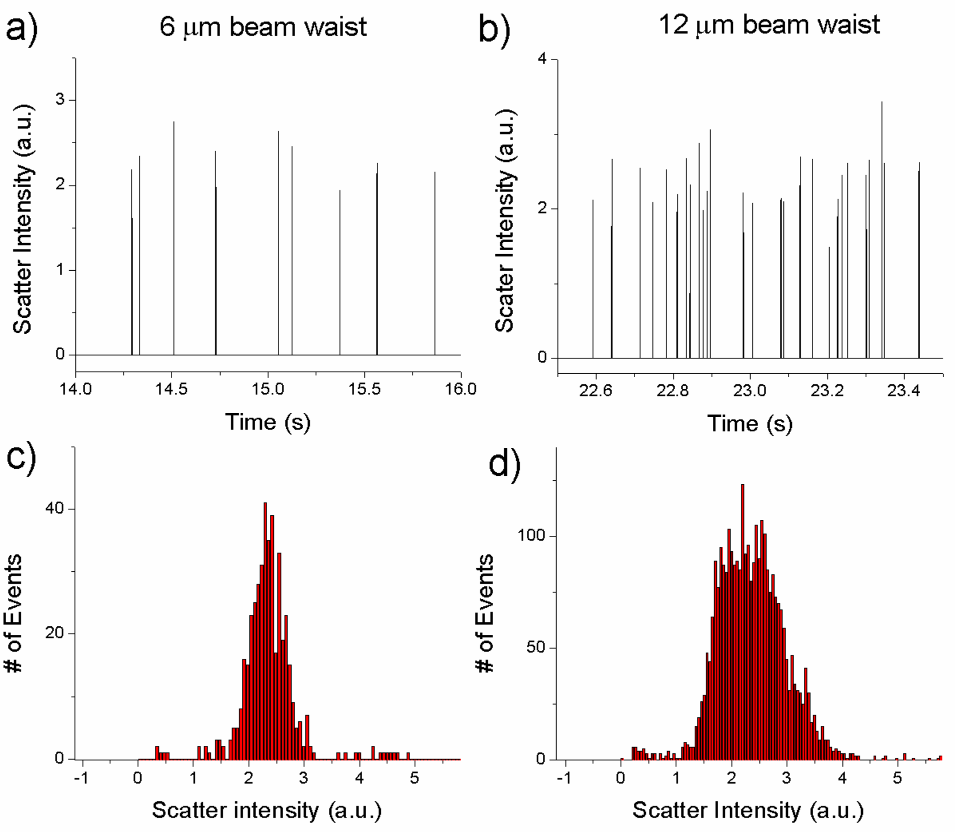

**Figure 4-48: Raw scatter data from (a) 6-um device and (b) 12-um device with 5-um blank beads. The histograms for the (c) 6-um and (d) 12-um devices indicate a relationship between bead size and beam width with respect to device performance. *Source*: Reprinted from reference 123.**

#### *4.2.2.2.1 Performance Summary*

Testing all the design beam shapes with the different bead sizes allows an accurate conclusion to be drawn about the deployment of devices on chip

Tests for several devices that formed different beam waists were performed with three different bead diameters in each: 1-, 2-, and 5 µm diameters. Devices that formed 3.6-, 6-, 10-, and 12 µm beam waists were used. Performance parameters collected from each device were the CV, the parameter to define the performance of a device; double detections (DD), to ascertain the device's ability

---

[††††††] This paragraph and analysis are from the author's work in reference 123.

to retain accuracy over single/aggregate particles; and the SNR, the ability of the device to distinguish bursts from background noise.[‡‡‡‡‡‡]

Data from all these tests is summarized in Table 4-7 showing the CV, SNR, and DD for all beam/bead size combinations

**Table 4-7: Collection of free-space collection data for three different bead sizes in four different beam sizes. Note a universal relationship does not exist for all bead/beam size combinations. From B. Watts Scatter paper currently being written.**

| Beam | 1µm | | | 2µm | | | 5µm | | |
|---|---|---|---|---|---|---|---|---|---|
| Waist (µm) | CV (%) | DD (%) | SNR | CV (%) | DD (%) | SNR | CV (%) | DD (%) | SNR |
| 3.6 | 28.0 | 5.5 | 6.0 | 18.8 | 2.1 | 8.7 | 16.5 | 3.2 | 8.8 |
| 6.0 | 22.7 | 5.5 | 2.4 | 11.0 | 2.4 | 5.4 | 12.5 | 3.15 | 11.7 |
| 10.0 | 16.4 | 6.3 | 3.5 | 14.6 | 2.3 | 5.5 | 17.0 | n/a | 6.7 |
| 12.0 | 17.5 | 13.4 | 9.7 | 19.1 | 2.0 | 13.9 | 16.5 | 2.4 | 32.3 |

Careful inspection of the table yields no obvious relationship that can be applied universally to bead diameter/beam size combinations, as was the case when the fluorescence parameter was investigated. The 1 µm diameter beads seem to have had best performance with a 10 µm beam waist in terms of the calculated CV. The 12 µm device yielded a larger SNR due to the larger collection of input light and thus, larger intensity at the point of interrogation. So, one could sacrifice accuracy as DD's increase due to the larger beam waist if it was necessary to have a strong signal. The 2 µm and 5 µm diameter beads have best performance with the 6 µm device. There is more deterioration of performance with 2 µm beads as the beam sizes move away from 6 µm beam geometry than with the 5 µm beads. The SNR increases with beam waist – as expected as larger beam waists collect more input light to focus at the interrogation point. One reason for the 1 µm beads having such a different CV than the other bead sizes could be due to hydrodynamic flow conditions. The sample flow rate was fixed with all bead sizes, however, tighter hydrodynamic focusing would force the sample fluid to move faster for smaller sample widths causing shorter interrogation times not compatible with the signal sampling rate.[§§§§§§]

---

[‡‡‡‡‡‡] This paragraph and analysis are from the author's work in reference 123.

[§§§§§§] This paragraph and analysis are from the author's work in reference 123.

As no obvious trend exists, it is necessary to deploy the lens system that yields the best results by consulting a table of results similar to Table 4-7. It is noteworthy that the scatter detection's SNR is significantly lower than the SNR from the fluorescence detection tests. This is contrary to normal reports in literature.

#### *4.2.2.2.2 Device Flexibility*

As discussed in section 4.2.2.1.2, devices could be required to handle a population of more than one specific sample size. In this case, the devices must be able to adequately resolve two or more populations clearly.

To test the versatility of devices and beam uniformity, a suspension containing different bead sizes was run through two different devices: the 6- and 12 µm devices. The bead solution combined an equal concentration of 2 µm and 5 µm beads. The devices were tested to determine whether performance was adequate enough to clearly resolve both bead sizes without the different populations interfering with each other. This is a tricky problem as hydrodynamic focusing is changed to suit the larger bead size, thus the results in Table 4-7 aren't the best choice. This is due to the 2 µm particles having a much larger deviation in the beam because of the 6 µm stream width to accommodate 5 µm particles.[*******]

Figure 4-49 shows a comparison between the performances of two devices. Figure 4-49a) shows histograms from the 12 µm device indicating clearly resolvable populations. Figure 4-49b) shows histograms from the 6 µm device and has slightly worse performance as the histograms are overlapping slightly. This would cloud further analysis of individual populations. It is interesting to note that there is not much difference in performance from either device with respect to the 5µm beads. This is expected as one can conclude from results in Table 4-7. However, the difference is in the analysis of the 2 µm particle. According to Table 4-7, 2 µm beads have better performance within a 6µm beam

---

[*******] This paragraph and analysis is from the author's work in reference 123.

waist, however, that is for tight hydrodynamic focusing. Relaxed flow conditions allow beads to traverse the edges of the intended illumination area in the beam and results in more variation of excitation. Therefore, since the 12 µm device has a larger region of uniform illumination, it is large enough to cover the 6 µm sample stream width and ensure more uniform illumination of particles.[†††††††]

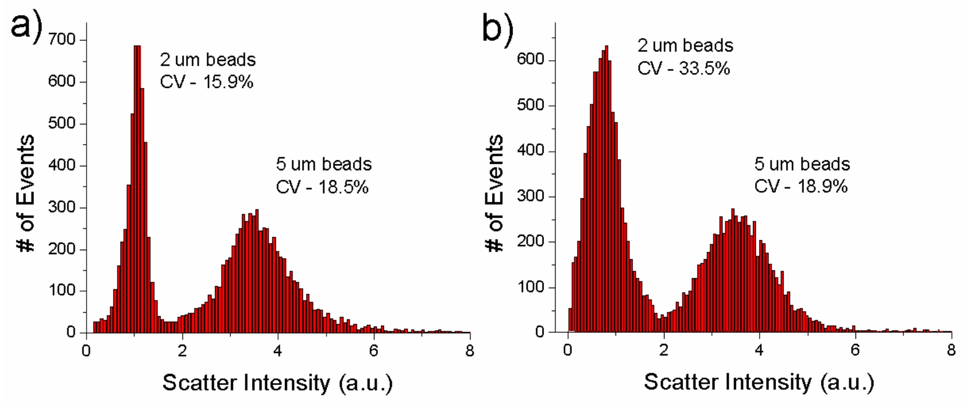

**Figure 4-49: Histogram plots from tests using a mixture of 2 and 5-um beads in devices forming beam widths of a) 12-um, and b) 6-um. *Source*: Reprinted from reference 123.**

#### *4.2.2.2.3 Reproducibility*

I have a couple tables to insert here that show device performance is repeatable from run-to-run, day-to-day, and device-to-device.

### 4.2.2.3 On-Chip Side Scatter

Up until this point all tests have been done with on-chip optics to perform excitation beam shaping with a free-space detection scheme to prove the function of the excitation optics. On-chip collection via a waveguide is the next step towards a fully integrated device and alleviates the dependence on free-space optics. It offers compact size, low equipment cost, excellent portability, and easy operation. Calibration steps are eliminated in this detection as fabrication automatically aligns the optics and guarantees calibrated chips.

---

[†††††††] This paragraph and analysis are from the author's work in reference 123.

Confirmation of the on-chip optical components was performed with a device that formed a 10 µm beam waist and used 5 µm beads as they would produce the largest signal from the beads used in previous tests. Results from the test are shown in Figure 4-50.

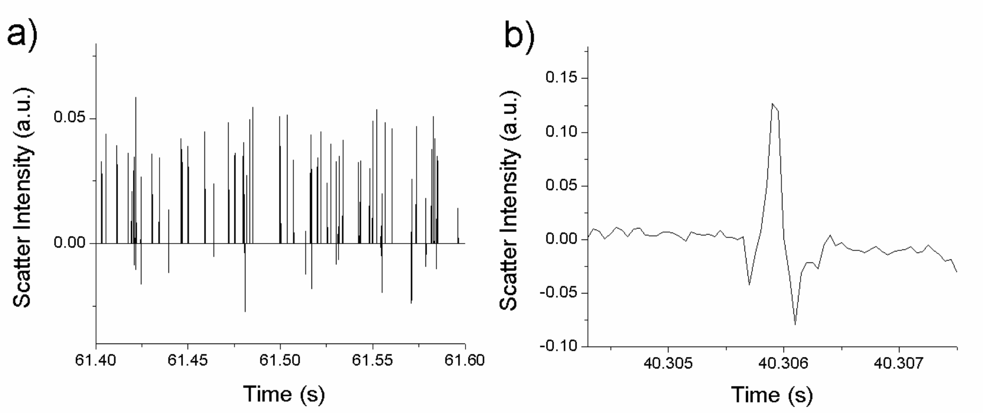

**Figure 4-50: Data from on-chip side scatter collection from a device deploying a 10-um beam waist showing a) 0.2 seconds of raw data and b) a detail of one of the pulses showing a clear negative burst before and after the positive burst. *Source*: Reprinted from reference 123.**

Raw data is shown in Figure 4-50a) with clear and distinguishable bursts, however, with varying intensity. Figure 4-50b) shows detail of a single pulse of data with an obvious negative burst before and after the positive burst. These artifacts are present in all bursts, though with varying intensity. This is due to the movement of the bead into the excitation beam. As the input and collection waveguides are directly across the channel from one another, the output will collect some stray light from the input beam. As the particle comes into the beam it will first deflect the stray light from the input away from the output waveguide. As the particle moves to the centre of the beam, the scattered light from the particle is directed towards the collection waveguide creating a positive burst. As the particle moves out of the beam the scattered light will disappear on the output waveguide as well as the stray light from the input as the particle blocks it. As the particle exits the beam fully, the signal will return to up to the baseline level. This is absent in free-space collection – as evident in Figure 3a - as the beam and the collection axes are not collinear and therefore the excitation beam is not coupled into the detection aperture

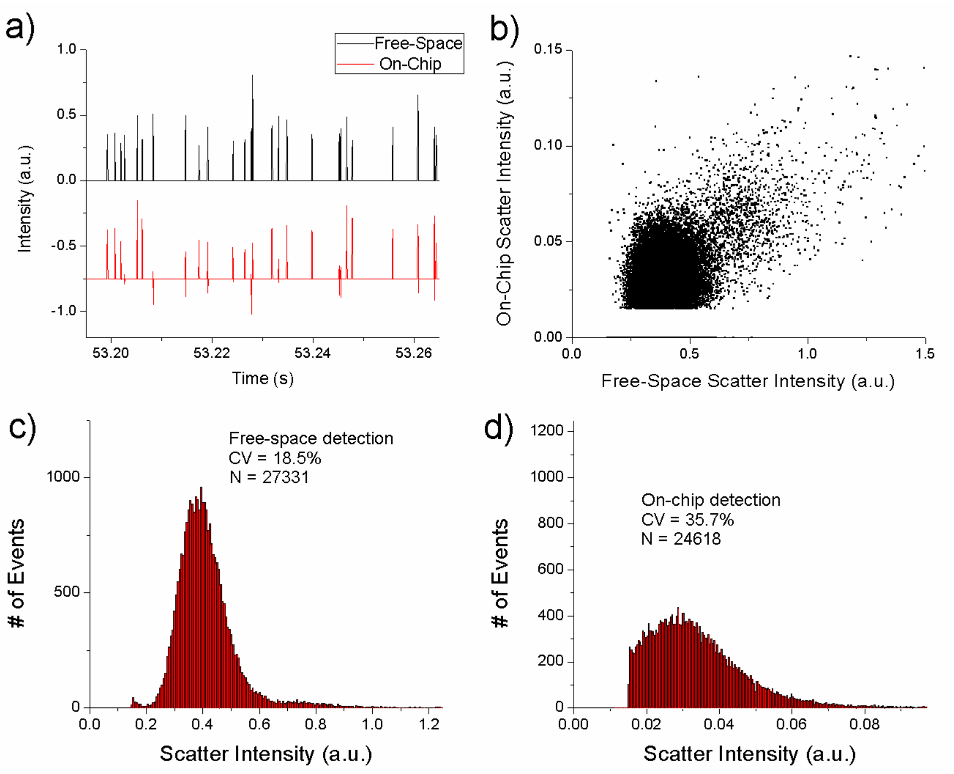

**Figure 4-51: Data from a 2-parameter collection of free-space scatter and on-chip scatter. a) a comparisson of raw data, b) a scatter plot showing an obvious population. Histogram plots from c) free-space and d) on-chip collection show similar populations. *Source*: Reprinted from reference 123.**

To verify the validity of the on-chip detection, the on-chip collection was compared to free-space detection. The free-space detection method is reliable…. The two collection methods were performed simultaneously and events from both methods should correlate exactly. Figure 4-51 shows the results from the test. A sample of raw data from both methods is plotted on the same axes shown in Figure 4-51a). Data shows simultaneous events from both methods and more intensity variation from bursts in the on-chip method. Figure 4-51b) shows a scatter plot of each event's free-space and on-chip scatter intensities. A clear population is visible with a slight double detection population visible - though controlled due to the beam width.[‡‡‡‡‡‡‡]

The histograms in Figure 4-51c) and d) are 1D populations depicting each one of the scatter plot's axis, free-space and on-chip, respectively. The calculated CV for the free-space collection was determined to be 18.4% while the on-chip collection CV was calculated to be 29%. The free-space CV is exactly what was expected (from Table 4-7) however, the on-chip CV was a bit high. This was most likely due to a large source of noise on the output waveguide due to a fibre/waveguide geometry mismatch allowing coupling into the substrate and sealing layer. This leaked light could traverse the device and couple into the output fibre quite easily. Furthermore, a lack of full 3D hydrodynamic focusing was thought to also be a large contributor to the increased CV as the particle could be found anywhere in the vertical dimension of the channel.[§§§§§§§]

To accurately quantify the performance of the on-chip detection scheme it is compared to the free-space scheme as there should be a perfect correlation between events from each detection arm. The procedure outlined in section 3.3.2 is used with the script from Appendix G to perform the analysis. Assuming that the free-space scheme is 'perfect' we can assume that lone free-space events are the total missed events by the on-chip scheme while the lone on-chip events are interpreted as false positives. The total number of free-space events totaled 27331 while the number of on-chip events totaled 24618. The total number of coincident events was 24475 meaning that 2856 lone free-space events occurred while 143 lone on-chip events occurred. This yields missed event and false positive rates of 10.4% and 0.4%, respectively. A coincident rate is calculated by dividing the total number of coincident events by the average of the free-space and on-chip events, expressed as a percent. Using this definition, the coincident

---

[‡‡‡‡‡‡‡] This paragraph and analysis is from the author's work in reference 123.
[§§§§§§§] This paragraph and analysis is from the author's work in reference 123.

rate was found to be 94.2% - a very high rate meaning that the on-chip method deployed here is very reliable.[********]

There are a fair number of missed events, 10.4%, due to a fairly low CV in the on-chip detection waveguide. This means that lower intensity events are often missed. Removal of noise sources at the collection waveguide (as discussed earlier) will increase the SNR and allow the lower intensity events to be detected and lead to a lower missed event rate. There were very few false positives meaning that the device is quite insensitive to noise with respect to confused detections. This is an excellent performance indicator, however, specific applications will determine the limits to performance in this case. The large coincident rate should be interpreted as an overall accuracy – similar to a correlation coefficient - as it takes into account the likelihood of an event actually occurring.[††††††††]

**Table 4-8: Comparison of the two detection methods shows that the on-chip method is very reliable. *Source*: Reprinted from reference 123.**

| | Free-space detection | On-chip detection |
|---|---|---|
| Number of events | 27331 | 24618 |
| Number of lone events | 2856 | 143 |
| False positives (%) | -- | 0.4 |
| Missed events (%) | -- | 10.4 |
| Coincident events | 24475 | |
| Coincident rate (%) | 94.2 | |

Overall, the reliability of detection agrees to a very high degree with the conventional free-space technique. The worst performance metric is from the missed events – this can be improved through a greater SNR achieved through improved device designs; specifically the coupling between the fibre and the waveguide mismatch.

### 4.2.2.4 On-Chip Forward Scatter

Analysis of the forward scatter is integral to the proper function of a flow cytometer, as discussed in section 1.1.2.2.1. The detection from the devices

---

[********] This paragraph and analysis is from the author's work in reference 123.
[††††††††] This paragraph and analysis is from the author's work in reference 123.

designed in this work are very similar to the on-chip side scatter detection performed in the previous section. The only change to the device design is the form of the lens system and the position of a waveguide, along with a very narrow collection facet. The simulations of the designs are shown in Figure 2-44 while final photomask design of the lens system is shown in Figure 2-52.

Similar to the results from the previous on-chip detection, the results from the forward scatter detection are shown in Figure 4-52. Figure 4-52a) shows two seconds or raw data while Figure 4-52b) shows the histogram from the full 100 second long test.

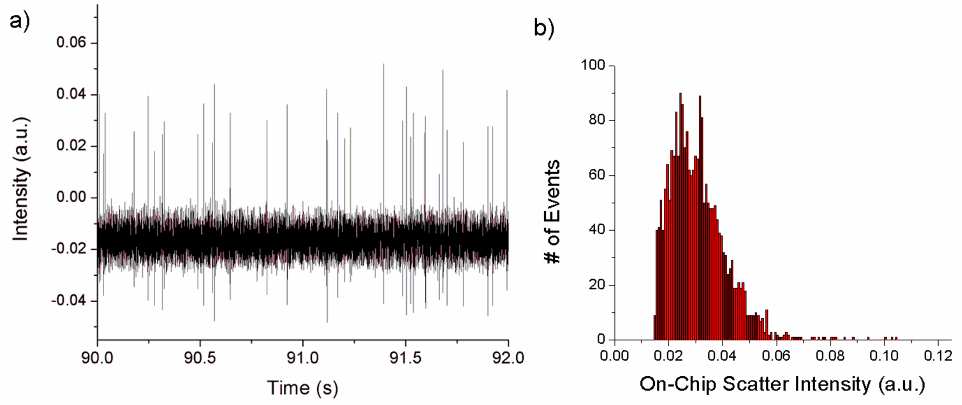

**Figure 4-52: a) raw data from a device that formed a 10 μm beam waist with the forward scatter modification and b) the associated histogram showing a clear population of 5 μm beads. *Source*: Reprinted from reference 124.**

The short run of raw data shown in Figure 4-52a) shows the forward scatter signal collected from the notch modified lens system. The bursts are clear, distinct from others around it, and are well above the noise level. Bursts are of a fairly uniform and regular intensity - a desirable feature as it is from a uniform population of spheres. SNR of detection is approximately 3 which is the minimum requirement for reliable detection. Sources of noise in detection are from diffraction of the notch image, scattering from channel walls and lens walls, and cross-coupling from the input side of the device via leaked modes to the PDMS cover and Pyrex substrate due to the 50 μm fibre and 30 μm waveguide geometry mismatch. Figure 4-52a) shows the histogram from many events in the full 100 second long scatter test. The histogram shows a distinct population with few double detection events. The CV is measured to be 29% - a decent result for a microchip-based device, though this is still far below the capabilities of conventional methods.[‡‡‡‡‡‡‡‡]

The same comparison technique for on-chip side scatter detection used in the previous chapter is deployed here. The comparison of the on-chip forward scatter detection is compared to a simultaneous free-space side scatter collection. It is impossible to do a free-space forward scatter with the on-chip excitation optics due to the architecture of the device; the forward scatter detection must be done on-chip. The simultaneous raw data from the free-space and on-chip scheme and the scatter plots are given in Figure 4-53a) and b), respectively. The comparison of the on-chip scheme to the free-space scheme can validate the on-chip scheme. The free-space scheme can be assumed to be perfect as many demonstrations have been shown to be a reliable means of detection in many publications.

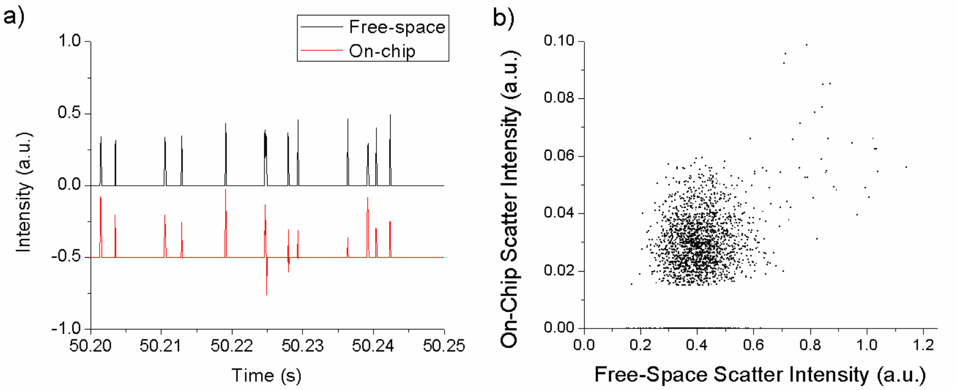

**Figure 4-53: a) raw data from simultaneous free-space and on-chip forward scatter detection showing good correlation between bursts and b) a scatter plot showing a celar population of 5 μm beads via the modified 10 μm device. *Source*: Reprinted from reference 124.**

Both sets of data show bursts that are clear, resolved, and coincide well with one-another. One significant difference between free-space and on-chip raw signals are the negative pulses before (and after) the positive burst for on-chip signals. As noted above, this is due to a bit of the input light making it to the

---

[‡‡‡‡‡‡‡‡] This paragraph and analysis is from the author’s work in reference 124.

collection waveguide. As the particle moves into the interrogation region, it blocks the extreme edges of the beam and thus, some of the light from reaching the detection waveguide. As the particle moves into the centre of the interrogation region this light is no longer blocked, while the forward scatter light is directed to the detection waveguide. The negative burst on the latter end of the pulse is the same phenomena as the particle exits the beam. This negative burst could be removed with subsequent design and improvements to the lens system. Free-space detection does not have this problem as it is side scatter and thus orientated 90 degrees to the chip and does not pick up any stray light from the beam and will not have any light blocked by the bead as it traversed the interrogation region. Figure 4-53b) shows a scatter plot comparing the on-chip and free-space scatter detection techniques. A clear population is resolved, while a sparse double detection population is visible, though kept under control due to the narrow beam waist used in the device, limiting the number of beads within the beam at one time.[§§§§§§§§]

A feature to note in Figure 4-52a) and Figure 4-53a) are the negative bursts that surround positive bursts on the forward scatter on-chip collection. This is for the exact same reasons as discussed in the previous section and is due to noise on the collection waveguide being partially blocked as the specimen moves into the interrogation region.

One advantage of the on-chip scheme is the much larger collection efficiency due to the proximity of the collection waveguide to the channel. The detection intensity is further improved due to the increase of excitation intensity from the beam shaping. The closer proximity allows a larger NA of collection from the particle and as the notch only blocks light from a small segment of the beam, this missing light doesn't affect overall intensity at the interrogation region much, less than 5% of the input intensity is lost. After adjusting for different amplification

---

[§§§§§§§§] This paragraph and analysis is from the author's work in reference 124.

settings between the on-chip and free-space intensity, the on-chip detection is 300 times greater than pulses collected from the free-space scheme.

Applying the same comparison script from Appendix G a similar comparison to the free-space detection as discussed in the previous section is applied. A summary of results is shown in Table 4-9. These results summarize the quantitative reliability of the device.

**Table 4-9: On-chip forward scatter detection compared to a simultaneous free-space detection scheme shows that the on-chip method is very reliable. *Source*: Data from reference 124.**

| | Free-space side detection | On-chip forward detection |
|---|---|---|
| Number of events | 2088 | 1953 |
| Number of lone events | 143 | 8 |
| False positives (%) | -- | 0.4 |
| Missed events (%) | -- | 6.8 |
| Coincident events | 1943 | |
| Coincident rate (%) | 96.3 | |

Evaluation of the performance of the forward scatter detection with the new designs is done by assuming the free-space detection is perfect. The total number of free-space events that occurred was 2088, while the total number of on-chip events that occurred was 1953. 1945 free-space and on-chip events happened simultaneously leaving 143 free-space and 8 on-chip events that happened in isolation. Assuming that the side scatter free-space detection techniques is perfect, this allows false positives and missed events to be discerned from the isolation events. Alone free-space events are missed events by the forward scatter method and are calculated to be 6.8%. Alone on-chip events are false positive by the forward scatter method and are calculated to be 0.4%. The coincidence coefficient (similar to a correlation) was 96.3% - a very good performance of the on-chip notched forward scatter design.[*********]

---

[*********] This paragraph and analysis is from the authors work in reference 124.

## 4.3 State of Devices

Device performance is compared to other devices reported in the literature to provide a good basis of whether the work to improve devices has indeed accomplished the goal. Comparing the device's individual design aspects to the similar characteristics of other devices reported in the literature is necessary. It allows justification of each step done in this work to design and optimize device function. The main performance aspects are divided as: free-space excitation and detection, on-chip optics, forward scatter detection, and comparison to conventional cytometry.

### 4.3.1 Free-space Excitation and Detection

The comparison of the device in this work must be compared to other devices of a similar microchip-based device based on the particular function of the waveguide, lens system, on-chip collection, or forward scatter function. The first function of the devices to be compared are the integrated on-chip excitation optics. Comparisons should be to devices that employ free-space excitation and collection. This allows the conclusion to be made that the process of integrated optics on chip is a step in the right direction.

The best demonstration of a free-space device to date has been from a PDMS-based flow cell that incorporated a 3D hydrodynamic focusing method.[55] The demonstrated CVs was measured to be 3% from 1.9- and 2.5 μm fluorescent beads. This device achieved a very high throughput of over 1200 particles/second.

Other demonstrations of miniaturized flow cells with 3D hydrodynamic focusing have demonstrated excellent results. Methods of 3D hydrodynamic focusing via an inertial focusing technique via a spiral microchannel demonstrated CVs of 18-20% with 6 μm fluorescent beads.[126]

Another free-space optical device used a microfluidic drifting method to focus the specimens hydrodynamically in three-dimensions and demonstrated CV values of 15.2% and 9.3% for 7.32- and 8.32 μm fluorescent beads, respectively.[127] The microweir technique used to vertically hydrodynamically focus the sample flow showed fluorescent CVs of 25.5% and 14.6% for 7 and 15 μm particles, respectively.[56]

The devices designed in this work have similar or better CVs than most of the devices listed here from the literature. Furthermore, the devices in this work did not deploy 3D hydrodynamic focusing; the addition of such would only further improve the performance of devices through the limitation of the deviation of the specimens in the vertical direction. The level of detection demonstrated by the device designed in this work is approaching the level of detection in the state-of-the-art device discussed above. Therefore, the on-chip optics are a viable solution and will produce reliable results.

### 4.3.2 On-chip Optics

Fully integrated devices are appearing more frequently in the literature. The most common method to integrate optical functionality on the chip is through the insertion of fibres into the device to deliver light directly to the channel. This method is popular because it is simple, quick, and reliable. However, this method almost exclusively deploys single-mode fibres and us a high quality single-mode source and forgo the entire process of beam shaping.

One such device uses inserted fibres to deliver light to the channel and also to collect 3 different wavelengths of light; one for fluorescent detection, one for side scatter, and one for forward scatter (discussed later).[99] The measured fluorescent CVs were 8.1% and 6.3% for 7.32- and 15.5 μm particles, respectively. The side scatter CVs measured were 17.1% and 16.4% for 7.32- and 15.5 μm particles, respectively. This device did require a high quality single-more source to operate properly. The devices in this work also showed similar performance for particles around the same size as the 6.0 μm spheres used in this work.

Another group used special geometry on waveguides to block most noise on the outputs.[130] The measured side scatter CVs were found to be 37.5%, 34.2%, and 27.7% for 5-, 10-, and 15 μm particles, respectively.

As a last example, a device that employed micro-weirs to complete focusing the sample in 3-dimensions also demonstrated a device that inserted fibres to do two colour applications.[128] The device demonstrated CV of 15% for 6 μm fluorescent spheres. Again, a high quality single-mode source was required for proper operation.

### 4.3.3 Forward Scatter Detection

Forward scatter has been a more difficult method to deploy on chip due to the necessity to have the excitation and detection axis coplanar with the channel while eliminating the transmitted light on the detection fibre – the largest source of noise in forward scatter detection. The common solution has been to use a nearly collimated beam from a high quality single-mode source for excitation while using a limited NA waveguide to collect the slightly off-axis light.

One device used fibres placed next to the top and bottom surfaces of the device to increase the proximity of the fibres to the channel to increase the collection efficiency.[129] The device was demonstrated with 3-, 4.8-, 6-, and 10.2 μm fluorescent beads. The measured CVs for each bead were 30.2, 31.2, 25, and 29.8%, respectively. The work in this report demonstrated a CV of 29% for 5 μm microspheres – a very similar result to the work just reported above. The reported device, however, is not a all on-chip integrated solution. This device still requires careful alignment to the device. Furthermore, the device required a high quality single-mode beam for correct function. The performance of the device is good, but not in a form that is an applicable solution to a POC or remote and on-line sensing application.

A device that employed an on-chip lens systems to form a 15 μm beam width in the channel was demonstrate for the detection of 4-, 8-, and 12 μm blank beads.[95] Also, this device deployed an integrated 3D hydrodynamic focusing on-chip. This device primarily measured the drop in signal from a waveguide directly across the channel. This is an absorption measurement which is very similar to forward scattering; the measured CVs of which were 32.9, 19.1, and 8.4% for the three bead sizes, respectively. This device displays a very wide range of detection accuracy and demonstrates the need to tune the beam deployed on-chip to the specific size of the targeted specimen size in the assay. Furthermore, the device used a high quality single-mode beam that is not conducive to applications in POC medicine and remote and on-line sensing abilities.

The devices demonstrated in this reported work from the literature used a lower quality source and did not deploy a method for 3D hydrodynamic focusing on-chip. The results indicate that this work could easily improve detection accuracies. Following up on these results, this group expanded their designs to show the addition of a 'drifting' fluid that formed a parabolic profile in the vertical direction.[94] Using this parabolic profile, optical focusing in the vertical direction is achievable in a fully integrated on-chip fashion. This device demonstrate and allows for full beam geometry control in the channel. Coupled with a method for 3D hydrodynamic focusing it produced excellent results. CVs of 7.8% with 12 μm particles for forward extinction were measured.

The same two devices that were discussed in the previous section, 4.3.2, also incorporated on-chip forward scatter collection capabilities. Reference 99 showed forward scatter from 7.32 and 15.5 μm beads measuring CVs of 9.1 and 6.8% respectively – much lower results than demonstrated by the results presented in the work from this thesis. However, this device used inserted fibres and a high quality single-mode source, again, a detriment to LOC and POC applications.

The other device, from reference 130, shows the collection of forward scatter light via a unique geometry of the on-chip waveguides. This work's device demonstrated forward scatter collection for 5-, 10-, and 15 μm beads and measured CV’s of 18.3, 13.2, and 9.7% for each bead, respectively. These, like the previous device, are very good results, however, it does not allow for on-chip beam shaping. The authors of this work mentioned that the largest source of error was from beam geometry variation across the channel – something that can be controlled with beam shaping. Due to the architecture of this device, deploying beam shaping on-chip is not feasible. Furthermore, this device demonstrated simultaneous side scatter (discussed above). The side scatter results are very large. Although this is a good solution for forward scatter detection alone, this does not appear to be an acceptable solution for multi-parameter collection. Deploying beam shaping in a similar device would be allow mitigation of these problems and a better functioning device.

### 4.3.4 Conventional Cytometry

The ultimate goal of microchip-based cytometers would be to completely mimic the detection capabilities of a conventional flow cytometer. This likely will remain and impossibility. However, microchip device can get close, and use in simple and specific functions will allow them to supplement their use in conventional applications.

The detection capabilities of a conventional cytometer routinely see these cytometers achieve CV’s of only a few percent. These machines can accurately determine the amount of excess DNA in a population that is undergoing growth and division; typically less than 2%. In fact, certain populations are used to calibrate cytometers as the fluctuation of DNA is so specific.

A sample of the beads used in this work - the 6 μm beads - was run through a flow cytometer in the McMaster flow cytometry lab. The cytometer was manufactured by BD and capable of over 6 simultaneous parameter detections with a library that allowed it the capability to recognize over 40 dyes. The fluorescence CV was measured to be 18.5%. This is a calibrated machine with very precise free-space optics – though, the machine probably needed adjustments before these results were obtained.  A scatter plot and histogram from this data are shown in Figure 4-54.

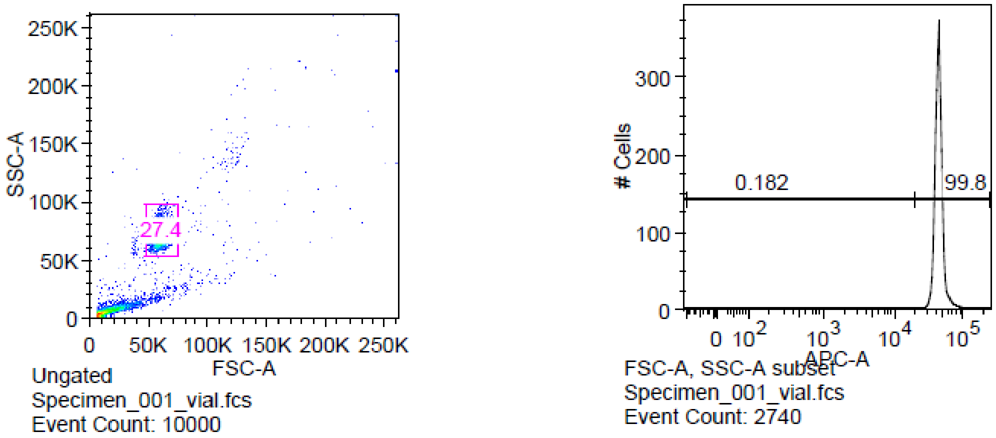

**Figure 4-54:  Data obtained from a flow cytometer manufactured by BD and current used in the flow cytometry lab at McMaster University.**

The devices produced in this work show a similar level of performance – even better performance in most cases from the microchip devices.  A well-maintained a properly calibrated conventional machine will yield better results, but the microchip devices in this work are close to achieving a comparable ‘best case scenario’ diction ability available from a conventional machine.  Though one can’t make prediction with the on-chip collection abilities, further testing will reveal the devices abilities.

# 5 Conclusion

This work has produced functioning devices suited for a variety of specific applications from the initial idea formulated at the onset of the project. Through careful review of the literature and from obtained knowledge and proper application of the appropriate technology and phenomena, this work has developed the idea that the excitation optics can be integrated on-chip to perform a beam shaping function to target a specific specimen. Device conception and ideas have been taken through the proper design steps to a suitable conclusion in the form of device performance evaluation. Evaluation of milestones or specific achievements has allowed this project to proceed through to achieve ultimately success with each minor milestone guiding and correction the design and development of device to eventual success.

## *5.1 Achievements*

The novelties of this work were conceived early on in the project and were the main source of direction throughout the project. The achievements met the goals of the project and were the basic functional components of the device. The achieved functionalities were: on-chip beam shaping, cytometric function (fluorescence and scatter detection) with on-chip excitation optics and beam shaping, on-chip detection, forward scatter improvement, and targeted particle detection. Furthermore, these devices enhanced the performance ability of the device by performing all such optical inspection techniques with a multimodal source that is low quality ensuring the feasibility of future operation with a simple low power and low cost source – such as an LED – a feature that is more compliant with LOC and POC applications.

### 5.1.1 Beam Shaping

Very specific beam geometries were formed in the channel of devices via all-integrated on-chip lens systems. These beam shapes were designed to form specific geometries in the middle of the channel to improve the reliability of detection through tailoring the intensity profile across the sample flow. Creating a uniform region of intensity that extends over a long region in the channel with a very well defined and uniform width will improve the reliability of detection in two ways: it ensures that each particle receives the exact same optical dose for excitation and ensures that each particle traverses the same width of intensity ensuring the same duration in the beam. This creates more homogeneous burst intensities and pulse widths from particles. Improved signal uniformity can allow any deviation in signal intensity to be shifted towards the actual specimen attributes and away from the device function.

This method of integrated optics removes the devices dependency on expensive and bulky free-space optics. The method of replicating the designed optical lens systems on-chip was confirmed through careful analysis of the formed beams. The beam geometries allow very large depth of focus across the channel. 1.5-, 3.6-, 6.0-, 10.0-, and 12 μm beam widths were designed via lens design simulation software. Realized devices did replicate the lens designs quite well, producing FWHM of 6.7-, 7.4-, 10.2-, 10.9-, and 10.1 μm for each of the lens systems mentioned, respectively. The smaller lens designs were assumed to be limited by the diffraction limit. However, when constructing the uniform region of intensity, the widths were found to be 1.0-, 2.0-, 2.6-, 5.0-, and 2.3 μm for each system, respectively. These regions extended across the channel measuring 3.9-, 8.3-, 10.2-, 14.3-, and 9.5 μm, respectively. All these parameters were summed up in Table 4-1. With major revisions to the 1.5- and 12 μm device, and minor changes to the 6.0- and 3.6 μm devices, the performance metrics were improved. New testing of the revised and improved designs yielded an improved FWHM of 13.3 μm for the 12 μm device. Improved dimensions of the uniform region are measured to be 1.5 by 8.5 μm, 3.4 by 9.5 μm, and 3.5 by 14.1 μm for the 1.5-, 6.0-, and 12 μm lens systems, respectively.

### 5.1.2 Fluorescence Detection

With the improved beam shapes, the devices were tested in standard cytometric detection applications. Simple fluorescence detection was performed using particle excitation with the on-chip beam shaping optics, and detected using a conventional free-space detections scheme. This testing found that the lens systems used on the chip drastically improved the performance of the device in three ways: improved CV, lower instance of DD's, and an improve SNR. All three of these parameters are improved through the enhanced uniformity, increased light density from focusing, and controlled beam width from the beam shaping optics investigated earlier.

Cytometric detection of 2.5- and 6.0 μm beads revealed different performance depending on the beam geometry involved. The smaller bead had optimal performance with the 3.6 μm beam while the large beads had better performance from the 10.0 μm device yielding CVs of 8.5% and 14.6%, respectively. In all cases, the SNR was huge; over 10 and in some cases a few hundred. This will ensure very easy recognition of bursts. As expected, DD's were kept very low – only a few percent of detections – while they increased with the beam width as more than one particle in the beam was a more probably outcome.

With revisions to lens designs, the CVs increase to 6.6% for the 3.6 μm device with 2.5 μm beads, however, the 6.μm beads showed best performance from the 1.5 μm device with a CV of 8.9%. This was only from a single run, but could be due to the very tiny beam waist and the large particle. These results are better than any other device reported in the literature that employs on-chip optics. This demonstrates the benefit from a device with integrated excitation optics deploying beam shaping for targeted detection.

### 5.1.3 Scatter Detection

In a similar fashion to the fluorescence detection, scatter detection was performed to demonstrate any dependence that the beam geometry and particle size had on device performance. Blank microspheres with 1.0-, 2.0-, and 5.0 μm diameters were run through a variety of beam geometries. Best results were CVs of 16.4% for a 10 μm device deployed with 1.0 μm beads, 11.0% for a 6.0 μm device deployed with 2.0 μm beads, and 12.5% for a 6.0 μm device deployed with 5.0 μm beads. Again, DDs were not a problem unless the beam width was considerably more than the bead size. One feature to note was the lower SNR – contrary to conventional observations

Devices were also able to resolve two different bead sizes from a mixture. It was discovered that with a mixture of particles the optimal beam/bead combination had to be changed for the smaller particle due to the relaxed hydrodynamic flow. This was found to not be a problem as larger beam sizes have sufficient uniform intensity to allow the CV of the small particles to only increase minimally.

### 5.1.4 On-chip Detection

#### 5.1.4.1 Side Scatter

Device function with the on-chip excitation optics was also performed with an on-chip waveguide to collect the scattered signal. A CV of over 30% was measured, however, the method was still deemed reliable as confirmed by a simultaneous detection of scattered light via a free-space collection scheme producing a coincident rate of 94.2%. Furthermore, the detected intensity was found to increase by over 300 times due to the increased proximity of the waveguide to the interrogation region.

#### 5.1.4.2 Forward Scatter

Forward scatter detection via the novel designs to improve SNR from an on-chip integrated collection waveguide was tested in much the same manner as the on-chip side scatter detection described immediately above. The CV of detection was measured to be 29% while the reliability of the device was deemed satisfactory with a coincident rate of 96.3% compared to a simultaneous free-space side scatter detection.

### 5.1.5 Targeted Particle Detection

One of the most important conclusions of this work was the fact that deploying a lens system on chip must account for the particle size targeted. Different beam geometries have a different interaction with different specimen sizes leading to a change in the performance of the device. The fluorescence detection found that best results were from a device the deployed a beam width which was approximately 1.5 times larger than the specimen's size. The scatter detection did not find a straight forward relationship; instead, the beam should be selected from a table that explores the different beam widths with different specimen sizes; as given in Table 4-7.

## *5.2 Recommendations and Future Work*

The scope of this work was huge. A lot of designs and simulations did not get tested due to time constraints. In addition, the knowledge gained from the tests that were performed would lead to better performance from design improvements. More advanced designs and structures could be integrated onto the chip to improve the performance.

### 5.2.1 Waveguide Coupling

Coupling to the waveguide is one of the most cumbersome and technically challenging aspects of device testing – not to mention one of the largest sources of inefficiency due to large coupling losses. To form a device that is feasible in the applications listed earlier in this work, the coupling method must be improved. Butt-coupling in this work is only used because it is suitable for rapid prototyping and testing of other device designs which were the focus of this work.

However, device designs can be modified to ease the coupling restrictions currently in place. Structures can be patterned into the device layer that will enhance the coupling ability of the waveguides. A simple Fresnel lens has been shown to greatly enhance the coupling capabilities from a fibre to a waveguide.[131] More advanced structures could further simplify the architecture problems of aligning a laser to the device. A modified grating in the device layer can ensure coupling from an almost normal direction to the plane of the device. This grating has a specially designed order that lies coincident with the plane of the chip and provides automatic alignment to the waveguide.

### 5.2.2 Beam Shaping

Based on the latest device designs and the improved device fabrication capabilities, refinements to designs can be made to improve the quality or geometry of the formed beams. Through more innovative lens designs the diffraction limit can be reduced by lowering the input aperture of the lens system. This would allow narrower beam waists to be created. Utilizing microchannels it would be possible to create liquid medium lenses. The introduction of different indices would allow for much more flexible lens design and allow more unique beam shaping capabilities of the device. Furthermore, devices can be tuned 'on-the-fly' through the simple change of material that is flowing through the lens system.

Improvement to detection abilities can be improved through the incorporation of the vertical beam shaping method as described in reference 94 in conjunction with these devices. The vertical focusing will allow a larger intensity of light at the point of interrogation while the geometry can be gently shaped to provide a more uniform region of light distribution in the vertical direction. Incorporation of this vertical optical focusing method would require deployment of a 3D hydrodynamic focusing method as particle flow at the channel extremes in the vertical direction would not be subjected to excitation.

Integration of a diffractive optical element (DOE) would drastically improve the quality of detection and create a plethora of new opportunities for excitation and detection via on-chip structure. A DOE has the ability to control an optical wave from a much more basic level then a simple refractive lens. Using the wavelength and the resulting interference effects from the wave, the construction of the region of intensity in the channel can be take on many different geometries not possible through simple refraction-based optics. This has the potential to formed ideal ‘top-hat’ structures in the channel with extremely large efficiencies.[132,133,134] In addition, device efficiency can be improved by the integration of a DOE as the focusing or shaping surface is comprised of a single structured surface as opposed to the multi-surface lens system. A reduction in the number of surfaces in the device leads to a reduction in the optical losses that are attributable to scattering from surfaces.

### 5.2.3 On-Chip Detection

The on-chip detection shown in this work is a first step and needs improvement before feasible deployment is possible. Device designs need to be refined so that noise is reduced on the collection output. This noise is due to two main sources. One is due to the geometry mismatch of the fibre and the waveguide. The 50 μm core diameter fibre ensures that a significant amount of light is injected into the top PDMS layer and bottom Pyrex substrate layers of the device. This light will propagate to the opposite side of the device and creates a detectable signal on the collection fibre. The second source is from scattering losses that occur from the surface roughness of the waveguide, lens surfaces, and channel wall. These scattering centres allow light to escape and some of the light will find its way to the collection side. The former problem is much easier to remedy than the latter. By increasing the thickness of the device layer to 50 μm, the matching of the fibre and waveguide geometry can be matched and reduce the light that escapes to the cover and substrate to a very minimal amount (due to scattering).

### 5.2.4 Further Testing

All of the proposed designs created in this work need to be tested. All structures designed into the photomask need to have all bead sizes run through them to determine if any revisions to the designs need to be made and furthermore, which designs work best with each specimen size and if the flexibility of designs is sufficient to work with multiple specimen sizes. Multiple parameter detection from all devices needs to be confirmed to be feasible with current designs, and again, design revisions should be made. Multiple devices or multiple input beams should be experimented with to prove the multiplexing capabilities of the designs.

Devices should be tested with actual specimens – such as simple detection of a bacterial population. This can be first done via free-space detection, then moved to on-chip single, and multi-parameter detection schemes. Eventually, extreme sub-characterizing of a population – or detection of a mixture of different populations – should be done via the 4 parameter on-chip detection scheme.

Testing of unique angled inputs should be done to determine the amount of noise reduction on the collection. This can be expanded to perform simultaneous detection of two parameters via two excitation beams.

Full testing and better characterization of new beams should be performed to show that a larger depth of focus improves results. More flexible designs can flow from the knowledge obtained from current designs.

## Appendix A Simulation to calculate channel and wall width affect on collection efficiency with air side cladding.

Calculations for a device with a 25 μm thick device layer and using air for the side cladding material. Highlighted sections are areas where the angle of collection is not maximized (ie. Not equal to the angle of possible collection)

| Geometry Parameters | | Projected Waveguide Facet onto channel wall | | Angle of collection | | Angle of possible collection based on waveguide NA | | Dimensions of collectable light at wall based on NA | | Efficiency of collection % of NA | Solid angle | % collection of Sphere |
|---|---|---|---|---|---|---|---|---|---|---|---|---|
| Wall Width | Channel half-width | Width (lateral) | Height (trans) | Lateral | Transverse | Lateral | Transverse | Width (lateral) | Height (trans) | % | STR | % |
| 50 | 5 | 2.777 | 1.347 | 29.0483 | 15.085 | 20.537 | 26.631 | 12.595 | 2.507 | 11.851 | 0.527 | 4.199 |
| 50 | 10 | 4.964 | 2.429 | 26.4023 | 13.653 | 20.537 | 26.631 | 25.191 | 5.014 | 9.546 | 0.435 | 3.462 |
| 50 | 15 | 6.743 | 3.317 | 24.2069 | 12.470 | 20.537 | 26.631 | 37.786 | 7.521 | 7.870 | 0.364 | 2.904 |
| 50 | 20 | 8.223 | 4.060 | 22.3514 | 11.476 | 20.537 | 26.631 | 50.382 | 10.029 | 6.608 | 0.310 | 2.470 |
| 50 | 25 | 9.476 | 4.691 | 20.7606 | 10.629 | 20.537 | 26.631 | 62.977 | 12.536 | 5.631 | 0.267 | 2.127 |
| 50 | 30 | 10.553 | 5.234 | 19.3807 | 9.898 | 20.537 | 26.631 | 75.573 | 15.043 | 4.859 | 0.232 | 1.850 |
| 50 | 35 | 11.488 | 5.707 | 18.172 | 9.261 | 20.537 | 26.631 | 88.168 | 17.550 | 4.237 | 0.204 | 1.624 |
| 50 | 40 | 12.308 | 6.121 | 17.1044 | 8.701 | 20.537 | 26.631 | 100.764 | 20.058 | 3.728 | 0.180 | 1.437 |
| 50 | 45 | 13.034 | 6.488 | 16.1544 | 8.204 | 20.537 | 26.631 | 113.360 | 22.565 | 3.306 | 0.160 | 1.280 |
| 50 | 50 | 13.681 | 6.815 | 15.3037 | 7.761 | 20.537 | 26.631 | 125.955 | 25.072 | 2.952 | 0.144 | 1.148 |

| Wall Width | Channel half-width | Width (lateral) | Height (trans) | Lateral | Transverse | Lateral | Transverse | Width (lateral) | Height (trans) | % | STR | % |
|---|---|---|---|---|---|---|---|---|---|---|---|---|
| 40 | 5 | 3.443 | 1.647 | 34.552 | 18.241 | 20.537 | 26.631 | 12.595 | 2.507 | 17.966 | 0.755 | 6.008 |
| 40 | 10 | 5.981 | 2.904 | 30.886 | 16.193 | 20.537 | 26.631 | 25.191 | 5.014 | 13.751 | 0.601 | 4.785 |
| 40 | 15 | 7.956 | 3.896 | 27.944 | 14.560 | 20.537 | 26.631 | 37.786 | 7.521 | 10.907 | 0.490 | 3.902 |
| 40 | 20 | 9.547 | 4.700 | 25.518 | 13.226 | 20.537 | 26.631 | 50.382 | 10.029 | 8.881 | 0.407 | 3.243 |
| 40 | 25 | 10.860 | 5.366 | 23.480 | 12.115 | 20.537 | 26.631 | 62.977 | 12.536 | 7.382 | 0.344 | 2.737 |
| 40 | 30 | 11.964 | 5.927 | 21.742 | 11.176 | 20.537 | 26.631 | 75.573 | 15.043 | 6.237 | 0.294 | 2.341 |
| 40 | 35 | 12.906 | 6.406 | 20.241 | 10.372 | 20.537 | 26.631 | 88.168 | 17.550 | 5.343 | 0.254 | 2.024 |
| 40 | 40 | 13.720 | 6.819 | 18.932 | 9.675 | 20.537 | 26.631 | 100.764 | 20.058 | 4.629 | 0.222 | 1.767 |
| 40 | 45 | 14.431 | 7.180 | 17.781 | 9.066 | 20.537 | 26.631 | 113.360 | 22.565 | 4.051 | 0.195 | 1.556 |
| 40 | 50 | 15.057 | 7.498 | 16.760 | 8.529 | 20.537 | 26.631 | 125.955 | 25.072 | 3.575 | 0.173 | 1.381 |

| Geometry Parameters | | Projected Waveguide Facet onto channel wall | | Angle of collection | | Angle of possible collection based on waveguide NA | | Dimensions of collectable light at wall based on waveguide NA | | Efficiency of collection % of NA | Solid angle | % collection of Sphere |
|---|---|---|---|---|---|---|---|---|---|---|---|---|
| Wall Width | Channel half-width | Width (lateral) | Height (trans) | Lateral | Transverse | Lateral | Transverse | Width (lateral) | Height (trans) | % | STR | % |
| 30 | 5 | 4.553 | 2.122 | 42.321 | 23.004 | 20.537 | 26.631 | 12.595 | 2.507 | 30.606 | 1.154 | 9.188 |
| 30 | 10 | 7.530 | 3.610 | 36.983 | 19.854 | 20.537 | 26.631 | 25.191 | 5.014 | 21.527 | 0.876 | 6.978 |
| 30 | 15 | 9.701 | 4.719 | 32.894 | 17.465 | 20.537 | 26.631 | 37.786 | 7.521 | 16.109 | 0.689 | 5.484 |
| 30 | 20 | 11.374 | 5.579 | 29.628 | 15.588 | 20.537 | 26.631 | 50.382 | 10.029 | 12.560 | 0.555 | 4.423 |
| 30 | 25 | 12.710 | 6.267 | 26.948 | 14.073 | 20.537 | 26.631 | 62.977 | 12.536 | 10.089 | 0.457 | 3.640 |
| 30 | 30 | 13.803 | 6.830 | 24.708 | 12.826 | 20.537 | 26.631 | 75.573 | 15.043 | 8.293 | 0.382 | 3.047 |
| 30 | 35 | 14.717 | 7.299 | 22.806 | 11.781 | 20.537 | 26.631 | 88.168 | 17.550 | 6.942 | 0.325 | 2.586 |
| 30 | 40 | 15.492 | 7.697 | 21.172 | 10.892 | 20.537 | 26.631 | 100.764 | 20.058 | 5.900 | 0.279 | 2.222 |
| 30 | 45 | 16.158 | 8.038 | 19.752 | 10.128 | 20.537 | 26.631 | 113.360 | 22.565 | 5.077 | 0.242 | 1.929 |
| 30 | 50 | 16.737 | 8.334 | 18.508 | 9.463 | 20.537 | 26.631 | 125.955 | 25.072 | 4.417 | 0.212 | 1.690 |

| Wall Width | Channel half-width | Width (lateral) | Height (trans) | Lateral | Transverse | Lateral | Transverse | Width (lateral) | Height (trans) | % | STR | % |
|---|---|---|---|---|---|---|---|---|---|---|---|---|
| 20 | 5 | 6.784 | 2.507 | 53.609 | 26.631 | 20.537 | 26.631 | 12.595 | 2.507 | 53.862 | 1.677 | 13.350 |
| 20 | 10 | 10.154 | 4.773 | 45.440 | 25.518 | 20.537 | 26.631 | 25.191 | 5.014 | 38.376 | 1.366 | 10.875 |
| 20 | 15 | 12.401 | 5.982 | 39.582 | 21.742 | 20.537 | 26.631 | 37.786 | 7.521 | 26.101 | 1.023 | 8.145 |
| 20 | 20 | 14.039 | 6.860 | 35.067 | 18.932 | 20.537 | 26.631 | 50.382 | 10.029 | 19.061 | 0.794 | 6.321 |
| 20 | 25 | 15.295 | 7.528 | 31.459 | 16.760 | 20.537 | 26.631 | 62.977 | 12.536 | 14.586 | 0.633 | 5.039 |
| 20 | 30 | 16.292 | 8.055 | 28.505 | 15.030 | 20.537 | 26.631 | 75.573 | 15.043 | 11.544 | 0.516 | 4.106 |
| 20 | 35 | 17.103 | 8.481 | 26.043 | 13.621 | 20.537 | 26.631 | 88.168 | 17.550 | 9.374 | 0.428 | 3.407 |
| 20 | 40 | 17.776 | 8.832 | 23.960 | 12.451 | 20.537 | 26.631 | 100.764 | 20.058 | 7.768 | 0.360 | 2.870 |
| 20 | 45 | 18.344 | 9.127 | 22.178 | 11.465 | 20.537 | 26.631 | 113.360 | 22.565 | 6.545 | 0.307 | 2.449 |
| 20 | 50 | 18.829 | 9.378 | 20.636 | 10.623 | 20.537 | 26.631 | 125.955 | 25.0725 | 5.591 | 0.265 | 2.113 |

| Geometry Parameters | | Projected Waveguide Facet onto channel wall | | Angle of collection | | Angle of possible collection based on waveguide NA | | Dimensions of collectable light at wall based on waveguide NA | | Efficiency of collection % of NA | Solid angle | % collection of Sphere |
|---|---|---|---|---|---|---|---|---|---|---|---|---|
| Wall Width | Channel half-width | Width (lateral) | Height (trans) | Lateral | Transverse | Lateral | Transverse | Width (lateral) | Height (trans) | % | STR | % |
| 10 | 5 | 12.595 | 2.507 | 68.348 | 26.631 | 20.537 | 26.631 | 12.595 | 2.507 | 100 | 2.138 | 17.020 |
| 10 | 10 | 15.222 | 5.014 | 56.697 | 26.631 | 20.537 | 26.631 | 25.191 | 5.014 | 60.427 | 1.774 | 14.119 |
| 10 | 15 | 16.960 | 7.521 | 48.509 | 26.631 | 20.537 | 26.631 | 37.786 | 7.521 | 44.884 | 1.518 | 12.080 |
| 10 | 20 | 18.190 | 8.888 | 42.287 | 23.960 | 20.537 | 26.631 | 50.382 | 10.029 | 31.998 | 1.198 | 9.540 |
| 10 | 25 | 19.104 | 9.414 | 37.385 | 20.636 | 20.537 | 26.631 | 62.977 | 12.536 | 22.781 | 0.919 | 7.319 |
| 10 | 30 | 19.806 | 9.808 | 33.433 | 18.104 | 20.537 | 26.631 | 75.573 | 15.043 | 17.087 | 0.725 | 5.771 |
| 10 | 35 | 20.363 | 10.112 | 30.191 | 16.116 | 20.537 | 26.631 | 88.168 | 17.550 | 13.307 | 0.585 | 4.655 |
| 10 | 40 | 20.814 | 10.355 | 27.490 | 14.514 | 20.537 | 26.631 | 100.764 | 20.058 | 10.664 | 0.481 | 3.827 |
| 10 | 45 | 21.186 | 10.554 | 25.211 | 13.199 | 20.537 | 26.631 | 113.360 | 22.565 | 8.741 | 0.401 | 3.198 |
| 10 | 50 | 21.499 | 10.719 | 23.266 | 12.099 | 20.537 | 26.631 | 125.955 | 25.072 | 7.297 | 0.340 | 2.709 |

| Wall Width | Channel half-width | Width (lateral) | Height (trans) | Lateral | Transverse | Lateral | Transverse | Width (lateral) | Height (trans) | % | STR | % |
|---|---|---|---|---|---|---|---|---|---|---|---|---|
| 5 | 5 | 12.595 | 2.507 | 68.348 | 26.631 | 20.537 | 26.631 | 12.595 | 2.507 | 100 | 2.138 | 17.020 |
| 5 | 10 | 19.435 | 5.014 | 62.773 | 26.631 | 20.537 | 26.631 | 25.191 | 5.014 | 77.153 | 1.964 | 15.632 |
| 5 | 15 | 20.434 | 7.521 | 53.719 | 26.631 | 20.537 | 26.631 | 37.786 | 7.521 | 54.078 | 1.681 | 13.377 |
| 5 | 20 | 21.170 | 10.029 | 46.628 | 26.631 | 20.537 | 26.631 | 50.382 | 10.029 | 42.0197 | 1.459 | 11.619 |
| 5 | 25 | 21.719 | 10.749 | 40.983 | 23.266 | 20.537 | 26.631 | 62.977 | 12.536 | 29.571 | 1.130 | 8.993 |
| 5 | 30 | 22.138 | 10.996 | 36.425 | 20.131 | 20.537 | 26.631 | 75.573 | 15.043 | 21.414 | 0.875 | 6.964 |
| 5 | 35 | 22.467 | 11.183 | 32.697 | 17.720 | 20.537 | 26.631 | 88.168 | 17.550 | 16.237 | 0.694 | 5.528 |
| 5 | 40 | 22.730 | 11.329 | 29.608 | 15.813 | 20.537 | 26.631 | 100.764 | 20.058 | 12.741 | 0.563 | 4.482 |
| 5 | 45 | 22.946 | 11.446 | 27.017 | 14.271 | 20.537 | 26.631 | 113.360 | 22.565 | 10.267 | 0.464 | 3.700 |
| 5 | 50 | 23.124 | 11.542 | 24.820 | 12.998 | 20.537 | 26.631 | 125.955 | 25.072 | 8.451 | 0.389 | 3.101 |

# Appendix B Simulation to calculate channel and wall width affect on collection efficiency with an adhesive side cladding.

Calculations for a device with a 25 μm thick device layer and using an adhesive material (index 1.52) as the side cladding material. Highlighted sections are areas where the angle of collection is not maximized (ie. Not equal to the angle of possible collection)

| Geometry Parameters | | Projected Waveguide Facet onto channel wall | | Angle of collection | | Angle of possible collection based on waveguide NA | | Dimensions of collectable light at wall based on waveguide NA | | Efficiency of collection % of NA | Solid angle | % collection of Sphere |
|---|---|---|---|---|---|---|---|---|---|---|---|---|
| Wall Width | Channel half-width | Width (lateral) | Height (trans) | Lateral | Transverse | Lateral | Transverse | Width (lateral) | Height (trans) | % | STR | % |
| 50 | 5 | 1.873 | 1.347 | 20.537 | 15.085 | 20.537 | 26.631 | 1.873 | 2.507 | 53.752 | 0.373 | 2.969 |
| 50 | 10 | 3.746 | 2.429 | 20.537 | 13.653 | 20.537 | 26.631 | 3.746 | 5.014 | 48.442 | 0.338 | 2.693 |
| 50 | 15 | 5.619 | 3.317 | 20.537 | 12.470 | 20.537 | 26.631 | 5.619 | 7.521 | 44.104 | 0.309 | 2.463 |
| 50 | 20 | 7.492 | 4.060 | 20.537 | 11.476 | 20.537 | 26.631 | 7.492 | 10.029 | 40.488 | 0.285 | 2.270 |
| 50 | 25 | 9.365 | 4.691 | 20.537 | 10.629 | 20.537 | 26.631 | 9.365 | 12.536 | 37.426 | 0.264 | 2.104 |
| 50 | 30 | 10.553 | 5.234 | 19.380 | 9.898 | 20.537 | 26.631 | 11.238 | 15.043 | 32.676 | 0.232 | 1.850 |
| 50 | 35 | 11.488 | 5.707 | 18.172 | 9.261 | 20.537 | 26.631 | 13.111 | 17.550 | 28.492 | 0.204 | 1.624 |
| 50 | 40 | 12.308 | 6.121 | 17.104 | 8.701 | 20.537 | 26.631 | 14.984 | 20.058 | 25.069 | 0.180 | 1.437 |
| 50 | 45 | 13.034 | 6.488 | 16.154 | 8.204 | 20.537 | 26.631 | 16.858 | 22.565 | 22.232 | 0.160 | 1.280 |
| 50 | 50 | 13.681 | 6.815 | 15.303 | 7.761 | 20.537 | 26.631 | 18.731 | 25.072 | 19.854 | 0.144 | 1.148 |

| Wall Width | Channel half-width | Width (lateral) | Height (trans) | Lateral | Transverse | Lateral | Transverse | Width (lateral) | Height (trans) | % | STR | % |
|---|---|---|---|---|---|---|---|---|---|---|---|---|
| 40 | 5 | 1.873 | 1.647 | 20.537 | 18.241 | 20.537 | 26.631 | 1.873 | 2.507 | 65.726 | 0.448 | 3.571 |
| 40 | 10 | 3.746 | 2.904 | 20.537 | 16.193 | 20.537 | 26.631 | 3.746 | 5.014 | 57.912 | 0.399 | 3.181 |
| 40 | 15 | 5.619 | 3.896 | 20.537 | 14.560 | 20.537 | 26.631 | 5.619 | 7.521 | 51.797 | 0.360 | 2.868 |
| 40 | 20 | 7.492 | 4.700 | 20.537 | 13.226 | 20.537 | 26.631 | 7.492 | 10.029 | 46.869 | 0.328 | 2.61 |
| 40 | 25 | 9.365 | 5.366 | 20.537 | 12.115 | 20.537 | 26.631 | 9.365 | 12.536 | 42.808 | 0.300 | 2.394 |
| 40 | 30 | 11.238 | 5.927 | 20.537 | 11.176 | 20.537 | 26.631 | 11.238 | 15.043 | 39.402 | 0.277 | 2.211 |
| 40 | 35 | 12.906 | 6.406 | 20.241 | 10.372 | 20.537 | 26.631 | 13.111 | 17.550 | 35.929 | 0.254 | 2.024 |
| 40 | 40 | 13.720 | 6.819 | 18.932 | 9.675 | 20.537 | 26.631 | 14.984 | 20.058 | 31.132 | 0.222 | 1.767 |
| 40 | 45 | 14.431 | 7.180 | 17.781 | 9.066 | 20.537 | 26.631 | 16.858 | 22.565 | 27.242 | 0.195 | 1.556 |
| 40 | 50 | 15.057 | 7.498 | 16.760 | 8.529 | 20.537 | 26.631 | 18.731 | 25.072 | 24.043 | 0.173 | 1.381 |

| Geometry Parameters | | Projected Waveguide Facet onto channel wall | | Angle of collection | | Angle of possible collection based on waveguide NA | | Dimensions of collectable light at channel wall based on waveguide NA | | Efficiency of collection % of NA | Solid angle | % collection of Sphere |
|---|---|---|---|---|---|---|---|---|---|---|---|---|
| Wall Width | Channel half-width | Width (lateral) | Height (trans) | Lateral | Transverse | Lateral | Transverse | Width (lateral) | Height (trans) | % | STR | % |
| 30 | 5 | 1.873 | 2.122 | 20.537 | 23.004 | 20.537 | 26.631 | 1.873 | 2.507 | 84.668 | 0.560 | 4.458 |
| 30 | 10 | 3.746 | 3.610 | 20.537 | 19.854 | 20.537 | 26.631 | 3.746 | 5.014 | 72.009 | 0.486 | 3.875 |
| 30 | 15 | 5.619 | 4.719 | 20.537 | 17.465 | 20.537 | 26.631 | 5.619 | 7.521 | 62.743 | 0.430 | 3.424 |
| 30 | 20 | 7.492 | 5.579 | 20.537 | 15.588 | 20.537 | 26.631 | 7.492 | 10.029 | 55.634 | 0.385 | 3.065 |
| 30 | 25 | 9.365 | 6.267 | 20.537 | 14.073 | 20.537 | 26.631 | 9.365 | 12.536 | 49.994 | 0.348 | 2.774 |
| 30 | 30 | 11.238 | 6.830 | 20.537 | 12.826 | 20.537 | 26.631 | 11.238 | 15.043 | 45.404 | 0.318 | 2.532 |
| 30 | 35 | 13.111 | 7.299 | 20.537 | 11.781 | 20.537 | 26.631 | 13.111 | 17.550 | 41.593 | 0.292 | 2.329 |
| 30 | 40 | 14.984 | 7.697 | 20.537 | 10.892 | 20.537 | 26.631 | 14.984 | 20.058 | 38.376 | 0.270 | 2.156 |
| 30 | 45 | 16.158 | 8.038 | 19.752 | 10.128 | 20.537 | 26.631 | 16.858 | 22.565 | 34.145 | 0.242 | 1.929 |
| 30 | 50 | 16.737 | 8.334 | 18.508 | 9.463 | 20.537 | 26.631 | 18.731 | 25.072 | 29.703 | 0.212 | 1.690 |

| Wall Width | Channel half-width | Width (lateral) | Height (trans) | Lateral | Transverse | Lateral | Transverse | Width (lateral) | Height (trans) | % | STR | % |
|---|---|---|---|---|---|---|---|---|---|---|---|---|
| 20 | 5 | 1.873 | 2.507 | 20.537 | 26.631 | 20.537 | 26.631 | 1.873 | 2.507 | 100 | 0.642 | 5.114 |
| 20 | 10 | 3.746 | 4.773 | 20.537 | 25.518 | 20.537 | 26.631 | 3.746 | 5.014 | 95.198 | 0.617 | 4.915 |
| 20 | 15 | 5.619 | 5.982 | 20.537 | 21.742 | 20.537 | 26.631 | 5.619 | 7.521 | 79.529 | 0.531 | 4.226 |
| 20 | 20 | 7.492 | 6.860 | 20.537 | 18.932 | 20.537 | 26.631 | 7.492 | 10.029 | 68.404 | 0.465 | 3.701 |
| 20 | 25 | 9.365 | 7.528 | 20.537 | 16.760 | 20.537 | 26.631 | 9.365 | 12.536 | 60.057 | 0.413 | 3.290 |
| 20 | 30 | 11.238 | 8.055 | 20.537 | 15.030 | 20.537 | 26.631 | 11.238 | 15.043 | 53.548 | 0.371 | 2.958 |
| 20 | 35 | 13.111 | 8.481 | 20.537 | 13.621 | 20.537 | 26.631 | 13.111 | 17.550 | 48.324 | 0.337 | 2.687 |
| 20 | 40 | 14.984 | 8.832 | 20.537 | 12.451 | 20.537 | 26.631 | 14.984 | 20.058 | 44.035 | 0.309 | 2.460 |
| 20 | 45 | 16.858 | 9.127 | 20.537 | 11.465 | 20.537 | 26.631 | 16.858 | 22.565 | 40.449 | 0.285 | 2.268 |
| 20 | 50 | 18.731 | 9.378 | 20.537 | 10.623 | 20.537 | 26.631 | 18.731 | 25.072 | 37.405 | 0.264 | 2.103 |

| Geometry Parameters | | Projected Waveguide Facet onto channel wall | | Angle of collection | | Angle of possible collection based on waveguide NA | | Dimensions of collectable light at channel wall based on waveguide NA | | Efficiency of collection % of NA | Solid angle | % collection of Sphere |
|---|---|---|---|---|---|---|---|---|---|---|---|---|
| Wall Width | Channel half-width | Width (lateral) | Height (trans) | Lateral | Transverse | Lateral | Transverse | Width (lateral) | Height (trans) | % | STR | % |
| 10 | 5 | 1.873 | 2.507 | 20.537 | 26.631 | 20.537 | 26.631 | 1.873 | 2.507 | 100 | 0.642 | 5.114 |
| 10 | 10 | 3.746 | 5.014 | 20.537 | 26.631 | 20.537 | 26.631 | 3.746 | 5.014 | 100 | 0.642 | 5.114 |
| 10 | 15 | 5.619 | 7.521 | 20.537 | 26.631 | 20.537 | 26.631 | 5.619 | 7.521 | 100 | 0.642 | 5.114 |
| 10 | 20 | 7.492 | 8.888 | 20.537 | 23.960 | 20.537 | 26.631 | 7.492 | 10.029 | 88.624 | 0.582 | 4.633 |
| 10 | 25 | 9.365 | 9.414 | 20.537 | 20.636 | 20.537 | 26.631 | 9.365 | 12.536 | 75.100 | 0.505 | 4.021 |
| 10 | 30 | 11.238 | 9.808 | 20.537 | 18.104 | 20.537 | 26.631 | 11.238 | 15.043 | 65.198 | 0.445 | 3.545 |
| 10 | 35 | 13.111 | 10.112 | 20.537 | 16.116 | 20.537 | 26.631 | 13.111 | 17.550 | 57.620 | 0.397 | 3.167 |
| 10 | 40 | 14.984 | 10.355 | 20.537 | 14.514 | 20.537 | 26.631 | 14.984 | 20.058 | 51.629 | 0.359 | 2.859 |
| 10 | 45 | 16.858 | 10.554 | 20.537 | 13.199 | 20.537 | 26.631 | 16.858 | 22.565 | 46.771 | 0.327 | 2.605 |
| 10 | 50 | 18.731 | 10.719 | 20.537 | 12.099 | 20.537 | 26.631 | 18.731 | 25.072 | 42.751 | 0.300 | 2.391 |

| Wall Width | Channel half-width | Width (lateral) | Height (trans) | Lateral | Transverse | Lateral | Transverse | Width (lateral) | Height (trans) | % | STR | % |
|---|---|---|---|---|---|---|---|---|---|---|---|---|
| 5 | 5 | 1.873 | 2.507 | 20.537 | 26.631 | 20.537 | 26.631 | 1.873 | 2.507 | 100 | 0.642 | 5.114 |
| 5 | 10 | 3.746 | 5.014 | 20.537 | 26.631 | 20.537 | 26.631 | 3.746 | 5.014 | 100 | 0.642 | 5.114 |
| 5 | 15 | 5.619 | 7.521 | 20.537 | 26.631 | 20.537 | 26.631 | 5.619 | 7.521 | 100 | 0.642 | 5.114 |
| 5 | 20 | 7.492 | 10.029 | 20.537 | 26.631 | 20.537 | 26.631 | 7.492 | 10.029 | 100 | 0.642 | 5.114 |
| 5 | 25 | 9.365 | 10.749 | 20.537 | 23.266 | 20.537 | 26.631 | 9.365 | 12.536 | 85.747 | 0.566 | 4.506 |
| 5 | 30 | 11.238 | 10.996 | 20.537 | 20.131 | 20.537 | 26.631 | 11.238 | 15.043 | 73.100 | 0.493 | 3.926 |
| 5 | 35 | 13.111 | 11.183 | 20.537 | 17.720 | 20.537 | 26.631 | 13.111 | 17.550 | 63.721 | 0.436 | 3.472 |
| 5 | 40 | 14.984 | 11.329 | 20.537 | 15.814 | 20.537 | 26.631 | 14.984 | 20.058 | 56.483 | 0.390 | 3.109 |
| 5 | 45 | 16.858 | 11.446 | 20.537 | 14.271 | 20.537 | 26.631 | 16.858 | 22.565 | 50.725 | 0.353 | 2.812 |
| 5 | 50 | 18.731 | 11.542 | 20.537 | 12.998 | 20.537 | 26.631 | 18.731 | 25.072 | 46.034 | 0.322 | 2.566 |

## Appendix C Sample code used to generate intensity value matrix from image.

```
1    //run a loop to cover each pixel in the roi tool

width=get_parameter("RoiTool0", "Width");
height=get_parameter("RoiTool0", "Height");

startx = int(width/2);
starty = int(height/2);

channelwidth=get_parameter("CaliperTool0", "ActualSize");
blobcentre=get_parameter("BlobTool0", "BestCentroidY");
channelcentre=get_parameter("CaliperTool0", "LocationCenterY");
startingposition=channelwidth/2 - height/2 + blobcentre-channelcentre;


file = fopen("C:/Documents and Settings/wattsb/My Documents/Script
files/June18_6um_ONGMM_0.58_500_1.txt", "w");

printf(file, "%d %f\n", int(height), startingposition);
printf(file, "%f\n", 50/channelwidth);


for (i=1;i<height;i++)
{
   //printf("\n%d", i);
   set_output_integer("roiY",  i-starty);
   printf(file, "\n%i ", i);
   for (j=1;j<width;j++)
   {
         set_output_integer("roiX", j-startx);
         run_step("Histogram0");
         //store the intensity of the particular pixel to file
         //printf("%d ", j);
         printf(file,"%d ", get_parameter("Histogram0", "Max")); /*writes*/

   }

}

close(file); /*done!*/
```

# Appendix D Sample code to find the points that define the region of 95% intensity

```
Sub Max_find()
'
' Max_find Macro
' Macro recorded 11/19/2009 by Benjamin
'
' Keyboard Shortcut: Ctrl+Shift+F
'
counter = 0
incre = 5
xval = 0
comparrer = ActiveCell.Offset(0, 2).Value
stopper = Range("b1").Value
counter = stopper
Do
   'SolverOk SetCell:=ActiveCell, MaxMinVal:=2, ValueOf:="0", ByChange:= _
    '   Range(ActiveCell.Offset(0, -4), ActiveCell.Offset(0, -1))
   'SolverSolve
   currentvalue = (ActiveCell.Offset(0, counter - incre - stopper).Value +
ActiveCell.Offset(0, counter - incre - stopper - 1).Value + ActiveCell.Offset(0,
counter - incre - stopper - 2).Value) / 3
   If (currentvalue < comparrer) Then
       xval = ActiveCell.Offset(ActiveCell.Offset(0, 3).Value, counter - incre -
stopper).Value
   End If
   counter = counter - 1
 Loop Until counter < stopper / 2

   ActiveCell.Value = xval
   ActiveCell.Offset(1, 0).Activate



End Sub
```

## Appendix E Sample Code for Pulse Detection and Cleaning

```
#include <stdio>
#include <stdlib>
#include <iostream>
#include <cstdlib>
#include <conio>
#define threshold 0.2
#define interval 0.00005

int main ()
{
        FILE *rawdata;
        FILE *refineddata;
        FILE *refinedhist;
        rawdata = fopen(/*"myfile.txt", "r");*/"d:/Ben - Research/Testing DATA/Flow Data/Test
Data/Flow Data - Raw/Sunday May 6/047-03-03 20-113 uL-hr -700V 1e7 100us run 4 5 PS SC.lvm",
"r");
        refineddata = fopen("d:/Ben - Research/Testing DATA/Flow Data/Test Data/Flow Data -
Raw/Sunday May 6/047-03-03 20-113 uL-hr -700V 1e7 100us run 4 5 PS SC - REFINED TESTRAW.txt",
"w");
        refinedhist = fopen("d:/Ben - Research/Testing DATA/Flow Data/Test Data/Flow Data -
Raw/Sunday May 6/047-03-03 20-113 uL-hr -700V 1e7 100us run 4 5 PS SC - REFINED TESTHIST.txt",
"w");

        float *peakvalues = NULL; //array to store values associated with a peak
        float *time = NULL;       //array to track time of peak values
        float beforepeak[5];      //array to hold values before peak
        float afterpeak[5];       //array to hold values after peak
        float hardpeak=0;         //value of peak - eliminating small artifact from each
        float hardtime=0;         //value of time with corresponding peak
        int count = 0;            //holds number of point in the peak
        float filecount;          //holds the raw data number point (to calculate time)
        float t;                  //holds calculated time (temp)
        int flag = 0;             //flags whether peak has been detected and should be
written to file
        float current;
        int i;
        while (!feof(rawdata))
        {
                fscanf(rawdata, "%f\t%f\n", &filecount, &current);
                printf("hello \ttime:%f\tvalue:%f\n", filecount, current);
                if (current > threshold)
                {
                        t = filecount*interval;
                        peakvalues = (float *) realloc (peakvalues, (count + 1) *
sizeof(float));
                        time = (float *) realloc (time, (count + 1) * sizeof(float));
                        peakvalues[count] = current;
                        time[count] = t;
                        flag = 1;
                        count++;
                        if (current > hardpeak)
                        {
                                hardpeak = current;
                                hardtime = t;
                        }
                }
                else if (flag == 1)
                {
                        i = 0;
                        fprintf(refinedhist, "%f\t%f\n", hardtime, hardpeak);
                        printf("\npeak value: %f at time %fs", hardpeak, hardtime);
                        fprintf(refineddata, "%f\t0\n", time[0]-.00005);
                        while (i<count)
                        {
                                fprintf(refineddata, "%f\t%f\n", time[i], peakvalues[i]);
                                i++;
                        }
                        fprintf(refineddata, "%f\t0\n", time[i-1]+.00005);
                        flag = 0;
                        hardpeak = 0;
                        count = 0;
                }
```

```
        }
        fclose(rawdata);
        fclose(refineddata);
        fclose(refinedhist);
        return(0);
}
```

# Appendix F Script to combine raw data files

```
#include <stdio>
#include <math>
#include <stdlib>
#include <iostream>
#include <cstdlib>
#include <conio>
#define thresholdCHIP 0.015
#define thresholdFREE 0.15
#define interval 0.00005
int main ()
{
        FILE *rawdataFREE;
        FILE *rawdataCHIP;
        FILE *refineddataFREE;
        FILE *refineddataCHIP;
        FILE *refinedhistFREE;
        FILE *refinedhistCHIP;
        FILE *combined;
        FILE *combinedHIST;
        rawdataFREE = fopen("d:/Ben - Research/Testing DATA/Flow Data/Test Data/Flow Data - Raw/Onchip june 24 (10um FSB excellent results for scatter paper)/04-08-02-02 10umFSB 100-565 uL-hr -800V 1e4 1e6 30us 5 PS SC run 1 freespace.lvm", "r");
        rawdataCHIP = fopen("d:/Ben - Research/Testing DATA/Flow Data/Test Data/Flow Data - Raw/Onchip june 24 (10um FSB excellent results for scatter paper)/04-08-02-02 10umFSB 100-565 uL-hr -800V 1e4 1e6 30us 5 PS SC run 1 onchip.lvm", "r");
        refineddataFREE = fopen("d:/Ben - Research/Testing DATA/Flow Data/Test Data/Flow Data - Raw/Onchip june 24 (10um FSB excellent results for scatter paper)/04-08-02-02 10umFSB 100-565 uL-hr -800V 1e4 1e6 30us 5 PS SC run 1 freespace - REFINED RAW.txt", "w");
        refinedhistFREE = fopen("d:/Ben - Research/Testing DATA/Flow Data/Test Data/Flow Data - Raw/Onchip june 24 (10um FSB excellent results for scatter paper)/04-08-02-02 10umFSB 100-565 uL-hr -800V 1e4 1e6 30us 5 PS SC run 1 freespace - REFINED HIST.txt", "w");
        refineddataCHIP = fopen("d:/Ben - Research/Testing DATA/Flow Data/Test Data/Flow Data - Raw/Onchip june 24 (10um FSB excellent results for scatter paper)/04-08-02-02 10umFSB 100-565 uL-hr -800V 1e4 1e6 30us 5 PS SC run 1 onchip - REFINED RAW.txt", "w");
        refinedhistCHIP = fopen("d:/Ben - Research/Testing DATA/Flow Data/Test Data/Flow Data - Raw/Onchip june 24 (10um FSB excellent results for scatter paper)/04-08-02-02 10umFSB 100-565 uL-hr -800V 1e4 1e6 30us 5 PS SC run 1 onchip - REFINED HIST.txt", "w");
        combined = fopen("d:/Ben - Research/Testing DATA/Flow Data/Test Data/Flow Data - Raw/onchip june 24 (10um FSB excellent results for scatter paper)/04-08-02-02 10umFSB 100-565 uL-hr -800V 1e4 1e6 30us 5 PS SC run 1 COMBINED.txt", "w");
        combinedHIST = fopen("d:/Ben - Research/Testing DATA/Flow Data/Test Data/Flow Data - Raw/onchip june 24 (10um FSB excellent results for scatter paper)/04-08-02-02 10umFSB 100-565 uL-hr -800V 1e4 1e6 30us 5 PS SC run 1 COMBINEDHIST.txt", "w");
        float *peakvaluesFREE = NULL;   //array to store values associated with a peak, will be sized depending on peak values
        float *peakvaluesCHIP = NULL;   //array to store values associated with a peak, will be sized depending on peak values
        float *time = NULL;             //array to track time of peak values
        float hardpeakFREE=0;           //value of peak - eliminating small artifact from each
        float hardtime=0;               //value of time with corresponding peak
        float hardpeakCHIP=0;
        int count = 0;                          //holds number of point in the peak
        float filecountFREE;            //holds the raw data number point (to calculate time)
        float filecountCHIP;
        float t;                        //holds calculated time (temp)
        int flag = 0;                   //flags whether peak has been detected and thus should be written to file
        float currentFREE;
        float currentCHIP;
        int i;
        while (!feof(rawdataFREE))
        {
                fscanf(rawdataFREE, "%f\t%f\n", &filecountFREE, &currentFREE);
                fscanf(rawdataCHIP, "%f\t%f\n", &filecountCHIP, &currentCHIP);
                printf("hello \ttime:%f\tvalue free:%f\tvalue chip:%f\n", filecountFREE, currentFREE, currentCHIP);
                if ((currentFREE > thresholdFREE) || (currentCHIP > thresholdCHIP))
                {
                        t = filecountFREE*interval;
                        peakvaluesFREE = (float *) realloc (peakvaluesFREE, (count + 1) * sizeof(float));
                        peakvaluesCHIP = (float *) realloc (peakvaluesCHIP, (count + 1) * sizeof(float));
                        time = (float *) realloc (time, (count + 1) * sizeof(float));
                        peakvaluesFREE[count] = currentFREE;
                        peakvaluesCHIP[count] = currentCHIP;
                        time[count] = t;
                        flag = 1;
                        count++;
                        if ((currentFREE > hardpeakFREE) && (currentFREE > thresholdFREE))
                        {
```

```
                hardpeakFREE = currentFREE;
                hardtime = t;
                //getch();
            }
            if ((currentCHIP > hardpeakCHIP) && (currentCHIP > thresholdCHIP))
            {
                hardpeakCHIP = currentCHIP;
                hardtime = t;
                //getch();
            }
        }
        else if (flag == 1)
        {
            i = 0;
            fprintf(combinedHIST, "%f\t%f\t%f\n", hardtime, hardpeakFREE, hardpeakCHIP);
            fprintf(refineddataFREE, "%f\t0\n", time[0]-.00005);
            fprintf(refineddataCHIP, "%f\t0\t0\n", time[0]-.00005);
            fprintf(combined, "%f\t0\t-.75\n", time[0]-.00005);
            while (i<count)
            {
                fprintf(refineddataFREE, "%f\t%f\n", time[i], peakvaluesFREE[i]);
                fprintf(refineddataCHIP, "%f\t%f\n", time[i], peakvaluesCHIP[i]);
                fprintf(combined, "%f\t%f\t%f\n", time[i], peakvaluesFREE[i], peakvaluesCHIP[i]*10-
.75);

                i++;
            }
            fprintf(refineddataFREE, "%f\t0\n", time[i-1]+.00005);
            fprintf(refineddataCHIP, "%f\t0\n", time[i-1]+.00005);
            fprintf(combined, "%f\t0\t-.75\n", time[i-1]+.00005);
            flag = 0;
            hardpeakFREE = 0;
            hardpeakCHIP = 0;
            count = 0;
        }

    }
    fclose(rawdataFREE);
    fclose(rawdataCHIP);
    fclose(refineddataFREE);
    fclose(refineddataCHIP);
    fclose(refinedhistFREE);
    fclose(refinedhistCHIP);
    fclose(combined);
    fclose(combinedHIST);

    return(0);
}
```

# Appendix G Script to perfrom simultaneous detection analysis

```
#include <stdio>
#include <math>
#include <stdlib>
#include <iostream>
#include <cstdlib>
#include <conio>
#define thresholdCHIP 0.015
#define thresholdFREE 0.15
int main ()
{
        FILE *combined;
        combined = fopen("D:/Research/Testing DATA/Flow Data/Test Data/Flow Data Raw/Onchip june 24 (10um FSB excellent results for scatter paper)/04-08-02-02 10umFSB 100-565 uL-hr -800V 1e4 1e6 30us 5 PS SC run 3 wow COMBINEDHIST.txt", "r");
        float valueFREE;
        float valueCHIP;
        int countFREE=0;
        int countCHIP=0;
        int countCOMBINED=0;
        float percentFREE;
        float percentCHIP;
        float time;
        int countloneFREE=0;
        int countloneCHIP=0;
        while (!feof(combined))
        {
                fscanf(combined, "%f\t%f\t%f\n", &time, &valueFREE, &valueCHIP);
                printf("%f\t%f\t%f\n", time, valueFREE, valueCHIP);
                if (valueFREE > thresholdFREE)
                {
                        countFREE++;
                }
                if (valueCHIP > thresholdCHIP)
                {
                        countCHIP++;
                }
                if ((valueFREE > thresholdFREE) && (valueCHIP > thresholdCHIP))
                {
                        countCOMBINED++;
                }
                if ((valueFREE > thresholdFREE) && !(valueCHIP > thresholdCHIP))
                {
                        countloneFREE++;
                }
                if ((valueCHIP > thresholdCHIP) && !(valueFREE > thresholdFREE))
                {
                        countloneCHIP++;
                }
        }
        percentFREE = (float)countCOMBINED / (float)countFREE * 100;
        percentCHIP = (float)countCOMBINED / (float)countCHIP * 100;
        printf("Total FREESPACE Hits:\t%d\nTotal lone FREE Hits:\t%d\nTotal ONCHIP Hits:\t%d\nTotal lone CHIP Hits:\t%d\nTotal Combined Hits:\t%d\nPercent free space:\t%f\nPercent on chip:\t%f\n", countFREE, countloneFREE, countCHIP, countloneCHIP, countCOMBINED, percentFREE, percentCHIP);
        fclose(combined);
        return(0);
}
```

# References

---

[1] B. Watts, Z. Zhang, and C-Q. Xu, “Microchip-Based Flow Cytometry in Photonic Sensing: Principles and Application for Safety and Security Monitoring,” 1st Edition, 2012, John Wiley & Sons, Hoboken, New Jersey.

[2] Invitrogen Corporation, accessed January 2011. http://probes.invitrogen.com/resources/education/tutorials/4Intro_Flow/player.html.

[3] H. M. Shapiro, “Practical Flow Cytometry,” 4th Edition, 2003, John Wiley & Sons, Hoboken, New Jersey.

[4] L. Spielman, and S. L. Goren, “Improving resolution in Coulter counting by hydrodynamic focusing,” J. Colloid Interface Sci. **26**(2), 1968, 175-182.

[5] Department of Biology, University of California at Berkeley, accessed January 2011. http://biology.berkeley.edu/crl/flow_cytometry_basic.html.

[6] N. Panchuk-Voloshina, R. P. Haugland, J. Bishop-Steward, M. K. Bhalgat, F. Mao, W. Y. Leung, and R. P Haugland, “Alexa dyes, a series of new fluorescent dyes that yield exceptionally bright, photostable conjugates,” J. Histohem. Cytochem. **47**(9), 1999, 1179-1188.

[7] S. M. Burrows, R. D. Reif, and D. Pappas, “Investigation of photobleaching and saturation of single molecules by fluorophore recrossing events,” Analytica Chim. Acta **598**(1), 2007, 135-142.

[8] G. van den Engh and C. Farmer, “Photo-Bleaching and Photon Saturation in Flow Cytometry,” Cytometry **13**(7), 1992, 669-667.

[9] K. M. Marks and G. P. Nolan, “Chemical labeling strategies for cell biology,” Nat. Methods **3**(8), 2006, 591-596.

[10] M. Sameiro and T. Goncalves, “Fluorescent Labeling of Biomolecules with Organic Probes,” Chem. Rev. **109**(1), 2009, 190-212.

[11] Olympus Corporation, accessed July 2012. http://www.olympusconfocal.com/java/dualprobes/index.html.

[12] S. C. De Rosa, J. M. Brenchley, and M. Roederer, “Beyond six colors: A new era in flow cytometry,” Nat. Medicine **9**(1), 2003, 112-117.

[13] M. Roederer, S. De Rosa, R. Gerstein, M. Anderson, M. Bigos, R. Stovel, T. Nozaki, D. Parks, L. Herzenberg, and L. Herzenberg, “8 Color, 10-Parameter Flow Cytometry to Elucidate Complex Leukocyte Heterogeneity,” Cytometry **29**(), 1997, 328-339.

[14] S. C. De Rosa, L. A. Herzenberg, L. A. Herzenberg, and M. Roederer, “11-color, 13-parameter flow cytometry: Identification of naive T cells by phenotype, function, and T-cell receptor diversity,” Nat. Medicine **7**(2), 2001, 245-248.

[15] S. P. Perfetto, P. K. Chattopadhyay, and M. Roederer, “Seventeen-colour flow cytometry: unraveling the immune system,” Nat. Rev. Immun. **4**(8), 2004, 648-655.

[16] J. J. H. Bleesing and T. A. Fleisher, “Immunophenotyping,” Semin. Hematol. **38**(2), 2001, 110-110.

[17] N. Baumgarth and M. Roederer, “A practical approach to multicolor flow cytometry for immunophenotyping,” J. Immunol. Methods **243**(1-2), 2000, 77-97.

[18] G. Garratty and P. A. Arndt, “Applications of flow cytofluorometry to red blood cell immunology,” Cytometry **38**(6), 1999, 259-267.

[19] H. Gabriel and W Kindermann, “Flow-cytometry – principles and applications in exercise immunology,” Sports Med. **20**(5), 1995, 302-320.

[20] J. J. H. Bleesing and T. A. Fleisher, “Cell Function-Based Flow Cytometry,” Semin. Hematol. **38**(2), 2001, 169-178.

[21] Z. Darzynkiewicz, E. Bedner, and P. Smolewski, “Flow Cytometry in Analysis of Cell Cycle and Apoptosis,” Semin. Hematol. **38**(2), 2001, 179-193.

[22] M. Stetler-Stevenson and R. C. Braylan, “Flow Cytometric Analysis of Lymphomas and Lymphoproliferative Disorders,” Semin. Hematol. **38**(2), 2001, 111-123.

[23] E. G. Weir and M. J. Borowitz, “Flow Cytometry in the Diagnosis of Acute Leukemia,” Semin. Hematol. **38**(2), 2001, 124-138.

---

[24] D. Campana and F. G. Behm, “Immunophenotyping of leukemia,” J. Immunol. Methods **243**(1-2), 2000, 59-75.

[25] J. Porter, D. Deere, M. Hardman, C. Edwards, and R. Pickup, “Go with the flow – use of flow cytometry in environmental microbiology,” FEMS Microbiol. Ecol. **24**(2), 1997, 93-101.

[26] P. L. Bergquist, E. M. Hardiman, B. C. Ferrari, and T. Winsley, “Applications of flow cytometry in environmental microbiology and biotechnology,” Extremophiles. **13**(),2009, 389-401.

[27] J. J. McSharry, “Uses of flow cytometry in virology,” Clin. Microbiol. Rev. **7**(4), 1994, 576-604.

[28] J. Giorgi, J. L. Fahey, D. C. Smith, L. E. Hultin, H. L. Cheng, R. T. Mitsuyasu, and R. Detels, “Early Effect of HIV on CD4 Lymphocytes in vivo,” J. Immunol. **138**(11), 1987, 3725-3730.

[29] B. H. Robertson, and J. K. A. Nicholson, “New microbiology tools for public health and their implications,” Annu. Rev. Public Health **26**(1), 2005, 281-302.

[30] BD Biosciences, accessed October 2012.
http://www.bdbiosciences.com/instruments/accuri/index.jsp.

[31] Beckman Coulter, accessed October 2012.
http://www.beckmancoulter.com/wsrportal/wsr/research-and-discovery/products-and-services/flow-cytometry/flow-cytometers/cyan-adp-analyzer/index.htm.

[32] Applied Biosystems, accessed October 2012.
http://www.appliedbiosystems.com/absite/us/en/home/applications-technologies/flow-cytometry/attune-acoustic-focusing-cytometer.html.

[33] S. F. Ibrahim and G. van den Engh, “High-speed cell sorting: fundamentals and recent advances,” Curr. Opin. Biotechnol. **14**(1), 2003, 5-12.

[34] D. R. Reyes, D. Iossifidis, P-A. Auroux, and A. Manz, “Micro Total Analysis Systems. 1. Introduction, Theory, and Technology,” Anal. Chem. **74**(12), 2002, 2623-2636.

[35] P-A. Auroux, D. Iossifidis, D. R. Reyes, and A. Manz, “Micro Total Analysis Systems. 2. Analytical Standard Operations and Applications,” Anal. Chem. **74**(12), 2002, 2637-2652.

[36] A. Manz, N. Graber, and H. M. Widmer, “Miniaturized Total Chemical Analysis Systems: a Novel Concept for Chemical Sensing,” Sens. Act. B **1**(1-6), 1990, 244-248.

[37] Y. Xia and G. M. Whitesides, “Soft Lithography,” Annu. Rev. Mater. Sci. **28**, 1998, 153-184.

[38] C. S. Effenhauser, A. Paulus, A. Manz, and H. M. Widmer, “High-Speed Separation of Antisense Oligonucleotides on a Micromachined Capillary Electrophoresis Device,” Anal. Chem. **66**(18), 1994, 2949-2953.

[39] D. J. Harrison, K. Fluri, K. Seiler, Z. Fan, C. S. Effenhauser, and A. Manz, “Micromachining a Miniaturized Capillary Electrophoresis-Based Chemical Analysis System on a Chip,” Science **261**(5123), 1993, 895-897.

[40] M. A. McClain, C. T. Culbertson, S. C. Jacobson, and J. M. Ramsey, “Flow Cytometry of *Escherichia coli* on Microfluidic Devices,” Anal. Chem. **73**(21), 2001, 5334-5338.

[41] D-Q. Li, “Electrokinetics in Microfluidics,” 1st Edition, 2004, Elsevier Ltd., London, UK.

[42] A. R. Leeds, E. R. Van Keuren, M. E. Durst, T. W. Schneider, J. F. Currie, and M. Paranjape, “Integration of microfluidic and microoptical elements using a single-mask photolithographic step,” Sens. Act. A **115**(), 2004, 5;71-580.

[43] R. Jackman, T. Floyd, R. Ghodssi, M Schmidt, and K. Jensen, “Microfluidic systems with on-line UV detection fabricated in photodefinable epoxy,” J. Micromech. Microeng. **11**(3), 2001, 263-269.

[44] K. B. Mogensen, J. El-Ali, A. Wolff, and J. P. Kutter, “Integration of polymer waveguides for optical detection in microfabricated chemical analysis systems,” Appl. Optics **42**(19), 2003, 4072-4079.

[45] D. C. Duffy, J. C. McDonald, O. J. A. Schueller, and G. M. Whitesides, “Rapid Prototyping of Microfluidic Systems in Poly(dimethylsiloxane),” Anal. Chem. **70**(23), 1998, 4974-4984.

[46] F. J. Blanco, M. Agirregabiria, J. Garcia, J. Berganzo, M. Tijero, M. T. Arroyo, J. M. Ruano, I. Aramburu, and K. Mayora, “Novel three-dimensional embedded SU-8 microchannels fabricated

---

using a low temperature full wafer adhesive bonding," J. Micomech. Microeng. **14**(7), 2004, 1047-1056.

[47] Z. Wang, O. Hansen, P. K. Petersen, A. Rogeberg, J. P. Kutter, D. D. Bang, and A. Wolff, "Dielectrophoresis microsystem with integrated flow cytometers for on-line monitoring of sorting efficiency," Electrophoresis **27**(24), 2006, 5081-5092.

[48] S. K. Sia, and G. M. Whitesides, "Microfluidic devices fabricated in poly(dimethylsiloxane) for biological studies," Electrophoresis **24**(21), 2003, 3563-3576.

[49] J. M. Ruano-Lopez, M. Aguirregabiria, M. Tijero, M. T. Arroyo, J. Elizalde, J. Berganzo, I. Aranburu, F. J. Blanco, and K. Mayora, "A new SU-8 process to integrate buried waveguides and sealed microchannels for a Lab-on-a-Chip," Sens. Act. B **114**(1), 2006, 542-551.

[50] K. B. Mogensen, H. Klank, and J. P. Kutter, "Recent developments in detection for microfluidic systems," Electrophoresis **25**(21-22), 2004, 3498-3512.

[51] G-B. Lee, C-I. Hung, B-J. Ke, G-R. Huang, B-H. Hwei, and H-F. Lai, "Hydrodynamic Focusing for a Micromachined Flow Cytometer," J. Fluids Eng. **123**(3), 2001, 672-679.

[52] C. Mu, F. Zhang, Z. Zhang, M. Lin, and X. Cao, "Highly efficient dual-channel and cytometric detection of micron-sized particles in a microfluidic device," Sens Actuators B Chem. **151**(2), 2011, 402-409.

[53] N. Sundararajan, M. S. Pio, L. P. Lee, and A. A. Berlin, "Three-Dimensional Hydrodynamic Focusing in Polydimethysiloxane (PDMS) Microchannels," J. Microelectromech. Sys. **13**(4), 2004, 559-567.

[54] C. Simonnet, and A. Groisman, "Two-dimensional hydrodynamic focusing in a simple microfluidic device," Appl. Phys. Lett. **87**(11), 2005, 114104 1-4.

[55] C. Simonnet, and A. Groisman, "High-Throughput and High-Resolution Flow Cytometry in Molded Microfluidic Devices," Anal. Chem. **78**(16), 2006, 5653-5663.

[56] H-C. Lee, H-H. Hou, R-J. Yang, C-H. Lin, and L-M. Fu, "Microflow cytometer incorporating sequential micro-weir structure for three-dimensional focusing," Microfluid. Nanofluid. **11**(4), 2011, 469-478.

[57] P. B. Howell Jr., J. P. Golden, L. R. Hilliard, J. S. Erickson, D. R. Mott, and F. S. Ligler, "Two simple and rugged designs for creating microfluidic sheath flow," Lab Chip **8**(7), 2008, 1097-1103.

[58] X. Mao, J. R. Waldeisen, and T. J. Huang, "'Microfluidic drifting' – implementing three-dimensional hydrodynamic focusing with a single-layer planar microfluidic device," Lab Chip **7**(10), 2007, 1260-1262.

[59] A. A. S. Bhagat, S. S. Kuntaegowdanahalli, and I. Papautsky, "Inertial microfluidics for continuous particle filtration and extraction," Microfluid. Nanofluid. **7**(), 2009, 217-226.

[60] S. S. Kuntaegowdanahalli, A. A. S. Bhagat, G. Kumar, and I. Papautsky, "Intertial microfluidics for continuous particle separation in spiral microchannels," Lab Chip **9**(20), 2009, 2973-2980.

[61] A. A. S. Bhagat, S. S. Kuntaegowdanahalli, and I. Papautsky, "Enhanced particle filtration in straight microchannels using shear-modulated inertial migration," Phys. Fluids **20**(10), 2008, 101702 1-5.

[62] A. A. S. Bhagat, S. S. Kuntaegowdanahalli, and I. Papautsky, "Continuous particle separation in spiral microchannels using dean flows and differential migration," Lab Chip, **8**(11), 2008, 1906-1914.

[63] T. D. Chung, and H. C. Kim, "Recent advances in miniaturized microfluidic flow cytometry for clinical use," Electrophoresis **28**(24), 2007, 4511-4520.

[64] C. Sakamoto, N. Yamaguchi, M. Nasu, "Rapid and Simple Quantification of Bacterial Cells by Using a Microfluidic Device," Appl. Environ. Microbiol. **71**(2), 2005, 1117-1121.

[65] J. M. Ramsey, "The burgeoning power of the shrinking laboratory," Nat. Biotechnol. **17**(11), 1999, 1061-1062.

[66] A. Y. Fu, H. P. Chou, C. Spence, F. H. Arnold, and S. R. Quake, "An integrated microfabricated cell sorter," Anal. Chem. **74**(11), 2002, 2451-2457.

---

[67] A. Y. Fu, C. Spence, A. Scherer, F. H. Arnold, and S. R. Quake, "A microfabricated fluorescence-activated cell sorter," Nat. Biotechnol. **17**(11), 1999, 1109-1111.

[68] P. S. Dittrich, and P. Schwille, "An Integrated Microfluidic System for Reaction, High-Sensitivity Detection, and Sorting of Fluorescent Cells and Particles," Anal. Chem. **75**(21), 2003, 5767-5774.

[69] C. M. Chang, S-K. Hsiung, and G-B. Lee, "A Micromachine-based Flow Cytometer Chip Integrated with Micro Pumps/Valves for Multiwavelength Detection Applications," Mater. Sci. Forum **505**, 2006, 637-642.

[70] P. S. Dittrich, K. Tachikawa, and A. Manz, "Micro Total Analysis Systems. Latest Advancements and Trends," Anal. Chem. **78**(), 2006, 3887-3907.

[71] H. M. Shapiro, and M. Hercher, "Flow Cytometers Using Optical Waveguides in Place of Lenses for Specimen Illumination and Light Collection," Cytometry **7**(2), 1986, 221-223.

[72] Y. C. Tung, M. Zhang, C. T. Lin, K. Kurabayashi, and S. J. Skerlos, "PDMS-based opto-fluidic micro flow cytometer with two-color, multi-angle, fluorescence detection capability using PIN photodiodes," Sens. Act. B **98**(2-3), 2004, 356-367.

[73] G-B. Lee, C-H. Lin, and G-L. Chang, "Micro flow cytometers with buried SU-8/SOG optical waveguides," Sens. Act. A **103**(1-2), 2003, 165-170.

[74] M. L. Chabinyc, D. T. Chiu, J. C. McDonald, A. D. Stroock, J. F. Christian, A. M. Karger, and G. M. Whitesides, "An Integrated Fluorescence Detection System in Poly(dimethylsiloxane) for Microfluidic Applications," Anal. Chem. **73**(18), 2001, 4491-4498.

[75] N. Hashemi, J. S. Erickson, J. P. Golden, and F. S. Ligler, "Optofluidic characterization of marine algae using a microflow cytometer," Biomicrofluidics **5**(), 2011, 032009, 1-9.

[76] K. B. Mogensen, N. J. Petersen, J. Hubner, and J. P. Kutter, "Monolithic integration of optical waveguides for absorbance detection in microfabricated eletrophoresis devices," Electrophoresis **22**(18), 2001, 3930-3938.

[77] K. B. Mogensen, Y. C. Kwok, J. C. T. Eijkel, N. J. Petersen, A. Manz, and J. P. Kutter, "A Microfluidic Device with an Integrated Waveguide Beam Splitter for Velocity Measurements of Flowing Particles by Fourier Transformation," Anal. Chem. **75**(18), 2003, 4931-4936.

[78] V. Lien, K. Zhao, Y. Berdichevsky, and Y-H. Lo, "High-Sensitivity Cytometric Detection Using Fluidic-Photonic Integrated Circuits with Array Waveguides," IEEE J. Sel. Top. Quant. **11**(4), 2005, 827-834.

[79] C-H. Chen, F. Tsai, V. Lien, N. Justis, and Y-H. Lo, "Scattering-Based Cytometric Detection Using Integrated Arrayed Waveguides with Microfluidics," IEEE Photon. Tech. L. **19**(6), 2007, 441-443.

[80] C. L. Bliss, J. N. McMullin, and C. J. Backhouse, "Rapid fabrication of a microfluidic device with integrated optical waveguides for DNA fragment analysis," Lab Chip **7**(10), 2007, 1280-1287.

[81] P. Fei, Z. Chen, Y. Men, A. Li, Y. Shen, and Y. Huang, "A compact optofluidic cytometer with integrated liquid-core/PDMS-cladding waveguides," Lab Chip **12**(19), 2012, 3700-3706.

[82] A. R. Hawkins, and H. Schmidt, "Optofluidic waveguides: II. Fabrication and structures," Microfluid. Nanofluid. **4**(1-2), 2008, 17-32.

[83] C. L. Bliss, J. N. McMullin, and C. J. Backhouse, "Integrated wavelength-selective optical waveguides for microfluidic-based laser-induced fluorescence detection," Lab Chip **8**(1), 2008, 143-151.

[84] D. Yin, D. W. Deamer, H. Schmidt, J. P. Barber, and A. R. Hawkins, "Integrated optical waveguides with liquid cores," Appl. Phys. L. **85**(16), 2004, 3477-3479.

[85] K. S. Lee, H. L. T. Lee, and R. J. Ram, "Polymer waveguide backplanes optical sensor interfaces in microfluidics," Lab Chip **7**(11), 2007, 1539-1545.

[86] D. B. Wolfe, D. V. Vezenov, B. T. Mayers, and G. M. Whitesides, "Diffusion-controlled optical elements for optofluidics," Appl. Phys. L. **87**(18), 2005, 181105, 1-3.

---

[87] K. W. Ro, K. Lim, B. C. Shim, and J. H. Hahn, "Integrated light collimating system for extended optical-path length absorbance detection in microchip-based capillary electrophoresis," Anal. Chem. **77**(16), 2005, 5160–5166.

[88] S. Park, Y. Jeong, J. Kim, K. Choi, K. C. Kim, D. S. Chung, and K. Chun, "Fabrication of Poly(dimethylsiloxane) Microlens for Laser-Induced Fluorescence Detection," Jpn. J. Appl. Phys. **45**(6B), 2006, 5614–5617.

[89] S.-K. Hsiung, C.-H. Lin, and G.-B. Lee, "A microfabricated capillary electrophoresis chip with multiple buried optical fibres and microfocusing lens for multiwavelength detection," Electrophoresis **26**(6), 2005, 1122–1129.

[90] Z. Wang, J. El-Ali, M. Engelund, T. Gotsaed, I. R. Perch-Nielsen, K. B. Mogensen, D. Snakenborg, J. P. Kutter, and A. Wolff, "Measurements of scattered light on a microchip flow cytometer with integrated polymer based optical elements," Lab Chip **4**(4), 2004, 372–377.

[91] B. R. Watts, T. Kowpak, Z. Zhang, C-Q. Xu, and S. Zhu, "Formation of bowtie-shaped excitation in a photonic-microfluidic integrated devices," Microw. Opt. Tech. L. **53**(11), 2011, 2583-2586.

[92] D. Barat, D. Spencer, G. Benazzi, M. C. Mowlem, and H. Morgan, "Simultaneous high speed optical and impedance analysis of single particles with a microfluidic cytometer," Lab Chip **12**(1), 2012, 118-126.

[93] S-K. Hsiung, C-H. Lee, and G-B. Lee, "Microcapillary electrophoresis chips utilizing controllable micro-lens structures and buried optical fibers for on-line optical detection," Electrophoresis **29**(9), 1866-1873.

[94] M. Rosenauer, W. Buchegger, I. Finoulst, P. Verhaert, and M. Vellekoop, "Miniaturized flow cytometer with 3D hydrodynamic particle focusing and integrated optical elements applying silicon photodiodes," Microfluid. Nanofluid. **10**(4), 2011, 761-771.

[95] M. Rosenauer, and M. J. Vellekoop, "Characterization of a microflow cytometer with an integrated three-dimensional optofluidic lens system," Biomicrofluidics **4**(4), 2010, 043005 1-12

[96] E. Schonbrun, P. E. Steinvurzel, and K. B. Crozier, "A microfluidic fluorescence measurement system using an astigmatic diffractive microlens array," Opt. Express **19**(2), 2011, 1385-1394.

[97] J. Godin, C-H. Chen, S. H. Cho, W. Qiao, F. Tsai, and Y-H. Lo, "Microfluidics and photonics for Bio-system-on-a-chip: a review of advancements in technology towards a microfluidic flow cytometry chip", J. Biophoton. **1**(5), 2008, 355-376.

[98] B. Watts, Z. Zhang, C-Q. Xu, X. Cao, and M. Lin, "A photonic-microfluidic integrated device for reliable fluorescence detection and counting," Electrophoresis **33**(), 2012, 3236-3244.

[99] X. Mao, A. A. Nawaz, S-C. S. Lin, M. I. Lapsley, Y. Zhao, J. P. McCoy, W. S. El-Deiry, and T. J. Huang, "An integrated, multiparametric flow cytometry chip using 'microfluidic drifting' based three-dimensional hydrodynamic focusing," Biomicrofluidics **6**(2), 2012, 024113 1-10.

[100] M. Ikeda, N. Yamaguchi, and M. Nasu, "Rapid On-chip flow cytometric Detection of *Listeria monocytogenes* in Milk," J. Health Sci. **55**(5), 2009, 851-856.

[101] S. K. Sia, and L. J. Kricka, "Microfluidics and point-of-care testing," Lab Chip **8**(), 2008, 1982-.

[102] S. Schumacher, J. Nestler, T. Otto, M. Wegener, E. Ehrentreich-Forster, D. Michel, K. Wunderlich, S. Palzer, K. Sohn, A. Weber, M. Burgard, A. Grzesiak, A. Teichert, A. Brandenburg, B Koger, J. Albers, E. Nebling, and F. F. Bier, "Highly-integrated lab-on-chip system for point-of care multiparameter analysis," Lab Chip **12**(), 2012, 464-.

[103] F. B. Myers, and L. P. Lee, "Innovations in optical microfluidic technologies for point-of-care diagnostics," Lab Chip **8**(), 2008, 2015-.

[104] T. D. Chung and H. C. Kim, "Recent advances in miniaturized microfluidic flow cytometry for clinical use," Electrophoresis **28**(), 2007, 4511-4520.

[105] D. Heikali and D. Di Carlo, "A Niche for Microfluidics in Portable Hematology Analyzers," J. Assoc. Lab Autom. **15**(4), 2010, 319-328.

[106] D. Boye, K. R. Hawkins, M. S. Steele, M. Singhal, and X. Cheng, "Emerging technologies for CD4 T-lymphocyte counting," Trends Biotechnol. **30**(1), 2012, 45-54.

---

[107] P. Kiesel, M. Beck, and N. Johnson, “Monitoring CD4 in Whole Blood with an Opto-fluidic Detector Based on Spatially Modulated Fluorescence Emission,” Cytometry A **79**(5), 2011, 317-324.

[108] M. Frankowski, N. Bock, A. Kummrow, S. Schadel-Ebner, M. Schmidt, A. Tuchscheerer, and J. Neukammer, “A microflow cytometer exploited for the immunological differentiation of Leukocytes,” Cytometry A **79**(8), 2011, 613-624.

[109] D. Mabey, R. W. Peeling, A. Ustianowski, and M. D. Perkins, “Diagnostics for the developing world,” Nature Rev. Microbiol. **2**(3), 2004, 231-240.

[110] UNICEF, UNAIDS, WHO, and MSF, “Sources and Prices of selected medicines and diagnostics for people living with HIV/AIDS,” Report prepared June, 2005.

[111] A. S. Daar, H. Thorsteinsdottir, D. K. Martin, A. C. Smith, S. Nast, and P. A. Singer, “Top ten biotechnologies for improving health in developing countries,” Nature Gen. **32**(2), 2002, 229-232.

[112] F. L. Pedrotti and L. S. Pedrotti, “Introduction to Optics,” 2nd Edition, 1993, Prentice-Hall, Upper Saddle River, New Jersey.

[113] R. Paschotta, “Field Guide to Lasers,” 1st Edition, 2008, SPIE Press, Bellingham, WA.

[114] R. Paschotta, “Encyclopedia of Laser Physics and Technology,” 1st Edition, 2008, Wiley-VCH, Berlin, Germany.

[115] R. Syms and J. Cozens, “Optical Guided Waves and Devices,” 1st Edition, 1992, McGraw-Hill, Berkshire, England.

[116] T. Kowpak, “Development of Photonic Integrated Microchip-Based Flow Cytometers: Device Fabrication,” Master’s Thesis, McMaster Univeristy, Hamilton Ontario, Canada, 2009.

[117] T. Kowpak, B. R. Watts, Z. Zhang, S. Zhu, and C-Q. Xu, “Fabrication of Photonic/Microfluidic Integrated Devices Using an Epoxy Photoresist,” Macromol. Mater. Eng. **295**(6), 2010, 559-565.

[118] B. R. Watts, T. Kowpak, Z. Zhang, C-Q. Xu, S. Zhu, X. Cao, and M. Lin, “Fabrication and Performance of a Photonic-Microfluidic Integrated Device,” Micromachines **3**(1), 2012, 62-77.

[119] Z. Zhang, P. Zhao, G. Xiao, B. R. Watts, and C-Q. Xu, “Sealing SU-8 microfluidic channels using PDMS,” Biomicrofluidics **5**(04), 2011, 045603 1-8.

[120] C. Mu, Z. Zhang, M. Lin, X. Cao, B. R. Watts, and C-Q. Xu, “A high performance interconnect for PDMS microfluidic devices,” submitted to Sensors and Actuators A.

[121] B. R. Watts, T. Kowpak, Z. Zhang, C-Q. Xu, and S. Zhu, “Formation and characterization of an ideal excitation beam geometry in an optofluidic device,” Biomed. Optics Exp. **1**(3), 2010, 848-860.

[122] B. R. Watts, Z. Zhang, C-Q. Xu, X. Cao, and M. Lin, “Integration of optical components on-chip for scattering and fluorescence detection in an optofluidic device,” Biomed. Optics Exp. **3**(11), 2012, 2784-2793.

[123] B. R. Watts, Z. Zhang, C-Q. Xu, X. Cao, and M. Lin, “Scattering detection using a photonic-microfluidic integrated device with on-chip collection capabilities,” submitted to Biomicrofluidics, November 2012.

[124] B. R. Watts, Z. Zhang, C-Q. Xu, X. Cao, and M. Lin, “A method for detecting forward scattered signals on-chip with a photonic-microfluidic integrated device,” submitted to Biomedical Optics Express, November 2012.

[125] F. Walther, P. Davydovskaya, S. zurcher, M. Kaiser, H. Herberg, A. M. Gigler, and R. W. Stark, “Stability of the hydrophilic behaviour of oxygen plasma activated SU-8,” J. Micromech. Microeng. **17**(3), 2007, 524-531.

[126] A. A. S. Bhagat, S. S. Kuntaegowdanahalli, N. Kaval, C. J. Seliskar, and I. Papautsky, “Inertial microfluidics for sheath-less high-throughput flow cytometry,” Biomed. Microdev. **12**(), 2010, 187-195.

[127] X. Mao, S-C. S. Lin, C. Dong, and T. J. Huang, “Single-layer planar on-chip flow cytometer using microfluidic drifiting based three-dimensional (3D) hydrodynamic focusing,” Lab Chip **9**(), 2009, .

[128] M. J. Kennedy, S. J. Stelick, L. G. Sayam, A. Yen, D. Erickson, and C. A. Batt, “Hydrodynamic optical alignment for microflow cytometry,” Lab Chip **11**(), 2011, 1138-1142.

---

[129] H. T. Chen and Y. N. Wang, "Optical microflow cytometer for particle counting, sizing and fluorescence detection," J. Microfluid. Nanofluid. **6**(), 2008, 529-537.

[130] J. Godin and Y-H. Lo, "Two-parameter angular light scatter collection for microfluidic flow cytometery by unique waveguide structures," Biomed. Optics Exp. **1**(5), 2010, 1472-1479.

[131] M. K. McGaugh, C. M. Verber, and R. P Kenan, "Modified integrated optic Fresnel lens for a waveguide-to-fiber coupling," Appl. Optics **34**(9), 1995, 1562-1568.

[132] C-Y. Han, Y. Ishii, and K. Murata, "Reshaping collimated laser beams with Gaussian profile to uniform profiles," Appl. Optics **22**(22), 1983, 3644-3647.

[133] C. C. Aleksoff, K. K. Ellis, and B. D. Neagle, "Holographic conversion of a Gaussian beam to a near-field uniform beam," Optical Eng. **30**(5), 1991, 537-543.

[134] J. Lavelle and C. O'Sullivan, "Beam shaping using Gaussian beam modes," J. Opt. Soc. AM. A. **27**(2), 2010, 350-357.